Institut für Festkörperphysik

FRIEDRICH-SCHILLER-UNIVERSITÄT JENA

Tieftemperaturphysik Prof. Dr. P. Seidel	**Angewandte Physik / Festkörperphysik** Prof. Dr. T. Fritz
Experimentelle Festkörperphysik Prof. Dr. C. Ronning	**Ionenstrahlphysik** Prof. Dr. W. Wesch
Photovoltaik Prof. Dr. C. Ronning	**Laborastrophysik und Clusterphysik** Prof. Dr. F. Huisken

Annual Report 2012

Institut für Festkörperphysik

Friedrich-Schiller-Universität Jena

Annual Report 2012

Editor: Prof. Dr. Torsten Fritz

Institut für Festkörperphysik
Friedrich-Schiller-Universität Jena
Max-Wien-Platz 1
D-07743 JENA

home page: http://www.ifk.uni-jena.de/

Prof. Dr. Torsten Fritz (director)	Tel.:	+49 (0) 3641 / 947400, 947411
	Fax:	+49 (0) 3641 / 947412
	e-mail:	torsten.fritz@uni-jena.de
	home page:	http://www.organics.uni-jena.de
Prof. Dr. Carsten Ronning	Tel.:	+49 (0) 3641 / 947300, 947301
	Fax:	+49 (0) 3641 / 947302
	e-mail:	carsten.ronning@uni-jena.de
	home page:	http://www.nano.uni-jena.de
		http://www.photovoltaik.uni-jena.de
Prof. Dr. Paul Seidel	Tel.:	+49 (0) 3641 / 947410, 947411
	Fax:	+49 (0) 3641 / 947412
	e-mail:	paul.seidel@uni-jena.de
	home page:	http://www.tieftemperaturphysik.uni-jena.de/
Prof. Dr. Frank Schmidl	Tel.:	+49 (0) 3641 / 947429, 947411
	Fax:	+49 (0) 3641 / 947412
	e-mail:	frank.schmidl@uni-jena.de
	home page:	http://www.tieftemperaturphysik.uni-jena.de/
PD Dr. Elke Wendler	Tel.:	+49 (0) 3641 / 947333
	Fax:	+49 (0) 3641 / 947302
	e-mail:	elke.wendler@uni-jena.de
	home page:	http://www.physik2.uni-jena.de/inst/exphys/ionen/
Dr. Cornelia Jäger	Tel.:	+49 (0) 3641 / 947354
	Fax:	+49 (0) 3641 / 947308
	e-mail:	cornelia.jaeger@uni-jena.de
	home page:	http://www.astrolab.uni-jena.de/

Preface

We like to take this annual report 2012 as an opportunity to thank a lot of people and organizations for their manifold support for our research at the Institute of Solid-State Physics at the Friedrich-Schiller-University Jena. Furthermore, this report, which is already the 17th in this series, is also addressed to the interested scientific community and to our colleagues within the university and from outside.

Special thanks go to the following organizations for their financial support:

- Deutsche Forschungsgemeinschaft – DFG
- Bundesministerium für Bildung und Forschung – BMBF
- Bundesministerium für Umwelt, Naturschutz und Reaktorsicherheit – BMU
- Bundesministerium für Wirtschaft und Technologie – BMWi
- Thüringer Ministerium für Bildung, Wissenschaft und Kultur – TMBWK
- Deutscher Akademischer Austauschdienst – DAAD
- Gesellschaft für Schwerionenforschung, Darmstadt – GSI
- Deutsches Elektronen Synchrotron, Hamburg – DESY
- Several industrial partners

We also like to thank all our colleagues at other universities and institutes which were or still are collaborating with us, but where the collaborative work has not been presented in the research articles of this report. Furthermore, we are very grateful for the work of our very motivated secretaries, technicians and the people in the mechanical and electrical workshops. All of them have contributed to our research in an outstanding way and, thus, to this report.

Prof. Dr. Torsten Fritz
(director)

Contents

7. Teaching activities

8. Personnel

1. Scientific Groups of the Institute

Applied Physics / Solid State Physics

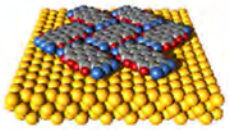

Prof. Dr. Torsten Fritz

- Preparation of highly ordered thin films of organic molecules by UHV-deposition (OMBE)
- Chemical vapor deposition and characterization of carbon nanotubes
- Epitaxial graphene
- Organic-organic heteroepitaxy
- K-doped organic superconductors
- Organic-inorganic hybrid solar cells
- *In situ* optical spectroscopy (DRS and PL) on ultrathin molecular layers
- Analyses of surfaces, layers and nanostructures using AES, XPS, LEED, RHEED, XPD, STM, AFM, and SEM

The group ***Applied Physics / Solid State Physics*** at the Institute of Solid State Physics is engaged in the research on nanostructures, solid surfaces and thin films of both organic and inorganic semiconductor materials.

Our main research interest lies in the discovery of structure-property-relations of structurally well defined ultrathin epitaxial layers, organic quantum wells, K-doped organic super conductors, and carbon nanotubes. The main target of our research is the development of basic principles for the use of nano materials in prospective devices.

For the analyses of the chemical composition and bonding at surfaces and in thin films we use surface analysis methods like photoelectron spectroscopy (XPS, UPS) and Auger electron spectroscopy (AES). The crystalline structure can be determined by electron diffraction (LEED, RHEED, XPD, and electron channeling). Scanning tunneling microscopy (STM), atomic force microscopy (AFM) and scanning electron microscopy (SEM) are used for high-resolution imaging of nanostructures and surfaces.

Our *in situ* optical spectroscopy, namely differential reflectance spectroscopy (DRS) is used to study organic (sub-)monolayers and heterostructures in terms of absorption spectroscopy to analyse the optical interaction between either the molecules itself, organic adsorbates and inorganic substrates, or molecules and dopants.

Experimental Physics / Solid State Physics

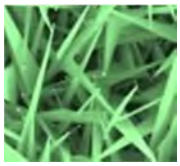

Prof. Dr. Carsten Ronning

- Synthesis, doping and functionization of semiconductor nanowires
- Photovoltaics
- Growth and functionalization of diamond-like materials
- Synthesis and modification of memoristive materials and devices
- Semiconductor physics: doping using ion beams

Recent work of the research group ***Experimental Physics / Solid State Physics*** in the field of semiconductor nanowires focuses both on the growth of desired nanostructures as well as on the modification of semiconductor nanowires for the use as photonic and electronic devices. This includes in realization of light-emitting diodes, field effect transistors, sensors for bio and chemical applications, and the observation of laser oscillations within single ZnO nanowires.

Another important scientific area of the group is the investigation of hard/soft interfaces in terms of biocompatibility. Here, the accelerator systems Mr. JIM Stringer and LEILA are used for the growth of diamond-like materials as well as for nanostructuring of surfaces (rippels). The biocompatibility and bioactivity of such thin films and surfaces is currently investigated in collaboration with the IMT.

The research on photovoltaics is directed to two different fields: (a) Preparation and development of $Cu(In,Ga)(Se,S)_2$ - based thin film solar cells (CIGS). The research aims at a better understanding of the materials science of the CIGS chalcopyrite semiconductor and the improvement of existing and the development of novel cell concepts. To this end, a complete baseline on a form factor of 10x10 cm^2 is available as well as various characterization tools including AM 1.5 solar simulation and spectral response. (b) Preparation and development of CdTe-based thin film solar cells. The research aims at a better understanding of the materials science of the II-VI semiconductor CdTe and the improvement of existing and the development of novel cell concepts. To this end, a complete baseline on a form factor of 10x10 cm^2 is available as well as various characterization tools including AM 1.5 solar simulation and spectral response.

Finally, it is worth to mention that on-going work of the group is performed in the area of ion beam doping of nanowires (in collaboration with several groups in the FOR 161), ion beam doping of Cu_2O thin films (Prof. Dr. B.K. Meyer, University of Gießen), and ion beam doping GaAs nanowires for spintronics (Prof. L. Samuelson, Lund U).

Low Temperature Physics

Prof. Dr. Paul Seidel

- Superconductivity within thin layers and layer systems
- Josephson effects, proximity effect, and tunnel effects in superconducting devices
- DC-SQUID's and their application in measurements, e.g. CCC, MRX
- cryogenic measurements of mechanical quality factor and optical properties
- Dynamics of superconducting Josephson arrays
- cryogenic engineering (cryocoolers, cryogenic storage)

The ***Low Temperature Physics*** group works on the following fields:

- preparation, characterization, modelling and application of Josephson junctions and SQUIDs (precision and magneto-relaxation measurements with LTS SQUIDs, development of HTS SQUIDs, intrinsic Josephson junctions and Josephson junctions with iron based superconductors)
- low temperature physics and cryogenic engineering (development of new kinds of pulse tube cryocoolers with magnetic regenerators, cryogenic storage, cryogenic current comparator CCC for particle beam analysis)
- experimental work within the SFB/TR7 on cryogenic measurements of the Q-factor and of optical properties of components for future gravitational wave detectors like the Einstein Telescope
- thin film technologies for insulators and other materials
- alternative preparation and properties of crystalline gold nanoclusters

The research is carried out in cooperations with other research groups in Thuringia (TU Ilmenau, IPHT Jena, SUPRACON Jena, Innovent e.V. Jena, Helmholtz Insitute Jena). Within common activities the group works together with the Gesellschaft für Schwerionenforschung Darmstadt, DESY Hamburg, MPI Heidelberg, IFW Dresden and the Zentrum für Raumfahrttechnologie und Mikrogravitation and DLR Bremen.

Several research activities exist with industrial partners e.g. with Chemicell Berlin, HTS Systeme Wallenfels, and the TransMIT center for adaptive cryotechniques Gießen. A long tradition of cooperation with the the Universities of Moscow (Russia), Bratislava (Slovak Republic), Kharkov (Ukraine), Glasgow (U.K.), Poznan (Poland), Padua, Torino and Florence (Italy), Twente (Netherlands) and the Universities of Osaka, Tokyo and Nagoya (Japan) is also remarkable.

Ion Beam Physics

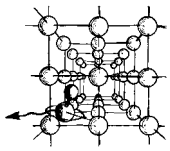

Prof. Dr. Werner Wesch / PD Dr. Elke Wendler

- Modification of solids by ion implantation and
- succeeding processes
- Ion beam analysis (RBS, PIXE, ERD, NRA)
- Ion beam synthesis of buried nanostructures
- Investigation of the effect of high electronic excitation on structural
- modification of crystalline and amorphous semiconductors

The ***Ion Beam Physics*** group deals with modification of solids and synthesis of buried nanostructures using ion beams and combined secondary processes. The studies cover fundamental processes of ion-beam induced structural modification in semiconductors and insulators being relevant for future electronic, optoelectronic and photonic device technologies.

Silver nanoclusters were successfully formed in LiNbO3 by ion beam synthesis and subsequent annealing and absorption due to plasmon resonance was experimentally proven. To optimise patterning of LiNbO3 by ion beam enhanced etching of this material, damage formation by nuclear and electronic energy deposition of the implanted ions continued to be investigated in collaboration with the Institute of Applied Physics. Here especially the built-up of strain was studied and related to the detected amount of structural damage. Primary effects of damage formation were also studied in crystalline semiconductors. For SiC this work was done in collaboration with the University of Pretoria in South Africa and it could be shown that at elevated temperatures the volume introduced by the implanted ions is decisive for the occurring processes. In collaboration with the University Minsk in Belarus we continued our work on ion beam synthesis of III-V compound nanoclusters in silicon.

Beside these activities on materials modification utilizing ion beams with conventional energies (several 10 keV to several MeV), the effect of high electronic excitation due to swift heavy ion irradiation (several 100 MeV) on plastic deformation and on the formation of voids and porous structures in amorphous Ge were studied in collaboration with the Australian National University Canberra in Australia.

Laboratory Astrophysics / Cluster Physics

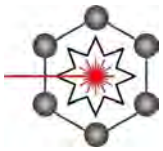

Dr. Cornelia Jäger

- Electronic spectroscopy of neutral and ionized polycyclic aromatic hydrocarbons (PAHs) in supersonic jets and cryogenic matrices
- Study of astrochemical reactions in liquid helium nanodroplets
- Low-temperature condensation of cosmic dust particles
- Study of gas-phase condensation processes of cosmic dust nanoparticles
- Study of the chemical and structural processing of dust grains and PAHs in astrophysical environments
- Photoluminescence studies of silicon and germanium nanocrystals produced by CO_2 laser pyrolysis

The ***Laboratory Astrophysics / Cluster Physics Group*** at the Institute of Solid State Physics results from a cooperation between the Max Planck Institute for Astronomy, Heidelberg, and the Friedrich Schiller University, Jena. Inaugurated in February 2003, it is now conducted by Prof. Dr. Thomas Henning and Dr. Cornelia Jäger.

The research of the Laboratory Astrophysics and Cluster Physics Group is devoted to fundamental astrophysical questions that can be answered by laboratory experiments, with particular emphasis on spectroscopy. The electromagnetic radiation reaching us from stellar objects is modified in a characteristic manner by interstellar molecules and dust particles. Many of these “fingerprints” are still far from being understood. In order to determine the species causing the modification of the electromagnetic signals detected by telescopes and satellites, comprehensive laboratory studies are urgently needed.

In our laboratory, we study the condensation, processing, and spectral properties of carbonaceous and siliceous dust grains and astrophysically relevant molecules that may play a role as progenitors of grain formation. Laboratory astrophysics is an interdisciplinary field whose research profits from sophisticated experimental facilities. We are able to simulate astrophysically relevant processes such as gas phase condensation of grains and molecules by laser-induced pyrolysis of hydrocarbons or laser ablation of solids in the laboratory. Interesting molecules, clusters, and nanoparticles are prepared in vacuum chambers under conditions coming close to those in interstellar or circumstellar environments (low pressures and definite temperatures ranges). Sophisticated analytical tools comprising optical spectroscopy, mass spectrometry, chromatography, and electron microscopy help us to characterise the composition and structure of the produced laboratory particulate and molecular analogues.

2. Scientific Reports

Vertical compression of organic heterostructures caused by van-der-Waals forces

Marco Grünewald, Kristin Wachter, Matthias Meissner, Roman Forker, and Torsten Fritz

In recent years organic thin films have been established in applications such as light emitting diodes (OLED), field effect transistors (OFET) and photovoltaic devices [1-3]. The understanding of the interaction mechanisms within a molecular layer but also at metal-organic and organic-organic interfaces is of fundamental importance to improve the efficiency of organic semiconductor components in the future.

The electronic as well as the optical properties of thin organic layers are determined significantly by the molecular arrangement. In order to analyze the complex molecular interaction mechanisms affecting the properties of the thin film we focus on model systems composed of highly-ordered ultra-thin molecular layers of the dye molecules 3,4,9,10-perylene-tetracarboxylic-dianhydride (PTCDA) and tin(II)-phthalocyanine (SnPc) prepared by molecular beam epitaxy (OMBE). Those molecules are suitable as they are known for an epitaxial growth on various single crystalline substrates [4-6].

Our group established an *in situ* optical absorption spectroscopy for the determination of optical properties of thin organic films known as Differential Reflectance Spectroscopy (DRS) [7]. The measured quantity, the differential reflectance spectrum (DRS), is rather simple:

$$DRS \coloneqq \frac{R(E,d) - R(E,d=0)}{R(E,d=0)} \qquad (1)$$

where $R(E,d)$ denotes the reflectance of the substrate inclusive the thin film with a thickness d. Accordingly, $R(E,d=0)$ can be understood as the reflectance of the pristine substrate depending on the photon energy E. As both the signal height and the spectral shape of the DRS strongly depend on the optical properties of the substrate, it is far from trivial to interpret the DR spectra itself in terms of light absorption. Instead of this, a numerical algorithm [8] has been developed by us in order to extract the real and imaginary part of the complex dielectric function $\hat{\varepsilon} = \varepsilon' - i\varepsilon''$ of the thin film.

In a previous work we found a strong electronic interaction between the respective first monolayer (ML) of PTCDA or SnPc and the Ag(111) substrate characterized by a charge transfer at the metal-organic interfaces [9]. In contrast, on much weaker interacting substrates, i.e., Au(111), the electronic interaction is predominately of van-der-Waals character. However, the respective second MLs decouples in both cases from the metal substrate and the first ML as well indicated by a monomer spectrum (cf. Fig. 1, upper parts, red lines). Strictly speaking, both metals precovered with 1 ML of SnPc behave like an inert substrate for further film depositon of PTCDA as elucidated in the lower parts of Fig. 1 (red lines). Obviously, in both cases there are peaks in the low energy region which cannot be assigned to the respective monomeric features. However, we found that the peak shapes correlates with the spectra obtained from the underlying SnPc monolayer which are strongly determined by the choice of the substrate as shown in the middle part of Fig. 1 (black line). Accordingly, the peaks observed in the lower energy region in Fig. 1 (upper part) could stem from a vertical

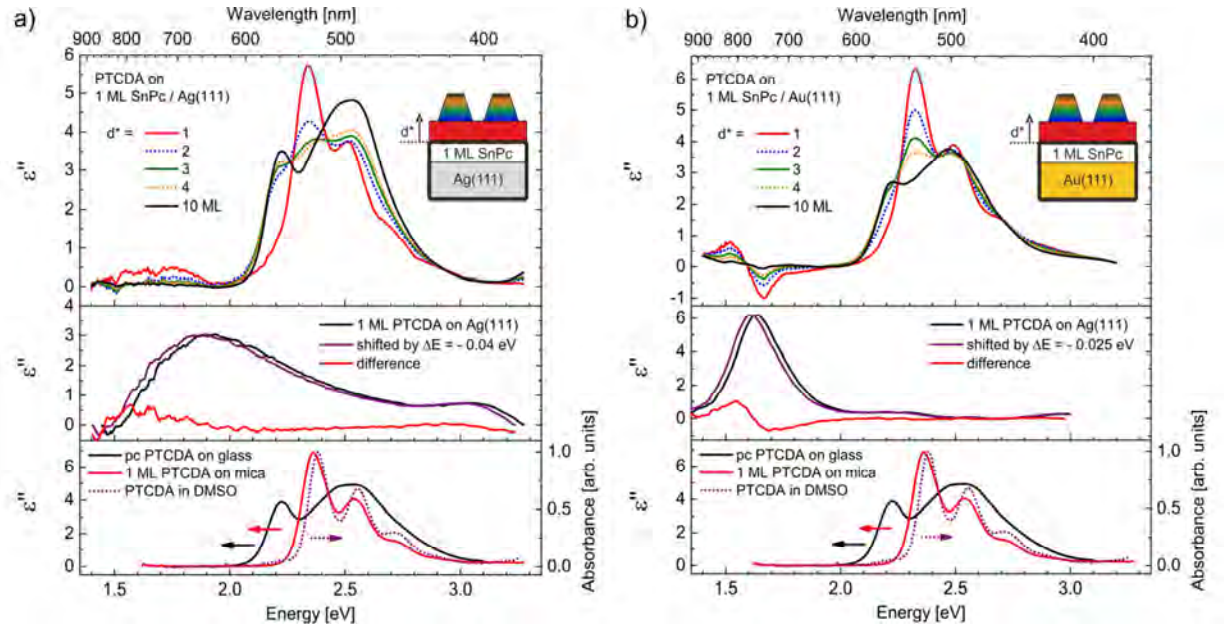

Fig. 1: The imaginary part ε'' of the dielectric function (upper parts) of PTCDA on **a)** 1 ML SnPc on Ag(111) [9] and **b)** 1 ML SnPc on Au(111) is shown together with the ε'' spectrum of 1 ML of PTCDA on inert mica, the ε'' spectra of one monolayer of SnPc on Ag(111) [9] and Au(111) [7] (middle parts), an extinction spectrum of PTCDA in solution [10] and an absorbance spectrum of a thick polycrystalline PTCDA film on glass [11,12] (bottom parts).

compression of the underlying SnPc monolayer as a consequence of van-der-Waals forces between the first ML of PTCDA and the metal substrate. In this case one would expect energetically slightly shifted spectra of the squeezed SnPc monolayer due to polarization effects. In Fig. 1 (middle parts, purple lines) the spectra of the respective first monolayers (black lines) were shifted hypothetically by $\Delta E = -0.04\,eV$ and $\Delta E = -0.025\,eV$ for the Ag(111) and the Au(111) substrate, respectively. The difference (cf. eq. 1) of the shifted and unshifted spectra fits well to the peaks obtained experimentally in Fig. 1 (upper part, red lines).

For further increasing film thickness the aggregates become larger and, consequently, the spectra converge asymptotically to the well-known spectra of polycrystalline films on glass as shown in the lower part of fig. 1 (black lines).

The present work gives an insight into the complex interaction mechanisms at metal-organic and organic-organic interfaces. Van-der-Waals forces within organic heterostructures have an impact on the absorption height of the molecules and consequently the optical response as well.

References

[1] S. Liu *et al.*, Adv. Mater. **21**, 1217-1232 (2009).

[2] N.R. Armstrong *et al.*, Macromol. Rapid Commun. **30**, 717-731 (2009).

[3] B. Rand *et al.*, *Appl. Phys. Lett.*, ***87***, 33508 (2005).

[4] C. Stadler *et al.*, *Nat. Phys.* **5**, 153-158 (2009).

[5] L. Kilian *et al.*, *Surf. Sci.* **573**, 359-378 (2004).

[6] L. Kilian *et al.*, *Surf. Sci.* **600** 2633-2643 (2006).

[7] R. Forker *et al.*, *Annu. Rep. Prog. Chem., Sect. C: Phys. Chem.* **108** 34–68 (2012)

[8] R. Nitsche *et al.*, Phys. Rev. B **70**, 195432 (2004).

[9] M. Grünewald, Diplomarbeit, FSU Jena (2011)

[10] M. Hoffmann et al, *Chemical Physics* **258**73-96 (2000).

[11] A. B. Djurišić *et al.*, *Opt. Commun.* **183** 123–132 (2000).

[12] F. Yang *et al.*, *Appl. Phys. Lett.* **92** 053310 (2008).

Optical constants of zinc(II)-phthalocyanine films

Michael Kozlik, Marco Gruenewald, Sören Paulke, Roman Forker, and Torsten Fritz

Organic molecules are increasingly used materials in new optoelectronic devices such as organic solar cells and organic light emitting devices. A prominent representative is zinc(II)-phthalocyanine (ZnPc) [1, 2], due to its strong and spectrally selective light absorption in the visible and ultraviolet range as well as the simple preparation by thermal evaporation and spin coating which results in the common α- and β-phase, respectively. The metastable α-phase is preferred for electronic devices because of the higher electric conductivity [3]. There are several methods to distinguish both phases, e.g., atomic force and scanning electron microscopy as well as optical spectroscopy [4]. Here we present a new method for the determination of the complex optical constants ($\hat{n} = n - ik$) taking surface roughness into account, where n and k denote the refractive index and extinction coefficient, respectively. Once the optical constants are known, they can be used for modeling layer systems or even photovoltaic devices, or vice versa for a non-destructive optical analysis of the crystallinity of ZnPc layers.

We prepare α-ZnPc (lattice parameters: a=2.39 nm, b=0.38 nm, c=2.59 nm and $\vartheta_\alpha = 26.5°$ (angle between b and molecular planes) [5]) films by thermal evaporation of ZnPc powder from a ceramic crucible with a rate of 0.6 Å/s at a pressure of 10^{-5} mbar on a substrate kept at room temperature. These thin films are stable at temperatures below 220°C. However, annealing at 240°C (and above) leads to a phase transition (see Fig. 1). After 3 hours the α-phase is completely converted into the β-phase (lattice

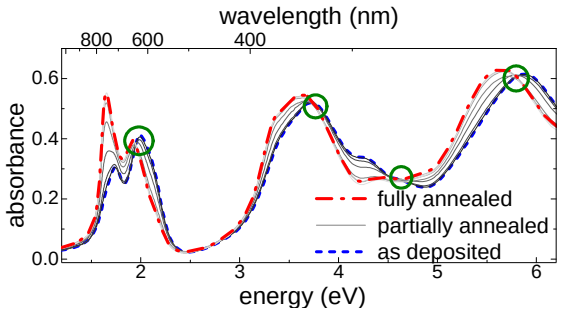

Fig. 1: The absorbance spectra of as deposited α-ZnPc (dashed blue line) and β-ZnPc (dash-dot red line) which results after annealing at 240°C. Four isosbestic points (green circles) could be observed.

parameters: a=1.94 nm, b=0.48 nm, c=2.39 nm and $\vartheta_\beta = 45.8°$ [5]). The isosbestic points, common intersections of several absorbance spectra, evidence a direct transition with no "reaction" steps in between. The low energy peak becomes more intense and is slightly red shifted because of the changed angle ϑ.

These spectra can be modeled by the optical constants or vice versa the optical constants can be obtained by these spectra by means of a numerical algorithm [6]. For this purpose, the exact film thickness is needed. Alternatively, the film thickness is treated as another degree of freedom by the algorithm using optical spectra of several samples of different thickness simultaneously. Hence, five samples with the nominal thickness of 30 nm, 60 nm, 90 nm, 120 nm and 150 nm are prepared and transmittance as well as reflectance spectra are measured at an incident angle of 0° and 12°, respectively. The objective function to be minimized is shown in equation (1)

$$\sum_j \sum_{i=1}^{N} A^{(j)}(E_i)\left\{X_{th}^{(j)}\left(n(E_i),k(E_i)\right) - X_{exp}^{(j)}(E_i)\right\}^2 = \delta \xrightarrow{n,k\ variation} min \quad (1)$$

where $X_{th}^{(j)}$ denotes a user-defined calculated quantity (e.g., transmittance (T)

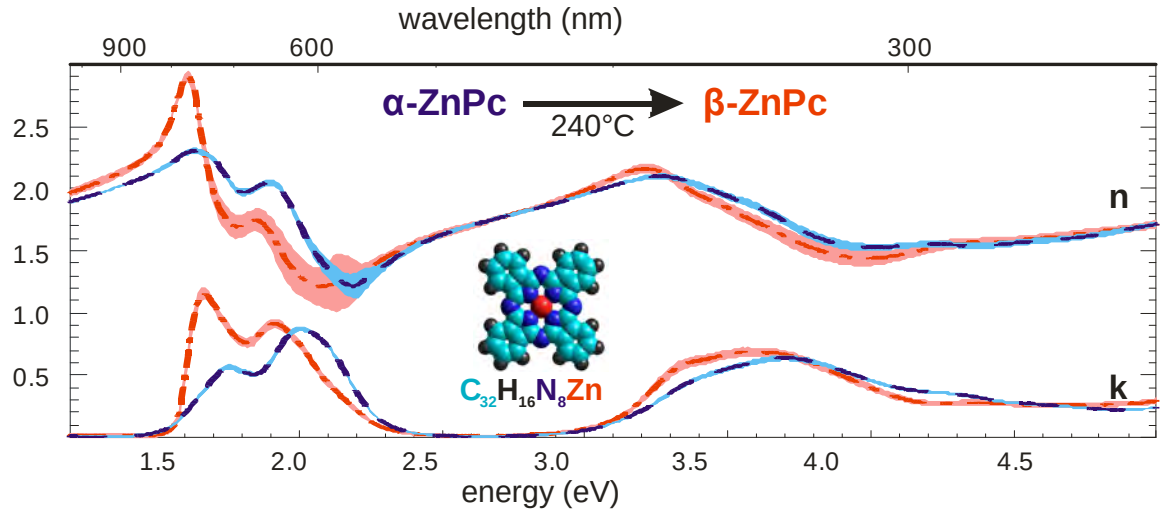

Fig. 2: Real- and imaginary part of the complex refractive index of α- (blue dashed line) and β-ZnPc (red dash-dotted line), respectively. The shaded error margin indicates the standard deviation (statistical errors from the fitting procedure, enlarged five times). The inset shows the molecular structure of ZnPc.

or differential reflectance spectra (DRS)) to be fitted to the respective experimental data $X_{exp}^{(j)}$. Each signal of T and DRS was weighted by a factor $A^{(j)}(E_i)$ in order to equalize the information $X^{(j)}(E_i)$ from all spectra having originally different magnitudes.

The advantage of this procedure is that the layer thickness can be optimized as well with an accuracy better than 0.1 nm using the nominal thicknesses as starting values (see Tab. 1). By doing so, it is important to cover an appropriate thickness range of layers fitted simultaneously as only thickness-dependent internal interference effects contribute significant new information to the fitting procedure. The results were checked in terms of model-free Kramers-Kronig consistency in the region of 1.2 eV to 2.6 eV (entire $S_0 \rightarrow S_1$ absorption band). The vertical surface variations have also been considered. Accordingly, the experimental roughnesses (measured by AFM) were in accordance with the values from the fitting procedure (not shown here).

Our data of α-ZnPc compare favorably with those of the almost identical molecule copper(II)-phthalocyanine (CuPc, α-phase) from Ref. [6].

Tab. 1: Nominal and optimized values of the film thickness of the samples used for the determination of optical constants. The errors given are statistical errors from the fitting procedure.

	α-ZnPc	β-ZnPc
Nom. thick. [nm]	Opt. thick. [nm]	Opt. thick. [nm]
30	36.95±0.03	36.15±0.05
60	65.30±0.04	61.90±0.07
90	96.63±0.04	94.65±0.08
120	132.15±0.05	129.09±0.07
150	168.90±0.07	167.88±0.07

References

[1] I. Kim *et al.*, *Chem. Mater.* **21** (2009) 4256-4260.

[2] S. Bereznev *et al.*, *Thin Solid Films* **515** (2007) 5759–5762.

[3] K. Wihksne *et al.*, *J. Chem. Phys.*. **34** (1961) 2184-2185.

[4] M. Kozlik *et al.*, *Org. Electron.* **13** (2012) 3291-3295.

[5] R. Hiesgen *et al.*, *Sol. E. Mat. Sol. Cells* **61** (2000) 73-85.

[6] T. Fritz *et al.*, *Thin Solid Films* **170** (1989) 249-257.

Characterization of crystalline substrates and adlayers with MCP-LEED

Christian Zwick, Falko Sojka, Matthias Meissner, Roman Forker, and Torsten Fritz

Low **E**nergy **E**lectron **D**iffraction (LEED) has become a popular and very important tool to examine long-range ordering of surfaces. It benefits from its potentially high accuracy at a low amount of time necessary for measuring, but it is often not used to full capacity due to systematic errors, which mainly take effect in distortions in the LEED images.

To determine and correct these distortions, and thereby to improve the accuracy of characterizations of crystalline substrates and adsorbate layers, the software *LEEDCal* [1, 2] is used, which allows to calibrate several device designs (i.e., conv. LEED, MCP-LEED, SPA-LEED). For the calibration only one sample with a well-known structure and a suitable high amount of diffraction spots in the LEED images over a wide interval of energy, such as Si(111)7x7, is needed.

The following results are obtained by the calibration of a *4-grid MCP2-SPECTALEED from Omicron* [3] with permanently deactivated suppressor (due to insufficient hardware), using a Si(111)7x7 sample (cf. Figure 1).

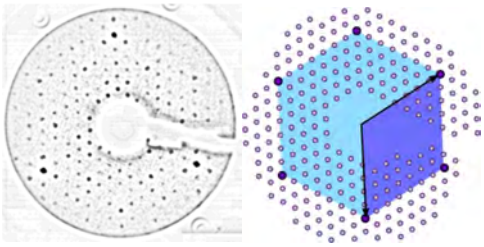

Fig. 1: LEED image of Si(111)-7x7 at 75.2 eV (left) and geometric simulation (right).

The distortion caused by the MCP-LEED can be separated into a radially symmetric and an asymmetric part, whereas the **asymmetric distortion** was not measurable. A **radial symmetric distortion**, which occurs in general, is well characterized and understood. Therefore, the influence of the recording camera is nearly negligible against the distortion caused by the MCP-LEED itself. Further, an energy dependency of the radially symmetric distortion between E = 50…110 eV is not significant. Thus, this leaves the sample misalignment as the main influence on the radially symmetric distortion (cf. Figure 2).

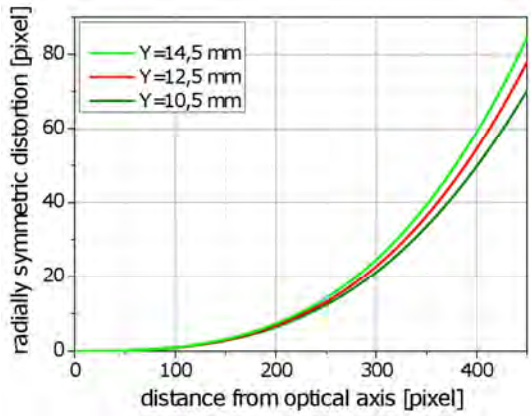

Fig. 2: Radially symmetric distortion for three different sample positions Y.

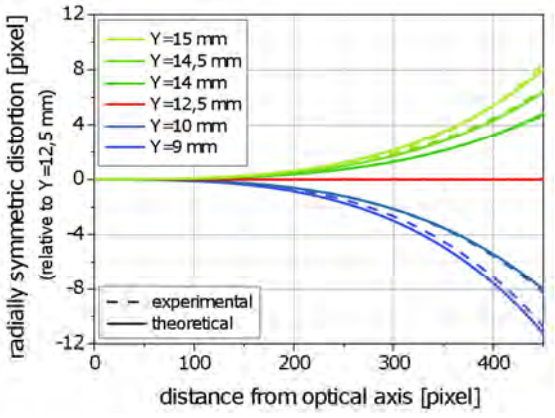

Fig. 3: Comparison of theoretical and experimental radially symmetric distortion relative to a defined sample position for different sample misalignments.

LEEDCal is able to correct images taken at the same sample position accurately, but for the first time the dependency of the distortion on the sample misalignment can be fully understood and described theoretically (cf. Figure 3).

Another systematic error, describing the difference between the true kinetic energy and the set acceleration voltage, can be characterized. This **energy offset** amounts to $\Delta E = (-0.21 \pm 0.05)$ eV and is specific to each device. It can be determined by a series of measurements at different energies, due to the proportionality of the size of the imaged reciprocal lattice to the root of the energy [4] (cf. Figure 4).

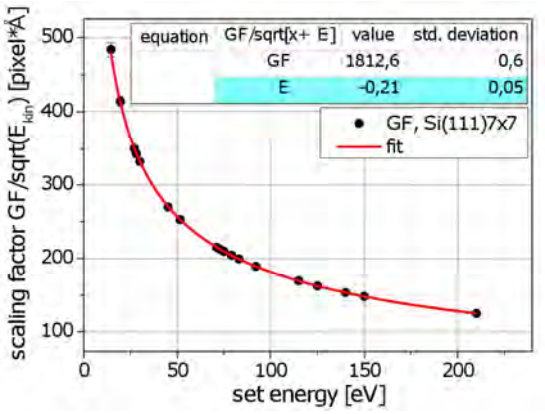

Fig. 4: Determination of the energy offset. The scaling factor is proportional to the size of the reciprocal lattice imaged.

When the sample surface is tilted, we can observe an additional **axial distortion**. This distortion can be described theoretically with the Ewald Construction (cf. Figure 5).

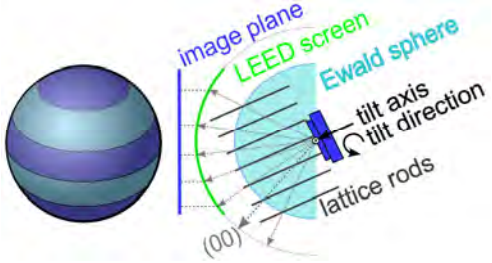

Fig. 5: Ewald construction considering a tilted surface (right) and projection of a tilted, striped ball to illustrate the axial distortion (left).

An algorithm, developed and implemented by *F. Sojka* [1], enables the correction of LEED images taken at tilted sample surfaces, after the determination of two geometrical parameters and the tilt angle. By this it is now possible to observe diffraction spots of higher and lower order simultaneously just by tilting the sample, which improves the accuracy of the characterization of the sample surface significantly.

The knowledge gained is applied to determine the lattice parameters of a PTCDA phase on Ag(111) accurately. The LEED images are corrected for all of these systematic errors (cf. Figure 6) and subsequently analyzed, using the software *LEEDLab* [2]. This type of analysis is very fast and reduces subjective influences caused by the experimenter.

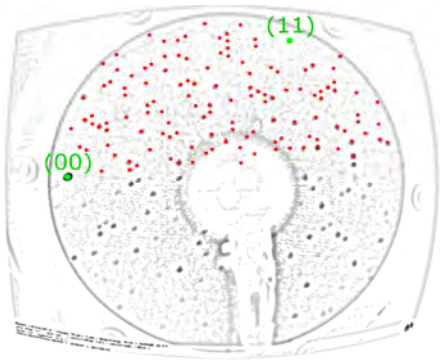

Fig. 6: LEED image of PTCDA on Ag(111) at 43 eV. The red dots describe the ideal simulated lattice.

For the current phase we found the epitaxial matrix, describing a commensurate structure, to be

$$E = (1 \pm .001)\begin{pmatrix} 5.989 \pm .037 & 0.995 \pm .019 \\ -3.003 \pm .006 & 4.995 \pm .025 \end{pmatrix}.$$

This matrix is, within the margin of errors, identical with the literature value

$$E_{Lit} = \begin{pmatrix} 6 & 1 \\ -3 & 5 \end{pmatrix}.$$

Thus, all characterizations and corrections done can be regarded as validated.

References

[1] F. Sojka: *Diploma Thesis*, FSU Jena (2011).
[2] Omicron NanoTechnology: Pico **16** (2011) 12.
[3] Omicron NanoTechnology: *MCP-LEED Optics and Electron Gun: User´s Guide* **1.0**, (2006).
[4] S. C. B. Mannsfeld: *Diploma Thesis*, TU Dresden (1999).

Persistence of photoconductivity in ZnO nanowires in different atmospheres

D. Cammi and C. Ronning

Due to the high surface to volume ratio, semiconductor nanostructures are excellent candidates for several applications such as electronic devices, photo-detectors, gas and bio-sensors. In particular, ZnO is a widely used material that shows for example a low sensing detection limit and an excellent UV sensitivity [1,2]. However, the major drawback for photo-detection applications is the photoconductivity, which persists for a long time, preventing a fast recovery of the dark current [3,4]. In order to develop faster UV photo-detectors it is necessary to achieve a better understanding of the processes involving the interaction between the surface of nanowires and the external environment. In the present report, we investigated the photoconductivity properties of ZnO nanowires in different atmospheres and we propose a possible model to explain the experimental results.

The nanowires were grown by VLS [5] and subsequently transferred to a new substrate (850 nm of SiO_2 on Si). After photolithography and metal deposition, the final devices consist of some nanowires bridging two Ti/Au electrodes. To perform the electrical measurements in vacuum conditions or in different gas atmospheres, the samples have glued on a commercial holder and contacted by electrical bonding. The electrical characterization has been carried out with a Source-measure Unit (SMU) Keithley (Model 237) applying a voltage difference between the drain and the source electrodes. The illumination source was a UV LED, with central emission wavelength at 375 nm, approximately corresponding to the ZnO band gap.

The typical time dependence of the photo-current in air is shown in Figure 1. Under UV excitation the current rises initially very quickly, and then the rate decreases until

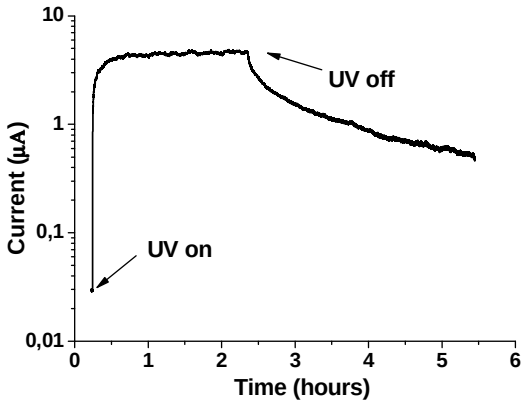

Fig. 1: Temporal dependence of the photo-current in ZnO nanowires contacted between Ti/Au electrodes. The measurement is performed at V_{DS} = 5 V in air and the excitation source is a UV LED.

reaching a saturation value. After removing the illumination, the current decay is extremely slow and the previous dark current is not reached after few hours.

As shown in Figure 2, the photo-current in-

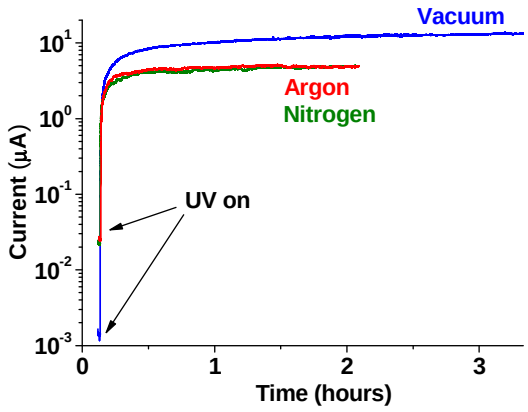

Fig. 2: Photo-current increase measured in vacuum, argon and nitrogen, with the same V_{DS} as in Figure1.

crease in nitrogen and argon is comparable to the one measured in air, whereas it is much higher in vacuum (10^{-5} mbar) and

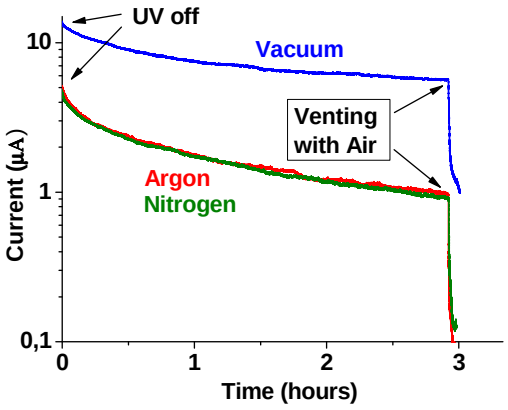

Fig. 3: Photo- current decay after removing the UV excitation, in vacuum, argon and nitrogen. When the air is let into the chamber, the decay rate increases considerably.

does not reach a saturation value even after 3 hours. The photo-decay is particularly slower in nitrogen, argon and vacuum than in air, as shown in Figure 3: after the air is let into the chamber during venting (after 3 hours), the current drops immediately.

The experimental results suggest that the oxygen plays the main role in the photoresponse properties of ZnO nanowires. It is known that the oxygen molecules tend to adsorb at the ZnO surface (in particular at the oxygen vacancy sites) [6], trapping electrons from the conduction band and inducing a band bending in the proximity of the surface. During the UV excitation, part of the oxygen desorbs and releases the trapped electrons, thus, the photo-generated carriers get separated due to the band bending, increasing their life-time. Both processes contribute to the increase of the conductivity.

When the UV light is removed, the oxygen can re-adsorb and localizes again electrons from the conduction band. This process is not immediate and gives origin to the slow decay of the current. When the concentration of oxygen in the atmosphere is low, as in vacuum or argon and nitrogen environments, the trapping of electrons from the conduction band is reduced, and correspondingly the decrease of the conductivity is slower.

The proposed model describes also why the photocurrent during the illumination rises at first quickly and progressively at slower rate. The band bending creates in fact a potential barrier for the electrons in the conduction band, and without any excitation they do not have enough energy to overcome it and get further localized at the surface. When the UV excitation starts the oxygen desorbs from the surface resulting in the band bending lowering. As a consequence, the barrier for the electrons is progressively reduced and few of them can be trapped at the surface while some oxygen molecules previously released can re-adsorb again. This partial trapping of electrons from the conduction band is responsible for the slower rate of photocurrent increase during the last part of the UV illumination. When the rate of oxygen desorption and readsorption during illumination reaches an equilibrium, the photocurrent does not increase further.

In conclusion, this work can provide further insights concerning the adsorption mechanism in ZnO, which can be useful for future development of faster UV photo-detectors and other surface-related applications such as sensing.

References

[1] C. Soci et al., Nano Lett., **7** (2007) 1003
[2] M.W. Ahn et al., Appl. Phys. Lett. **93** (2008) 263103
[3] Prades et al., Nanotechnology **19** (2008) 465501
[4] Bao et al., Nanoscale Research Letters **6** (2011) 404
[5] C. Borchers et al., J. Phys. Chem. B **110** (2006) 1656
[6] Wei An et al., J. Phys. Chem. C **112** (2008) 5747

Composition-dependent atomic-scale structure of $Cu(In,Ga)S_2$

S. Eckner, H. Kämmer, T. Steinbach, M. Gnauck, A. Johannes, C. Stephan, S. Schorr*, C. S. Schnohr*

**Helmholtz-Zentrum Berlin für Materialien und Energie, Hahn-Meitner-Platz 1, 14109 Berlin*

For $Cu(In,Ga)S_2$ as a promising solar cell material one of the most interesting properties is the band gap and its nonlinear change with composition known as band gap bowing [1]. The band gap energy thereby depends in a crucial way on the local structure, in particular on the position of the S anion within the unit cell [2, 3].

Both the ternary compounds, namely $CuGaS_2$ and $CuInS_2$, and the mixed compound $Cu(In,Ga)S_2$ crystallize in the chalcopyrite structure depicted in Fig. 1, with the lattice constants varying linearly with composition between the values of the ternary compounds [4]. Since each group-III lattice position is occupied by either In or Ga the first nearest neighbour configurations around the S anions differ. Apart from the two Cu atoms, the first nearest neighbour shell can contain zero, one or two Ga atoms and two, one or zero In atoms, respectively. It is known from the analogue compound system $Cu(In,Ga)Se_2$, that the anion position with its remarkable influence on the band gap depends sensitively on the first nearest neighbour environment [5]. Therefore, the atomic-scale structure of $Cu(In,Ga)S_2$ has been studied as a function of composition using extended x-ray absorption fine structure spectroscopy (EXAFS).

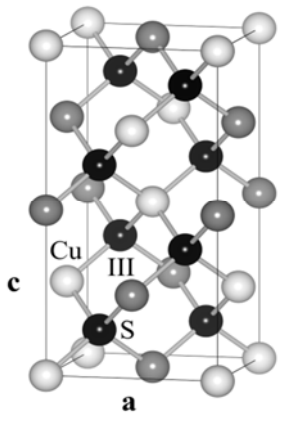

Fig. 1: Schematic showing the chalcopyrite type crystal structure of $Cu(In,Ga)S_2$.

$Cu(In,Ga)S_2$ powder samples were synthesized by solid state reaction, using wavelength dispersive x-ray analysis to determine the elemental composition [6]. Low temperature (17 ± 1 K) EXAFS measurements of the Cu, Ga and In K-edges corresponding to edge energies of 8.979, 10.367 and 27.940 keV, respectively, were performed in transmission mode at Beamline C of HASYLAB (DESY) in Hamburg. For data processing and analysis the IFEFFIT code [7] was used together with the user interfaces ATHENA and ARTEMIS [8]. Phase shifts and scattering amplitudes were calculated using FEFF9 [9]. The mean value R and the standard deviation σ^2 of the first nearest neighbour distance distribution were fitted with all higher cumulants set to zero. The coordination number was fixed to four whereas the amplitude reduction factor S_0^2 and the threshold energy E_0 were set to average values determined from all samples. The element specific bond lengths $R_{Cu\text{-}S}$, $R_{Ga\text{-}S}$ and $R_{In\text{-}S}$ thus determined are plotted in Fig. 2 as a function of the In/III ratio. The overall uncertainties amount to ±0.003Å.

In $CuGaS_2$, the S anion is displaced towards the group-III sites, equivalent to a larger $R_{Cu\text{-}S}$ compared to $R_{Ga\text{-}S}$. In contrast, the anion in $CuInS_2$ is displaced towards the Cu atoms as seen from the smaller $R_{Cu\text{-}S}$ compared to $R_{In\text{-}S}$. This behaviour is in good agreement with neutron powder diffraction studies [6]. For the mixed $Cu(In,Ga)S_2$ compounds, the element-specific bond lengths measured with EXAFS remain close to their ternary values over the whole compositional range, very similar to the trend observed in $Cu(In,Ga)Se_2$ [5]. An explanation for this

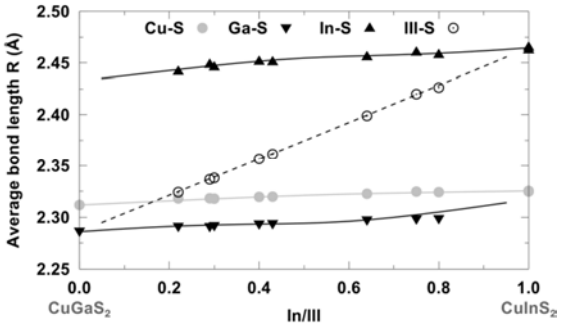

Fig. 2: Element-specific bond lengths *R* (mean value of the first nearest neighbour distance distribution) measured at the Cu, Ga and In K-edges as a function of the In/III = In/(In+Ga) ratio of Cu(In,Ga)S_2.

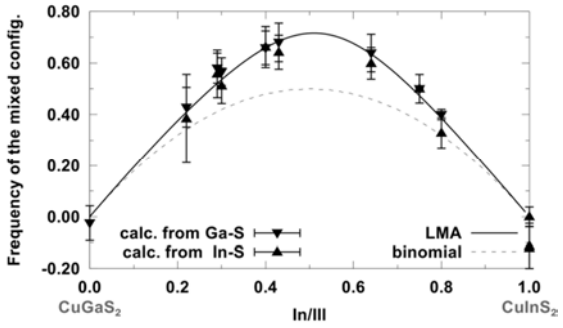

Fig. 3: Frequency of occurrence of the mixed nearest neighbour configuration calculated from the experimental average element-specific bond length using simulated individual bond lengths (symbols) and modelled probability for a strictly random occupation (dotted line) or using a law of mass action (LMA) approach (solid line).

behaviour known from other tetrahedrally coordinated systems like (In,Ga)P is the energetically motivated preference for bond bending over bond stretching [10]. The weighted average of the Ga-S and In-S bond lengths, R_{III-S}, shows a linear increase with increasing In/III ratio, again very similar to Cu(In,Ga)Se_2 [5].

More precisely, the element-specific bond lengths determined with EXAFS are the *average* values over the different first nearest neighbour configurations of the S anion. These configurations were modelled using a simple valence force field approach to obtain the minimum-energy anion position, from which the *individual* bond lengths were calculated. It is then possible to use the average element-specific bond lengths determined from the EXAFS measurement along with the simulated individual bond lengths to estimate the frequency of occurrence for each S first nearest neighbour configuration. The results for the mixed configuration, namely two Cu, one Ga and one In atom, are shown in Fig. 3. The uncertainties plotted were propagated from the average element-specific bond length uncertainties. Obviously, this mixed configuration occurs more often than expected for a strictly random occupation of the group-III lattice sites, which would lead to a binomial distribution. This can be explained by the lower strain energy associated with the mixed configuration, leading to a competition between energy minimisation and entropy maximisation, which can be modelled by a law of mass action approach leaving one parameter, i.e. the equilibrium temperature, free to fit the data. Using this fitted distribution to obtain an average element-specific bond length from the simulation, plotted as solid lines in Fig. 2, leads to excellent agreement with the experimental values.

References

[1] S.-H. Wei, A. Zunger, J. Appl. Phys. **78**, 3846 (1995).

[2] J. E. Jaffe, A. Zunger, Phys. Rev. B **29**, 1882 (1984).

[3] J. Vidal *et al.*, Phys. Rev. Lett. **104**, 056401 (2010).

[4] K. Oishi *et al.*, Thin Solid Films **515**, 6265 (2007).

[5] C. S. Schnohr *et al.*, Phys. Rev. B **85**, 245204 (2012).

[6] C. Stephan, PhD thesis, Freie Universität Berlin/Helmholtz-Zentrum Berlin, Germany (2011).

[7] M. Newville, J. Synchrotron Radiat. **8**, 322 (2001).

[8] B. Ravel, M. Newville, J. Synchrototron Radiat. **12**, 537 (2005).

[9] J. J. Rehr *et al.*, Phys. Chem. Chem. Phys. **12**, 5503 (2010).

[10] C. S. Schnohr *et al.*, Phys. Rev. B **78**, 115201 (2008).

Luminescence and energy transfer processes in Tb implanted ZnS nanowires

Sebastian Geburt, Franziska Riedel, Uwe Kaiser[1], Sebastian Gies[1], Wolfram Heimbrodt[1], Carsten Ronning

[1] *Department of Physics and Material Sciences Center, Philipps-University Marburg, Renthof 5, 35032 Marburg, Germany*

Terbium (Tb) doped ZnS is a well-known phosphor with high emission efficiency and therefore widely used for thin-film electro-luminescence devices [1]. The transfer of this technology to semiconductor nanowires is therefore a promising approach for the realization of a nanoLED based on Tb doped ZnS nanowires. Although the doping of nanowires is difficult due to the self-organized synthesis, successful doping of nanowires was achieved by ion implantation [2]. For efficient nanowire devices, the luminescence characteristics of the implanted nanowires as well as the efficiency-limiting energy transfer processes have to be investigated.

ZnS nanowires with a typical diameter of 100 – 300 nm and length up to 50 µm were grown by a vapor-liquid-solid process on Si substrates [3]. After growth, the nanowires were dispersed onto clean Si-substrates (Fig. 1 inset). The implantation was simulated using the Monte-Carlo *iradina* [4], which takes the correct 3D nanowire geometry into account and the nanowires were implanted with ^{159}Tb using multiple ion energies in the range of 30 – 380 keV in order to provide a homogenous doping profile over the whole nanowire diameter [2]. By adjusting the ion fluences to $2\cdot10^{15}$(10^{16}) ions/cm², a Tb concentration of 0.2(2.0) at.% was realized. Subsequent annealing at 600°C for 30 min in vacuum recovered the majority of the induced defects and activated the intra-4f-luminescence of the implanted dopants [5].

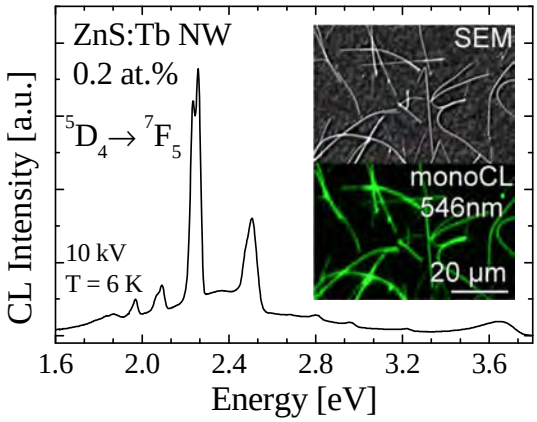

Fig. 1: Tb implanted ZnS nanowires (0.2 at.%) emit an intense and sharp intra-4f luminescence superimposed to the ZnS emission. The SEM image in the inset shows the dispersed nanowires. The monochromatic CL image confirms the homogeneous Tb emission of the implanted nanowires.

The luminescence properties were investigated using cathodoluminescence (CL). The ZnS:Tb nanowires show an intense and sharp luminescence originating from several infra-4f-transition from the $^5D_3$ and $^5D_4$ level to the ^7F_J multiplets (Fig. 1). Homogeneous emission could be confirmed by spatial resolved monochromatic imaging of the Tb luminescence (Fig. 1 inset).

Time resolved photoluminescence (TRPL) measurements give access to the interplay of the Tb ions with defects and are therefore helpful for the investigation of the energy transfer processes. After excitation by a 355 nm nanosecond laser pulse, the Tb luminescence of the most intense $^5D_4 \rightarrow {}^7F_5$ transition could be detected using an intensified CCD at delay times ranging from some hundred ns up to several ms. The transients of the ZnS:Tb

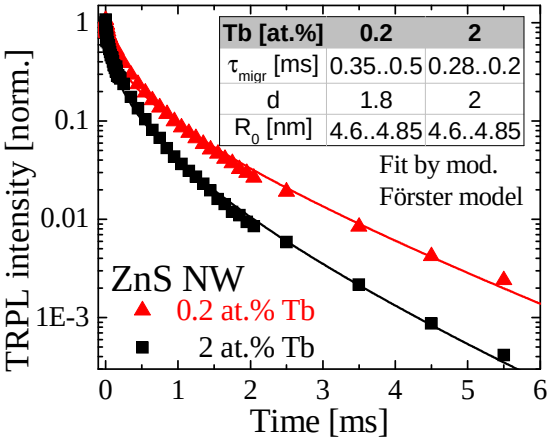

Fig. 2: The transients of the Tb implanted ZnS nanowires can be well fitted using the modified Förster model. The decay is faster for the higher Tb concentration due to the more efficient energy transfer in the Tb subsystem to killer centers (concentration quenching).

nanowires with 0.2(2.0) at.% are displayed in Fig. 2. The deviation from a mono-exponential decay displays the presence of energy transfer processes between Tb ions and non-radiative defect sites (killer centers). The experimental data were fitted using a Förster dipole-dipole energy transfer model [6], which was modified for the influence of the low-dimensional nanostructures [7].

The model (Eq. 1) uses the natural lifetime τ_{Tb}, the defect concentration n, the Förster Radius R_0, the migration time τ_{migr} and the dimensionality D to fit the transient. τ_{Tb} = 2.06 ms was determined from a mono-exponential fit at times later than 2 ms after the excitation pulse. A larger dimensionality D and smaller Förster radius R_0 has to be used to the Tb decay compared to the values for equally prepared ZnS:Mn nanowires [8], which accounts to the higher shielding of the 4f-electrons from the surrounding. The

$$\langle I(t)\rangle = I_0 \cdot exp\left(-\frac{t}{\tau_{Tb}}\right) \cdot exp\left(-\alpha \cdot n^D \cdot R_0^D \cdot \left(\frac{t}{\tau_{migr}}\right)^{D/6}\right) \quad (1)$$

uncertainty in R_0 leads to the range of migration times τ_{migr}, as both parameter are correlated and cannot be determined alone. However, the model can accurately fit the experimental determined transients for Tb implanted ZnS nanowires.

The temporal decay of the nanowire ensemble (~ 10^3 nanowires) was investigated in comparison to a microscopic ensemble (~ 10) and even a single nanowire in order to uncover possible deviations in the decay characteristic due to the nanowire morphology. However, identical decay characteristics were investigated, which could be related to the large number of Tb ions (10^6) present in a single nanowire. Thus, possible deviations are already averaged in the single nanowire, which therefore is representative for the decay characteristic of the ensemble.

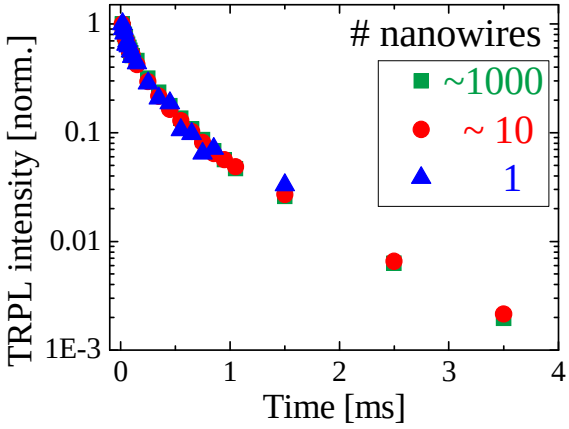

Fig. 3: The transients of a macroscopic ensemble (~ 10^3 nanowires), a microscopic ensemble (~10) and a single nanowire are identical.

References

[1] E. Chase *et al.*, JAP **40**, 2512 (1969).
[2] C. Ronning *et al.*, Mat. Sci. Eng. R **70**, 30 (2010).
[3] C. Borchers *et al.*, Nanotech. **17**, 1067 (2006).
[4] C. Borschel *et al.*, NIM B. **269**, 2133 (2011).
[5] F. Riedel, Diplomarbeit, FSU Jena (2011).
[6] T. Förster, AdP. **437**, 55 (1948).
[7] L. Chen *et al.*, Phys. Rev. B. **76**, 115325 (2007).
[8] U. Kaiser *et al.*, J. Appl. Phys. accepted (2013).

A method for the deposition of CdTe layers at very low substrate temperatures

C. Kraft, C. Heisler, A. Harpf, M. Brückner, H. Metzner, and W. Wesch

For the deposition of CdTe thin films as solar cell absorber layers, a novel high vacuum apparatus was developed which is shown in Fig. 1 (left). Around a centric source for the evaporation of CdTe, additional sources are arranged for the evaporation and sputtering of supplementary elements. The substrate holder is located directly above the CdTe source and designed for substrates with a size of up to 10 x 10 cm².

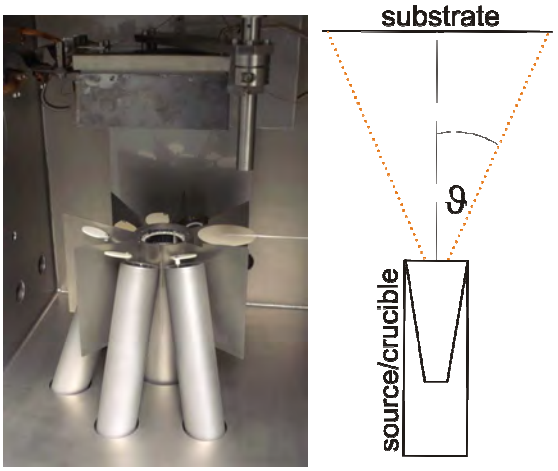

Fig.1: Evaporation sources under the substrate holder (left) and schematic view of the crucible inset (right).

The new method for the deposition of CdTe is based on the PVD principle using effusion cells from the molecular beam epitaxy technology which were produced by *CREATEC FISCHER Corporation*. If one considers Knudsen-evaporation only, the distribution of the material on the substrate is proportional to $\cos^4\theta$ [1,2] where θ is the angle between the normal of the source aperture and the direction from the source to one point on the substrate, see Fig. 1 (right). Modifications of the $\cos^4\theta$ distribution like the Clausing factor [3,4] have to be considered if the source differs from an ideal Knudsen source. Therefore the distribution of the material on the substrate has to be determined empirically or by modeling and simulation [5]. As a result of the simulations, for the evaporation with a conventional effusion cell, the PVD method results in a lower homogeneity at lower evaporation rates and a lower material yield compared to the common close-space-sublimation method (CSS). In order to adjust the material beam and thus achieve high homogeneities and evaporation rates, in the present evaporation concept the source aperture has been modified by a conical shaped inset (Fig.1b).

The properties of the source with the conical inset were investigated by the laterally resolved measurement of the layer thickness. Over a large area around the center of the substrate, a constant thickness was achieved, while the relative layer thickness decreases to about 88 % in the outermost edges of the substrate. In Fig. 2, the measured layer thickness along a line between the center and an edge of the substrate is shown. It is compared to the $\cos^4\theta$ distribution and a simulation which has been performed by the manufacturer of the source considering the geometry of the conical inset and the distance between source and substrate [6]. The comparison shows that an improved homogeneity is achieved compared to the Knudsen theory. However, the reference values of the simulation are barely achieved. The material yield is determined by the measurement of the mass of the evaporation source before and after evaporation. This mass is compared to the deposited mass on the corresponding substrate which is determined by the

measurement of the mean film thickness and its area. It is about 11.5 % and thus twice as high as one could expect from the Knudsen theory but less than the achieved material yields of the CSS method.

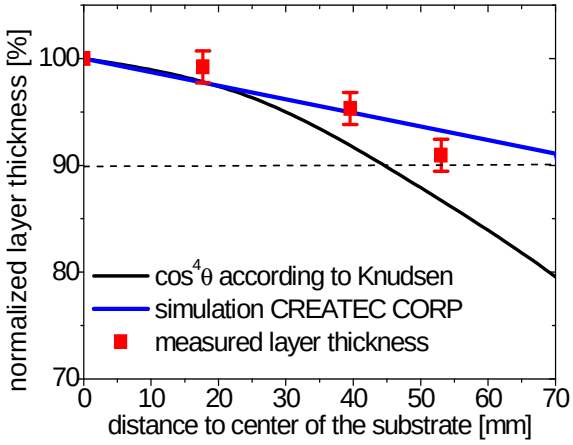

Fig. 2: Comparison of simulated and measured homogeneity with the $\cos^4\theta$-distribution.

The PVD build-up features a high distance between the substrate and the evaporation source. Therefore the evaporation source does heat the substrate only slightly and it is possible to deposit CdTe thin films at very low temperatures. CdTe layers were grown at a source temperature of 700 °C and different substrate temperatures of 180 °C to 300 °C in order to investigate the influence of the substrate temperature on the solar cell characteristics. The solar cells grown by the PVD process show remarkable efficiencies of up to 11.7 % at substrate temperatures of 300 °C. Furthermore, the characteristics of the cells are well reproducible, as it was proved by measuring a total of eleven cells with a mean efficiency of 10.5 % (Tab. 1). The mean values and standard deviations of the characteristics of solar cells whose absorber layers were grown at even lower substrate temperatures than 300 °C are also displayed in Tab. 1. They are compared with cells which were produced with CSS-grown CdTe layers (indicated with an asterisk) for substrate temperatures of 320 °C and 450 °C. The rest of the production process for the CSS-grown samples was equal to the PVD-grown samples. Hence, with the new baseline at low substrate temperatures the solar cell performance is not only kept but even improved. The further reduction of the substrate temperature results in solar cells with efficiencies of up to 8.8 % for substrate temperatures of 190 °C at a mean value of 8.2 % efficiency. However, a substrate temperature of 180 °C abruptly results in a poor solar cell performance with low efficiencies of about 0.6 %. This decrease of the solar cell characteristics is due to an excess of Te in the layer which was determined by means of energy dispersive x-ray analysis.

T_{sub} [°C]	V_{oc} [mV]	J_{sc} [mA/cm²]	FF [%]	η [%]	η_{max} [%]
320*	617±51	19.0±0.8	44±2	5.2±0.6	5.9
450*	741±9	20.9±0.8	62±3	9.5±0.7	10.5
300	773±16	20.3±0.7	67±2	10.5±1.2	11.7
260	742±6	19.8±0.8	67±1	9.9±0.5	11.1
220	722±8	19.1±1.2	60±1	8.2±0.4	8.8
200	739±12	19.6±1.1	60±3	8.7±0.5	9.6
190	662±7	19.9±0.7	62±2	8.2±0.3	8.8
180	384±15	4.9±2.7	30±1	0.6±0.3	0.8

Table 1: Mean values and standard deviation of the solar cell for different substrate temperatures T_{Sub} and different fabrication methods. The lines indicated with an asterisk represent measurements on solar cells which were produced by the CSS method.

References

[1] M. Möller, diploma thesis, University Heidelberg, Germany, 2007.

[2] M.A. Herman *et al*., Molecular Beam Epitaxy, Fundamentals and Current Status, Springer Verlag, Berlin, 1988.

[3] P. Clausing, *Zeitschrift für Physik* ***66***, 471 (1930).

[4] M. Knudsen, *Annalen der Physik* **353**, 1113 (1916).

[5] O.D. Crisalle *et al*., *Future CIS Manufacturing Technology Development, University of Florida* (2003).

[6] C. Kraft *et al.*, Annual Report 2009, Institute of solid state physics.

Connecting of Eu implanted ZnO NWs for electroluminescence applications

Y. Haj Hmeidi, S. Geburt, M. Junghanns, and C. Ronning

ZnO nanowires have got recreantly a huge interest because of their unique physical properties. ZnO is a wide band gap (3.37 eV) semiconductor material at RT with a large excitonic binding energy [1]. These properties make it a good candidate as host material for visible and infrared emission of various rare earth ions, which are good luminescence centers due to their narrow and intense emission lines originating from 4f-intrashell transitions [2]. Recent photoluminescence studies of Eu^+ implanted ZnO nanowires proved an energy transfer from host ZnO nanowires to Eu^+ ions [2]. The energy transfer should be also possible by applying an alternating current. The mechanism is based on excitation of luminescence centers in ZnO nanowires [3].

The ZnO nanowires were grown via VLS mechanism, and then implanted with varied ion energies and fluencies according to box-like concentration profile (Fig. 1).

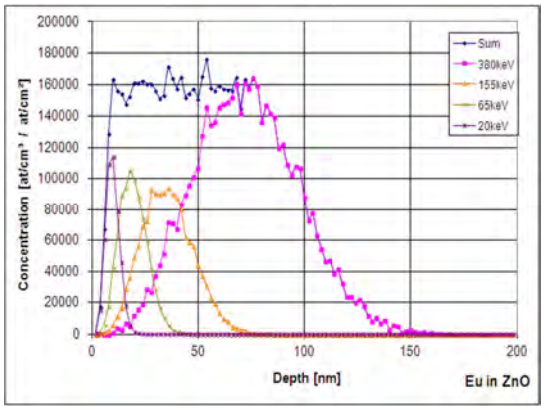

Fig. 1: Box-like implantation profile of Eu^+ implanted into ZnO matching the nanowires diameter.

The Eu^+ ion fluence was 2.5×10^{15} cm^{-3} resulting into concentration of 0.7 at%. The implanted nanowires were annealed for 30 minutes at 700 °C in O_2 ambient. The implanted ZnO nanowires were imprinted randomly on SiO_2/Si substrates. Photolithography was done to define electrical pads, and metal contacts on both ends of the nanowires were deposited via electron beam evaporation.

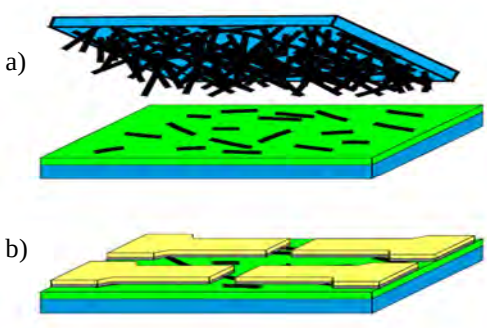

Fig. 2: (a) Transfer ZnO nanowires by imprint after implantation with Eu^+, (b) Sketch of final device [4].

A few implanted ZnO nanowires could be connected and were investigated using scanning electron microscopy, as shown in figure 2.

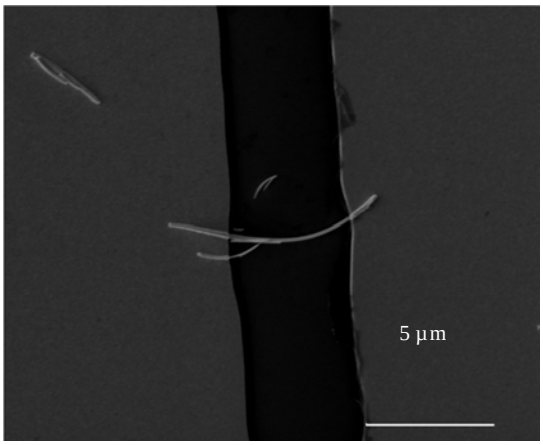

Fig. 3: SEM image of one connected implanted ZnO nanowire.

The current-voltage characteristics were measured by using a Keithley 237 source measurement unit and indicated a double Schottky diode behavior for the implanted ZnO nanowires. The resistivity of implanted ZnO nanowires was larger than as-grown ZnO nanowires due to the damage

and defects, which were created during the implantation. Furthermore, we determined the threshold voltage to destroy the ZnO nanowires and it was in the range of 8-20 V. The voltage differs because each connected ZnO nanowire has different manufacture conditions such as photolithography, lift–off and metallization.

The micro-photoluminescence setup was used to investigate any possible electroluminescence during applying an alternaing voltage to the wires, using varying frequency (10 KHz to 1 MHz) and peak-to-peak voltage (4 to 20 V). However, no electroluminescence was observed at all. However, after each step the photoluminescence was measured for the implanted ZnO nanowires, and a representative spectrum is shown in figure 4.

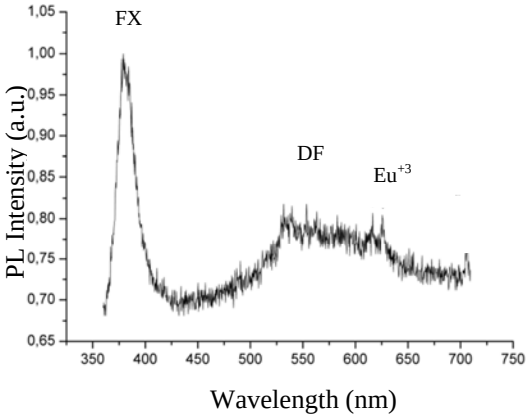

Fig. 4: Photoluminescence spectra of Eu^{+} implanted ZnO nanowires.

The typical features of ZnO are visible in the PL-spectra: the near-band edge and free excitons (FX), as well as the green luminescence (DF), which is usually assigned to intrinsic bulk defects. In addition the sharp intra-4f luminescence of Eu^{+3} are well observed.

The Eu^{+} implanted ZnO nanowires were successfully connected. Its current-voltage behavior was well studied. The photoluminescence of Eu^{+} implanted ZnO nanowires was also specially resolved observed, as shown in figure 5. These results are quite promising even though, that the electroluminescence has been not observed yet.

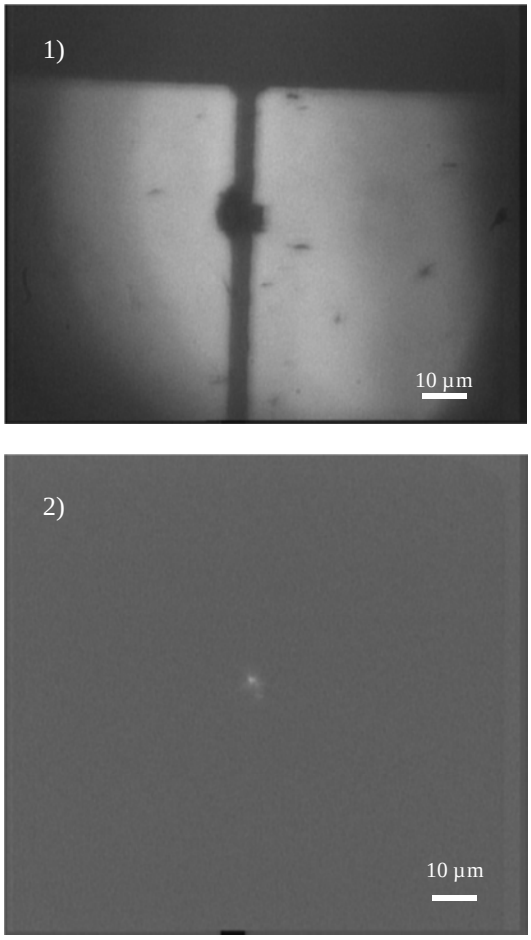

Fig. 5: (1) Microscope image of implanted ZnO nanowire. (2) µPL emission of implanted ZnO nanowire.

References

[1] B. K. Meyer PSS (b) **241** (2004) 231
[2] S. Geburt, D. Stichtenoth, S. Müller, W. Dewald, C. Ronning, J. Wang, Y. Jiao, Y. Y. Rao, S. K. Hark, Q. Li. J. Nanosci. Nanotechnol. **8** (2008) 244
[3] D. Dachi, K. Takei, T. Toyama, H. Okamoto. Japanese JAP **47** (2008) 83
[4] R. Niepelt, PhD thesis, FSU Jena (2012)

Wiring Quantum Dots

Andreas Johannes, Benjamin Fuchs, and Carsten Ronning

The size of nanoclusters varies their physical properties until at very small scales quantum confinement potentially brings entirely new properties. Combining these with nanowires (NWs) adds the advantage of quasi-one-dimensional transport in the direction of the nanowires. This allows for large interaction with the QDs through channeled transport and/or a large surface to volume ration depending on the application. The combination can be optimized for a variety of applications including optoelectronics [1], photovoltaics [2], sensing [3], and thermoelectronics [4].

This contribution outlines a possibility of the synthesis of such nanoscaled heterostructures with the example of ZnO NWs and Cu_2O nanoclusters. ZnO NWs have themselves show waveguiding [5] and even lasing [6]. A promising QD material in the ZnO matrix is copper-I-oxide. The optical properties of Cu_2O (bandgap: 2,2 eV) have gained some interest [7,8]. As the bandgap is smaller than that of ZnO (3.4 eV) a quantum well structure could be achieved. Also excited carriers in the ZnO can migrate to the QD and recombine in there.

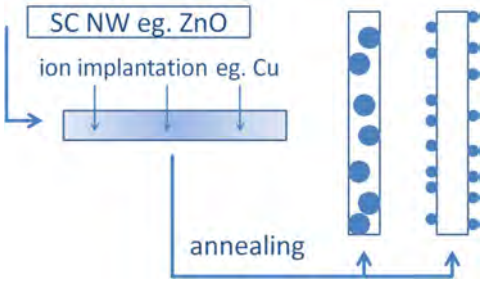

Fig. 1: Principle of synthesis of nanowires/ nanocluster heterostructures via in-implantation and annealing.

The principal approach is sketched in Fig. 2. Nanowires are implanted with the material desired as a QD. The implantation is not limited to solubility limits and is continued until an oversaturated solid is formed. In a subsequent high temperature annealing step the material will segregate and form clusters. The size, position, distribution and composition of the clusters will depend on the implantation parameters and annealing time, temperature and atmosphere.

Homogenous doping was achieved with a special-built rotating and heatable stage shown schematically in Fig.3. Nanowires grown perpendicular to their substrate can thus be implanted from all sides. The implantation profiles in nanostructures can be accurately simulated with *iradina* [9]. The concentration in the supersaturated solid can be accurately controlled in a wide range.

After the implantation, the NWs were

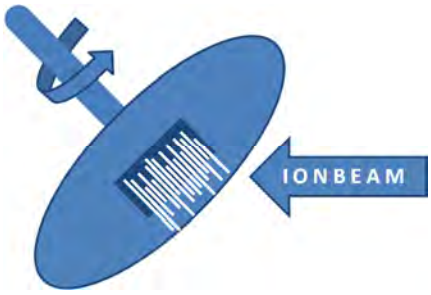

annealed to increase the mobility of the incorporated atoms. This allows the agglomeration of clusters and thus formation of QDs. It is assumed that the copper will oxidize at least partly in an oxide matrix and during annealing. Hence, the nanoclusters will be named CuO even

Fig. 2: Sketch of the rotating implantation of upstanding nanowires. Neither the implanted nor nanowires material is particularly constrained by this approach.

though the exact stoichiometry is unknown and not trivially obtainable.

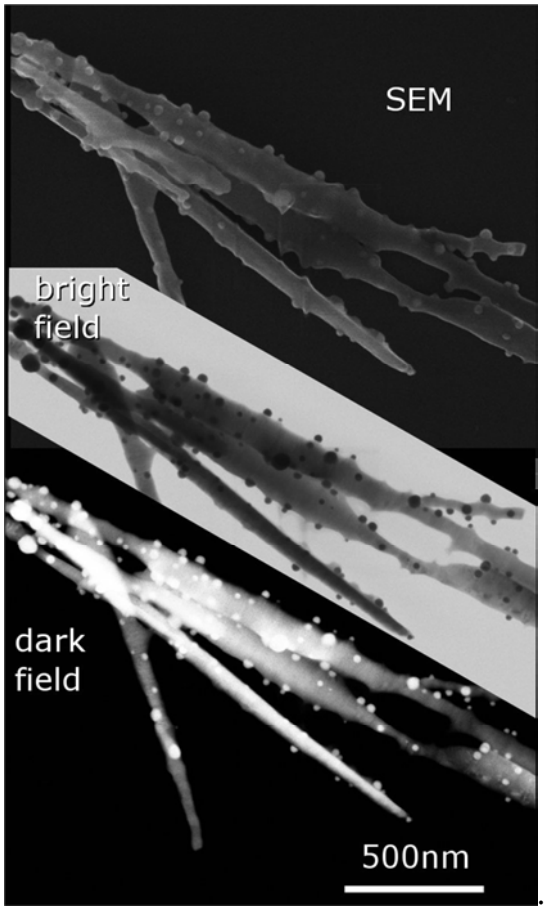

Fig. 3: SEM and STEM (bright- and dark-field) images of the first ZnO-CuO nanowire-nanocluster hererostructures synthesized via ion-implantation and subsequent annealing.

The ZnO nanowires were implanted with 6 at.% Cu and annealed at 800°C for 30min. Fig.4 shows a standard SEM Image along with scanning transmission microscope (STEM) images in bright- and dark-field geometry. Clearly clusters with varying radii (30-80nm) were formed. The dark-field STEM images reveal that some defects were created within the NWs. However, no clusters can be seen inside the wires.

Selected area electron diffraction patterns (SAED) shown in Fig. 5, reveal, that the NW has retained its crystal structure and that the nanoclusters are polycrystalline. Due to their small volume it has so far not been possible to analyze the crystal structure of the nanoclusters in any further detail.

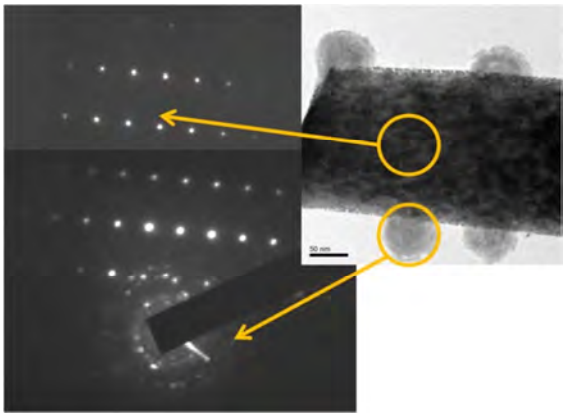

Fig. 4: TEM image with indications where the aperture was placed to collect selected area electron diffraction patterns.

The approach illustrated has been used successfully to synthesize nanowire-nanocluster heterostructures via ion-implantation. Variation of used NW and nanocluster materials will yield a large variety of new nanostructures for multiple possible applications.

References

[1] S. Reitzenstein and A. Forchel, J. Phys. D: Appl. Phys. **43** 033001 (2010)
[2] S. Rühle *et al.*, ChemPhysChem **11**, 2290-2304 (2010)
[3] S. Shao *et al.*, J. Mater. Chem. **22**, 18101-18110 (2012)
[4] G. J. Snyder and E. S. Toberer, Nature Materials **7**, 105-114 (2008)
[5] T. Voss *et al.*, Nano Letters **7**, 3675-3680 (2007)
[6] M.A.Zimmler *et al.*, Semicond Sci Tech. **25**, 024001 (2010)
[7] K. Das *et al.*, J. Appl. Phys. **107**, 024316 (2010)
[8] Z. Yang *et al.* Nanotechnology **19**, 025604 (2008)
[9] C. Borschel *et al* Nucl. Instrum. Meth. B, **19**, 2133-2138 (2011)

Spatially-resolved measurements of charge carrier lifetimes in CdTe

C. Kraft, H. Hempel, V. Buschmann[1], T. Siebert[1], C. Heisler, W. Wesch, and C. Ronning
[1] *PicoQuant GmbH, Rudower Chaussee 29, 12489 Berlin*

A promising but also challenging approach to increase the CdTe cell efficiency is the increase of the intrinsic concentration of charge carriers by extrinsic doping [1]. However, a higher doping level results in a reduced depletion area. Hence, the carrier lifetime has to be increased for a preferably high carrier collection to gain reasonable current densities. Currently, the lifetime of minority charge carriers of high performance CdTe solar cells is in the range of approximately 1 ns [1]. It has been shown experimentally [2] and theoretically [3] that the minority carrier lifetime (MCL) strongly influences the performance of the CdTe solar cell. A suitable method to determine the MCL in CdTe thin film devices is the measurement of time resolved photoluminescence (TRPL). Since the $CdCl_2$ activation is essential for the functionality of CdTe solar cells, it was indicated by means of TRPL that the recombination is reduced due to this treatment [4].

We performed laterally resolved TRPL measurements, which allow the decay curves and the MCL to be analyzed for very small structures and not only from an integrated luminescence signal. To this end, as-grown and activated samples were compared, which were grown using close space sublimation (CSS) [5]. Additionally, high resolution TRPL measurements were performed on samples in cross section configuration. Thus, carrier lifetimes next to the interface can be directly compared to the lifetimes in direct proximity to the CdTe surface.

The difference of the carrier lifetime distributions of the as-grown sample and the activated sample is shown in Fig. 1. By means of space-resolved TRPL measurements, a lifetime mapping can be generated and the sample surface can be divided into grains and grain boundaries. The distributions should have the tendency to a Gaussian distribution, but it is clearly asymmetric in the as-grown case. Considering the subdivision in grains and inter grain areas, two single lifetime histograms are deduced, which have a Gaussian character each, except of a shoulder at the long lifetime edge of the inter grain curve. It becomes apparent that in inter-grain areas the carrier lifetimes of the charge carriers are lower than in grains

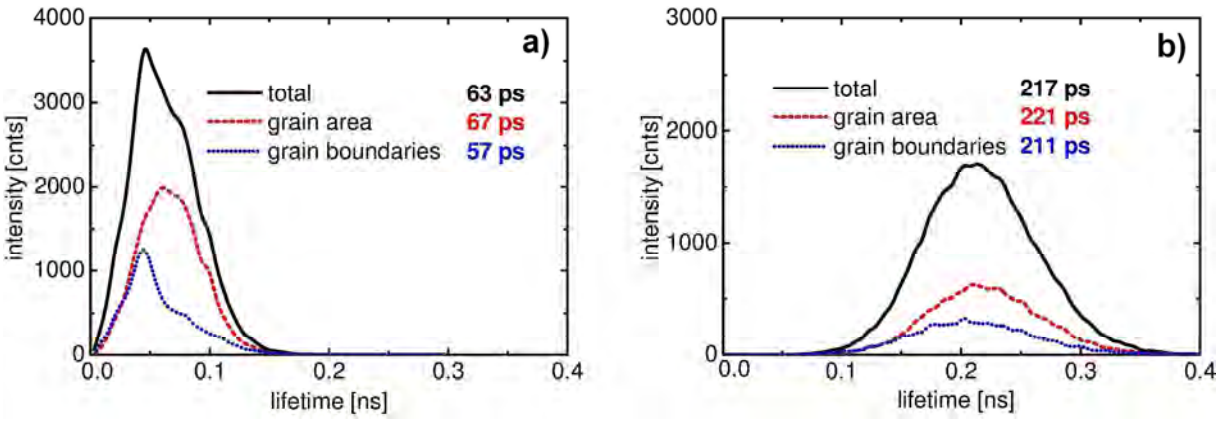

Fig. 1: The carrier lifetime distribution of an as-grown sample (a) compared to an activated sample (b).

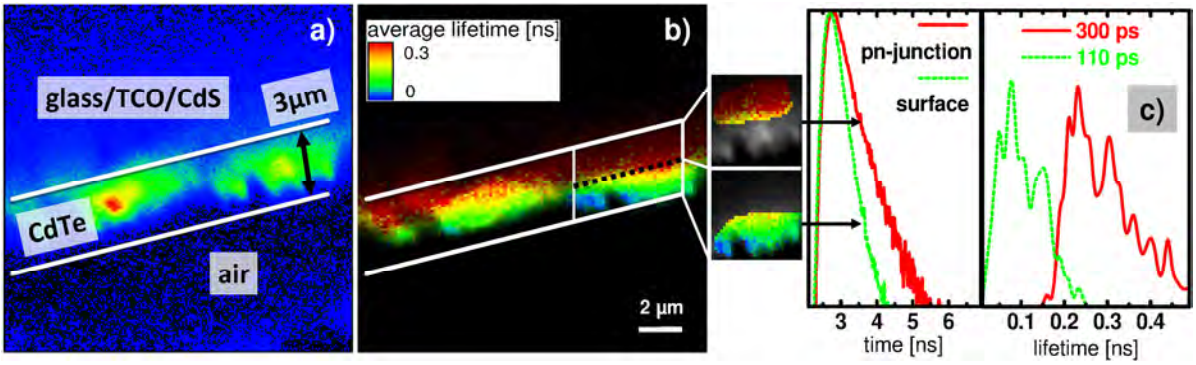

Fig. 2: Luminescence image (a), and carrier lifetime distribution (b) of an activated PVD-grown sample recorded in cross section configuration. The rectangles in section b) indicate the investigated areas in section c), which shows the decay behaviour of the charge carriers near the surface and near the pn-junction as well as the distributions of the respective lifetimes in the regarded areas.

(and the luminescence intensity as well) due to a higher recombination rate at the grain boundaries. For the activated sample, the differentiation in grains and inter grain areas on the basis of the carrier lifetime mapping is difficult due to similar lifetimes in both areas. However, the carrier lifetime histograms show a Gaussian carrier lifetime distribution for all regarded areas with almost the same average carrier lifetimes of about 220 ps. Hence, in contrast to the as-grown sample, the lifetime distribution of the activated sample is independent on the surface morphology. According to reference [6], this is due to the passivation of grain boundaries as a consequence of the activation step. The results are supported by a recent study, in which a strong influence of the $CdCl_2$ activation on the carrier lifetimes is observed [4].

The luminescence signal of the cross-section measurement is shown in Fig. 2(a) in order to determine the lifetime at the interface between glass/TCO/CdS and the CdTe absorber material. In Fig. 2(c), the lifetime distribution is shown for an activated sample next to the pn-junction and at the surface together with the respective decay curves. The corresponding lifetime mapping is shown in Fig. 2(b). The increase of the carrier lifetime with increasing distance from the surface is clearly visible. In the first µm below the surface, the carrier lifetime is in the range of 50 to 150 ps (blue areas) and increases to about 300 ps (red areas) close to the pn-junction. Furthermore, it can be seen in the luminescence picture in Fig. 2(a) that the luminescence signal is not correlated to the carrier lifetime. The maximum luminescence intensity can be found in the centre of the bulk material and not at the interface, where the carrier lifetime is the highest. Probably the ratio of luminous recombination next to the interface and the surface is low due to the respective interface and surface defects.

References

[1] J.R. Sites and J. Pan, Thin Solid Films **515**, 6099-6102 (2007).

[2] X. Wu, Sol. Energy **77**, 803-814 (2004).

[3] L.A. Kosyachenko and E.V. Grushko, Semiconductors **44**, 1375-1382 (2010).

[4] W.K. Metzger *et al.*, J. Appl. Phys. **99**, 103703 (2006).

[5] M. Hädrich *et al.*, Thin Solid Films **515,** 5804-5807 (2007).

[6] K. Durose *et al.*, J. Cryst. Growth **197**, 733-742 (1999).

Optical damage characterization of Ag implanted $LiNbO_3$

Steffen Milz, Jura Rensberg, Werner Wesch and Carsten Ronning

Embedded metal nanoclusters are of special interest in optical devices (optical filters [1], waveguides [2], etc.) due to their unique plasmonic properties. The advantage over surface nanoclusters is that they have a defined and homogeneous surrounding with a constant dielectric function leading to a well-defined surface plasmon resonance (SPR).

Embedded silver nanoclusters were synthesized inside lithium niobate ($LiNbO_3$), which is one of the most important materials for integrated optics due to its unique electro-optical and nonlinear optical properties [3]. The synthesis was achieved by the implantation of 380 keV silver ions to a fluence of $1 \cdot 10^{17}$ cm^{-2}. Post implantation annealing as well as implantation at elevated temperatures (400 °C) were carried out in order to minimize the irradiation damage [4].

Optical spectroscopy with light polarized along the ordinary or extraordinary axis of $LiNbO_3$ was used to measure the position of the SPR. The SPR position depends on various parameters, e. g. the cluster size distribution and the dielectric function of the clusters and the host material. For a given nanocluster material and similar cluster size distributions the refractive index of the host material is the dominating effect of the SPR position. Lithium niobate has different refractive indexes depending on the crystal structure and the direction of the incoming light (crystalline: n_o=2.286, n_e=2.202, amorphous: n_a=2.100). Therefore the SPR position is highly sensitive to the crystal quality.

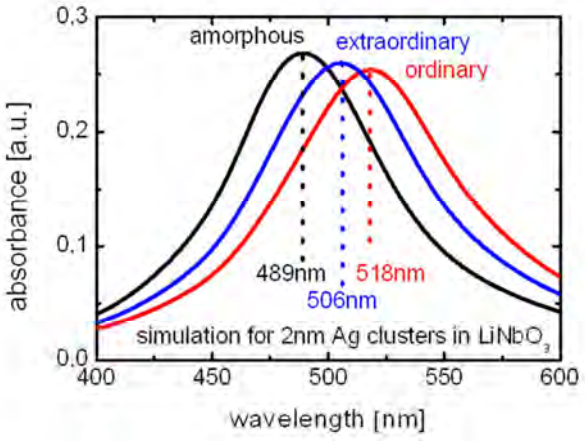

Fig. 1: Simulation of the SPR of Ag nanoclusters (r=2nm) in amorphous and crystalline (ordinary/ extraordinary) $LiNbO_3$.

A simulation program based on Mie's theory [5] has been developed to simulate the SPR for a given nanocluster material, size distribution and refractive index of the host material. Figure 1 shows the results for Ag clusters with radii of 2 nm embedded in amorphous and crystalline $LiNbO_3$. In the case of crystalline $LiNbO_3$ the SPRs along the ordinary and extraordinary direction differ due to the different refractive indexes. Amorphous $LiNbO_3$ is isotropic and therefore not dependent on the direction of the incoming light.

Comparing the measured SPR positions with the simulated ones allows estimating the crystal quality of $LiNbO_3$ after the silver implantation. Fig. 2a and b show STEM images of Ag clusters implanted at room temperature (RT) and the corresponding optical spectra along the y- and z-axis, respectively. Both spectra show nearly identical SPR peaks at about 490 nm. Comparing this with the simulation in figure 1 indicates a complete amorphization of the $LiNbO_3$ matrix during room temperature implantation.

Increasing the implantation temperature to 400 °C changes the cluster size distribution as well as the optical properties (Fig. 2c and d). The growth of the Ag nanoclusters

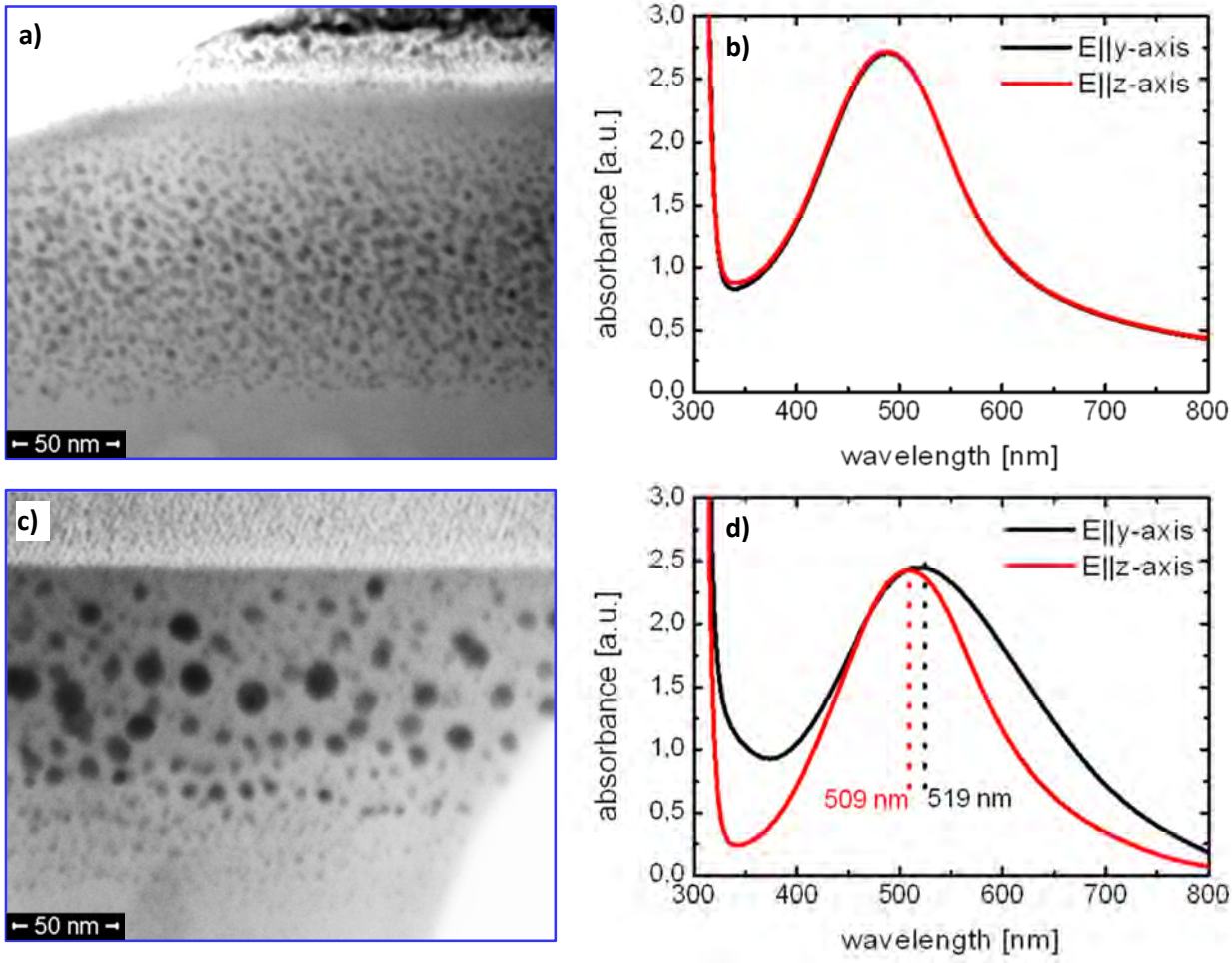

Fig. 2: STEM images and the corresponding UV-VIS spectra of silver implanted lithium niobate (380 keV, $1 \cdot 10^{17}$ cm^{-2}) at room temperature (a, b) and 400 °C (c, d), respectively.

due to Ostwald ripening at elevated temperatures has a practically negligible influence the SPR position. The UV-VIS spectra with light polarized along the y- and z-axis (Fig. 2d) show two different SPR peaks – one centered around 509 nm and the other at 519 nm. This is in very good agreement with the simulated SPR positions for crystalline $LiNbO_3$ (Fig. 1). Obviously, the elevated implantation temperature leads to dynamic annealing and efficiently avoids most of the amorphization due to irradiation damage.

Additionally, it could be shown that applying post implantation annealing successively up to 600 °C after RT implantation gives results comparable to the 400 °C implantation.

To conclude, it has been shown that measuring the polarization dependent SPR of silver nanoclusters embedded in $LiNbO_3$ and comparing them to simulations based on Mie's theory is a suitable tool to easily characterize the damage fraction of the $LiNbO_3$ matrix. This will help to optimize the irradiation and annealing parameters in order to obtain Ag nanoclusters embedded in high quality $LiNbO_3$.

References

[1] D. M. Wu *et al.*, *Appl. Phys. Lett.*, **83**, 201-203 (2003).

[2] S. A. Maier *et al.*, *Nat. Mater.*, **2**, 229-232 (2003).

[3] F. Chen, *J. Appl. Phys.*, **106**, 081101 (2009).

[4] S. Milz *et al.*, *NIMB*, **286**, 67-71 (2012).

[5] G. Mie, *Annalen der Physik*, **25**, 377-445 (1908).

Computerized optimization of CIGSe thin film solar cell efficiencies for industrial application

Michael Oertel, Alexander Kusch, Sven Schönherr, Philipp Schöppe, David Stoll, Claudia Schnohr, Udo Reislöhner and Carsten Ronning

$Cu(In,Ga)Se_2$ solar cells are the most promising thin film solar cells in order to compete against the common crystalline and multi-crystalline silicon solar cells in terms of efficiency [1]. Hence, in 2007, the comCIGS-project was initiated, which aimed to a better understanding of the relationships between the structural and electro-optical properties of the $Cu(In,Ga)Se_2$ bulk and their solar cell efficiencies by means of ab-initio calculation and experimental validation [3],3]. In August 2012 the follow-up project "ComCIGS II" started. The emphasis now is on the investigation of interfaces and inhomogeneities in $Cu(In,Ga)Se_2$ thin film solar cells with ab-initio and experimental methods to describe their contributions to efficiency limitations.

A strong consortium was formed between industrial and academic research groups named IBM Germany GmbH, Schott AG, Manz CIGS Technology GmbH, Bosch CISTech GmbH, Robert Bosch GmbH, Helmholtz-Zentrum Berlin für Materialien und Energie GmbH, Johannes-Gutenberg-University Mainz and the Friedrich-Schiller-University Jena represented by the Institute of Solid State Physics (IFK).

With a high expertise in electro-optical and structural analysis of semiconductors, the IFK is mainly responsible for the characterization of the $Cu(In,Ga)Se_2$ thin film solar cells in the project. Therefore, many characterization techniques are available, e. g. scanning electron microscopy, focused ion beam (FIB) preparation of samples for tunnel electron microscopy (as shown figure 1), energy dispersive x-ray spectroscopy, extended x-ray absorption fine structure analysis (in cooperation with large synchrotron facilities), µ-photo- and cathodo-luminescence, illuminated and non-illuminated current-voltage- (I-U) and capacitance-voltage-measurements, quantum efficiency (QE)-measurement and admittance spectroscopy.

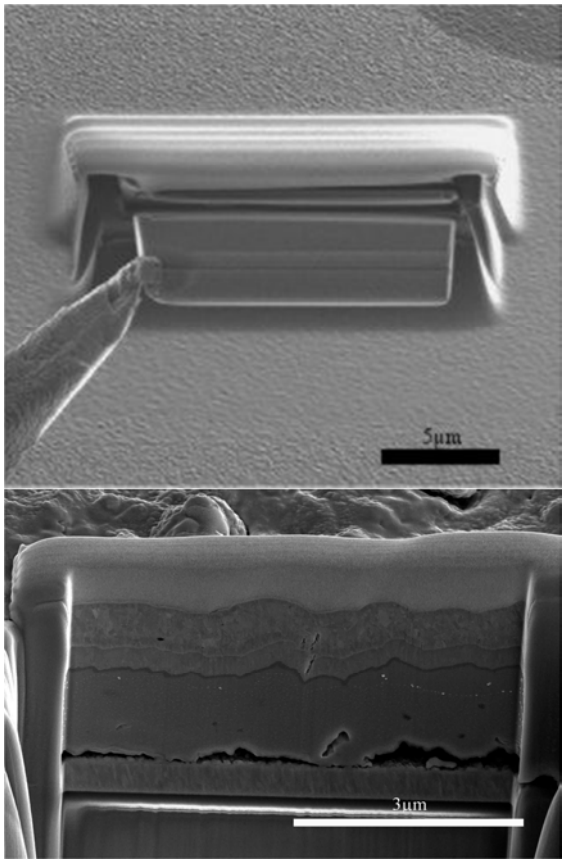

Fig. 1: (top) Lift off of a FIB-prepared TEM lamella; (bottom) FIB-prepared $Cu(In,Ga)Se_2$ solar cell cross-section.

This large portfolio gives the IFK the possibility to correlate structural and electro-optical properties of $Cu(In,Ga)Se_2$ thin film solar cells even on micro- and nanometer scale. By investigating solar cells produced with totally different industrial techniques at Manz CIGS Technology GmbH (former Wuerth Solar) [4] and

Bosch CISTech GmbH (former Johanna Solar) [5] it will be possible to separate pure material properties from production technique based ones. This knowledge will be used for exact simulations and ab-initio calculations at the Johannes-Gutenberg-University Mainz and IBM.

Besides the investigation of industrially produced samples, the IFK built up an own process line for manufacturing chalcopyrite thin film solar cells with a scale factor of 10x10cm^2. The line works on the basis of the sequential approach for Cu(In,Ga)Se_2 solar cell production described in principal in [6]. To fulfill the requirement of a maximum of process control the reactive annealing of the metallic precursor is done in an open system, where the reactive atmosphere of elemental selenium vapor is generated by a Knudsen type evaporation source in a high vacuum environment. Figure 2 shows results of I-U- and external QE-measurements for typical Cu(In,Ga)Se_2 solar cells produced in this line. The results are shown for an integral gallium content of around 30% and without gallium in the absorber. The external quantum efficiency measurements show a clear shift of the absorption edge of the $CuIn_{0.7}Ga_{0.3}Se_2$ sample to shorter wavelength compared to the gallium free sample due to the incorporation of gallium in the absorber close to the p-n-junction. This also results in a higher open circuit voltage and an only slightly lower short current density which leads to a total area conversion efficiency of 13.3%. The incorporation of gallium close to the p-n-junction is insofar remarkable as in general gallium rich phases tend to segregate near the back contact due to reaction kinetics or special treatments are necessary to avoid the segregation [7,8]. In our process no such treatments are necessary.

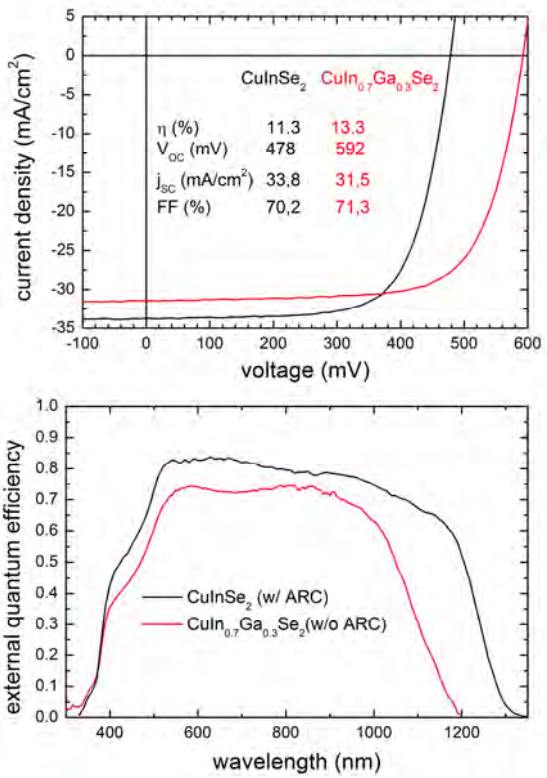

Fig. 2: (top) Typical I-U-graphs of $CuInSe_2$ and $CuIn_{0.7}Ga_{0.3}Se_2$ solar cells produced at the IFK (both w/o antireflective coating (ARC)); (bottom) Corresponding quantum efficiencies ($CuInSe_2$ solar cell was measured at ISE Freiburg w/ ARC).

Acknowledgement

The authors thanks the Bundesministerium für Umwelt, Naturschutz und Reaktorsicherheit for its financial support.

References

[1] M. A. Green et al., Prog. Photovolt: Res. Appl. **20** 606-614 (2012).

[2] C. Ludwig et al., Phys. Rev. Lett. **105** 025702 (2010).

[3] J. Haarstrich et al., Solar Energy Mater. and Solar cells **95** 1028-1030 (2011).

[4] M. Powalla et al., Solar Energy Mater. and Solar cells **90** 3158-3164 (2006)

[5] V. Alberts, TSF **517** 2115-2120 (2009)

[6] M.Oertel et al., Phys. Stat. Sol. C **6** 1253-1256 (2009)

[7] J. Palm et al., Solar Energy **77** 757-765 (2004)

[8] V. Alberts, Semicon. Sci. Techn. **19** 65-69 (2004)

Maxwell-Wagner Polarization in $Cu(In,Ga)(S,Se)_2$

Udo Reislöhner and Carsten Ronning

Inhomogeneous semiconductors are of great importance, because this material class is essential for low cost devices, as for example the remarkable market development of highly efficient thin-film solar cells based on $Cu(In,Ga)(S,Se)_2$ (=CIGS) impressively demonstrates. The impact of inhomogeneity on the properties of such devices is of special interest, in particular when polycrystalline devices reach world record efficiencies over 20%, as in the case of CIGS solar cells.

However, the consequence of inhomogeneities in CIGS on the response to an ac-voltage has not yet been adressed. This response to ac-voltage is the basis of standard semiconductor characterization methods that measure the capacitance of the space charge region like CV-profiling, thermal admittance spectroscopy (TAS) or deep-level-transient spectroscopy (DLTS).

We investigated $CuInSe_2$-cells (CIS), prepared in a sequential process [1], as well as industrial $Cu(In, Ga)(Se, S)_2$-cells produced in the AVANCIS pilot-line [2]. The conductance G of the CIS sample measured at T=32K shows a constant plateau at low frequencies and increases with a power law at higher frequencies like $G = G_0+h^*\omega^s$, as depicted in Fig. 1(a), similar to the conductance observed in CIGS [3] but with an additional constant component G_0. The exponent s is a number typically around 0,8 and h^* determines the amplitude of ac-conductivity. The continuous increase of G requires a distribution of capacitive elements, which play an increasing role with increasing frequency by shorting other capacitive or resistive pathways. This yields the well known pattern of "Universal Dielectric Response" (UDR) as a common phenomenon in disordered or inhomogeneous solids [4].

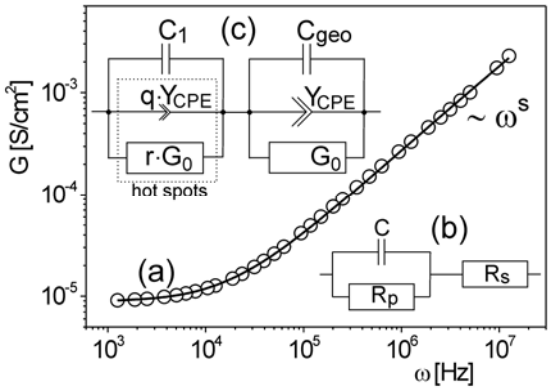

Fig. 1: The data points are the measured conductance G in $CuInSe_2$ at T=32K and the straight line is a simulation using circuit (c). Inset (b) shows the standard equivalent circuit, which is usually assumed when standard semiconductor characterization methods are applied. Equivalent circuit (c) is developed in this study and allows a correct description of $Cu(In,Ga)(S,Se)_2$-cells.

The basis for this behavior is Maxwell-Wagner polarization, that generally occurs when an electric current flows through regions of different electrical conductivity due to pile up of charges at the interfaces [5]. This does not only hold for grain boundaries due to their repellent property on holes but also for crystallographic coherent interfaces at nanodomains with varying stoichiometry and thus varying conductivity as confirmed by Yan et al. [6] as well as the known potential fluctuations. These differently conducting regions ensure Maxwell-Wagner polarization in the CIGS absorber entailing UDR with its progression of conductance G with increasing frequency. The consequent mathematical description yields for the bulk the general complex admittance Y $Y_{bulk}=G_0+h(i\omega)^s$, where the second term is

equivalent to a constant phase element (CPE). The additional consideration of the leakage characteristic of the pn-junction [7] results in the two serial circuits shown in Fig. 1(c) possessing the total impedance $Z=Z_1+Z_2$ with $Z_1=(rG_0+qY_{CPE}+i\omega C_1)^{-1}$ and $Z_2=(G_0+Y_{CPE}+i\omega C_{geo})^{-1}$.

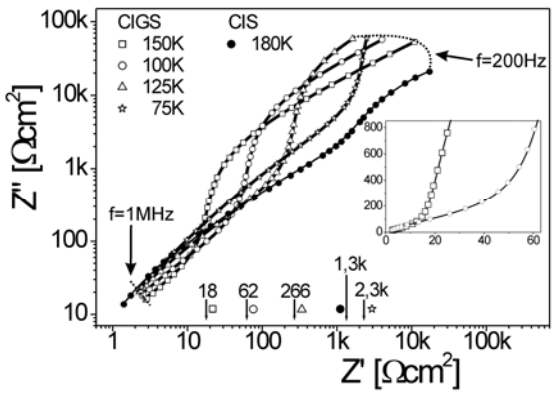

Fig. 2: Nyquist-plots (the imaginary part of the impedance is plotted over the real part) show a strong kink that shifts with temperature. The calculation (straight lines) perfectly match the data points and the extracted series resistances $R_0=1/G_0$ are indicated at the Z'-axis.

The Nyquist-plot of Z''=Im(Z) as function of Z'=Re(Z) is shown in Fig. 2. In a Nyquist-plot, a single parallel RC-circuit gives a semicircle in the Z'-Z''plane, which is shifted to the right by the amount of an additional series resistance, i. e. the series resistance is obtained from the intercept with the Z'-axis at high frequencies, while the sum of series and parallel resistance is given by the intercept at low frequencies at the right side of the semicircle. Here, the Nyquist-plots show an abrupt and strong kink for higher frequencies and continue to the origin of the Z'-Z''diagram. The approach to the origin expresses the decreasing absolute value of the impedance with increasing frequency and confirms the model. The continuation of the circle gives the series resistance $R_0=1/G_0$, which increases strongly with decreasing temperature confirming results from earlier current-voltage characteristics [3] taken at the identical cells. The here developed equivalent circuit, as shown in Fig. 1(c), enables a perfect adaption (straight lines in Fig. 2) of the measured Nyquist-plots.

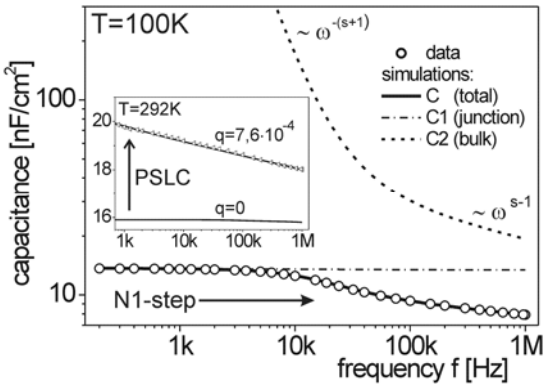

Fig. 3: The N1-step is caused by conduction phenomena due to inhomogeneities within the bulk (Maxwell-Wagner polarization). The step is equivalent to the corresponding kink in the Nyquist-plot in Fig. 2. The inset illustrates the impact of "phase shifted leakage currents" PSLC (amplitude q, T=292K) as introduced Ref. [7].

The total capacitance (Fig. 3) shows a pronounced step, which is exactly the discussed N1-signal of CIGS solar cells [3]. Thus, the series connection of the inhomogeneous semiconductor and the depletion layer capacitance causes a step in the total capacitance $C(\omega)$ at a characteristic frequency ω_c which is shown to obey the proportionality $\omega_c^s \sim G_0$ [7]. In more detail, we show in Ref. [7] that inhomogeneous chalcopyrites comprise a percolation network of capacitive and resistive pathways, where the transmissibility of the latter is strongly narrowed down with decreasing temperature and is depending on voltage.

References

[1] M. Oertel et al., PSS C **6**, 1253 (2009).
[2] J. Palm et al., Sol. Energy **77** (6), 757 (2004).
[3] U. Reislöhner et al., PRL **104** , 226403 (2010).
[4] A. Jonscher, Nature **267** (5613), 673 (1977).
[5] Wagner, Archiv f. Elektrotechn. 2, 371 (1914).
[6] Y. F. Yan et al., APL **87**, 121904 (2005).
[7] U. Reislöhner et al., APL **100**, 252111 (2012).

Optical and Electrical Properties of Tungsten Doped VO_2 Thin Films

J. Rensberg, S.Vatterodt, D. Bürger[1], H. Schmidt[2], C. Ronning

[1] Institute of Ion Beam Physics and Materials Research, Helmholtz-Zentrum Dresden-Rossendorf, Germany
[2] Department of Materials for Nanoelectronics, Chemnitz University of Technology, Germany

Vanadium dioxide (VO_2) undergoes a reversible metal to insulator transition (MIT) along with a first-order crystallographic transition from a high-temperature tetragonal rutile phase to a low-temperature monoclinic phase at a critical temperature (T_C) of about 68°C [1]. This transition is accompanied by considerable changes in electrical resistivity and optical properties. The critical temperature can be decreased by doping the lattice with high-valent cations such as Nb^{5+} [2] or W^{6+} [3-5] that are known to generate donor-like defects. VO_2 thin films are thus promising candidates for memristive as well as switchable optical applications [6,7].

In this study we investigated the effect of tungsten doping on both the electrical as well as the optical properties of VO_2 thin films. For this purpose VO_2 thin films were deposited onto quartz substrates by pulsed laser deposition (PLD). Since the morphology and stoichiometry of the films strongly depend on the growth temperature two sets of samples were prepared at substrate temperatures of 580°C and 630°C, respectively. Codoping was achieved by ablating tungsten doped vanadium dioxide targets, thus, samples with nominal W-dopant concentrations of 1.0 and 1.9 at.% were prepared. Further details for the PLD film preparation have been described elsewhere [8].

The electrical properties of the films have been investigated in the temperature range from below room temperature up to 100°C by measuring their temperature-dependent resistivity in VAN DER PAUW geometry. These measurements are summarized in figure 1.

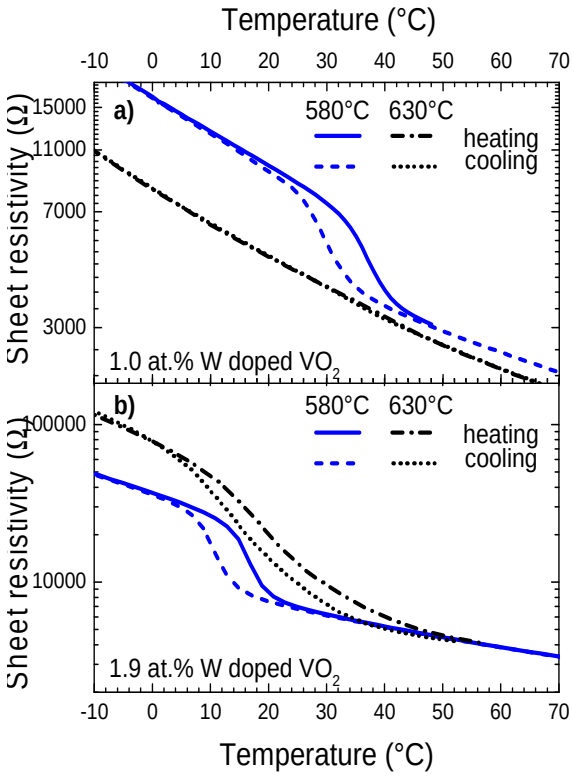

Fig. 1: Sheet resistivity of nominel 1.0 at.% (**a**) and 1.9 at.% (**b**) tungsten doped VO_2 thin films prepared by PLD at 580°C and 630°C as a function of temperature.

The pure VO_2 thin films exhibit a MIT at T_C of about 68 °C (not shown). With increasing W-dopant concentration from 1.0 at.% to 1.9 at.% the critical temperature of the MIT decreases to a value of about 35°C and 15°C, respectively, as shown in figure 1. The reduction in T_C upon W doping can be explained either by an electronic or structural mechanism. On the one hand the substitution of V^{4+} with W^{6+} results in an enhancement of the carrier concentration. If a critical carrier density in the material is reached, a phase transition could occur due to electron-electron interaction effects, i.e. correlation (often

referred to as Mott-Hubbard MIT) [6]. On the other hand, the MIT could be also correlated with the relative larger ionic size of W compared to V [3]. In this case, the reduction in T_C occurs from an electron-phonon interaction, which is referred to as Peierls MIT [4].

The amplitude of the MIT, which is defined as the difference between the resistivity at the insulating and metallic state, is dependent on both the growth temperature and the level of tungsten doping. Although it was found to be highest for the 1.9 at.% tungsten doped VO_2 film grown at 630°C, it is almost four orders of magnitude lower compared to single crystalline VO_2, where a change of up to five orders of magnitude can be observed [4]. This is most likely due to the presence of an amorphous phase [8] composed not only of V^{4+} but also of V^{3+} and V^{5+} [9]. In the investigated temperature range here V_2O_3 is metallic; whereas, V_2O_5 is insulating. This results into a decrease of the resistivity of the VO_2 films in the insulating phase and an increase of the resistivity in the metallic phase, respectively.

Optical properties of the films were studied at ambient temperature using a Varian Cary 5000 double beam spectrophotometer in dual beam configuration. The significant change of the spectral transmittance in the IR-part of the spectra for the different W-dopant concentrations, which is shown in figure 2, is due to the MIT. If the temperature during the measurement is below the critical temperature of the MIT, the doped film is in the insulating state and therefore IR transparent above 1000 nm. However, if the sample is above the critical temperature of the MIT, as it is the case for the higher W-doped film at RT, the film is in a metallic and hence IR-reflective state, which can be nicely seen in figure 2.

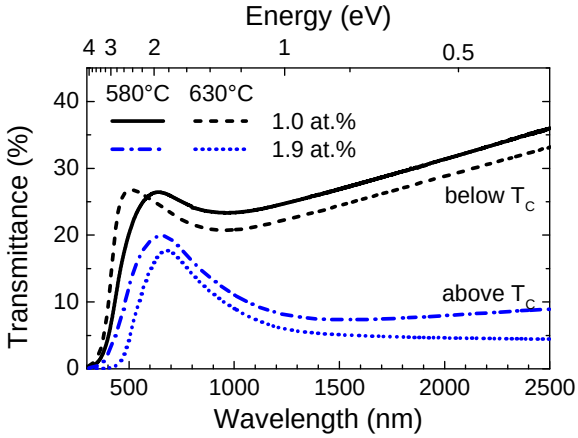

Fig. 2: Spectral transmittance of 1.0 at.% and 1.9 at.% tungsten doped VO_2 thin films prepared by PLD at various substrate temperatures of 580°C and 630°C.

As we demonstrated here, the critical temperature of the MIT can be reduced to room temperature by introducing W-dopants into the lattice of VO_2 during PLD film growth. The amplitude of the MIT strongly depend on the crystalline quality of the films and hence on the growth parameters. For all investigated tungsten doped VO_2 films in this study the electrical as well as the optical measurements indicate the presence of an amorphous phase and therefore low crystalline quality. Further investigations should aim at improving the crystalline quality

References

[1] F.J. Morin, Phys. Rev. Lett. **3,** 34-36 (1959)
[2] C. Piccirillo *et al.*, Eur. J. Inorg. Chem. 4050-4055 (2007)
[3] P. Jin *et al.*, Thin Solid Films **324,** 151-158 (1998)
[4] R. Binions *et al.*, Surf. Coat. Tech. **201,** 9369-9372 (2007)
[5] F. Béteille *et al.*, J. Sol-Gel Sci. Techn. **13,** 915-921 (1998)
[6] Z. Yang *et al.*, Annu. Rev. Mater. Res. **41,** 337-367 (2011)
[7] W. Huang *et al.*, Appl. Phys. Lett. **96** 261908 (2010)
[8] G.J. Kovács *et al.*, J. Appl. Phys. **109**, 063708 (2011)
[9] Y.-B. Kang, J. Eur. Ceram. Soc. **32,** 3187-3198 (2012)

Slope efficiency of CdS nanowire lasers

Robert Röder, Sebastian Geburt, and Carsten Ronning

Future research can face the limitations of conventional electronic integrated circuits by reinforced work in the field of nano-photonics for the development of on-chip optical components [1]. Since semiconductor nanowires offer efficient waveguiding [2] and mark the physical size limit of photonic laser [3, 4], they are promising for providing optical data transmission and processing.

The green spectral range around an emission wavelength 517 nm is opened up by high quality cadmium sulfide nanowires synthesized via vapor-liquid-solid mechanism. Under optical pumping CdS nanowires reveal strong Fabry-Pérot laser oscillations with remarkable low threshold 10 kW/cm² at room temperature [4].

Optical processing is specified by the direct emission of the device, thus recent research is addressed to the development of a “head-on” µPL setup schematic in inset Fig. 1(a). The measurement geometry with a CdS nanowire partially suspended in air in Fig. 1(c) is suitable for the direct detection of light output originating out of the facet end along the nanowire axis without any scattering of the substrate.

At low excitations below 10 nW pump power, only broad spontaneous emission is emitted at the nanowire end. In the lasing regime, when sharp and equidistant modes dominate the emission spectrum as shown in Fig. 1(a), the calculated ratio of nanowire light output to excitation pump power in Fig. 1(b) increases from ≤1% for the spontaneous emission to a slope efficiency of 5-10%.

Optical resonators are typically characterized by the quality factor $Q=\lambda/\Delta\lambda$. With Q factors up to 1200 the investigated CdS nanowire reveals much higher quality factors than comparable structures in the literature [5].

CdS nanowires stand as candidate for an efficient, nanoscaled, coherent light source operating at room temperature.

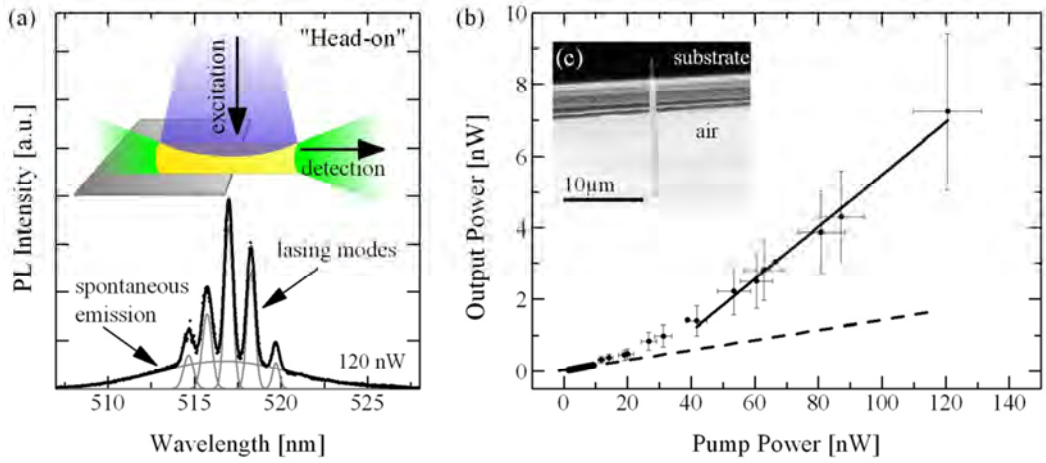

Fig. 1: (a) Emission out of nanowire facet end detected at 120 nW with sharp lasing modes superimposed to spontaneous emission. (b) “Head-on” measured output power originating from nanowire facet end vs. average pump power shows typical lasing characteristics; estimated lasing slope efficiency of 5-10%. (c) SEM image of the CdS nanowire (diameter ~700 nm, length 17 µm).

References

[1] B. Piccione *et al*., *Nat. Nanotechnol*. **7**, 640-5 (2012).

[2] T. Voss *et al*., *Nano Lett*. **7**, 3675-3680 (2007).

[3] M. Zimmler *et al*., *Semicond. Sci. Tech.* ***25***, 024001 (2010).

[4] S. Geburt *et al*., *Nanotechnology* **23**, 365204 (2012).

[5] Q. Zhang *et al*., *Nano Lett.* **11**, 4270-4 (2011).

Determination of voltage dependent series resistance of solar cells

Sven Schönherr, Michael Oertel and Carsten Ronning

Generally, the most common used characterization method of solar cells is the interpretation of their current-voltage-curves. Independent from the underlying model, the solar cell parameters display the basic properties of a cell and serve as guideline for all following characterization steps. The most popular parameter is the solar cell efficiency and the fill-factor. But both depend strongly on the other parameters like the shunt and the series resistance, the open circuit voltage, the photocurrent, the diode quality factor and the saturation current.

Especially the series resistance has a strong effect on the current-voltage-curve in forward bias direction. With increasing series resistance the fill-factor drops rapidly and reduces the cell efficiency. But the determination of the series resistance is quiet difficult, because it depends on the diode setup and the measurement condition. Several semiconductors show a voltage dependent resistance depending on the bias direction and the absolute value [1][2].

For CIGS ($Cu(In,Ga)(S,Se)_2$) solar cells the one-diode-model with parasitic resistances is the most common used model to characterize the current-voltage-characteristics of CIGS-solar cells and is based on one diode with a shunt and a series resistance. The behavior could be described as:

$$\mathrm{j(V)} = \mathrm{j_S}\left(\mathrm{e}^{\frac{\mathrm{q(V-r_S j)}}{\mathrm{nkT}}} - 1\right) - \frac{\mathrm{V-r_S j}}{\mathrm{r_{shunt}}} - \mathrm{j_L} \quad (1)$$

with the saturation current j_S, the photo current j_L, the diode quality factor n, the series and the shunt resistance r_S and r_{shunt}, the elementary charge q, the Boltzmann constant k and the temperature T. The determination of the solar cell parameters is based on the method described by Werner et al. [3], which uses only one current-voltage-curve. First the curves are corrected on the shunt resistance and the photo current by a linear fit in the bias region around zero. Afterwards three plots can be used, which utilize the small signal conductance dI/dV to determine the outstanding cell parameters by the points of intersection and the slope.

For the determination of the voltage dependent series resistance one CISe cell was used, which was prepared in a sequential process.

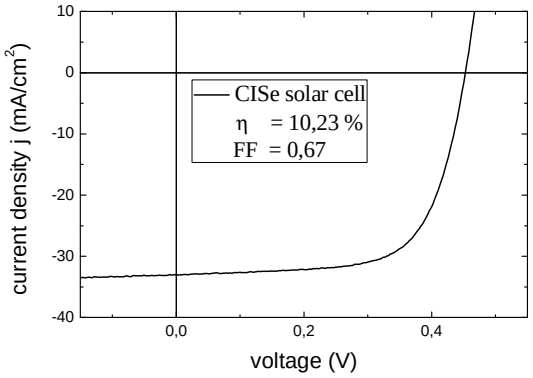

Fig. 1: The current-voltage-curve at room temperature of a CISe solar cell prepared at the IFK, which was used for the following researches.

The determined cell parameters at room temperature taken out of one IV-curve shown in figure 1 are: $j_L = 33\,mA/cm^2$, $j_S = 4.17 * 10^{-4} mA/cm^2$, $n = 1.55$, $r_{shunt} = 396\,\Omega cm^2$ and $r_S = 0.381$ in the bias region around the open circuit voltage $V_{OC} = 448.8\,mV$.

The Suns V_{OC} method uses different illumination intensities to measure a current-voltage-curve without the influence of the series resistance. Certainly the photocurrent strongly depends on the illumination intensity but also the open circuit voltage. The photo current is a measure of the light intensity and the open circuit voltage is the voltage measured under no current influence. At this condition no current flows through the device and so no voltage drops over the series resistance. Both, the measured photo current and the open circuit-voltage build a pair of value for each light intensity and from these a second current-voltage-curve could be calculated without the influence of the series resistance.

This method was realized with a high number of neutral density filters and a variation of the solar simulator intensity. For each illumination intensity, a whole IV-curve was measured and the photocurrent and the open circuit voltage were determined with a linear fit in the respective region. The calculated curve is shown in figure 2 in comparison with the curve measured under AM1.5 conditions.

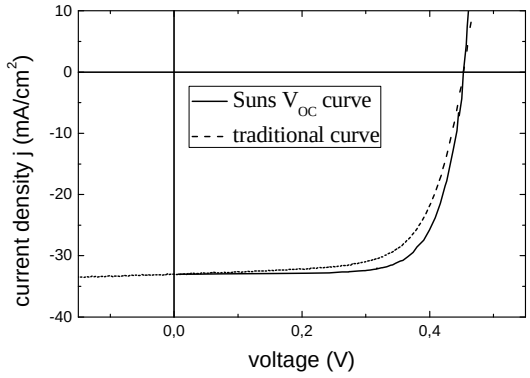

Fig. 2: The current-voltage-curve at room temperature build from the Suns V_{OC} measurement (solid line), in comparison with the curve measured under AM1.5 conditions (dashed line).

Based on the current different between both curves, the effect of the series resistance could be recalculated. Assuming, that the Suns V_{OC}-curve could be described by equation (1), the difference in current should be described as:

$$\Delta j = j - j(r_S = 0) \qquad (2)$$

$$\Delta j = j_S \, e^{\frac{q}{nkT}V}\left(e^{\frac{q}{nkT}r_S j} - 1\right) + \frac{r_S j}{r_{shunt}} \qquad (3)$$

This equation can be solved numerically in order to determine the series resistance depending on the voltage.

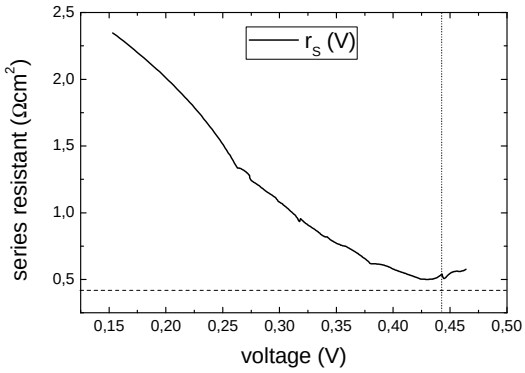

Fig. 3: The calculated series resistance depending on the voltage (solid line). In comparison the calculated series resistance with the method described by Werner (dashed line) and the open circuit voltage under AM 1.5 conditions (dotted line)

Figure 3 shows the voltage dependent series resistance in good agreement with the determined resistance at the open-circuit-voltage with the method from Werner et al. [3]. The decreasing behavior with higher voltages could come from the decreasing space charge region and smaller spikes at the puffer-absorber interface.

References

[1] S. R. Dhariwal *et al.*, Solid-Stare Electronics **27**, No. 3, 267-273 (1984),

[2] Ö. Tüzün *et al.*, Material Science and Engineering B **134**, 291-295, (2006),

[3] J.H. Werner, Appl. Phys. A **47**, 291-300 (1988)

Ion beam induced stress formation and relaxation in germanium

T. Steinbach, A. Reupert, E. Schmidt, and W. Wesch

It is well known that ion irradiation of crystalline materials leads to radiation damage [1]. In addition, based on the structural modification induced density change the formation or relaxation of mechanical stress can be observed. In the literature a model was proposed, which describes the fluence dependence of the stress by a rate equation that contains basic ion beam induced effects: densification, plastic flow and anisotropic deformation [2]. The purpose of this work was to investigate the stress evolution in Ge to get a deeper insight in the underlying basic mechanisms [3].

The ion beam induced stress caused by room temperature irradiation of crystalline Ge with 3.0 MeV I-ions is shown in Fig. 1 as a function of ion fluence. Despite the variation of the fluence rate Φ over two orders of magnitude, the ion beam induced stress shows a similar evolution with increasing ion fluence. For all rates Φ used, the stress evolution is characterized by a strong increase at low ion fluences, a stress maximum and a steady decrease of stress until it reaches a saturation value $S_S \neq 0$. Moreover, up to an ion fluence of $2.0 \times 10^{13}\,cm^{-2}$ the stress values for different fluence rates are similar and the stress maximum amounts to $S_{max} = (229 \pm 4)$N/m. Thus, the stress formation and stress relaxation seem to be independent of the fluence rate. In contrast, with further increasing ion fluence a difference in the saturation value S_S can be observed. It can be clearly seen that the saturation stress increases with increasing ion fluence rate Φ [3].

As described in the literature [2], the strong increase in stress at low ion fluences can be attributed to the ion beam induced defect formation which will be discussed in the following by means of Fig. 2. The measured defect profiles $n_{da}(z)$ with a maximum located at a depth of z = 575 nm shows a good agreement with the calculated depth distribution of the displaced lattice atoms. With increasing ion fluence, the defect distribution increases and broadens towards the surface and into the depth until a homogenous amorphous surface layer has formed. Finally, the amorphous layer exhibits a thickness of approximately $d_{am} \approx 1\ \mu m$ at an ion fluence of $N_I = 4.0 \times 10^{13}\,cm^{-2}$ [3]. Based on the defect profiles the relative defect concentration taken in the defect maximum n_{da}^{max} and the average defect concentration $n_{da}^{average}$ are shown in Fig. 2 (right) as a function of ion fluence. The curve of $n_{da}^{average}$ is shifted to higher ion fluences compared to the curve of n_{da}^{max}. Nevertheless, in both cases the defect concentration increases continuously until it reaches a value of $n_{da} = 1$ which corresponds to completely amorphised material [3].

The comparison between the defect formation (Fig. 2) and the stress evolution (Fig. 1) shows that the strong increase in stress at low ion fluences is correlated with

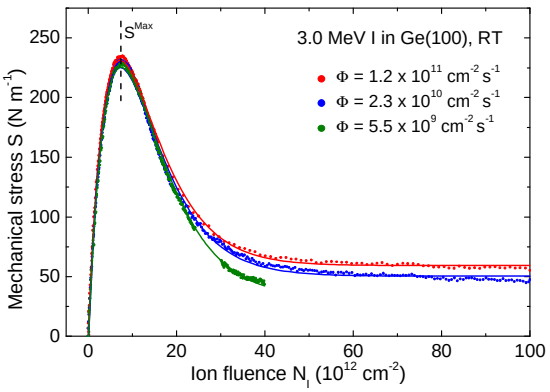

Fig. 1 Mechanical stress S as a function of ion fluence N_I for the irradiation of c-Ge with 3.0 MeV Iodine at room temperature and different fluence rates Φ. The solid lines represent the best fit.

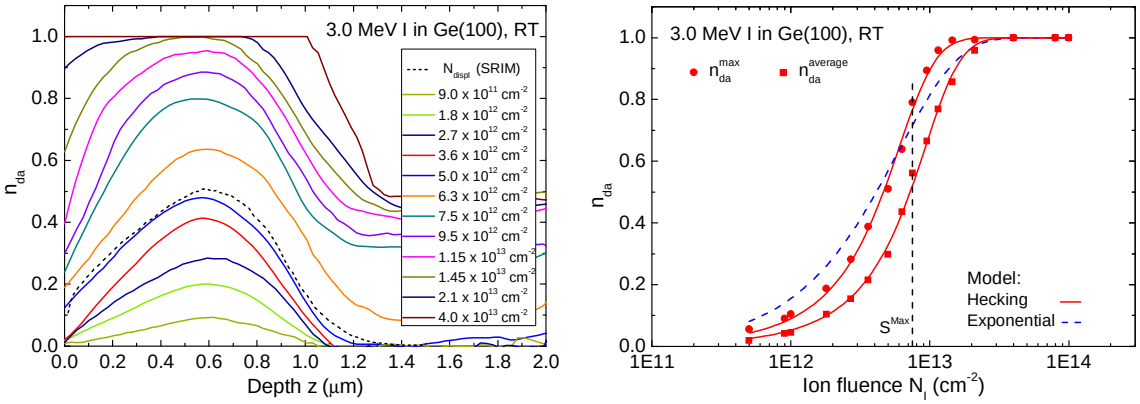

Fig. 2 Left: Relative defect concentration n_{da} versus depth z are shown for Ge irradiated with 3.0 MeV I-ions (Φ = 2.0 x 10^{10} cm^{-2} s^{-1}) compared to the calculated displaced lattice atoms N_{displ} (SRIM2008). Right: The relative defect maximum and the average defect concentration as a function of ion fluence N_I.

the defect formation in crystalline material. That means at the beginning of the irradiation predominantly point defects are created which obviously lead to strong mechanical stress. With increasing ion fluence the ions hit more and more damaged material. The collision cascades of the ions start to overlap. Hence, at rising ion fluence the amorphization process, i.e. the accumulation of point defects to amorphous clusters, becomes dominant. For $N_I > 4.0 \times 10^{13}$ cm^{-2} the stress is constant. This correlates with the average defect concentration which reaches a value of $n_{da} = 1$. That means a final amorphous layer has formed and no more structural modification takes place with further ion irradiation. Hence, the saturation stress value is reached if the amorphization process is completed [3].

Further experiments were performed on special prepared amorphous and prestressed Ge samples in order to investigate the ion beam induced stress relaxation in more detail. The main result is that the ion beam induced stress relaxation cannot be attributed to a radiation enhanced plastic flow process as proposed in the literature [2]. For more information see Ref. [3]. In fact, our investigations demonstrate that the strong stress increase at the beginning of the irradiation is connected with the formation of defects, such as point defects. The relaxation of stress, however, becomes dominant if these defects accumulate to complex defect clusters and amorphous regions. Therefore, we propose the ion beam induced phase transformation to the amorphous phase as the dominant process of stress relaxation. This assumption is supported by the fact that the relaxation process is completed when the amorphization process of the whole irradiated layer is completed. All results lead to the conclusion that the proposed effects as plastic flow and plastic deformation seem to play only a minor role in ion beam induced stress evolution and the relaxation of stress is rather attributed to a phase transition, i.e. a reorganization of the randomly distributed point defects to amorphous regions. Based on the investigations a modified model for the ion beam induced stress evolution is necessary, in which the stress formation and relaxation are solely attributed to ion beam induced structural modifications [3].

Work presented at IBMM2012, Qingdao.

References

[1] E. Wendler, NIM. B, 267, 2680 (2009).
[2] E. Snoeks, A. Polman and C.A. Volkert, Appl. Phys. Lett. 65, 2487 (1994).
[3] T. Steinbach, A. Reupert, E. Schmidt, and W. Wesch, NIM B, in press (2013).

High Energy Elastic Recoil Ion Detection Analysis

M. Bender[*], *D. Severin*[*], *H. Kollmus*[*], *M. Wengenroth*[*], *T. Steinbach, and W. Wesch*

[*]GSI, Darmstadt, Germany

Elastic recoil ion detection (ERDA) with heavy ions has become a powerful tool for stoichiometrical analysis of multifaceted samples. Briefly, projectile ions scatter target ions from a binary collision out of the target in forward direction. These ejectiles (sputtered ions) are analyzed concerning their atomic number (Z_2 and M_2) and kinetic energy E_2 which reveals the depth of the scattering collision inside the target. While the energy of the sputtered target atoms depends on the mass relation of the scattering partners and the scattering angle ϕ (equation 1), the differential cross section for scattering the target atom into the detector is furthermore dependent on the atomic number Z and the projectile energy E_1 (equation 2).

$$(1)\quad E_2 = E_1 \cdot \frac{4M_1M_2}{(M_1+M_2)^2}\cos^2\phi$$

$$(2)\quad \frac{d\sigma}{d\Omega} = \left(\frac{Z_1Z_2e^2(M_1+M_2)}{8\pi\varepsilon_0 M_2 E_1}\right)^2 \cdot \frac{1}{\cos^3\phi}$$

Especially with heavy ions, e. g., Xe or heavier, element specific depth profiles for atomic masses up to Cr, Fe and Ni, the components of technical steel, can be easily obtained.

Elastic recoil ion detection as a standard analytic tool in industry as well as for research purposes is typically performed with projectile energies of $E_1 = 1$ MeV/u or less. At the Helmholtzzentrum für Schwerionenforschung (GSI), elastic recoil ion detection has been performed at the high charge state injector with $E_1 = 1.4$ MeV/u Xe ions. The performance of non evaporable getters has been studied, as these are used in the heavy ion synchrotron (Schwerionensynchrotron SIS18) vacuum system [1].

In 2012 we have performed elastic recoil ion detection for the first time at the M3-branch of material science with $E_1 = 3.6$ MeV/u Au ions. At this kinetic energy the coulomb threshold is not reached and thus, the necessary elasticity of the binary collision is still guaranteed. We can already show qualitatively the promising results of high energy elastic recoil ion detection. Please note, no complete analyzed data are shown here, but raw data sets without kinematic correction and without the transfer to real depth profiles.

Various samples have been probed with $E_1 = 3.6$ MeV/u Au beam under an incident angle of 67.5° to surface normal. The scattered atoms have been analyzed under an angle of 45° with respect to the incident beam by a $\Delta E/E_{rest}$-telescope similar to the one used in [2]. The detector has a solid angle of 1.7 msr and an acceptance angle of

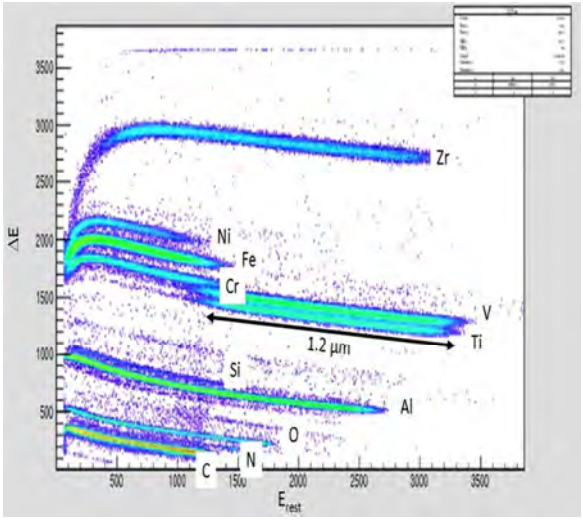

Fig. 1 Elastic recoil ion detection spectrum (raw data) of a getter (Ti, V, Zr) coated stainless steel sample on an Al-target holder. Irradiation parameters: 709 MeV Au-ions.

2.8° in the scattering plane. It consists of an ionization chamber working with isobuthane at 30 mbar pressure, decoupled from the experimental vacuum by a 1 µm thick Mylar foil. Hence, the kinetic energy of the sputtered ions is characterized by the energy loss within the ionization chamber ΔE and the "rest" energy E_{rest} which is detected by a silicon detector. All data were recorded event by event in list mode.

From equation 2, the cross section of the new collision system is similar to the one in [2]; the reduction due to higher incident energy is almost compensated by the higher atomic number of the projectile and the modified scattering angle.

The first investigations were performed to obtain information on the capability of high energy elastic recoil ion detection concerning resolution of elements and energy which is needed for the depth profiling. Both parameters depend on the target atom mass. Figure 1 shows the raw data of a getter coated stainless steel. All elements are clearly resolved. The getter layer consists of Ti, V and Zr and has a thickness of roughly 1.2 µm. Under the getter layer, the steel substrate is clearly visible. This emphasizes the capability of high energy elastic recoil ion detection to investigate buried layers as well as the interfaces between different layers and the substrate. The pronounced aluminum line can be attributed to the Al sample holder. Figure 2 shows a barrier detector consisting of a 100 nm thick Al layer on a Si substrate. The neighboring elements Si and Al are clearly resolved. However, the 100 nm thickness of the Al layer is distributed on roughly 100 channels of the acquisition chain. With respect to the gauss-shaped borders (front and back edge) of the layer, the depth resolution of the system is towards several 10 nm, being yet poor as compared to low energy elastic recoil ion

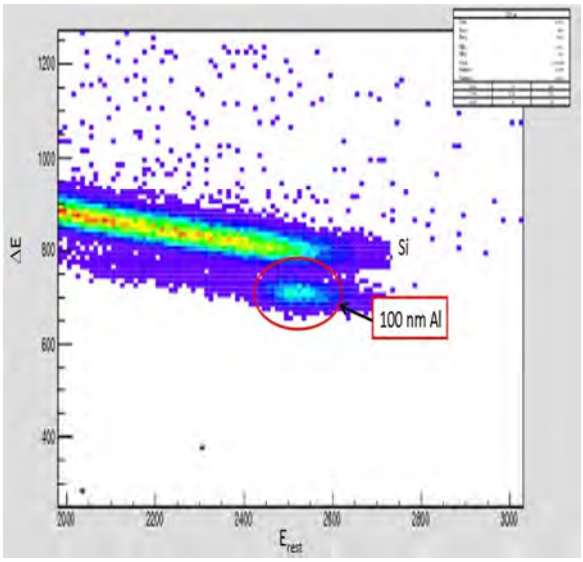

Fig. 2 Elastic recoil ion detection spectrum (raw data) of an Al layer on Si substrate. Irradiation parameters: 709 MeV Au-ions.

detection systems [3]. The authors are presently working on improvements for the depth resolution. These are the elimination of the binning combined with minimization of noise in the electronic system, a modified E_{rest}-detector with a better energy resolution and the implementation of kinematic correction to eliminate the haziness in energy due to the acceptance angle in scattering plane.

Work supported by BMBF, contract no. 05K10SJ1

References

[1] M.C. Bellachioma, et al., Vacuum 82 (2008) 435.
[2] M. Bender, et al., NIM B 268 (1997) 1986.
[3] K. Kimura, et al., Analytical Sciences 26 (2010) 223.

Comparison of low- and room-temperature damage formation in Ar ion implanted GaN and ZnO

E. Wendler, W. Wesch, A. Yu. Azarov [a],
N. Catarino [b], *A. Redondo-Cubero* [b], *E. Alves* [b],*K. Lorenz* [b]

[a]*University of Oslo, Norway*
[b]*IST/ITN Universidade Técnica de Lisboa, Portugal*

GaN and ZnO are wide bandgap semiconductors suitable for applications in optoelectronics and high temperature, high frequency and high power devices. Prototypes of GaN-based field effect transistors and LEDs employing processing by ion implantation were reported [1] and ion implantation was successfully used for optical doping of nitrides with rare earth ions (see [2] and references therein). However, despite their strong radiation resistance (see [3, 4] and references therein) ion implantation is not yet routinely applied in these materials. One reason for that is the formation of a complicated defect structure which is hard to anneal after implantation. Therefore, further work is necessary to better understand the mechanisms of ion induced damage formation and the effects of the implanted ions to finally find out suitable implantation and annealing conditions for certain applications. Furthermore, the study of ion-beam induced damage formation is also of scientific interest, because the origin of the high radiation resistance of these materials is still not fully understood.

Usually the target temperature during implantation plays an important role and in many materials a comprehensive description of ion-induced damage formation is obtained on the base of critical temperatures [5]. However, GaN and ZnO show a significantly different behaviour which cannot be represented in this way.

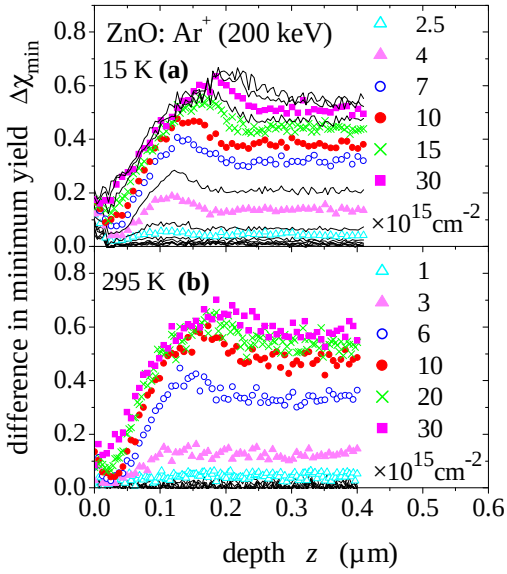

Fig. 1

Difference in minimum yield $\Delta\chi_{min}$ versus depth z for Ar ion implanted ZnO with implantation and subsequent measurement being performed at 15 K (a) and at 295 K (b). Solid lines are results for intermediate fluences which are not included in the legend for clarity purposes.

In our studies GaN and ZnO are implanted at 15 K and 295 K with 300 keV Ar and 200 keV Ar ions, respectively. Damage analysis is performed with RBS using 1.4 MeV He ions in channelling configuration. Each implantation step was followed by an immediate measurement at the respective temperature (quasi-insitu measurement). The difference in minimum yield ($\Delta\chi_{min}$, calculated from the yield Y of backscattered ions in aligned (al) and random (ra) direction of virgin (vir) and implanted (impl) samples $\Delta\chi_{min} = (Y_{al}^{impl} - Y_{al}^{vir}) / Y_{ra}$) is taken as a measure of the amount of damage produced.

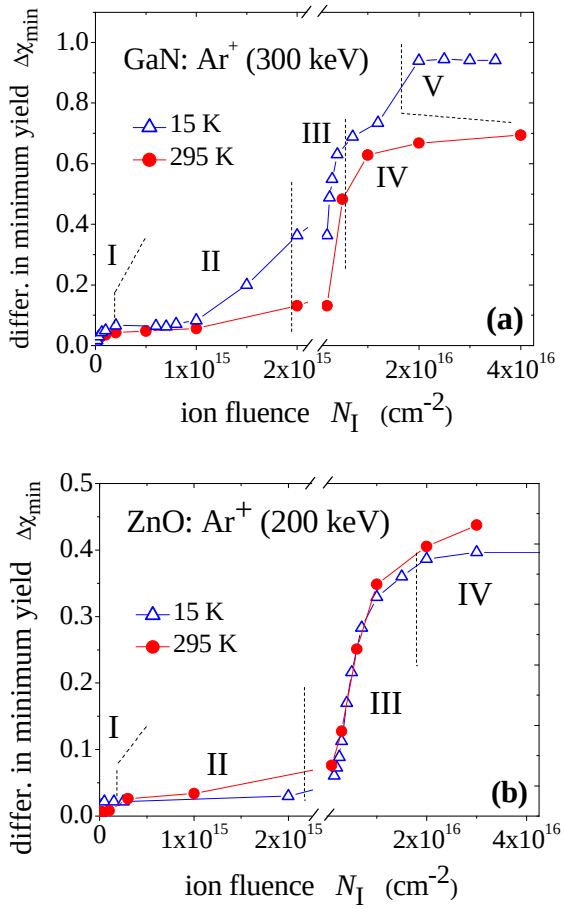

Fig. 2
Difference in minimum yield $\Delta\chi_{min}$ versus ion fluence N_I for Ar ion implanted GaN (a) and ZnO (b). Data are average values over a depth of 30 nm taken at the depth z_{max} of maximum energy deposition into the displacement of lattice atoms with z_{max} = 125 nm for GaN and 80 nm for ZnO. Stages of damage formation are indicated.

The most striking result is that in GaN and ZnO the ion-induced damage formation is only weakly influenced by the target temperature during implantation. This can be seen from Figs. 1 and 2 which show the minimum yield $\Delta\chi_{min}$ versus depth z for ZnO and the fluence dependence of $\Delta\chi_{min}$ for GaN and ZnO implanted with Ar ions. For both materials and both temperatures the minimum yield versus depth indicates the existence of a mixture of point defect clusters and extended defects with the latter being proven by TEM for implantation at 295 K (see [6]) and references therein). From the fluence dependence of $\Delta\chi_{min}$ plotted in Fig. 2 it is obvious that damage formation proceeds in multiple steps. In ZnO these steps are the same for both temperatures. In GaN the main difference is that at 15 K amorphisation is eventually reached which is not the case at 295 K, but before the effect of temperatures is low. Therefore, it follows that the general mechanisms of damage formation (represented by the various steps) are not influenced by the temperature of implantation.

Taking into account results from previous papers and other authors (see [6] and references therein), it can be concluded that in GaN and ZnO extended defects form already during implantation at a temperature of 15 K. This clearly suggests that the formation of extended defects is not driven by the thermal mobility of point defects. It is supposed that in GaN and ZnO damage-induced strain plays a dominant role and the formation of extended defects seems to be energetically favourable in comparison to the formation of larger randomly ordered agglomerates of defects.

References

[1] S.J. Pearton, C.R. Abernathy, F. Ren, *Gallium Nitride Processing for Electronics, Sensors and Spintronics*, Springer, London, 2006.

[2] K. Lorenz, E. Alves, F. Gloux, P. Ruterana, in: *Rare Earth Doped III-Nitrides for Optoelectronic and Spintronic Applications*, Topics in Applied Physics 124 (2010) 25.

[3] S.O. Kucheyev, J.S. Williams, C. Jagadish, Vacuum 73 (2004) 93.

[4] K. Lorenz and E. Wendler, "Implantation damage formation in GaN and ZnO" Chapter in "Ion Implantation" ed. M. S. Goorsky, INTECH 2012.

[5] E. Wendler, Nucl. Instrum. Methods Phys. Res. B 267 (2009) 2680.

[6] E. Wendler, W. Wesch, A. Yu. Azarov, N. Catarino, A. Redondo-Cubero, E. Alves, K. Lorenz, Nucl. Instrum. Methods Phys. Res. B, 2013, in press.

Empirical modelling of the cross section of damage formation in ion implanted III-V compounds

E. Wendler, L. Wendler[a]

[a]*Anna-Siemsen-Str. 66, 07743 Jena*

Substantial efforts have been made to understand the susceptibility of various materials to ion-beam induced damage formation and to describe the processes of amorphisation. To date, most authors have concentrated on the amorphisation of materials [1-3] that occurs at relatively high ion fluences where the collision cascades of individual ions overlap. Much less attention is devoted to the questions of how much damage remains from a single collision cascade of an ion impinging on crystalline material and how this damage concentration depends on the energy transferred from the implanted ions to the lattice atoms by nuclear and electronic interactions.

We studied the damage formation in various III-V compound semiconductors implanted with different ion species (see [4] and references therein). The damage produced per individual ion is represented by the cross section σ_d defined as the increase of the relative damage concentration n_{da} per ion fluence increment at very low ion fluences N_I. The relative damage concentration is determined by Rutherford backscattering spectrometry in channelling configuration applying the computer code DICADA [5] and the data are taken at the depth of maximum damage. Ion implantation and subsequent quasi-insitu damage analysis are performed at a temperature of T≈15 K. At this temperature thermal effects can probably be excluded. This allows σ_d to be expressed as a function of the primary quantities σ_{SRIM} and S_{el}. σ_{SRIM} is the cross section for the formation of displaced lattice atoms due to the primary energy deposition in atomic displacements and S_{el} is the energy deposited in electronic excitations per ion and unit depth. Both quantities are calculated using the code SRIM [6] (see also [4]).

Based on experimental findings the empirical formula

$$\sigma_d = \xi \frac{\sigma_{SRIM}^{1.8}}{S_{el}} \qquad (1)$$

is deduced and the parameter ξ is obtained to be $\xi = (4.68 \pm 0.4) \times 10^{21}$ eVcm$^{-13/5}$ as an optimum value for various ion species implanted into different III-V compounds [4]. Eq. (1) well represents experimental data of σ_d within its uncertainty of about 35% which is mainly determined by the long-term reproducibility of the ion fluence. Predicting σ_d is also a demand for the calculation of semiconductor devices [7] and Eq. (1) can serve as a starting point for further quantitative modeling including secondary effects such as temperature and ion flux.

References

[1] K. Trachenko, J. Phys.: Condens. Matter 16 (2004) R1491.

[2] H. M. Naguib and R. Kelly, Radiat. Eff. 25 (1975) 1.

[3] E. Wendler, W. Wesch, and G. Götz, Nucl. Instrum. Methods Phys. Res. B 55 (1991) 789.

[4] E. Wendler, L. Wendler, Appl. Phys. Lett. 100 (2012) 192108.

[5] K. Gärtner, Nucl. Instrum. Methods B 227 (2005) 522.

[6] J. P. Biersack and J. F. Ziegler, The Stopping and Ranges of Ions in Matter, (Pergamon, Oxford, 1985), Vol. 1.

[7] G. Hobler and G. Otto, Mater. Sci. Semicond. Process. 6, (2001) 1.

Low-temperature damage formation in ion implanted InP

E. Wendler, A. Stonert [a], A. Turos [a,b], W. Wesch

[a]National Center of Nuclear Research, 05-400 Swierk/Otwock, Poland

[b]Institute of Electronic Materials Technology, Wolczynska 133, 01-919 Warsaw, Poland

InP is a semiconductor with superior carrier mobility and a direct band gap resulting in various device applications. Furthermore, there is a continuous research to apply ion beams in InP device technology (see references in [1]). However, any application of ion beams requires a sufficient understanding of the processes of ion-solid interaction and the formation of radiation damage.

Because of dynamic damage annealing [2-4], the study of primary effects of ion-solid interaction in InP requires implantation and subsequent damage analysis to be done at cryogenic temperatures.

<100> oriented single crystalline InP samples are implanted with 30 keV He, 150 keV N, 350 keV Ar and 350 keV Ca ions. Rutherford backscattering spectrometry (RBS) with 1.4 MeV He ions and a scattering angle of 170° is used to collect the spectra in aligned and random direction. All experiments are performed quasi-insitu at (15±2) K. The depth distribution of the relative concentration of displaced lattice atoms, n_{da}, is calculated using the code DICADA [5].

Fig. 1 summarises the damage evolution at the maximum of the distribution as a function of the ion fluence N_I. For comparison of the results for different ion species N_I is converted to the number of displacements per lattice atom n_{dpa} with $n_{dpa} = N_I\, N_{displ}^{*} / N_0$. N_0 is the atomic density of InP and N_{displ}^{*} the number of displacements per ion and unit depth taken at the maximum of the distribution (calculated with SRIM [6]). Fig. 1 shows

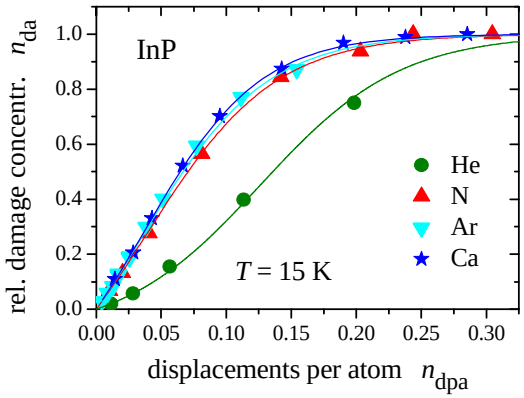

Fig. 1
Relative damage concentration at the maximum of the distribution, n_{da}, versus the number of displacements per lattice atom, n_{dpa}, for 30 keV He, 150 keV N, 350 keV Ca and 350 keV Ar ion implantation into InP at 15 K. The lines are fitted to the experimental data using Eq. (1) with the ion fluences N_I converted to n_{dpa} as described in the text.

that for all ion species studied a continuous transition towards amorphisation (n_{da}=1) is observed. This can be well represented assuming two mechanisms contributing to damage formation: (i) damage formation within direct ion impacts with the cross section σ_d and (ii) stimulated growth of already existing damage with the cross section σ_g. These assumptions result in [7]

$$n_{da}(N_I) = 1 - \frac{\sigma_d + \sigma_g}{\sigma_g + \sigma_d \exp\left[\left(\sigma_d + \sigma_g\right) N_I\right]}. \quad (1)$$

The curves shown in Fig. 1 are fitted to the experimental data by adjusting the parameters σ_d and σ_g. σ_d follows from the almost linear increase of the relative damage concentration n_{da} with ion fluence at very low concentrations, whereas σ_g accelerates the transition towards the

saturation value n_{da}=1. The resulting parameters are plotted in Fig. 2 versus the cross section σ_{SRIM} which is given by $\sigma_{SRIM}=N_{displ}^{*}/N_0$. The dependence $\sigma_d(\sigma_{SRIM})$

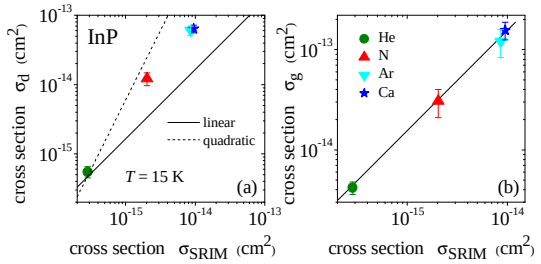

Fig. 2

Cross sections of damage formation σ_d (a) and of stimulated growth of damage σ_g (b) versus the calculated cross section σ_{SRIM} for InP ion implanted at 15 K. In part (a) the solid and dashed lines indicate a linear and quadratic dependence of σ_d on σ_{SRIM}, respectively. The line in part (b) is calculated with $\sigma_g = 15.6\ \sigma_{SRIM}$ which was obtained as a mean value for various III-V compounds exhibiting a stimulated growth of damage [8].

is between a linear and a quadratic one and follows an empirical dependence deduced for a wide range of implants in III-V compounds [1, 8].

Fig. 1 shows that almost no difference occurs in n_{da}^{max} versus n_{dpa} for ion species between N and Ca. In these cases InP is amorphised at 15 K when the energy deposited into displacement processes corresponds to 0.2...0.25 dpa. In difference to that a higher number of displacements per atom is required for the light He ions.

The cross section σ_d is the area integral over the relative damage concentration produced per ion at the depth of maximum damage. If one assumes a homogeneous damage distribution across the area, σ_d is given by the product of the area and the relative damage concentration per ion. If one further assumes that each ion produces an amorphous cluster corresponding to a relative damage concentration per ion equal to unity, then σ_d is the area damaged by one ion at the corresponding depth. Under these assumptions the diameter of the clusters produced by individual ions is 0.24 nm for He, 1.28 nm for N, 2.74 nm for Ar and 2.88 nm for Ca implantation. The distance between nearest neighbours in InP is d_{nn} = 0.254 nm. For He implantation the diameter of the assumed cluster is of the same size as d_{nn}. This means the clusters would consist of very few atoms only for which an amorphous state cannot be defined. This suggests that at least for He ions the assumption of complete amorphisation within a single ion impact is not correct. For the other ion species the estimated diameters are not in conflict with the assumption that heavily damaged and/or amorphous material is produced within a single ion impact. For the light element He the situation is different. The formation of heavily damaged or amorphous clusters is not to be expected. In this case one may suspect that amorphisation occurs homogeneously on a finer scale by the coalescence of point defects and point defect complexes as suggested for ion implanted SiC [9].

References

[1] E. Wendler, A. Stonert, A. Turos, W. Wesch, Nucl. Instrum. Methods Phys. Res. B (2013) in press.

[2] E. Wendler, B. Breeger, C. Schubert, W. Wesch, Nucl. Instrum Methods Phys. Res. B 147 (1999) 155.

[3] R. Ratajczak, A. Turos, A. Stonert, L. Nowicki, W. Strupinski, Acta Phys. Pol. A 120 (2010) 136.

[4] U.G. Akano, I.V. Mitchell, F.R. Shepheard, Appl. Phys. Lett. 59 (1991) 2570.

[5] K. Gärtner, Nucl. Instrum. Methods Phys. Res. B 227 (2005) 522.

[6] J.P. Biersack and J.F. Ziegler, The Stopping and Ranges of Ions in Matter, Vol. 1 (Pergamon Press, Oxford, 1985).

[7] W.J. Weber, Nucl. Instrum. Methods Phys. Res. B 166-167 (2000) 98.

[8] E. Wendler, L. Wendler, Appl. Phys. Lett. 100 (2012) 192108.

[9] W.J. Weber, L.M. Wang, N. Yu, N.J. Hess, Mater. Science Engin. A 253 (1998) 62.

Optical properties of Sn-doped CdS nanowires

Marcel Wille, Sebastian Geburt, Robert Röder, Mengyao Zhang[1], *Jia Grace Lu*[1] *and Carsten Ronning*

[1]Department of Physics and Electrical Engineering, University of Southern California, Los Angeles, USA

CdS nanowires (NWs) are promising candidates for future optoelectronic applications due to their possibility of light amplification and efficient waveguiding [1]. The controlled modification of their electrical and optical properties, for example by doping, will continue the consequent progress in NW research. The in-situ doping during the VLS synthesis is a difficult task due to the restricted solubility of dopants in gold (Au), which is typically used as catalyst.

Therefore, we investigate in a collaboration with the University of Southern California an alternative catalyst (Sn) in order to succeed in successful doping during growth [2]. The synthesis of high quality tin doped CdS NWs was performed in a horizontal tube furnace by a chemical vapor deposition method. Our research focuses on the tin incorporation and the modification of the electronic band structure. Optical transitions of tin doped CdS NWs were investigated by cathodoluminescence (CL) measurements. Figure 1 a) shows a SEM picture of an as grown CdS:Sn NW ensemble, which demonstrate the size and shape variation while the growth process. The CL spectra of a NW ensemble shown in figure 2 can be divided into three characteristic parts:

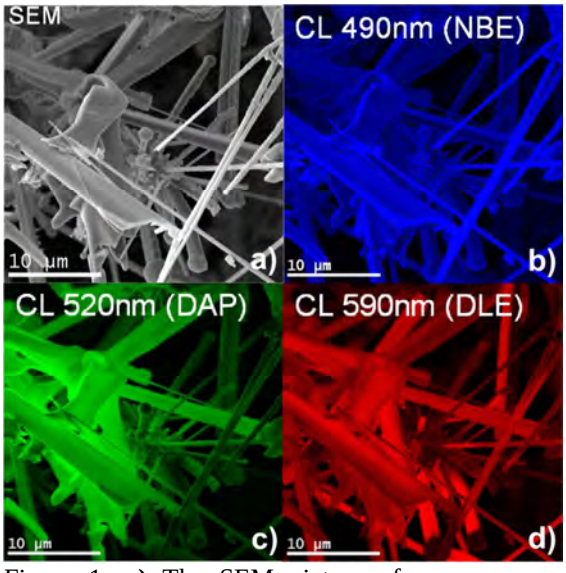

Figure 1: **a)** The SEM picture of an as grown Sn:CdS nanostructure ensemble; **b)-d)** Mono-CL pictures taken at 490nm, 520nm and 590nm wavelength.

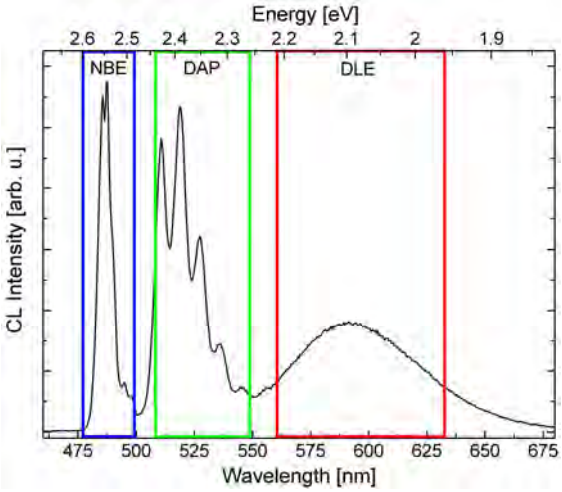

Figure 2: The CL spectra of the NW ensemble at 8K, divided into three characteristic parts.

1. The wavelength regime 480-500 nm (blue) corresponds to the near band edge emission (NBE), which originates directly through recombination of charge carriers near the band edge of pure CdS [3];
2. The features at 510-550 nm (green) originate through a donor-acceptor-pair (DAP) transition with its longitudinal-optical-phonon replica with an energy distance of ΔE=38meV. This DAP emission is directly caused by the incorporated tin [4];
3. The broad band around 560-630 nm (red) can be attributed to deep level defect emission (DLE). This band has been

associated with radiative transitions from donor levels, arising from Cd atoms located in interstitial sites, to the valence band, [5].

Long and straight NW's, which are of major interest for possible applications, show a strong NBE but a weak DAP emission, as shown in the monochromatic CL pictures in figures 1 b) and c). This is a hint for the high crystalline quality of the grown nanowires and a nominal incorporation of tin. Thick structures exhibit a strong DAP emission, which indicate most likely a lot of incorporated tin. The Mono-CL picture taken at 590nm in figure 1 d) demonstrates a homogenous distribution of defects over the observed area.

An efficient vapour-liquid-solid growth route was developed to yield long and straight NW's with optical active DAP transitions and high optical quality. The successful incorporation of tin was demonstrated via CL investigations.

References

[1] Agarwal et al., Appl. Phys. A 85, 209–215 (2006)
[2] Dai et al., Chem. Phys. Lett.,497, 85-88 (2010)
[3] Thomas and Hopfield, J. Appl. Phys. 33, 3243-3249, (1962);
[4] Huang, Contemp. Phys., 22, 6, 599-612 (1981)
[5] Aguilar-Hernández et al., Semicond. Sci. Technol. 18 (2003) 111–114

Quantum-to-classical transition in transport characteristics of double-barrier tunnel junctions

Mikhail Belogolovskii[1]*, Sebastian Döring, and Paul Seidel*

[1]*Donetsk Institute for Physics and Engineering, 83114, Donetsk, Ukraine*

One of the major tasks of the modern fundamental physics, in particular, in the areas of quantum computation, quantum cryptography, teleportation, etc., is the understanding of the transition from quantum to classical behavior in the objects studied. A significant part of techniques proposed for this purpose is based on the application of heterostructures consisting of nanometer-thick layers of dielectrics and normal, superconducting and/or ferromagnetic metals. Such stochastic systems (even if they are models) allow one to address some practically important aspects of decoherence and quantum-information transfer in stochastic systems. In particular, they can be used for studying effects of elastic and inelastic scatterings of charge carriers on transport characteristics like average current and its fluctuations in meso- and nanoscopic conductors, to know the spatial bounds for transferring quantum information, to understand the time scale of the degradation effects.

In this work, we have studied, as a paradigmatic example, charge transport across a double-barrier metal – insulator – metal – insulator - metal (MIM′IM) system with a nanometer-thick conducting M′ film. Its transport characteristics depend on the relationship between fundamental length scales: the Fermi wave length l_{F}, the typical distance between two successive elastic collisions with impurities l_{el}, the phase-breaking length l_{inel} related to inelastic events like electron-electron and electron-phonon interactions or coupling to an external environment, and the thickness d of the M′ layer. If the M′ interlayer is clean ($l_{\mathrm{F}} < d << l_{\mathrm{el}} < l_{\mathrm{inel}}$), the charge-transport regime will be phase-coherent with various interesting features due to the interference between electron wave functions. In this case charge flow can be described with the conventional quantum-mechanical scattering theory. If not ($l_{\mathrm{F}} < l_{\mathrm{el}} << d < l_{\mathrm{inel}}$ or even $l_{\mathrm{F}} < l_{\mathrm{el}} < l_{\mathrm{inel}} < d$) the information encoded in a quantum-mechanical phase could be lost partially or completely.

One of the most popular concepts applied to such stochastic systems is based on a semiclassical evaluation of the Feynman path integral in terms of saddle point approximations [1]. In the first part of the work we have studied how trajectory-based semiclassical results can be directly obtained from the quantum-coherent approach and examine the limits of their applicability to stochastic nanostructured systems. We have shown that the semiclassical approximation follows from a purely coherent picture after averaging over different Feynman paths as an effect of the phase randomization. It means that corresponding results can be easier calculated with the real-space Green function technique than using the Boltzmann-Langevin approach (see also related arguments in [2]). In particular, this statement explains the long-standing question why the semiclassical shot-noise power in diffusive conductors (one-third of the Poisson noise) is identical with corresponding quantum calculations [3,4].

Whereas the semiclassical formalism can be a good approximation for a disorder-average quantum structure with elastic scatterings, we need a more adequate formalism to deal with a classical-like regime when electronic transport is (at least, partly) described by the Ohm's law. We have used the decoherence–probe approach [4] to study an effect of inelastic scatterings in the M′ interlayer. To reveal the difference with semiclassical results, it is useful to transfer one of the M electrodes in a superconducting (S) state and to introduce two new issues into the scheme [4] developed for

normal (N) metals, namely, (i) Andreev reflection when electrons incident from the normal side are rejected back by the pairing potential Δ as time-reversed particles (holes), and (ii) a three-dimensional generalization important for anisotropic superconductors, in particular, those with a *d*-wave order parameter symmetry. To proceed with a scattering-like technique, we introduce two wires leading from the M′ layer to a fictitious phase-memory erasing reservoir with a chemical potential, which is a function of the applied bias V and can be found from a requirement of coincidence of currents I incoming and outcoming from the interlayer. The total current is a sum of two non-interfering components, those of phase-coherent and incoherent channels. We suppose that a current carrier has a probability $\zeta(\theta) = 1 - d/\left(l_{\text{inel}} \cos\theta\right)$ to undergo phase-destroying scatterings in the M′ interlayer and a probability $1-\zeta(\theta)$ to cross it without loss of the phase memory. Using a developed numerical technique for calculations of the average current and current fluctuations and applying it to double-barrier $NI_1N'I_2S$ heterostructures, we have shown that non-equilibrium electronic shot noise is very sensitive to the presence of a phase-destroying agent in a multilayered structure.

Phase-coherent subgap conductance G of a junction with comparatively low barriers differs from zero due to non-vanishing probability of simultaneous passage of two electrons and it can be confirmed by the value of the Fano factor F, the ratio of the shot-noise power to the Poisson value, which should be equal to 2 in this case. As the parameter ζ increases, the coherent character of the charge transmission is partly destroyed and the F value is suppressed up to the normal-state value. At the same time with increase of the incoherent scatterings the *G*-*V* dependence transforms from a single-peaked curve to that with two maxima and in the limit $l_{\text{F}} < l_{\text{inel}} << d$ it looks like a usual conductance characteristic of a MIS sample but with a peak considerably shifted from $V = \Delta/e$ to higher voltage biases. Hence, simultaneous measurements of charge current and its fluctuations (see Fig. 1) is a powerful diagnostic tool revealing properties of nanoscaled heterostructures inaccessible with mean current measurements.

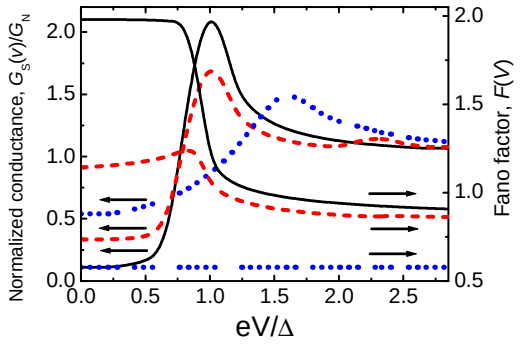

Fig. 1: Effect of decoherence on the differential conductivity normalized to the normal state and the Fano factor $F(V)$ of a $NI_1N'I_2S$ structure with barrier transparencies of T_1=T_2=0.5. The smooth curves correspond to a ratio d/l_{in} = 0, the dashed curves to d/l_{in} = 0,1, and the dotted curves to d/l_{in} >> 1. The temperature is equal to zero, e is the elementary electrical charge, Δ is the energy gap of a superconducting electrode with *s*-wave pairing.

Using the developed theory, we have analyzed and explained unconventional effects in *I*-*V* curves observed by us earlier in point contacts formed by a silver counter-electrode with a T_c superconductor bulk [5]. The experiments [5] were performed by us earlier using point contacts of silver and superconducting cuprates. They showed that in such systems temperature of the surrounding medium can serve as an effective parameter for controlling the decoherence process. A systematic shift of the gap feature to higher voltages with decreasing temperature is the result of enhanced decoherence near the Ag-cuprate interface.

References

[1] M.V. Berry, B.F. Buxton, and A.M.O. De Almeida. Rad. Eff. **20**, 1, 1973.

[2] M. Gu, K. Wiesner, E. Rieper, and V. Vedral, Nature Commun. **3**, 762, 2012.

[3] M.J.M. de Jong and C.W.J. Beenakker. Phys. Rev. B 51, 16867, 1995.

[4] Ya.M. Blanter and M. Büttiker. Phys. Rep. 336, 1, 2000.

[5] M. Belogolovskii, Yu. Revenko, V. Svistunov, M. Grajcar, and P. Seidel. Physica C **367**, 218, 2002.

Possible Influence of a Proximity Effect on the Spectra of Edge-Type $Ba(Fe_{1-x}Co_x)_2As_2$/Pb Junctions

Sebastian Döring, Stefan Schmidt, Sandra Gottwals, Martin Feltz, Noor Ali Hasan, Frank Schmidl, Volker Tympel, Kazumasa Iida[1], Fritz Kurth[1], Bernhard Holzapfel[1], and Paul Seidel

[1] *Institute for Metallic Materials, IFW Dresden, Helmholtzstraße 20, D-01069 Dresden*

To investigate the superconducting properties of pnictides we designed and applied layouts for homojunctions [1] as well as different heterojunctions [2-4]. One of the layouts we use is the so called edge-type junction (see fig. 1). It consists of a $Ba(Fe_{1-x}Co_x)_2As_2$ (Ba-122) base electrode, a Pb counter electrode (covered by In) and a barrier interface, that is engineered during the preparation process by contact with chemicals and air, but mostly by ion beam etching (IBE).

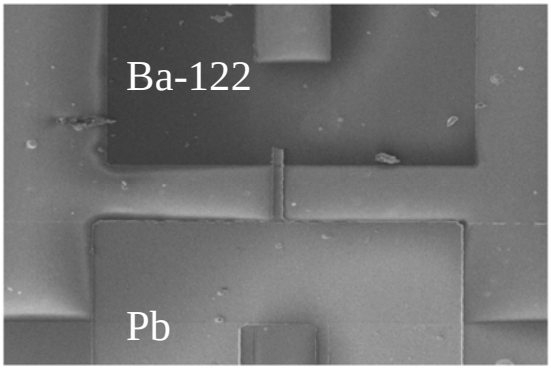

Fig. 1: Scanning electron microscope image of a processed edge-type junction (top view). [5]

Due to the anisotropy of the Ba-122 unit cell, this junction design allows the investigation of current transport mechanisms in the *ab*-plane.

During the preparation process of such a junction (described in detail in ref. [4]), the Ba-122 film was covered by a gold protection layer. This layer could act as an additional parallel shunt depending on the transparencies of the engineered Ba-122/Pb interface and the gold layer (plus possibly the interfaces between gold and Ba-122 and Pb, respectively).

Our photolithographic mask design allows it to remove this layer in the junction area by an additional preparation step of IBE. By doing so, a possible disturbing influence of the gold shunt should be avoided but contamination of the Ba-122 with ion implantation and concomitantly a decrease of the superconducting properties is possible. To avoid a contamination of the whole thin film the exact etching rates of gold and Ba-122 were examined. Thus, we were able to stop etching right after the interface, leaving over a Ba-122 layer of sufficient thickness. To examine a possible influence of the gold layer we prepared and investigated both junction options (fig. 2).

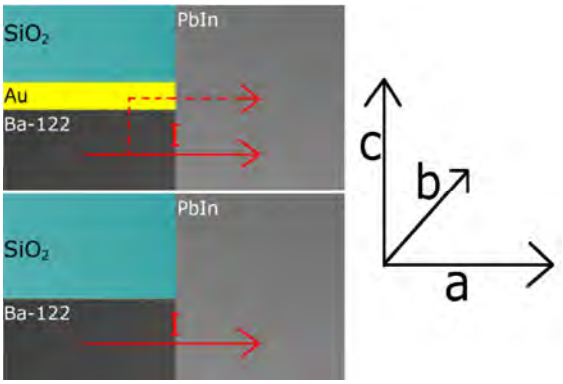

Fig. 2: Left: Schematic cross section image of the investigated junctions. Top: Junction with a gold layer. Bottom: Junction without gold layer. The red arrows show the possible current paths.
Right: The corresponding crystallographic axes of Ba-122. [5]

First results of junctions with gold layer were still published [6,7] but without further interpretation. To obtain information about the superconducting order parameter (OP) one uses differential

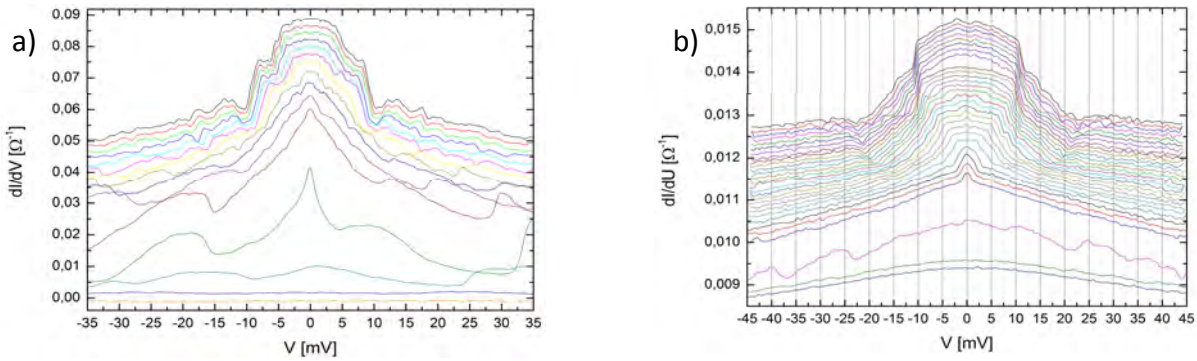

Fig. 3: Conductance versus voltage of a junction with gold shunt layer (a) and without gold shunt layer (b). The temperatures for both diagrams range from between 8K (top line) to 25K (bottom line).

conductance G in dependence of the voltage applied to the junction. These conductance spectra can be modeled within the BTK-model [8] including different extensions [9]. This model predicts a maximum normalized conductance $G(V=0)$ of 2 for a s-wave OP and possibly higher for a d-wave OP. For the used non-point contact junctions there should be noticeable scattering effects leading to high Dynes parameters [10] and dramatically lowering G_0. In contrast, an additional normal conducting layer causes a proximity effect at the interface. This now could act like a parallel Josephson junction and therefore the measured conductance could be increased noticeably.

Results measured on junctions with the gold layer (fig. 3a) show, that in the most cases G_0 is nearly or even higher than 2. Additionally, Josephson-like structures were found in early measurements [6].

By removing the gold shunt, the conductance spectra dramatically change. As can be seen in fig. 3b the conductance still keeps its general shape, the increase at zero voltage is just a few percent. Comparing the obtained values for G_0 of both junction options (fig. 4) it is noticeable, that they are much higher for gold shunted junctions in most cases. This let one assume that actually the gold layer influences the measured conductance of the junction due to a proximity effect.

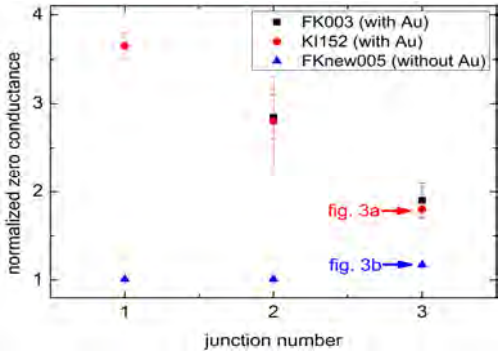

Fig. 4: Normalized zero conductance for different samples. Data points for fig. 3a and 3b are marked. Same junction numbers belong to same junction cross sections.

We thank the EC (project IRON-SEA), the Landesgraduiertenförderung Thüringen and the DFG (SPP 1458) for financial support.

References

[1] S. Schmidt *et al.*, IEEE Trans. Appl. Supercond. **23**, 7300104 (2012).
[2] S. Schmidt *et al.*, Appl. Phys. Lett. **97**, 172504 (2010).
[3] S. Döring *et al.*, Physica C **478**, 15-18 (2012).
[4] S. Döring *et al.*, Supercond. Sci.Technol. **25**, 084020 (2012).
[5] S. Döring, Diploma Thesis (2011).
[6] S. Schmidt *et al.*, Phys. Proc. **36**, 82-87 (2012).
[7] S. Döring *et al.*, Phys. Proc. **27**, 296-299 (2012).
[8] G.E. Blonder *et al.*, Phys. Rev. B **25**, 4515-4532 (1982).
[9] D. Daghero and R.S. Gonnelli, Supercond. Sci. Technol. **23**, 043001 (2010).
[10] A. Plecenik *et al.*, Phys. Rev. B **49**, 10016-10018 (1994).

An Improved Cryogenic Current Comparator for FAIR

R. Geithner[*]*, R. Neubert, W. Vodel*[*]*, and P. Seidel*
[*]Helmholtz-Institut Jena, Fröbelstieg 3, 07743 Jena

A non-intercepting detection of high brightness, high intensity primary ion beams as well as low intensities of rare isotope beams is required for the high-energy transport beam lines at FAIR [1]. The expected beam currents in these beam lines are in the range of few nA up to several µA. The Cryogenic Current Comparator (CCC) [2, 3, 4] optimally fulfils the requirements for the FAIR beam parameters.

Since the CCC is an assembly of different parts with own noise contributions, the total intrinsic noise of the complete CCC is composed by the intrinsic noise of the SQUID itself and its electronics as well as the magnetization noise of the embedded coils. The current spectral density $\langle I^2 \rangle$ of a coil at a temperature T could be calculated with the Fluctuation-Dissipation-Theorem (FDT) and the measured frequency dependent serial inductance $L_S(\nu)$ respectively serial resistance $R_S(\nu)$ in the equivalent circuit diagram of a real coil, whereas $R_S(\nu)$ represents the total losses [5]:

$$\left\langle I^2 \right\rangle = 4k_B T \int \frac{R_S(\upsilon)}{\left(2\pi\upsilon\left(L_{SQUID} + L_S(\upsilon)\right)\right)^2 + \left(R_S(\upsilon)\right)^2} d\upsilon \quad (1)$$

For the presented noise measurements the pick-up coil is directly coupled to the input coil of the SQUID. That means that the total noise calculation have to include the SQUID's input coil inductance L_{SQUID}. The input coil does not contain a lossy core material. Therefore the serial resistance could be neglected and the serial inductance is assumed to be frequency independent in the considered frequency range. As one can see in Equation (1) the current noise decreases while $L_S(\nu)$ is as high as possible and $R_S(\nu)$, which corresponds to the losses in the core material, remains low over the whole frequency range. Therefore we are searching for core materials with highest possible permeability at liquid helium temperatures with the highest possible cut-off frequency.

For the previous installation of the CCC [7], we used Vitrovac 6025F [6] as core material for the pick-up coil which is also well known for many other cryogenic applications.

Based on the results of preliminary investigations [4] cores of nanocristalline ferromagnetic Nanoperm M764-01 [8] with the final dimensions (outer diameter: 260 mm, inner diameter: 205 mm, width: 97 mm) were ordered. After welding the single-turn toroidal niobium winding, the coil (afterwards referred to as Nanoperm pick-up coil) was characterized at 4.2 K in a customized wide-neck cryostat.

The serial inductance and the serial resistance of the coils were measured with the help of a commercial Agilent E4980A LCR-Meter, as described in detail in [4].

The noise measurements were performed with a SQUID UJ111 and a SQUID Control 5.3 electronics of Jena University [9]. The pick-up coils were directly coupled to the SQUID input coil by superconducting wires. The output voltage noise density of the SQUID electronics was measured by an HP 35670A dynamic signal analyser. The current noise density was calculated using the flux and current sensitivity of the SQUID sensor. The Nanoperm pick-up coil was shielded against external magnetic fields with the help of two niobium pots fitted into each other. The DESY-CCC pick-up coil was already enclosed into the meander-shaped shielding during the noise measurements.

The serial inductance as well as the serial resistance of the Nanoperm pick-up coil and the DESY-CCC pick-up coil are depicted in Fig. 1.

One can see that the inductance of the welded coil with the Nanoperm M-764-01 core is almost constant for frequencies below 10 kHz (see (a) in Fig. 1). That would provide a linear transfer function in this frequency range. Moreover, it is shown that the inductance of the Nanoperm M-764-01 coil is four times higher at 4.2 K than the inductance of the DESY-CCC pick-up coil (see (b) in Fig. 1). Regarding Equation (1) this should lead to an approximately

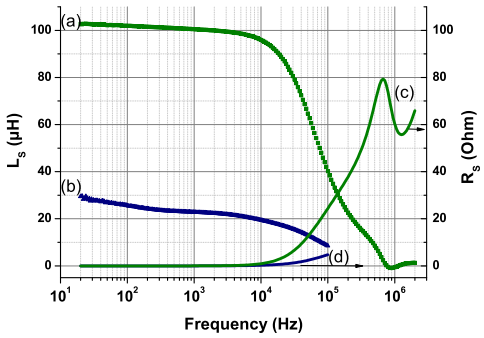

Fig. 1 Comparison L_S (ν) and R_S (ν) of the welded pick-up coil with Nanoperm M-764-01 core ((a) and (c)) and the DESY-CCC pick-up coil with Vitrovac 6025F core ((b) and (d)) 4.2 K.

four times lower current noise with a serial resistance in the same range.

The measured current noise density of the Nanoperm pick-up coil (see (a) in Fig. 2) is lower by a factor of 2 - 5 than the current noise density of the DESY-CCC pick-up coil (see (d) in Fig. 2). It was decreased to 35 pA/Hz$^{1/2}$ compared to 110 pA/Hz$^{1/2}$ at 7 Hz and to 2.7 pA/Hz$^{1/2}$ compared to 13.3 pA/Hz$^{1/2}$ at 10 kHz. Above 1 kHz the current noise density of the Nanoperm coil is in the same range as the intrinsic current noise density the SQUID sensor (see (c) in Fig. 2). The total noise of the Nanoperm coil is calculated to be 1.2 nA in the frequency range from 0.2 Hz to 10 kHz. In the case of the DESY-CCC pick-up coil the predictions from the FDT (see (e) in Fig. 2)

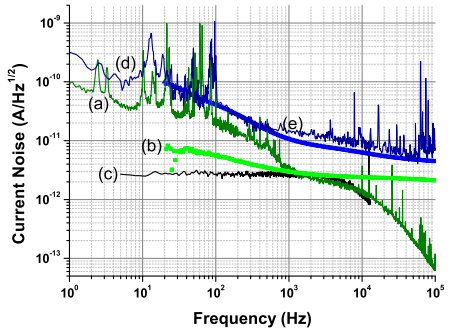

Fig. 2 Measured (a) and calculated (b) current noise of the welded pick-up coil with Nanoperm M-764-01 core as well as the measured current noise of the SQUID sensor with rf-shunted input (c). The measured (a) and calculated (b) current noise of the welded coil with Nanoperm M-764-01 core are compared with the measured (d) and calculated (e) current noise of the DESY-CCC pick-up coil with Vitrovac 6025 F core.

matches very well to the noise measurements. But there is seen an additional noise contribution in the low frequency range up to 1 kHz compared to the FDT (see (b) in Fig. 2) in the case the Nanoperm coil. This arises from the less effective shielding of the coil due to the two niobium pots during the noise measurement compared to the meander-shaped shielding.

The CCC has shown its capability as beam monitor for ions as well as electrons. With the usage of the presented material Nanoperm M-764-01 a linear transfer function up to 10 kHz could be expected. The current noise density of the pick-up coil was reduced by a factor of two to five. With the increased attenuation factor of the meander-shaped shielding a further noise reduction in the low frequency range up to 1 kHz should be possible. This would allow the detection of beam currents below 1 nA.

In subsequent experiments, measurements of the current noise distribution of the Nanoperm coil enclosed in the meander-shaped shielding are planned to verify the results from the FDT. Thereafter the complete commissioning, the functional test, and the characterization of the CCC in a noise reduced laboratory environment will be done.

[1] "An International Accelerator Facility for Beams of Ions and Antiprotons", Conceptual Design Report, Darmstadt, 2000, http://www.gsi.de/GSI-Future/cdr/.
[2] I. K. Harvey, Rev. Sci. Instrum. 43 (1972) 11, p 1626.
[3] K. Grohmann, H. D. Hahlbohm, D. Hechtfischer, and H. Lübbig, Cryogenics 16 (1976) 10, p 601.
[4] R. Geithner, R. Neubert, W. Vodel, M. Schwickert, H. Reeg, R. von Hahn, and P. Seidel, IEEE Trans. Appl. Supercond. 21 (2011) 3, pp. 444-447 .
[5] H. P. Quach, T. C. P. Chui, Cryogenics 44 (2004) 6, p 445.
[6] VACUUMSCHMELZE GmbH & Co. KG, Gruener-Weg 37, D-63450 Hanau, Germany.
[7] R. Geithner, R. Neubert, W. Vodel, P. Seidel, K. Knaack, S. Vilcins, K. Wittenburg, O. Kugeler, and J. Knobloch, Rev. Sci. Instrum. 82 (2011) 013302.
[8] MAGNETEC GmbH, Industriestrasse 7, D-63505 Langenselbold, Germany.
[9] W. Vodel, K. Mäkiniemi, Meas. Sci. Technol. 3 (1992), p 1155.

Conductance spectra of planar junctions based on $Ba(Fe_{0.9}Co_{0.1})_2As_2$–superconductor thin films

Sandra Gottwals, Sebastian Döring, Stefan Schmidt, Martin Feltz, Noor Ali Hasan, Frank Schmidl, Volker Tympel, Kazumasa Iida[1], Fritz Kurth[1], Ingolf Mönch[2], Bernhard Holzapfel[1], and Paul Seidel

[1] *Institute for Metallic Materials, IFW Dresden, Helmholtzstraße 20, D-01069 Dresden*
[2] *Institute for Integrative Nanosciences, IFW Dresden, Helmholtzstraße 20, D-01069 Dresden*

Andreev reflection (AR) studies are an important tool to investigate the electrical properties of iron arsenide. Superconductors planar junctions offer a possibility to characterize the energy gap(s) and the symmetry of the order parameter.

We prepare planar hybrid superconductor – normal metal - superconductor (SNS') junctions in thin film technology. $Ba(Fe_{0.9}Co_{0.1})_2As_2$ (Ba-122) was used as base electrode that was fabricated via pulsed laser deposition at the IFW Dresden. A sputtered gold layer forms the barrier of normal metal. Pb was thermally evaporated and forms the counter electrode.

We measured *I-V* characteristics at temperatures between 4.2 and 25 K of each electrode as well as of the junction itself. By means of the numerical derivation, we investigated the differential resistance. Such AR spectra were typically evaluated Blonder–Tinkham–Klapwijk (BTK) model [1]. This theory describes all interface effects by a single dimensionless parameter *Z*.

It has been shown in former works [2-4] that both electrodes could influence the differential resistance of the junction when they are close to or higher than transition temperature. In this case the junction can be expressed as a series connection of resistance of the electrodes and the junction [5,6]. The additional resistance is called spreading resistance R_S. The presence of R_S changes the zero bias conductance value and shifts the *G(V)* curve to larger voltages. In thin film R_S is not negligible applied to the resistance of the junction.

Pb has a constant contribution of resistance at T>7.2K, which is the critical temperature of Pb. The measured spectra can be corrected by:

$$V_{junction} = V_{measured} - R_{Pb} \cdot I_{bias}.$$

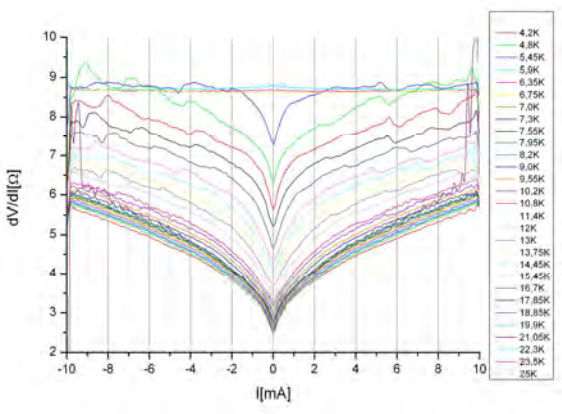

Fig. 1: Differential resistance versus current of the junction. The normal resistance of Pb electrode is corrected.

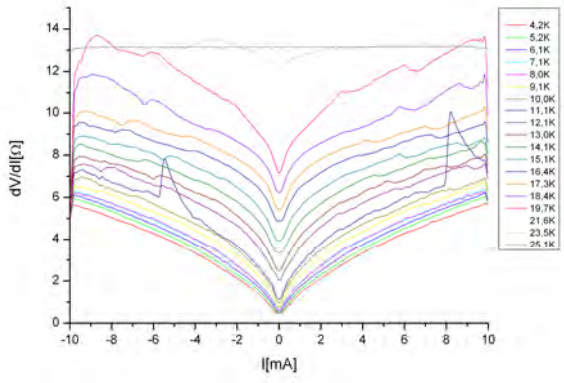

Fig. 2: Differential resistance versus current of a Ba-122 electrode.

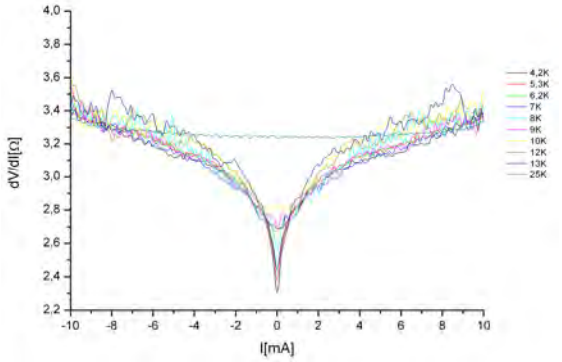

Fig. 3: Differential resistance versus current of the same junction as in Fig. 1 corrected by the resistance of Pb electrode and the weighted resistance of the Ba-122 electrode.

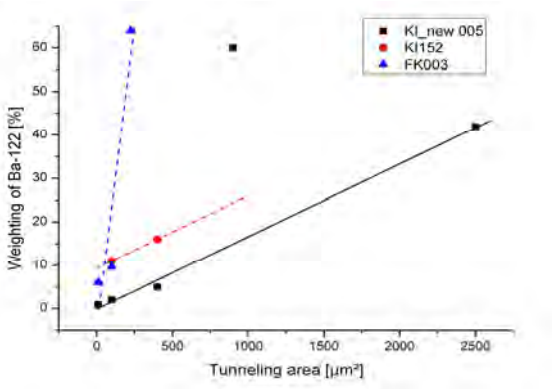

Fig. 4: Weighting of Ba-122 versus area.

Such corrected differential resistance is shown in Fig. 1. Typically the resistance slightly increases with temperature in the investigated range.

In contrast Ba-122 has a strongly nonlinear resistance. To correct this we adapt an equation like it is used for point contact spectroscopy [7]. The resistance of a contact is expressed by:

$$R = \frac{4\rho l}{3\pi a^2} + \Gamma(K)\frac{\rho}{2a}.$$

The Sharvin term $4\rho l/(3\pi a^2)$ based on the ballistic property of electrons without scattering and depends only on the contact geometry. The Maxwell term $\rho/2a$ describes a thermal contribution on the basis of inelastic scattering. Using the example R depends on the radius a. For large contacts ($a>l$, l is the mean free path) the Maxwell term dominates, the Sharvin term ($a<<l$) becomes important in small ones. Γ is a complex integral that depends on the Knudsen ratio $K = \frac{l}{a}$ [8].

To calculate this factor Γ we compare the differential resistance of Ba-122 with this of the junction. Fig. 2 shows the differential resistance of Ba-122 from the same junction like Fig. 1. It can be seen that for both curves the resistance increases with increasing temperatures.

At different temperatures the curve does not end in the same value of resistance for high current values. At 4.2 K the resistance is 5.6 Ω and at 25.1 K it is 13.1 Ω, which is a difference of 7.4 Ω. In Fig. 1 the resistance difference for the junction in the measured temperature range is 3 Ω. We define a weighting factor like Γ as the ratio of the resistance difference of the junction to the resistance difference of Ba-122. In the mentioned example it is about 41 %.

To correct the differential resistance of the junction we subtract the product of weighting factor and differential resistance of Ba-122. As a result of these corrections we obtain the pure differential resistance of the junction (Fig. 3). The resistance difference is currently about 0 Ω. With these corrections we also investigate the pure conductance spectrum within known models.

Different junctions show different weighting of Ba-122 depends on its tunneling area (Fig. 4). The weighting increases with increasing surface. That means the Maxwell contribution predominates as the theory predicted.

References

[1] Blonder *et al.*, Phys. Rev. B **25** 4515-4532 (1982)
[2] Döring *e. al.*, Institute report (2010)
[3] Döring *et al.*, Physica C **478** 15-18 (2012)
[4] Schmidt *et al.*, Physics Procedia **36** 82-87 (2012)
[5] Woods *et al.*, Phys. Rev. B **70** 054416 (2004)
[6] Baltz *et al.*, J. Phys.: Condens. Matter **21** 095701 (2009)
[7] Daghero *et al,*, Supercond. Sci. Technol. **23** 043001 (2010)
[8] Wexler, Proc. Phys. Soc. **89** 927-941 (1966)

Coherent radiation of Josephson junctions in a transmission line

Alexander Grib[1] and Paul Seidel

[1] *Physics Department, Kharkiv V. N. Karazin National University, 61022, Kharkiv, Ukraine*

Recently, it was shown [1] that the array of intrinsic Josephson junctions can be a geometrical resonator and synchronize radiation of Josephson junctions. It was shown also that the temperature along the measured samples of intrinsic Josephson junctions can be strongly inhomogeneous [2].

In the present paper we consider the formation of a standing wave in the resonant transmission line with open ends and the influence of it on synchronization of junctions embedded in the line [3]. In our model instead of continues layers of intrinsic junctions there is a set of 'elementary junctions' which form a two-dimensional array inside the transmission line. In the model we reproduce three main particularities of experiments: (i) the self-induced resonant steps in IV-characteristics, (ii) the coherent radiation at these resonant steps and (iii) the strongly inhomogeneous distribution of the temperature along the radiating system.

The transmission line is divided into *N* cells (see Fig. 1), each of them includes the inductance *L*, capacitance *C* and the electrical resistance *R*. Parameters of the system are characterized by three indices, namely the number of the cell *j* = 1 ... *N*, the number of the high-frequency line *l* = 1 ... *N*-1 which separates two adjacent cells and the number of the junction in the high- frequency line *i* = 1 ... *n*. In the RCSJ model of the Josephson junction, every junction with indices (*i*, *l*) is represented as a parallel connection of the capacitance $C_{i,l}$, the resistance $R_{i,l}$ and the source of the

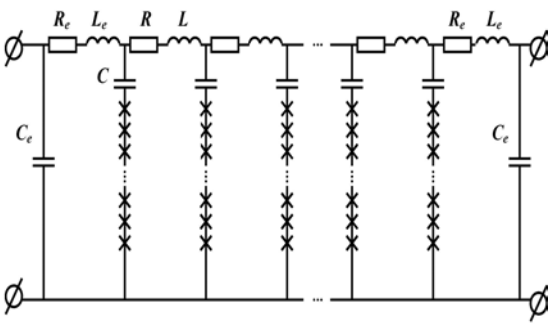

Fig. 1: The high-frequency scheme of the system. Junctions are marked by crosses.

Josephson current $I_{i,l} = I_{ci,l}\sin\varphi_{i,j}$, where $\varphi_{i,l}$ is the difference of phases of the order parameter of a superconductor across the junction and $I_{ci,l}$ is the critical current of the junction. Each of the stacks has the source of the direct current I_b. Dynamics of phases $\varphi_{i,l}$ is described by a system of equations (note that $l = 1...N-1$, $j = 2...N-1$, $j = l$):

$$\alpha_{i,l}\ddot{\varphi}_{i,l} + \chi_{i,l}\dot{\varphi}_{i,l} + I_{ci,l}\sin\varphi_{i,l} = I_b - q_j + q_{j+1},$$

$$L\ddot{q}_j + R\dot{q}_j + \frac{2q_j}{C} = \sum_{i=1}^{2}\varphi_{i,l-1} - \sum_{i=1}^{2}\varphi_{i,l}, \quad \text{(1a,b)}$$

where $\dot{\varphi}_{i,l}$ and $\ddot{\varphi}_{i,l}$ are the first and the second time derivative of the phase difference, q_j is the charge which passes the inductance of the *j*-th cell, $\alpha_{i,l} = (\Phi_0 C_{0i,l})/(2\pi)$, $\chi_{i,l} = \Phi_0/(2\pi R_{i,l})$, Φ_0 is the quantum of magnetic flux. We keep all critical voltages across junctions $V_{ci,l} = I_{ci,l}R_{i,l} = V_c$ to be the same for all junctions.

The boundary conditions are follows:

$$L_e\ddot{q}_1 + R_e\dot{q}_1 + \frac{q_1}{C_e} = -\sum_{i=1}^{2}\varphi_{i,1}, \qquad \text{(1c)}$$

$$L_e \ddot{q}_N + R_e \dot{q}_N + \frac{q_N}{C_e} = \sum_{i=1}^{2} \varphi_{i,N-1} \,. \qquad (1d)$$

We solved equations (1a) - (1d) for the system consisted of two layers (n = 2) and 58 stacks. Parameters of the junctions are as follows. Critical currents of junctions are $I_c(1-\delta)$ for the upper layer (junctions with i=1) and $I_c(1+\delta)$ for the lower layer (junctions with i=2) with $I_c = 15$ mA and $\delta = 0.023$. Critical voltage is $V_c = 2$ mV. The McCumber parameter of all the junctions is $\beta_C = 1$. Parameters of the transmission line are $L = 1.62$ fH and $C = 0.12$ pF, $R = 10^{-4}$ Ohm, $L_e = L, C_e = C$, $R_e = 0$. The length of the cell is 1 micrometer (see Ref. 3 for the relation between the length of the cell and the length of the wave in the line). In Fig. 2 the IV-characteristics of junctions from the first stack on the left side of the system are shown. The IV-characteristic contains resonant steps. Note that these steps are self-induced, i.e. they appear without the external irradiation but only as the result of the electromagnetic interaction of junctions inside the transmission line.

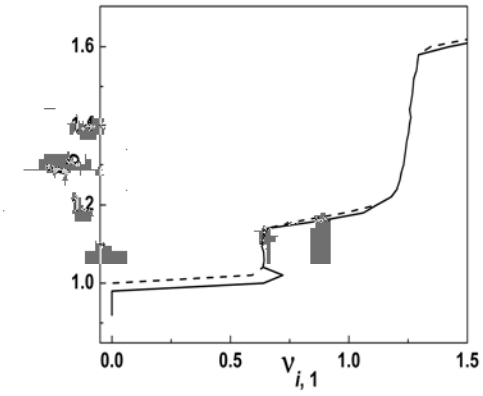

Fig. 2: The IV- characteristics of junctions from the first row of the transmission line (l = 1). Solid line is for the first junction and dashed line is for the second junction.

We calculated values of the averaged over time instant power in the stack

$$P_l = \left\langle \frac{\Phi_0}{2\pi} \sum_{i=1}^{2} \dot{\varphi}_{i,l} \left(I_b - \dot{q}_l + \dot{q}_{l+1} \right) \right\rangle \quad \text{with } j = l.$$

This value is responsible for the Joule heat extracted from the given stack l. We also introduce the value of

$$S_l = \left\langle \left(\sum_{i=1}^{2} \left(\frac{\Phi_0}{2\pi} \varphi_{i,l} - \langle V_{i,l} \rangle \right) \right)^2 \right\rangle$$ that is the square of the ac voltage over the l-th stack. The value of S_l is proportional to ac power of coherent radiation of junctions in the l-th stack. Distributions of values of P_l and S_l along the transmission line are shown in Fig. 3.

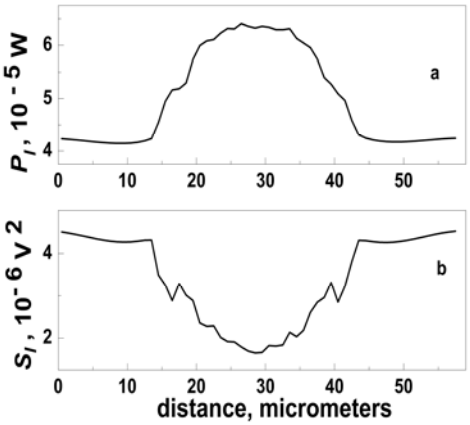

Fig. 3: Distributions of the power P_l from the l-th stack (the upper panel) and the value of S_l (the lower panel) along the transmission line for the bias current $1.14I_c$ (the upper edge of the resonance step in Fig. 2, the main harmonic of the resonance).

It is seen from Fig. 3 that the maxima of the ac power of coherent radiation are placed at edges of the line and therefore coherent radiation is emitted from edges of the system, whereas the maximum of the full averaged extracted power is placed in the center of the line and therefore the overheating of the system can appear in this place.

References

[1] L. Ozyuzer et al., Science 318, (2007) 1291.

[2] C. Kurter et al., IEEE Trans. Appl. Supercond. 19 (2009) 428.

[3] A. Grib and P. Seidel, Low Temp. Phys. 38 (2012) 321.

Coaxial pulse tube refrigerator for 4 K

R. Habibi, M. Thürk, and P. Seidel

Two stage pulse tube refrigerators (PTR) in U-tube design are the standard for cooling devices at temperatures below 10 K down to 2 K. Cooling capacities in the range of 100 mW at 4.2 K are reached by several research prototypes and commercially available two-stage PTRs in U-tube design [1-7]. In the U-tube configuration, vibrations perpendicular to the axis of the coldfinger cannot be avoided because they are inherent by the design. This problem is the topic of current research [8]. The well-known coaxial configuration has the ability to avoid this disadvantage. The coaxial arrangement of the pulse tube and the regenerator combines the advantages of the pulse tube concept (non-existing moving part within the coldfinger) and the compact design of a GM-type refrigerator. Therefore, the two-stage PTR in coaxial configuration opens up the areas of GM-type application.

A new type of a two-stage PTR in an entire coaxial configuration was introduced [9]. Fig.1 shows a sectional view of the three dimensional CAD-layout of the PTR We report on the inhomogeneous set-up of the second stage regenerator matrix, which consists of our self-made electroplated lead screen material, ErNi-spheres, and crushed ErNiCo as it is shown in Fig.2. The 1st stage regenerator is filled with 1250 disks of 200 mesh stainless steel screens as reported in previous papers [10-11]. Due to the coaxial design an additional thermal contact occurs between the two pulse tubes and the respective regenerators at intermediate temperatures. The resulting heat transfer could reduce the refrigerator efficiency seriously. To prevent losses in the cooler efficiency to a greater extent we had to match the coldfinger-components properly. We use corresponding results from various sources [12, 13].

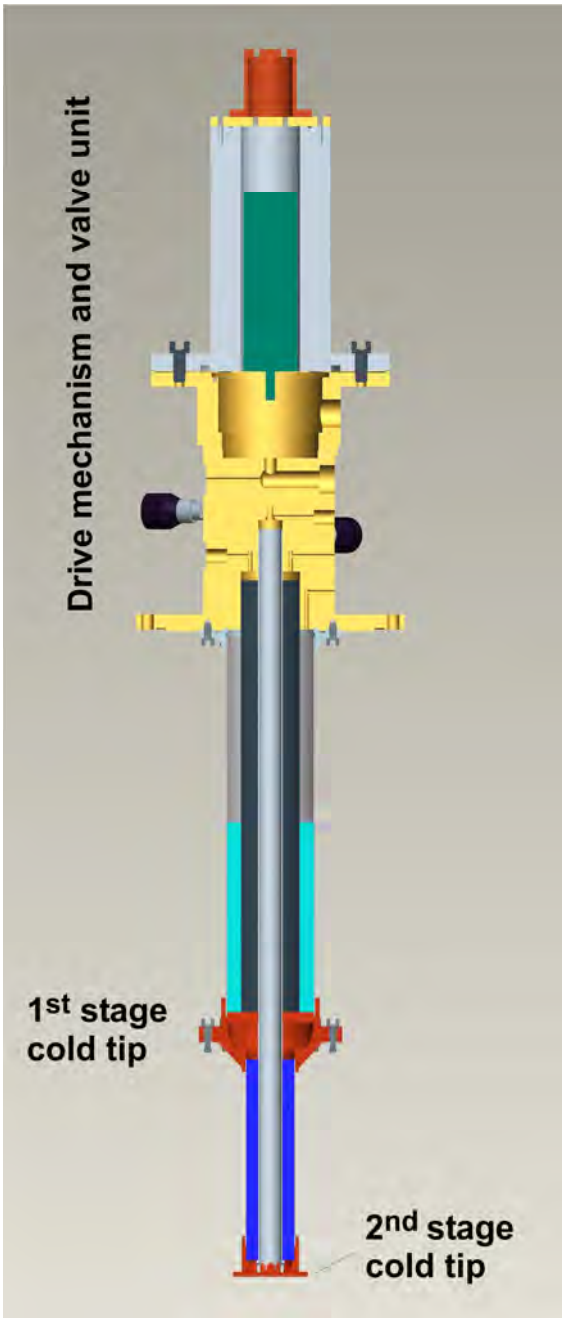

FIGURE 1 Sectional view of the new developed two stage PTR in coaxial design. The 2nd stage pulse tube is located inside the respective regenerator and additionally inside 1st stage pulse tube.

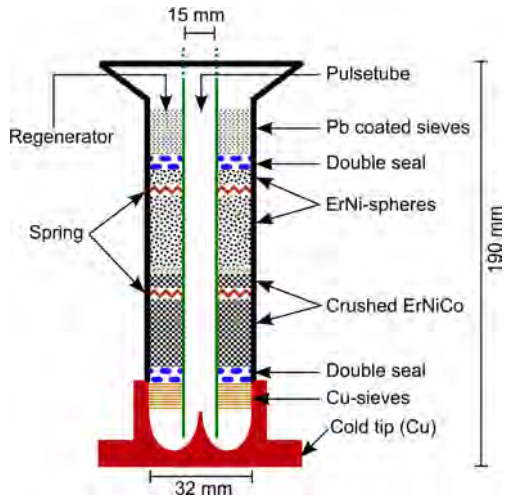

FIGURE 2 Multi-layer lead and rare-earth 2nd stage regenerator

EXPERIMENTAL RESULTS

The whole cryocooler performance including a heat input at the 1st stage cold tip is shown in Fig. 3. The optimal working frequency for this design is 2.3 Hz.

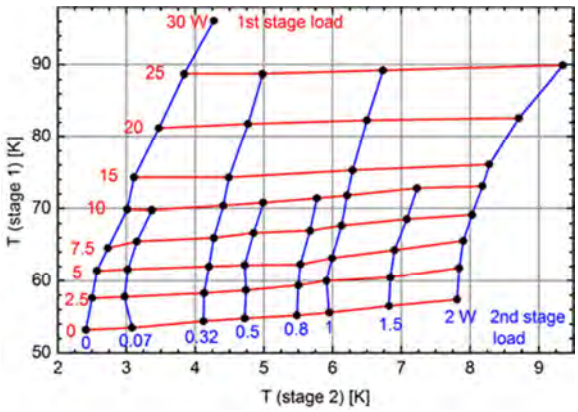

FIGURE 3 Two parametric plot of the cooling performance of the two stage PTR. The parameters are the values of heat input P_1 and P_2 at the respective stages. Compressor unit Leybold RW 6000 - 6.2 kW of input power.

CONCLUSIONS

We demonstrate a new type of a two-stage PTR, successfully. The PTR provides a cooling capacity of 320 mW at 4.2 K in an entire coaxial design. This is worldwide the first demonstration that a full coaxial design of a two staged pulse tube refrigerator is able to accomplish the 4.2K-level [14]. The achieved cooling performance is comparable with standard PTRs in U-tube design.

REFERENCES

[1] N. Jiang, U. Lindemann, F. Giebeler, G. Thummes, Cryogenics 44 (2004), 809-816.
[2] C. Wang, G. Thummes, C. Heiden, Cryogenics 37(1997),857-863.
[3] C. Wang, Cryogenics 41 (2001), 491-496.
[4] M. Tanaka, T. Nishitani, T. Kodama, T. Araki, E. Kawaguchi, and M. Yanai, Adv Cryo Eng 41 B (1995), pp. 1487-1491.
[5] T. Inoue, T. Matsui, S. Kawano, Y. Ohasi, Proceedings of the ICEC 16, Japan, (1996), pp. 299-302.
[6] A. Hofmann, H. Pan, and L. Oellrich, Cryocoolers, 11. (2001), pp. 221-227.
[7] G. Chen et al., Cryogenics 37 (1997) 5, pp.271-273.
[8] T. Tomaru et al., Cryogenics 50 (2010), pp. 309-317.
[9] T. Koettig, S. Moldenhauer, R. Nawrodt, M. Thürk, P. Seidel, Cryogenics 46 (2006), pp. 888-891.
[10] T. Köttig, A. Waldauf, M. Thürk, and P. Seidel, Adv Cryo Eng 49 B (2004), pp. 1445-1450.
[11] T. Koettig, R. Nawrodt, S. Moldenhauer, M. Thürk , P. Seidel, Adv Cryo Eng 51 A (2006), pp. 35-40.
[12] ATAM de Waele, IA Tanaeva, YL Ju,, Cryogenics 40 (2000) 8, pp. 459-464.
[13] T. Koettig, S. Moldenhauer, M. Patze, M. Thürk, and P. Seidel , Cryogenics 47 (2007), pp. 137-142.
[14] R. Habibi, M. Thuerk, and P. Seidel Cryocoolers 17 (2012), pp. 197-202.

Thermal noise of anisotropic substrate materials

Daniel Heinert, Paul Seidel, and Ronny Nawrodt

The direct detection of gravitational waves is one of the most challenging projects of physics in our days. Due to the tiny effect of these waves a highly sensitive detector is required. Thus, the noise processes in these detectors have to be systematically investigated and minimized. Thermal noise sources have been identified to mainly limit the detector in its most sensitive detection band.

Current detectors are based on an interferometric scheme and use fused silica as the substrate material for the optical components. These detectors are operating at room temperature. One possibility to increase the detector's sensitivity can be found in decreasing the working temperature. Nevertheless amorphous materials as fused silica exhibit highly increased mechanical losses at low temperatures. Due to the fluctuation dissipation theorem their thermal noise will be increased too. In this sense the use of crystalline substrate materials represents a possible alternative for low temperature detectors. Thus for the future cryogenic detectors KAGRA [1] and ET-LF [2] the use of sapphire and silicon, respectively, is proposed.

Existing theories for thermal noise are restricted to isotropic materials. For this reason an investigation of the effect of anisotropy of the substrate material on its thermal noise is crucial and will be investigated in this work. Here we consider only the most crucial components, i.e. Brownian noise of the substrate and the coating. Brownian noise results from microscopic volume fluctuations in the material, which is elastically transformed to a spatial fluctuation of the reflecting surface. Consequently, a phase noise is imposed onto the reflected light.

Following the direct approach of Levin [3] the Brownian noise of a mirror can be obtained by applying a virtual pressure on the reflecting surface exhibiting the intensity profile of the readout beam.

$$p(r) = \frac{F_0}{\pi r_0^2} \exp\left(-\frac{r^2}{r_0^2}\right). \qquad (1)$$

Here $r_0$is the beam radius of the Gaussian laser beam, where intensity has dropped to 1/e of its maximum value and F_0 is an arbitrary amplitude. In a second step the elastic energy E_{tot} in the substrate and the coating is calculated. The noise density is finally obtained by the dissipated power P_{diss} as

$$S_x(\omega) = \frac{8k_B T}{\omega^2} \frac{P_{diss}}{F_0^2}. \qquad (2)$$

Here k_B is Boltzmann's constant, T is temperature and ω the radial frequency. With the model of anelastic damping P_{diss} is identified as $\omega\phi E_{tot}$.

Tab. 1: Geometry parameters of ET-LF.

Substrate diameter	50 cm
Beam radius $w_0 = \sqrt{2}r_0$	9 cm
Substrate height	46 cm

We obtain E_{tot} numerically. With the help of the finite element (FE) method, namely the packages COMSOL and ANSYS, we calculate the elastic energy in an anisotropic silicon cylinder which is oriented along the crystallographic axes ⟨100⟩, ⟨110⟩ and ⟨111⟩. The geometry parameters of the sample have been adopted from the ET-LF design and are presented in Tab. 1. The anisotropic result is then compared to the isotropic model. For this purpose we use effective elastic constants (Young's modulus Y, Poisson

Tab. 2: Mechanical energy in an anisotropic silicon substrate. All values are given in 10^{-12} J for a total applied force of $F_0 = 1$ N. The numerical results have been obtained by a harmonic analysis at $f = 100$ Hz.

	Y, σ	analytic	ANSYS	COMSOL
Isotropic	130 GPa, 0.28	15.3	15.5	15.7
100	130 GPa, 0.28	15.3	13.9	14.0
110	169 GPa, 0.06	12.8	12.6	12.8
111	188 GPa, 0.18	11.1	12.2	12.4

ratio σ) of silicon as proposed in [4]. Finally, our numerical code was checked on the analytical approach by Liu and Thorne [5]. All mentioned results are presented in Tab. 2.

The first line indicates the comparison for an isotropic substrate between the analytic and the numerical results. The FE results show a slightly higher value for the elastic energy. As the convergence has been checked to be around 3% for ANSYS and below 1% for COMSOL the discrepancy is likely to stem from an approximation performed in the analytical approach.
Further our investigations clearly indicate a typical difference between the correct anisotropic calculations and the averaged isotropic approach of up to 10%. Interestingly, the sign of the deviation depends on the orientation of the crystal. Thus, no general statement is possible, whether the simple model overestimates or underestimates the elastic energy.

Tab. 3: Energy density in coating layers attached to isotropic and anisotropic substrates. All values are given in 10^{-10} J/m.

	tantala	silica
Y [GPa]	140	72
Poisson ratio σ	0.23	0.17
Isotropic (analytic)	1.70	2.78
COMSOL		
isotropic	1.65	2.78
100	1.63	2.77
110	1.63	2.76
111	1.63	2.77

Further the analysis of the energy in the coating was performed. Following the method of Harry et al. [6] we used the boundary conditions to obtain the coating energy from the response of the substrate to the applied virtual force. The results of this work are presented in Tab. 3. Here we only used COMSOL for the numerical calculations due to its faster convergence behavior compared to ANSYS.

In contrast to the result of the substrate energy no significant deviation of the elastic energy is observable. Thus, a change in the substrate orientation is no adequate mean to reduce the amount of Brownian noise of the coating. As this is the major thermal noise contribution an improvement of the detector's sensitivity is not expected by a different crystallographic orientation of the substrate.

This work was supported by the DFG under contract SFB Transregio 7.

References

[1] K. Somiya, Class. Quantum Grav. **29**, 124007 (2012).
[2] S. Hild *et al.*, Class. Quantum Grav. **28**, 094013 (2011).
[3] Yu. Levin, Phys. Rev. D **57**, 659-663 (1998).
[4] J. J. Wortman and R. A. Evans, J. Appl. Phys. **36**, 153-156 (1965).
[5] Y. T. Liu and K. S. Thorne, Phys. Rev. D **62**, 122002 (2000).
[6] G. Harry et al., Class. Quantum Grav. **19**, 897-917 (2002).

Mechanical loss of single crystalline sapphire fibres

Gerd Hofmann, Yusuke Sakakibara[*]*, Julius Komma, Christian Schwarz, Daniel Heinert, Kazuhiro Yamamoto*[*]*, Ronny Nawrodt, and Paul Seidel*

[*] Institute for Cosmic Ray Research, University of Tokyo, Japan

Gravitational wave detectors like VIRGO, LIGO and GEO600 utilize Michelson interferometers with arm lengths up to 4 km to detect disturbances caused by gravitational waves. All of these detectors suffer from different noise sources like seismic noise, quantum noise or thermal noise in the optical components and their suspensions. Thermal noise is directly affected via the fluctuation dissipation theorem by the mechanical loss of the material [1]. Fused silica shows very low mechanical loss and therefore it is used as mirror material. In the case of LIGO and VIRGO it was suspended by loops of metal wires which typically have a mechanical loss of 10^{-4} [2]. To improve the sensitivity current detectors are updated to the second generation . One major effort is to reduce thermal noise in the low frequency range that is caused by the suspension system. Thus monolithic suspensions also made of fused silica are used which were pioneered in GEO600 [3, 4]. Further improvements are expected in future generations of gravitational wave detectors as these will be operated under ground and use cooled test masses to overcome further limitations by gravity gradient and thermal noise. In Europe this next step in gravitational wave astronomy is set up by the Einstein Telescope design study [5]. Meanwhile Japanese colleges attempt to build such a detector within the next few years. Despite of silicon which is a promising candidate material for the European Einstein Telescope because of its low mechanical loss at low temperatures, sapphire is the material of choice for the Japanese KAGRA detector [6]. The suspension of the sapphire mirrors will be realized by the use of monocrystalline sapphire fibres. We characterized such fibres in terms of their mechanical loss.

The mechanical loss of a solid is determined by the dissipation of energy in each cycle of a vibration. Various mechanisms like air damping, energy loss in support structures, thermo-elastic damping, Akhiezer damping and internal friction limit the lowest achievable loss.

We investigated two single crystalline sapphire fibres with a diameter of 1.8 mm and 85 mm respectively 350 mm in length and both fibers on one side with a monolithic “head” of 10 mm diameter and 5 mm in height to support the fibre (see fig. 1).

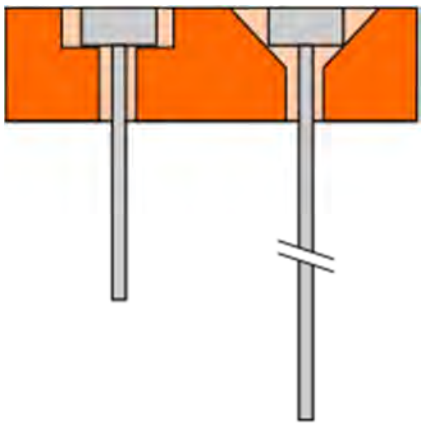

Fig. 1: Two fibres of 85 mm and 350 mm length were investigated. The “head” of the fibre was clamped in a massive copper support by the use of a flat sink respectively a cone.

The head of the fibre is clamped in a special build massive copper structure to provide a rigid mechanical mount and good thermal contact. We used a flat sink

as well as a cone to clamp the head as shown in the picture. The support structure is mounted inside a cryostat that allows temperatures between 5 K and 300 K. Additional damping due to residual gas is avoided by a pressure below 10^{-4} mbar.
An electrostatic driving plate is used to excite the sample to resonant modes. After switching off the excitation an exponential decay of the mechanical vibration is recorded. The mechanical loss is then given by means of the frequency f_{res} of the resonant mode and the time constant τ_{ring} of the ring down according to [7]:

$$\phi = \frac{1}{\pi f_{res} \tau_{ring}}. \qquad (1)$$

The behaviour of a solid in consideration of mechanical loss might be described by the model of anelasticity. Intrinsic loss processes are then given by:

$$\phi = \Delta \frac{\omega\tau}{1+\omega^2\tau^2} \qquad (2)$$

with the frequency $\omega = 2\pi f$ and the characteristic time τ of the loss process. In case of thermo elastic damping the so called relaxation strength Δ is described by:

$$\Delta = \frac{Y\alpha^2 T}{C\rho}. \qquad (3)$$

Thereby Y gives the Young's modulus, α is the linear expansion coefficient of the fibre, T is the temperature, C stands for the heat capacity and ρ is the density of the material. For a circular cross-section of the sample the characteristic time τ is set by:

$$\tau = \frac{C\rho d^2}{4.32\,\pi\kappa}, \qquad (4)$$

where κ is the thermal conductivity of the material and d gives the diameter of the fibre.

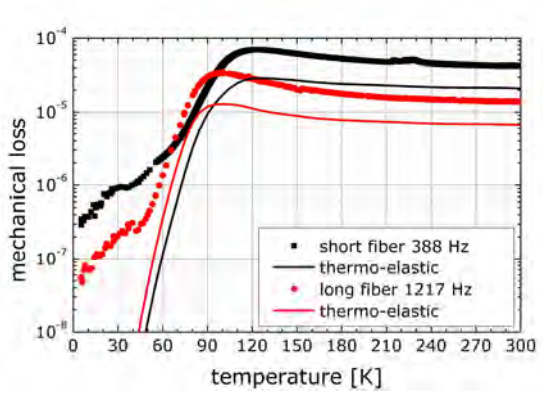

Fig. 2: The mechanical loss of one mode each of the short as well as of the long fibre is shown. While for higher temperatures thermo-elastic-loss (solid lines) dominates in the low temperature region other mechanisms like interaction with the support or surface loss have to be taken into account.

Our measurements show a coincidence of the obtained mechanical loss with the theoretical predictions on thermo-elastic damping for temperatures above 60 K. In the low temperature region other mechanisms set a limit the lowest loss. Nevertheless the lowest obtained loss is even below 10^{-7} (see fig. 2). Thus, together with its high thermal conductivity, sapphire is suitable to build monolithic and ultra-low noise suspensions for the future KAGRA detector.

This work is supported by the DFG under contract SFB TR7.

References

[1] H. B. Callen and T. A. Welton, Phys. Rev. **83**, 34 (1951).
[2] G. H. Hammond et al., Class. Quantum Grav. **29**, 124009 (2012).
[3] B. Willke et al., Class. Quantum Grav. **19**, 1377-1387 (2002).
[4] J. R. Smith et al., Class. Quantum Grav. **21**, S1091–S1098 (2004)
[5] M. Punuturo et al., Class. Quantum Grav. **27**, 194002 (2010).
[6] K. Somiya, Class. Quantum Grav. **29**, 124007 (2012).
[7] P. S. Saulson, Phys. Rev. D **42**, 2437-2445 (1990).

Matrix-induced in situ growth of plasmonic Au nanoparticles for biological sensor devices

C. Katzer, P. Michalowski, G. Schmidl, W. Fritzsche* and F. Schmidl*

*Institute of Photonic Technology (IPHT), Albert-Einstein-Str. 9, 07745 Jena, Germany

The establishment of surface plasmon resonance (SPR) based techniques marked an important step in the field of developing efficient detection strategies for bio-molecules [1]. Localized surface plasmon resonances (LSPR) represent a related bioanalytical technique which is also based on excited plasmons at metal-dielectric interfaces [2]. However, in contrast to SPR, LSPR is occurring at metal nano-particles, thus offering the potential for massive integration in sensor devices.

For future applications an in-situ preparation of such nanoparticles directly at the substrate surface would be favorable, allowing to overcome typical solution based problems such as aggregation of particles. Although those nanoparticles can easily be prepared through a dewetting of thin metal layers [3], already very thin layers lead to a broad size distribution due to Ostwald ripening. Very recently we presented the possibility of preparing monocrystalline and anisotropic gold nanoparticles in a $SrTiO_3$ matrix [4]. Unfortunately, to access these particles for biosensor applications the matrix material has to be removed which is difficult in the case of $SrTiO_3$ (STO). However, it is quite simple using an $YBa_2Cu_3O_{7-\delta}$ (YBCO) matrix.

Prior to the deposition of the matrix, a thin Au seed layer was deposited on STO and MgO substrates using pulsed laser deposition. This smooth seed layer self-assembles into crystalline gold nano-particles during the subsequent preparation process due to the elevated temperatures. The mean particle diameter thereby can be controlled via the thickness of the Au seed layer [5]. The resulting nanoparticles were overgrown by YBCO, whereby their shape and distribution can be influenced by the interaction with the matrix. For distinct preparation parameters kindly refer to refs. [4] and [6]. The gold nanoparticles can be found at the substrate/matrix interface, within the matrix itself and also on top of the matrix layer. Thus, their distribution density on top of the matrix can be controlled via the matrix thickness [6]. Hence, nanoparticle size and distribution density can be controlled individually, which is a great advantage over simple dewetting methods. Furthermore, using a matrix based method of fabricating gold nanoparticles our experiments indicate that one has the opportunity of controlling the nanoparticle shape and crystalline structure. Using standard YBCO deposition parameters to achieve c-axis-oriented orthorhombic films, the nanoparticle shape was found to be nearly spherical, although highly faceted. TEM and XRD investigations thereby revealed a quasi-epitaxial relation between the Au

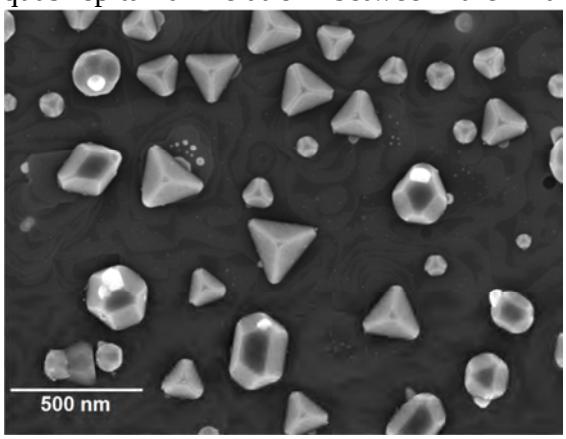

Fig. 1: SEM image of anisotropic crystalline Au nanoparticles on top of a YBCO matrix.

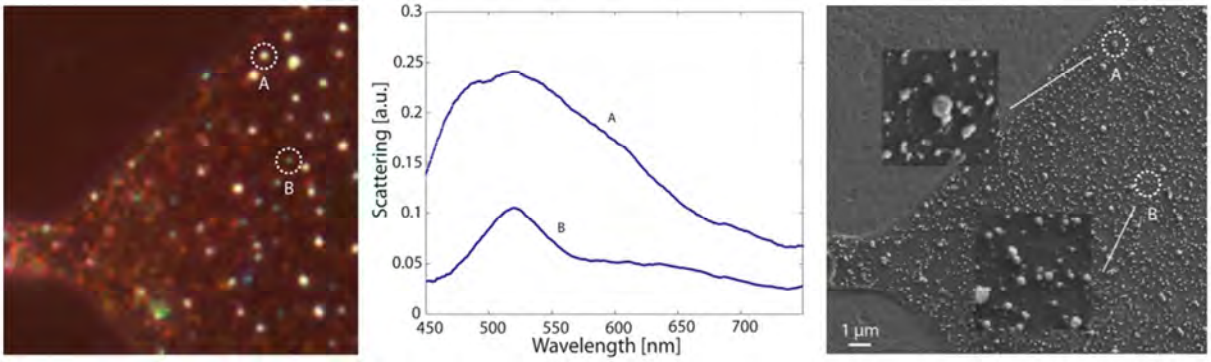

Fig. 2: Correlative optical dark-field, spectroscopic and SEM study of extracted Au nanoparticles which formerly were grown in a YBCO matrix. **Left** Dark-field microscopy image. **Center** VIS spectra of the particles A and B marked in the dark-field microscopy image. **Right** SEM image of the same region as in part a, with zooms in the regions investigated by spectroscopy.

nanoparticles and the surrounding YBCO matrix with the $\langle 100 \rangle_{Au}$, $\langle 110 \rangle_{Au}$ or $\langle 111 \rangle_{Au}$ directions parallel to the YBCO c-axis. On the other hand, using STO as matrix material, crystalline rod-like Au particles are grown. This is highly favorable because the observed wavelength shift when binding an analyte at the particle surface is significantly pronounced for anisotropic particles. But even when using a YBCO matrix crystalline and anisotropic nanoparticles can be created by varying the YBCO deposition parameters (see fig. 1).

As stated above, an important point for applications in biosensors is whether or not the particles can be extracted from the surrounding matrix. In the case of YBCO this was achieved by a 10 minute etching process in citric acid solution and subsequent rinsing with distilled water. After the extraction process only tiny amounts of Cu and Y could be found in XRD and EDX investigations, indicating an almost complete dissolution of the matrix. For biological applications the intention is to pick an extracted Au particle to subsequently bind an analyte, which then could be detected by measuring the resulting spectral shift of the resonance wavelength. Therefore, first optical investigations were performed based on dark field microscopy in combination with microspectroscopy (see fig. 2) [6]. It is also worth to note, that the initial Au seed layer can be patterned to restrict the nanoparticles only to distinct areas. As we could show, a subsequent dissolution of the matrix does not influence the nanoparticle distribution. Furthermore, there is no indication for any re-attachment of removed Au particles in areas which were not covered by the initial Au seed layer. Thus, the combination of microstructuring and subsequent matrix dissolution seems highly suitable for the preparation of crystalline Au nanoparticles in well-defined patterns.

Acknowledgement

C. Katzer would like to thank the Landesgraduiertenförderung Thüringen for financial support.

References

[1] B. Liedberg *et al.*, Sens. Actuator **4**, 299 (1983).
[2] A. Csaki *et al.*, Philos. Trans. A **369**, 3483 (2011).
[3] H.R. Stuart and D. G. Hall, Appl. Phys. Lett. **69**, 2327 (1996).
[4] S. Christke *et al.*, Opt. Mater. Express **1**, 890 (2011).
[5] V. Grosse *et al.*, Phys. Status solidi RRL **4**, 97 (2010).
[6] C. Katzer *et al.*, J. Nanopart. Res. **14**, 1285 (2012).

Thermo-optic coefficient of silicon at 1550 nm at low temperatures

Julius Komma, Gerd Hofmann, Christian Schwarz, Daniel Heinert, and Ronny Nawrodt

Silicon is a promising material for cryogenic gravitational wave detectors [1,2] or for cavities used for laser frequency stabilization [3] due to its low mechanical loss at cryogenic temperatures.

To estimate thermal lensing effects caused by optical absorption in applications with higher laser power the thermo-optic coefficient $\beta = dn/dT$ is a crucial parameter. Likewise the thermo-optic coefficient has a meaning for the calculation of thermo-refractive noise [4] caused by statistical temperature fluctuations.

In this work the thermo-optic coefficient of silicon was measured from 5 K to 300 K [5]. An interferometric scheme used by Cocorullo et al. [6] was adjusted for a cryogenic measurement. The experimental setup is shown in Fig. 1.

In this technique the sample is used as Fabry-Perot-Cavity (FPC). Here the intensity of the reflected light by a FPC is determined by:

$$I_R = \frac{I_0}{1 + 1/(F\,sin^2\Theta)}, \qquad (1)$$

with I_0 as the incident light intensity and a phase change Θ for a single pass at normal incidence. The phase change is:

$$\Theta = 2\pi nL/\lambda, \qquad (2)$$

L is the geometric distance between the mirrors of the FPC, n is the refractive index of the material between the mirrors and λ is the wavelength of the incident light. The finesse coefficient F of the FPC can be calculated by the reflectance R of the mirrors:

$$F = \frac{4R}{(1-R)^2}. \qquad (3)$$

In our experiment the polished surfaces of the silicon form the cavity mirrors, thus the reflectance R is constituted by the Fresnel reflection.

Changing the sample temperature has two effects on the phase Θ given above: First a variation of the geometrical path length takes place due to the thermal expansion coefficient α Second the temperature dependence of the refractive index n causes a change in the optical path length as well. The temperature derivation of the phase term is given by:

$$\frac{\delta\Theta}{\delta T} = \frac{2\pi}{\lambda}\left(L\frac{\delta n}{\delta T} + n\frac{\delta L}{\delta T}\right) = \frac{2\pi L}{\lambda}\left(\frac{\delta n}{\delta T} + n(T)\alpha(T)\right). \qquad (3)$$

This temperature dependence change in the phase affects the reflected light intensity I_R as shown in Fig. 2.

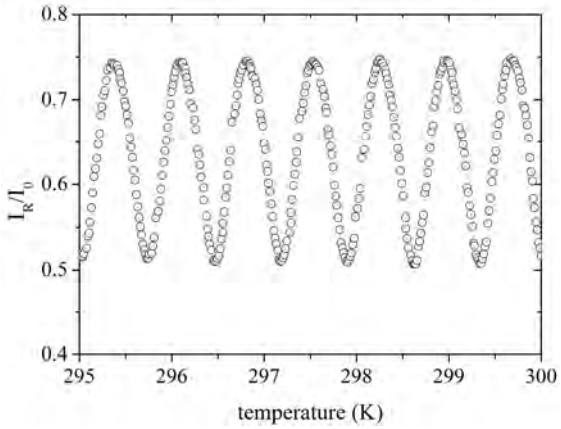

Fig. 2: Measured intensity change of the reflected light for a 6 mm long silicon FPC over a temperature range from 295 K to 300 K.

Between two interference maxima a phase shift of π occurs. This phase shift corresponds to a temperature change of ΔT of the sample. The thermo-optic coefficient can then be expressed as:

$$\beta(T) = \frac{\delta n}{\delta T} = \frac{\lambda}{2L\Delta T} - n(T)\alpha(T). \qquad (4)$$

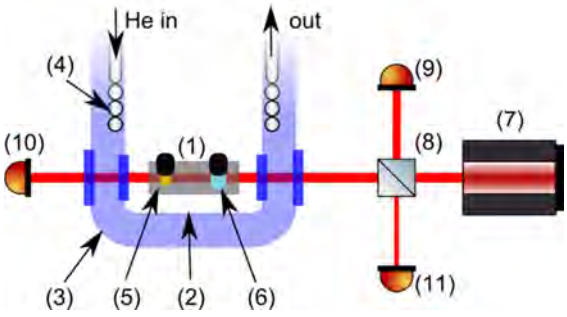

Fig. 1: The sample (1) is placed inside the probe chamber (2) of a continuous flow cryostat. This chamber is surrounded by vacuum (3) for thermal insulation against room temperature. By use of a cooling coil (4) it is possible to cool down the cryostat with a liquid helium flow. A calibrated temperature sensor (5) and an electrical heater (6) are placed on the surface of the sample. The laser beam of a 1550nm laser (7) is led through a beam splitter (8). One beam is directed to a photo diode (9) for a reference measurement. The other part of the laser beam hits the sample. Two other photo diodes measure the transmitted (10) and the reflected (11) light intensity.

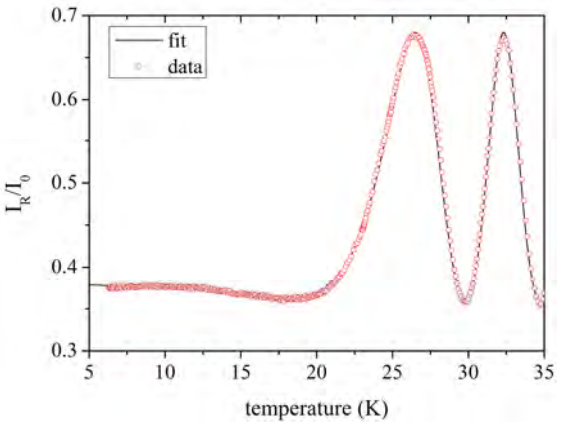

Fig. 3: Measured data in the low temperature region and fit curve for the calculation of the thermo-optic coefficient.

Starting with a literature value for the refractive index n at room temperature [7] and a temperature dependent coefficient of thermal expansion [8] we calculated the thermo-optic coefficient down to 26 K. Below this temperature the change of the refractive index with temperature becomes very small so that no next maximum appears. The values for the temperature region from 26 K to 5 K were received from a fit of the measured data points using equation (1) and equation (2) as shown in Fig. 3.

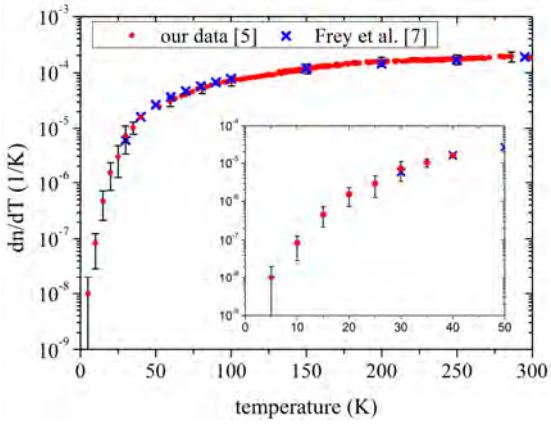

Fig. 4: Results for the thermo-optic coefficient of silicon at 1550 nm. Data are given for a temperature range from 5 K to 300 K. The values by Frey et al. show a good agreement.

This work was supported by the DFG under contract SFB Transregio 7

References

[1] R. Nawrodt et al., Gen. Relativ. Gravit. **43**, 593 (2011).
[2] S. Hild et al., Class. Quantum Grav. **28**, 094013 (2011).
[3] T. Kessler et al., Nature Photonics **6**, 687-692 (2012).
[4] V. B. Braginsky et al., Phys. Lett. A **271**, 303 (2000).
[5] J. Komma et al., Appl. Phys. Lett. **101**, 041905 (2012).
[6] G. Cocurullo et al., Appl. Phys. Lett. **74**, 3338 (1999).
[7] Frey et al., e-print arXiv:physics/0606168v1.
[8] K. G. Lyon et al., J. Appl. Phys. **48**, 865 (1977).

Superconducting thin film structures prepared by nanoscale wedge polishing

Peter Michalowski, Christian Katzer, Frank Schmidl, Dagmar Meier, Tetyana Shapoval*, and Paul Seidel*

*IFW Dresden, Institute for Metallic Materials, PO Box 270116, D-01171 Dresden, Germany

When building electronic devices using a multi-layer technology, surface roughness is a crucial factor [1]. This holds especially for thin films of high-temperature superconductors as droplets and outgrowths originating from the pulsed laser deposition are quite common [2]. Some HTSC magnetic field sensors contain superconductor-conductor crossovers, where droplets of amorphous $YBa_2Cu_3O_{7-\delta}$ (YBCO) may shunt the insulating SiO_2 layer (fig. 1) [3]. Since a thicker SiO_2 layer would raise problems when lifting it off, we went for a new mechanical nanopolishing method to reduce the surface roughness [4]. Furthermore, the performance of direct current superconducting quantum interference device (dc-SQUIDs) gradiometers strongly depends on the spread of the critical current I_C and the normal state resistance R_N of the Josephson junctions. Therefore, it could be useful to tune these superconducting properties by decreasing the film thickness after the preparation of the devices.

All samples discussed in this text were prepared by pulsed laser deposition of 150 nm of YBCO on bi-crystal $SrTiO_3$ substrates using a KrF excimer laser. To provide a low contact resistance a gold layer was grown on the contact area of the YBCO film. Subsequently, the samples have been structured using photolithography and ion beam etching. For more details on the sample preparation see [5].

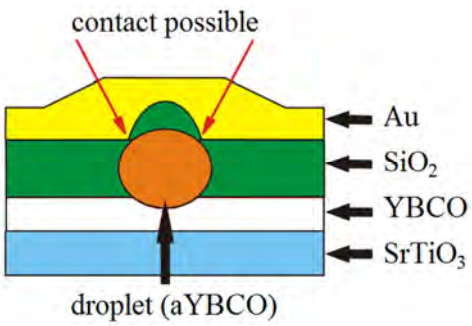

Fig. 1: Scheme of the different layers at a crossover. The droplet of amorphous YBCO shunts the insulating SiO_2 film.

Before we turned to samples with Josephson junctions, we started our investigations with the polishing of unstructured YBCO films on $SrTiO_3$ single-crystal substrates. As shown in fig. 2 the roughness of the YBCO film decreases substantially through polishing and particularly large bumps are removed. This strongly reduces the possibility of shunts in multilayer processes. Thereby, it yields the potential to improve superconducting components and sensors with crossovers.

As the next step, we applied the polishing technique to a YBCO film grown on a $10 \times 10\ mm^2$ bi-crystal substrate before patterning it into dc-SQUIDs. Starting from the center, the YBCO film was polished to both sides along the grain boundary, leading to a double-wedge-shaped surface as illustrated in fig. 3a). This particular shape was chosen, because bi-crystal grain boundaries tend to show an increase or decrease of j_C along the grain boundary. Thus, we minimized the influence of a reduction of I_C caused by the properties of the grain boundary. The results of the electrical characterization are presented in fig. 3b).

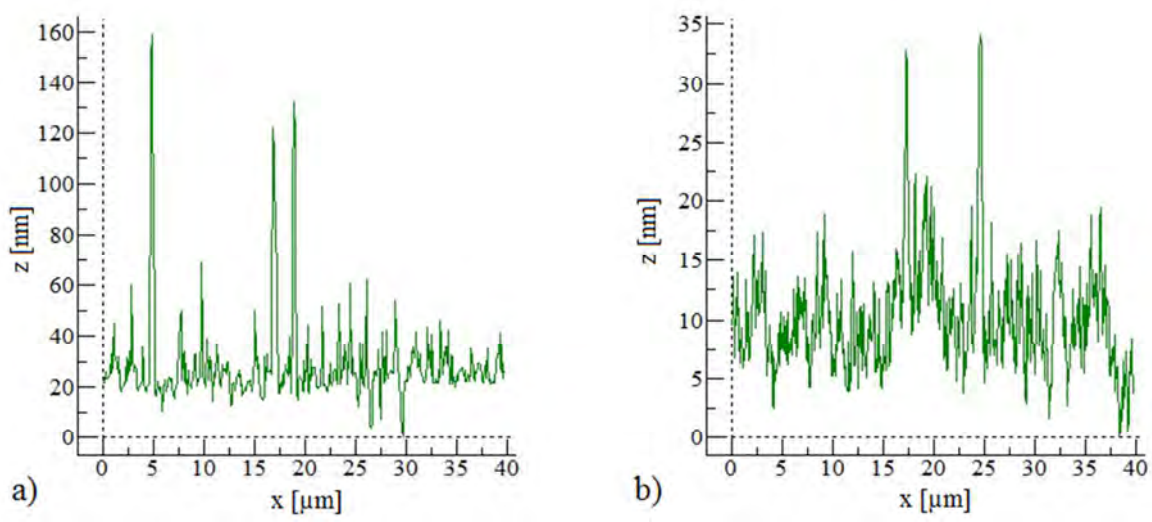

Fig. 2: AFM measurements (a) before and (b) after polishing.

SQUIDs with thicker YBCO films in the region of the Josephson junctions, i.e. those in the middle of the sample, exhibit higher critical currents I_C than those at the edges. The deviations occurring could originate from local disorders of the grain boundary, as often occur in bi-crystal substrates.

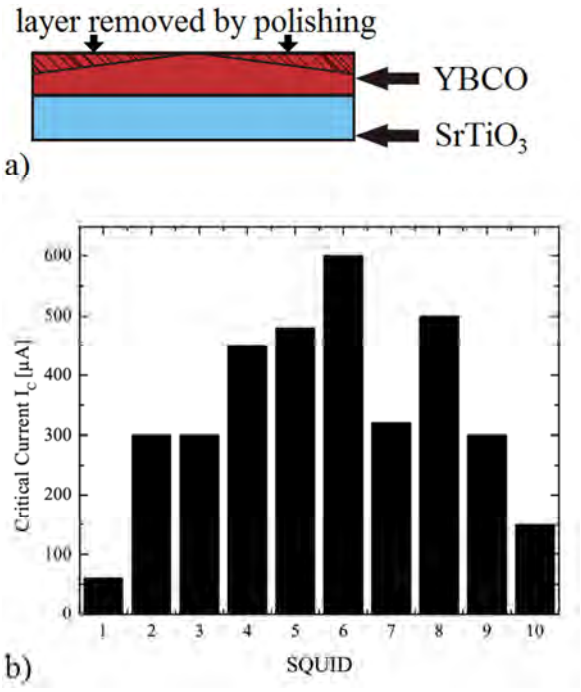

Fig. 3: a) Scheme of the shape of the polished YBCO film. b) Critical current as a function of the position of the dc-SQUID on a 10 x 10 mm^2 bi-crystal substrate. SQUIDs 1 and 10 are at the edges whereas 5 and 6 are in the middle of the sample. All dc-SQUIDs possess the same junction width and original film thickness before nanopolishing.

In another approach, we tried to modify the junction parameters after the structuring of the sample. For this, flip-chip gradiometers were patterned on 10 × 10 mm^2 bi-crystal substrates and characterized. Subsequently, the samples were polished and measured again. The polishing parameters were chosen in order to reduce the film thickness in the region of the Josephson junctions, thereby changing their superconducting parameters. As it turned out, the polishing led to a decrease of I_C and an increase of R_N, leaving the characteristical I_CR_N product approx. unchanged, which is favorable for the operation of magnetic field sensors [6].

Acknowledgement

C. Katzer would like to thank the Landesgraduiertenförderung Thüringen for financial support.

References

[1] P. A. Nilsson *et al.*, IEEE Trans. Appl. Supercond. **5**, 1653-6 (1995).

[2] J. D. Pedarnig *et al.*, Thin Solid Films **518**, 7075-80 (2010).

[3] K. Peiselt *et al.*, Supercond. Sci. Technol. **16**, 1408-12 (2003).

[4] T. Shapoval *et al.*, Supercond. Sci. Technol. **21**, 105015 (2008).

[5] P. Michalowski *et al.*, Supercond. Sci. Technol. **25**, 115019 (2012).

[6] K. Enpuku *et al.*, J. Appl. Phys. **73**, 7929-34 (1993).

Mechanical loss of Ag implanted thin tantala films at low temperatures

Ronny Nawrodt, Julius Komma, Bastian Walter, Christian Schwarz, Gerd Hofmann, Daniel Heinert, and Claudia S. Schnohr

Gravitational wave detectors based on Michelson-like interferometers are limited by different types of noises. In the mid-frequency range around 100 Hz the limiting noise source is Brownian thermal noise of the high-reflectivity coatings of the optical components [1]. These high-reflectivity coatings are formed by alternating layers of high refractive index and low refractive index dielectric layers. Typically, tantala (Ta_2O_5) is used as the high refractive index material and silica (SiO_2) is used as low index material.

The mechanical loss of a material is connected with its thermal Brownian noise via the fluctuation-dissipation-theorem. Low mechanical loss provides low thermal Brownian noise. It was shown [2] that tantala has a much higher mechanical loss compared to silica and is thus the dominating noise source in such a highly reflective layer stack.

The mechanical loss spectrum at cryogenic temperatures shows a broad plateau between 20 K and 100 K whose origin is proposed to be a position change of oxygen atoms inside the tantala. Co-doping of tantala with titania (TiO_2) during the layer deposition reduces the mechanical loss of the tantala layer significantly [3]. The underlying mechanism, however, is not yet understood. Unfortunately, the process of co-doping during layer deposition is both time consuming and expensive hindering the study of doping effects on the mechanical loss of the tantala layers. Additionally, only a few companies are able to provide co-doped layers in a sufficient quality. We therefore investigate the possibility of ion implantation as an alternative route to modify the mechanical loss of the material. Ion implantation enables the study of a large variety of dopant species and offers excellent control over concentration and depth distribution of the impurity atoms.

Tantala is deposited onto silicon flexures providing resonant systems to study the mechanical loss. A standard ring-down technique is used to determine the mechanical loss before and after ion implantation [4]. The 500 nm thick tantala layers were implanted at room temperature with 750 keV silver ions. The resulting implantation profile was calculated with SRIM2008 [5] and is shown in fig. 1. A fluence of 2×10^{15} Ag/cm^2 was used leading to a peak concentration of roughly 0.1 at%.

The mechanical loss of the tantala films was studied in a wide temperature range from 5 to 300 K. The comparison of the results of the dielectric layer before and after ion implantation is given in fig. 2.

The mechanical loss is generally increased by the ion implantation. Additionally, two loss peaks at 25 K and 50 K are observed indicating changes in the amorphous microstructure and/or Ag related loss

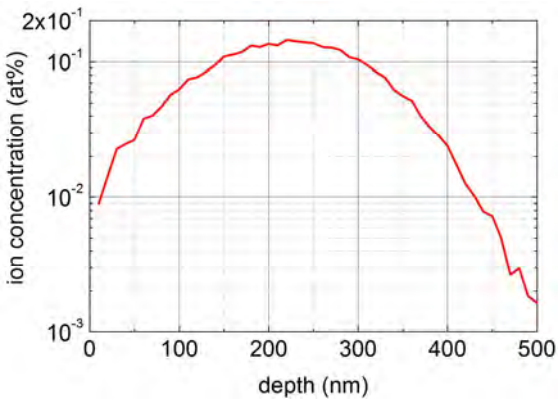

Fig. 1: Implantation profile of 750 keV Ag ions into 500 nm thick tantala layers.

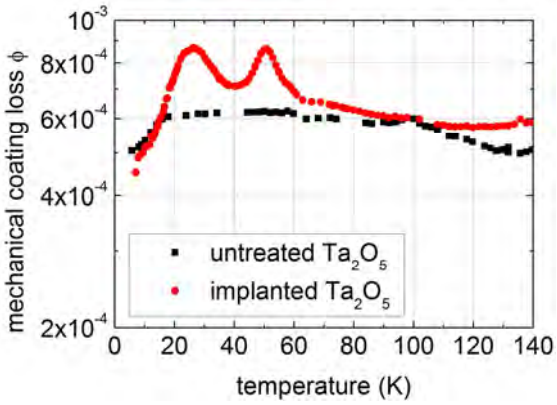

Fig. 2: Comparison of the mechanical loss of a tantala layer before and after implantation with 750 keV Ag ions.

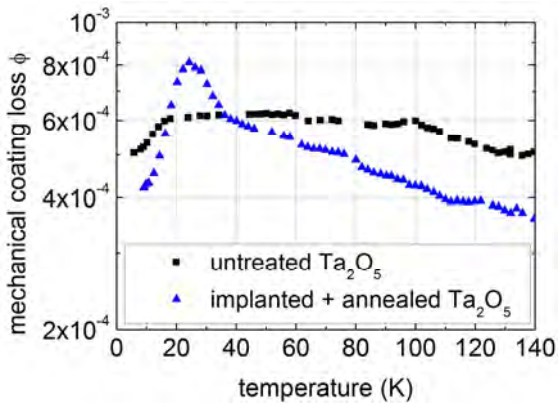

Fig. 3: Comparison of the mechanical loss of a tantala layer before and after Ag implantation and annealing. The implanted layer was annealed for 12 hours at 300 degrees Celsius in air.

effects. Subsequent annealing can potentially reduce these peaks. However, it is well known that heat treatment also changes the mechanical loss behavior of un-doped tantala layers [6]. Using low temperatures up to 300 degrees Celsius so far could not show any change of the tantala and thus a temperature of 300°C was chosen to anneal the implanted samples. Fig. 3 shows the comparison of the implanted and annealed tantala layer with the untreated layer.

Low temperature annealing of the implanted layer slightly reduces the loss peak at 25 K while the peak at 50 K disappears completely. Compared to the untreated layer, the mechanical loss of the implanted and annealed layer is still higher in the temperature range between 20 K and 40 K but is significantly lower than the initial values for all other temperatures.

The origin of the reduction of the mechanical loss can be manifold and is yet not understood. A possible mechanism is the blocking of microscopic states of the oxygen by the implanted ions. Thus, the oxygen is not able to switch between two stable positions and consequently there is a reduced number of processes causing mechanical loss. This possible scenario could be confirmed by using different types of ions with different ion radii for implantation as the measured loss spectra should be strongly related to the the size of the implanted ions.

It was shown that implantation of thin tantala films with silver ions can change – and especially lower – their mechanical loss over a wide temperature range. Ion implantation thus provides a versatile technique to study and understand intrinsic loss mechanisms in amorphous tantala layers.

This work was supported by the German science foundation DFG under contract SFB TR7. Claudia S. Schnohr further acknowledges the support of the Carl-Zeiss-Stiftung, Germany.

References

[1] R. Nawrodt, S. Rowan, J. Hough, M. Punturo, F. Ricci, J.-Y. Vinet, Gen. Relativ. Gravit. **43**, 593 (2011).
[2] S. D. Penn et al., Class. Quantum Grav. **20**, 2917 (2003).
[3] G. M. Harry et al., Class. Quantum Grav. **24**, 405 (2007).
[4] S. Reid et al., Physics Letters A **4-5**, 205 (2006).
[5] J. F. Ziegler, J. P. Biersack, U. Littmark, *The Stopping and Range of Ions in Solids*, Pergamon, New York (2003).
[6] I. W. Martin et al., Class. Quantum Grav. **27**, 225020 (2010).

Processing of Co-doped Ba-122 single crystals for manufacturing of Josephson junctions

D. Reifert, S. Schmidt, S. Döring, T. Wolf, F. Schmidl, and P. Seidel*

** Karlsruhe Institute of Technology, Institute of Solid State Physics, 76021 Karlsruhe, Germany*

In order to understand the nature of the superconductivity in iron pnictides it is necessary to examine their electrical properties. Therefore we are using Josephson junctions which are a suitable tool to investigate the gap structure. Also in combination with phase sensitive measurements it is possible to test the symmetry of the order parameter of these iron pnictide superconductors. Additional to previous work [1-5] in which we investigated Josephson and Andreev dominated junctions on pnictide thin films we want to realize similar junctions on Ba-122 ($BaFe_2As_2$) single crystals.
Therefore we have to solve several issues. Especially, achieving a high surface quality with an RMS roughness less than 5nm is a challenging task. A high surface quality is necessary since we are planning to realize the junctions via photolithography similar to the processing of the Ba-122 thin films (in our previous work).

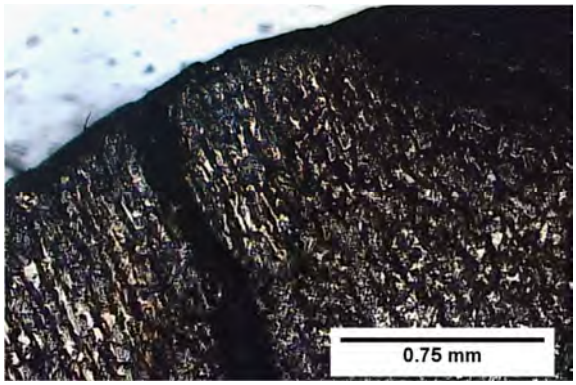

Fig. 1**:** Microscope picture of the surface of a Ba-122 crystal after polishing. There are several defects visible on the surface which were caused by the polishing procedure.

The preparation of our crystals include the planarization of the crystals, etching of a base electrode with an argon ion beam, deposition of an insulating SiO_2 barrier by sputtering, deposition of a tunneling barrier (normal metal or insulator) also by sputtering, and deposition of a lead-indium counter electrode by thermal evaporation. The structuring of these different layers is realized in a photolithography process.
The Ba-122 single crystals were produced by the Karlsruhe Institute of Technology with a self flux method. Further details of this process can be found in [6, 7].
Due to the low availability and growing time of these Co-doped single crystals we used non-superconducting undoped and more available crystals to develop and optimize a processing technology. Our first attempt was to polish the crystal with a standard chemical-mechanical polishing procedure. This produces a rather rough surface which is not suitable for our application. An example of such a surface can be seen in Fig.1. Measurements of the surface profile revealed that the roughness has increased after the polishing (RMS roughness >1µm). Therefore we investigated the effects of several other planarization techniques such as mechanical polishing, ion beam planarization, and cleaving of the crystal.

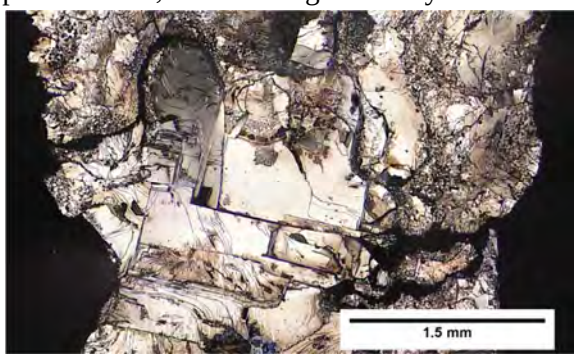

Fig. 2**:** Microscope picture of a cleaved surface. In the center flat surface areas are visible.

The etching rate of an ion beam (in our case Argon) is strongly dependent on the angle of incidence. This can lead to a smoothing of the surface if the angle of incidence is well-chosen.
We prepared some samples with a coarse planarization process (RMS roughness approximately 250nm) and etched them under different angles. With this method we achieved a reduction of the

surface roughness to a value of approximately 60nm (RMS roughness). However we were not able to reduce the roughness any further to a useful level. But since we have observed this surface smoothing it might be possible to use this effect to further enhance the quality of already flat surfaces. We will investigate this in future experiments.

The cleaving of single crystals can lead to very flat surfaces so we tested different cleaving techniques. But only small areas with high difference in altitude between them could be achieved. As can be seen in Fig.2 there are some impurities visible that's why we investigated the surface with electron backscatter diffraction (EBSD) and Energy-dispersive X-ray spectroscopy (EDX). These show that the crystal contains two different phases which can be seen in Fig.3. This led us to the assumption that those samples are not single crystals. This could be an explanation for the low quality of our cleaved surfaces.

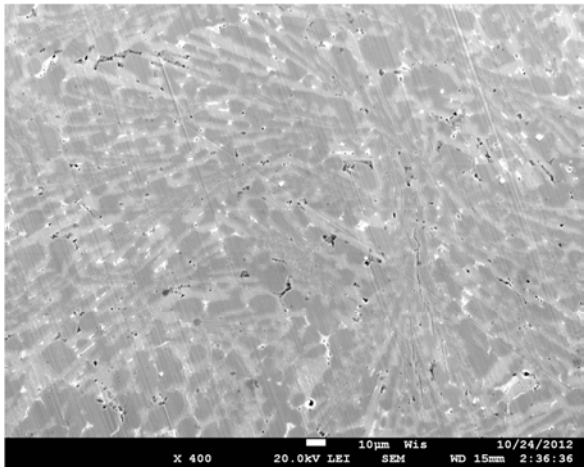

Fig. 3: SEM picture of a polished undoped crystal (R_{RMS}≈30nm). EDX measurements show that the dark areas consist of $BaFe_2As_2$ whereas in the brighter areas no Ba could be found.

Scanning electron microscope (SEM) images of Co-doped crystals indicate that there aren't such impurities. So we think that cleaving of those doped crystals could be more successful. Nevertheless, cleaving can be used to obtain multiple samples out of one crystal which is useful since only very few crystals are available.

We tested several mechanical polishing methods but mostly they require some kind of lubricant e.g. water or oil in which oil cannot be used because we aren't able to remove it after the polishing due to the vulnerability of the crystals to solvents (e.g. acetone). During these experiments we realized that our samples are also vulnerable to water. Since we have no polishing solution that didn't erode the surface we tried to polish it by hand without any liquid involved.

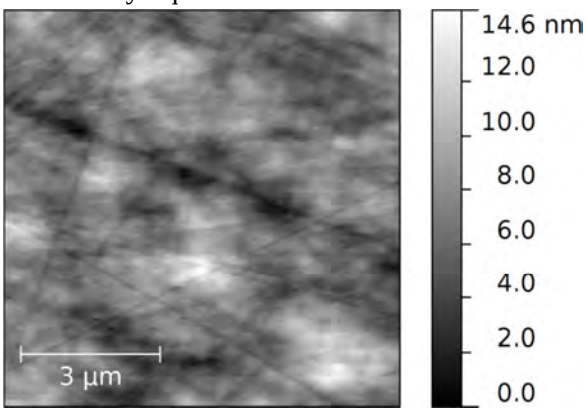

Fig. 4: Atomic force microscope measurement of a polished surface R_{RMS}=2nm

These experiments included some rather offbeat polishing agents. Nevertheless we found a method to achieve a RMS roughness better than 5nm (best sample (2.5±0.5)nm Fig.4). The first step was to grind the sample with a coarse SiC polishing foil. Then we continued with gradually finer SiC foil. Finally, we polished the sample on a piece of leather. Producing a surface with a relatively high quality this process lacks on reproducibility. Therefore further optimization is necessary and will be investigated in future work. There are still some other issues to solve e.g. the fact that our current photolithography process involves the use of water which erodes the surface.

This work was partially supported by DFG within SPP 1458 under project no. (SE 664/15-1),, and the Landesgraduiertenförderung Thüringen.

Reference

[1] S. Döring *et al.*, *Phys C Supercond* **478**, 15–18 (2012).
[2] S. Döring *et al.*, *Supercond. Sci. Technol.* **25**, 084020 (2012).
[3] S. Döring *et al.*, *Phys. Proc.* **27**, 296 (2012).
[4] S. Schmidt *et al.*, *Appl. Phys. Lett.* **97,**, 172504 (2010).
[5] S. Schmidt *et al.*, *Phys. Proc.* **36**, 82 (2012).
[6] F. Hardy *et al.*, *Phys. Rev.* B **81**, 060501 (2010).
[7] F. Hardy *et al.*, *Europhys. Lett.* **91**, 47008 (2010).

Antenna-coupled thermal radiation detectors for THz spectroscopy

U. Schinkel and H.-G. Meyer
Institute of Photonic Technology, PO Box 100239, D-07702 Jena, Germany

In recent years THz detectors have become more and more common for different applications in the fields of security screening, medicine, gas sensing, food industry and spectroscopy. For various types of THz detectors, antennas are an efficient way for coupling to the detector. In these sensors, the energy of the terahertz radiation is absorbed by an appropriate planar antenna and dissipated in a conducting strip acting as the impedance-matched load resistor of the antenna. There, the absorbed radiation energy is converted into Joule's heat. In order to amplify the resulting of temperature, this load resistor can be placed on a micromechanical air-bridge serving as a thermal isolation structure. The temperature rise can be transduced into an electric signal voltage by the thermoresistive effect using a bolometer [1,2,3,4] or by the Seebeck effect employing a thermocouple [5,6].

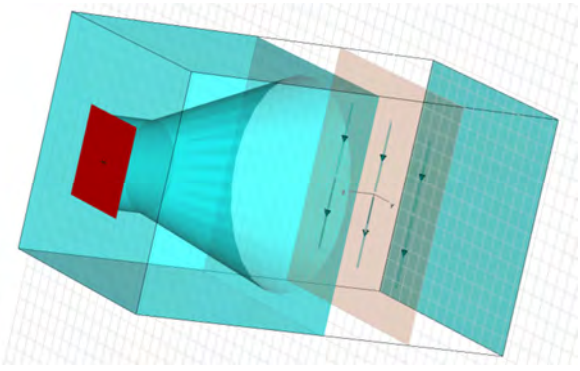

Fig. 1: CST Model of an antenna array with horn antenna (left) and reflector (right) for EM simulation.

Important for such sensors is the antenna characteristic. To obtain a high antenna gain, the coupling of the radiation to the antenna and the antenna layout needs to be investigated. For the modelling the program CST Microwave Studio was used. Fig. 1 shows a CST model of our detector concept. On the left side a horn antenna is focusing the radiation which is emitted by a waveguide port (red square, WGP) to the antennas. The antennas are placed in a distance of $\lambda/2$ to the horn. The antenna array consists of two times three half-wave dipole antennas that are connected in series. The absorbed radiation is dissipated in a resistor in the middle of the antenna. A reflector placed at a distance of $(2n+1)\lambda/4$ improves further the absorption. The absorption characteristic of an optimized sensor is shown in Fig. 2. At 350 GHz the absorption is 0.75 and the full width half maximum is about 40 GHz. The results are very convenient, c.f. [6], but for spectroscopic purposes the maximum at 600 GHz needs to be removed. In order to suppress such maxima, a filter can be placed in front of the horn antennas. As filters, frequency selective surfaces (FSS) are particularly useful [7]. FSS are periodically arranged flat metal structures (here cross slots), with the dimensions in the range of the wavelength. They are

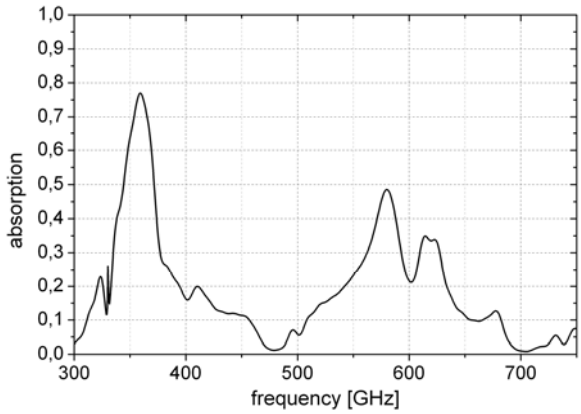

Fig. 2: Absorption of an optimized detector for 350 GHz.

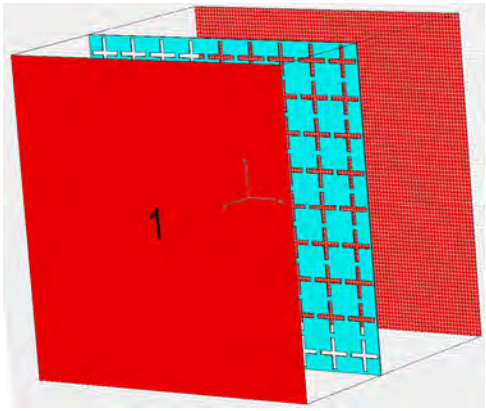

Fig. 3: Frequency selective surface between two waveguide ports (red).

acting as an active medium for the electromagnetic radiation and, therefore, show a characteristic response depending on the geometrical structure (band-pass, low-pass or high-pass). Fig. 3 shows a model of a FSS structure with 9x9 cross slots between two WGPs. The transmission characteristic can be seen in Fig. 4. This FSS structure transmits at 350 GHz up to 1, while at other frequencies the transmission is significantly reduced. Thus, by combination of the FSS and the antenna array it is possible to suppress the maximum at 600 GHz, while obtaining a sharp peak at

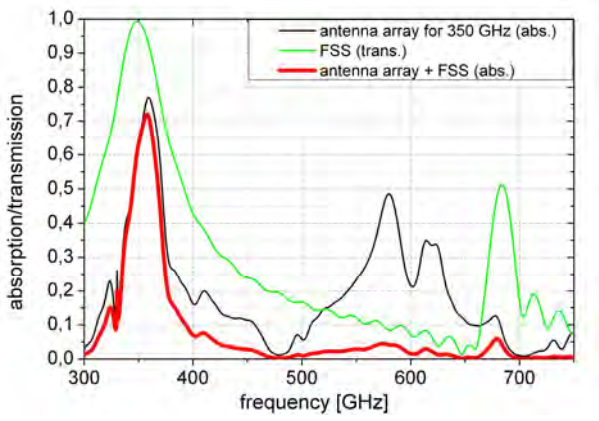

Fig. 4: Absorption of a narrow band antenna array for 350 GHz (black), transmission of frequency selective surface (green) and the convolution of the two curves (red).

350 GHz, see Fig. 4. The maximum transmission at 350 GHz is reduced by only a few percent from 0.75 to 0.725. All other peaks are suppressed to values less then 0.05.

The shown antenna arrangement is the basis of a miniaturized spectrometer for measurements from 350 to 700 GHz, that will consist of a number of detectors designed for different frequency bands with a segmentation of 50 GHz .

In the present work we show a narrow band antenna array for 350 GHz for an antenna coupled detector. In order to reduce the absorption at other frequencies, FSS are used. In this way antenna arrays are frequency-selectively and can be used for THz spectrometers. To improve the absorption in a narrow band, further research on antenna structures is necessary. Additionally, the dimensional parameters of the thermocouples have to be optimized.

The author (U. Schinkel) would like to thank Prof. Seidel for mentoring and scientific support.

References

[1] A. Luukanen *et al, Proc. SPIE* **5411** 121-126 (2004)
[2] J.P. Rice *et al., Appl. Phys. Lett.* **65** 773-775 (1994)
[3] A.J. Miller *et al. , Proc. SPIE* **5411** 18-24 (2004)
[4] E. Peytavit *et al., Proc. IRMMW-THz Conf.* 257-258 (2005)
[5] A. Ihring *et al., MEE* **98** 512-515 (2012)
[6] J.A. Cox *et al, Proc. SPIE* **7311** 73110R 1-11 (2009)
[7] A. Broemel *et al., Proc. IRMMW-THz Conf.* (2012)

SQUID-based setup for the absolute measurement of magnetic fields

T. Schönau[1], M. Schmelz[1], V. Zakosarenko[1], R. Stolz[1], M. Meyer[2], S. Anders[1], L. Fritzsch[1] and H.-G. Meyer[1]

[1]*Institute of Photonic Technology, PO Box 100239, D-07702 Jena, Germany*
[2]*Supracon AG, An der Lehmgrube 11, D-07751 Jena, Germany*

Magnetic sensors based on SQUIDs exhibit outstanding sensitivity and bandwidth. But, due to their periodic voltage-flux characteristic, they are not suited for absolute magnetometry. Furthermore, their application in unshielded environment is challenging, because magnetic transients may interrupt the flux locking loop (FLL) and introduce step-like shifts into the output signal that cannot always be corrected by data postprocessing.

To solve this problem, we propose to use a cascaded SQUID setup as depicted in figure 1, consisting of several coplanar SQUID magnetometers with different effective pickup areas, which are integrated on a single chip. Because of their spatial proximity and equal orientation, they ideally measure the same magnetic field. The smallest SQUID, herein named reference magnetometer, is designed to have an effective area $A_r \approx 0.05\ \Phi_0/\mu T$ small enough to provide a unique voltage-flux characteristic within a desired region of magnetic field strength B_{max}. It therefore acts as an absolute magnetometer as long as the measured magnetic field component B fulfills the condition

$$|B| < \frac{\Phi_0}{2A_r} = B_{max}\,. \qquad (1)$$

The effective areas of the intermediate and the sensitive SQUID are $A_i \approx 3.7\ \Phi_0/\mu T$ and $A_s \approx 334.3\ \Phi_0/\mu T$, correspondingly. The absolute output of the reference SQUID is now used to calculate the branch

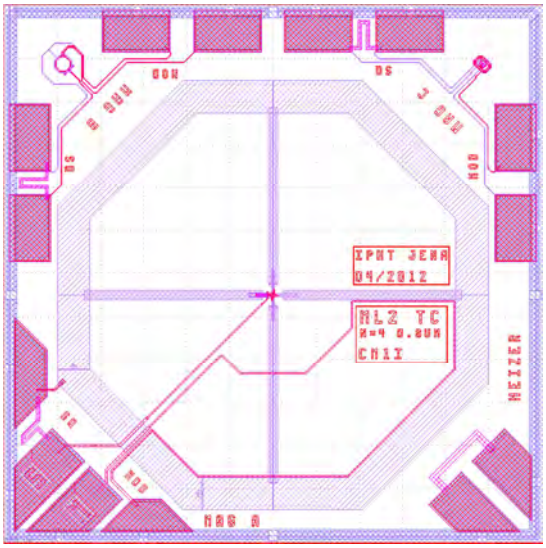

Fig. 1: View of the square 2.5 mm chip with three SQUID magnetometers. The sensitive four loop magnetometer is situated in the centre of the chip. The intermediate and the reference magnetometer are located in the upper and lower right corner, respectively. The chip is equipped with a heater in the upper left corner.

of the voltage-flux characteristic on which the next SQUID in the cascade (the intermediate SQUID) is locked, resulting in a more precise absolute value of the measured magnetic field component. This principle is repeated up to the most sensitive SQUID in the cascade, which determines the noise level of the final measurement value. The white noise level of the sensitive SQUID in our setup is about $B_{n,s} = 6\ fT/Hz^{1/2}$. The dynamic range of the system, defined as the ratio of the maximum peak-to-peak signal amplitude to the achievable signal resolution limited by the noise $B_{n,s}$ in a 1 Hz bandwidth, is about 190 dB.

Absolute magnetometry requires sensors without closed superconducting loops,

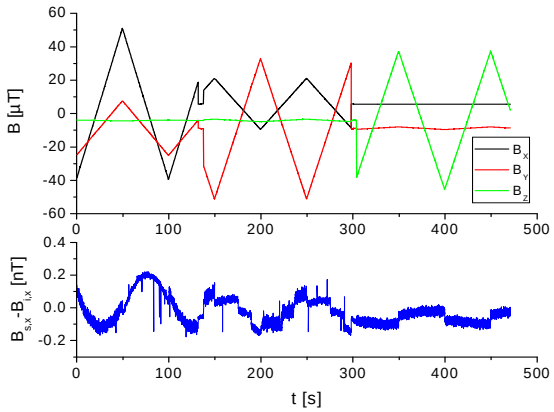

Fig. 2: A magnetic field of ±50 µT was applied with a three-axis Helmholtz coil. After system calibration and all numerical corrections, the difference $B_{s,x}$-$B_{i,x}$ between the x-components of the magnetic field measured by the sensitive and the intermediate SQUID is below ±0.2 nT.

which would freeze an unknown amount of flux during cool down. Thus, our sensors are designed without any flux transformer circuitry. The design of the sensitive magnetometer was previously published as "ML2B" in [1] and is based on the multi-loop magnetometer principle [2,3]. The intermediate and reference magnetometer are washer SQUIDs. All SQUIDs were fabricated with our 0.8 µm cross-type Josephson junctions. Due to their small width, the critical field strength for flux trapping in the junction region could be shifted to 3.9 mT during cool-down [4].

Three such chips have been mounted on a GRP (glass fiber reinforced plastic) cube to realize a three axis absolute vector magnetometer. Early experiments revealed the existence of an on-chip 3 x 3 crosstalk matrix that can be explained by the coupling of each feedback coil to each SQUID of the chip. Furthermore, it turned out that the SQUIDs are also sensitive to magnetic fields parallel to the chip plane. Thus, their effective sensing vectors are not exactly parallel. But, after an extensive characterization of the sensors, a numerical correction of these parasitic effects is possible. We were able to demonstrate the proper work of our setup in a magnetic field with a modulation amplitude of about ±50 µT applied with a three-axis Helmholtz coil (see figure 2). After all corrections, the deviation between the intermediate and the sensitive sensor stage could be reduced to less than ±0.2 nT. The typical inverse effective area of a sensitive SQUID is $A_s^{-1} \approx 2.9\ \mathrm{nT}/\Phi_0$, thus deviations of less than ±1.45 nT assure the correct calculation of the branches on which the sensitive SQUIDs are locked. The current version of data acquisition electronics furthermore guarantees an operation without any remarkable drift within several hours.

However, after a full thermal cycling, a new calibration of the system is necessary. We expect the reason to be caused by small rotations of the sensors due to thermal stress. Our next approach is therefore to directly mount the sensor chips on a silicon cuboid or at least on a material with a similar thermal expansion coefficient. Another issue that needs further investigation is the long term reproducibility of the sensor offsets, which could still be affected by flux trapping in some larger superconducting structures on the chip, like e.g. the washer of the sensitive SQUID or the bond pads.

The author T.S. likes to thank his supervisor Prof. Paul Seidel.

References

[1] M. Schmelz *et al*., Supercond. Sci. Technol., **24,** 065009 (2011).

[2] J. E. Zimmermann *et al*., J. Appl. Phys., **42,** 4483–7 (1971)

[3] D. Drung *et al*., J. Appl. Phys., **77,** 4088–98 (1995)

[5] M. Schmelz *et al*., Supercond. Sci. Technol., **24**, 015005 (2011)

Mechanical loss of thermal silicon oxide layers at low temperatures

C. Schwarz, J. Komma, G. Hofmann, D. Heinert, P. Seidel, and R. Nawrodt

High reflective optics are well known as a possible limiting source of thermal noise in high precision experiments as frequency stabilisation of lasers using cavities [1] or interferometric gravitational wave detectors [2]. These optics gain their high reflectivity from stacks of alternating high and low refractive index material layers. One of these materials is silicon dioxide (SiO_2). To improve the thermal noise performance of these experiments more detailed investigation on the temperature dependent mechanical loss of these dielectric materials are necessary.

In this work we present detailed investigations regarding the mechanical loss of thin thermal oxide layers thermally grown on silicon cantilevers.

For sufficiently high oxidation rates dry nitrogen gas was feed through a gas bubbler filled with water at 92 – 95 °C. Enriched with water vapour the nitrogen gas was then feed in a tube furnace operating at 1090°C. Inside this tube furnace 50 µm thick silicon cantilevers [3] were placed in the gas flow to ensure maximum growth rates for this configuration. This setup allows us to grow oxides layers reaching from a few ten nanometres up to several micrometres.

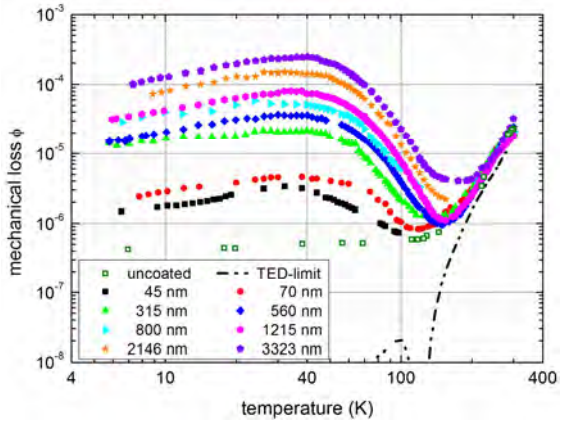

Fig. 1: Temperature dependent loss of a silicon cantilever (green squares) coated with silicon oxide layer reaching from 45 up to 3323 nm in thickness. The resonant frequency was 3.5 kHz @ 300 K.

To determine the mechanical loss φ different mechanical resonances were excited and the free ringdown of the vibration has been recorded. From the exponential amplitude decay the so called ringdown time τ can be assigned. Using π and the resonant frequency f the mechanical loss can be calculated as:

$$\varphi^{-1} = \pi f \tau \,. \qquad (1)$$

Fig. 1 shows the temperature dependent mechanical loss for several different coating thicknesses. Typically the loss of the cantilever is limited by thermo-elastic damping of the pure cantilever material between 150 K and 300 K. Within this temperature region silicon cantilevers are no appropriate coating substrates for the precise identification of the coating loss. At temperatures below 150 K the loss of the coating dominates. Because the total mechanical loss φ_{tot} (as shown in fig. 1) of a coated cantilever consists of different contributions the loss φ_{cant} of the uncoated cantilever needs to be measured separately.

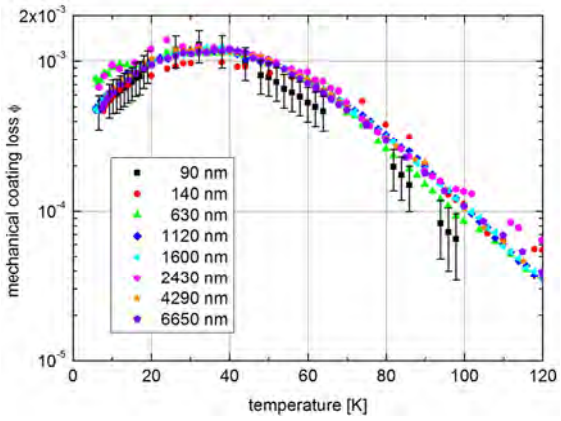

Fig. 2: Calculated mechanical loss φ for different oxide layer thicknesses. The loss of all layers coincides within the exemplarily shown error bars (black) which implies a thickness independent loss.

With the following expression:

$$\varphi_{tot} = \varphi_{cant} + \frac{E_{coat}}{E_{cant}}\varphi_{coat} \qquad (2)$$

and [4]:

$$\frac{E_{coat}}{E_{cant}} \approx \frac{1}{3}\frac{Y_{cant}}{Y_{coat}}\frac{a}{h} \qquad (3)$$

one can then calculate the contribution from the coating. Y_{cant} and Y_{coat} are the Young's modulus of the materials respectively. Eq. (2) assumes that the mechanical energy E_{coat} stored in the coating is much smaller than the energy E_{cant} in the cantilever.

Fig. 2 shows a broad maximum of the mechanical loss around 30 to 40 K for all investigated oxide layers. Furthermore a characteristic shift of the maximum loss with increasing temperature and resonant frequency implies a thermally driven relaxation loss process whose activation energy E_a follows the Arrhenius law. Due to the amorphous arrangement of the atomic composition of the dielectric coating no distinct peak appears as known form crystalline materials [5] but rather a distribution of single peaks.

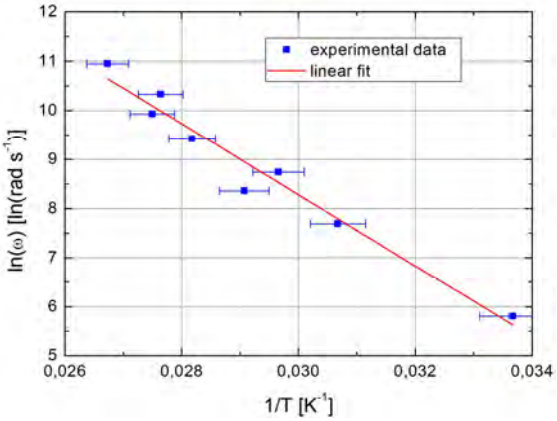

Fig. 3: Arrhenius plot of eight resonant frequencies for an oxide layer thickness of 3323 nm. From the plot an activation energy E_a of 62.3 meV and a relaxation constant τ of 9.5×10^{-14}s can be derived.

Plotting the natural logarithm of the angular frequency of each resonant mode vs. the inverse of the temperature, where the maximum loss occurs, leads to the plot in fig. 3. From the linear fit of the data points the activation energy E_a and relaxation constant τ^* can be derived.

Fig. 4 shows the activation energy E_a as a function of the oxide layer thickness.

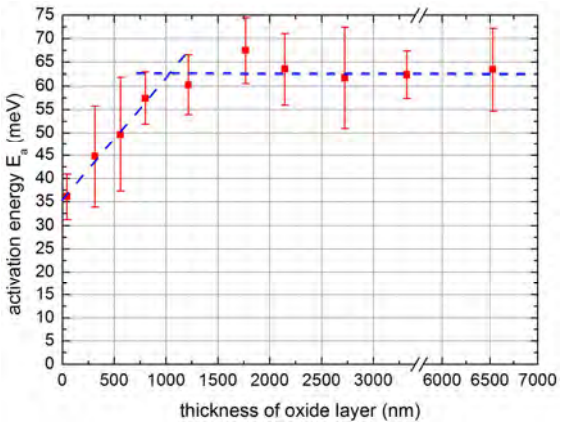

Fig. 4: Variation of the activation energy (red squares) for different oxide layer thicknesses.

The presented data of the relaxation process at low temperatures revealed a linear dependence of the activation energy E_a for layer thicknesses up to $\approx 1\,\mu m$. Above 1µm the values of E_a remain constant at 63 meV for all investigated silicon oxide coatings. Another remarkable effect is the non-vanishing activation energy (35 meV) for layers close to zero nanometres. This means that even under these conditions the mechanical loss of the silicon oxide shows a broad dissipation peak and behaves as the bulk material fused silica [6] does.

This work was supported by the DFG under contract SFB Transregio 7.

References

[1] S. Seel *et al.*,Phys. Rev. Lett **78**, 4741-4744 (1997).
[2] G. M. Harry *et al.*, Class. Quantum Grav. **27**, 084006 (2010).
[3] R. Nawrodt *et al.*, arXiv:1003.2893 (2010).
[4] A. Heptonstall *et al.*, Phys. Lett. A **354**, 353-359 (2006).
[5] C. Schwarz *et al.*, Phys. Status Solidi A **208**, 2719-2723 (2011).
[6] O. L. Anderson and H. E. Bömmel, J. of the American Ceramic Society **38**, 125-131 (1955).

Quasiparticle transport characteristics of superconducting junctions with strongly inhomogeneous tunnel barriers

Vladimir Shaternik[1], Andrej Shapovalov[1], Mikhail Belogolovskii[2], Stefan Schmidt, and Paul Seidel

[1] *G.V.Kurdyumov Institute for Metal Physics, 252680 Kyiv, Ukraine*
[2] *Donetsk Institute for Physics and Engineering, 83114, Donetsk, Ukraine*

Overdamped Josephson junctions with nonhysteretic current-voltage (*I-V*) characteristics are needed for the most part of superconducting digital applications including RSFQ logic circuits and programmable voltage standards. The main advantage of superconductor (S) - normal metal (N) - superconductor trilayers is intrinsic shunting, whereas superconductor – insulator (I) - superconductor (SIS) devices require external shunt resistors which are a large drawback for complex design. At the same time, SNS samples demonstrate lower characteristic voltages, relatively. One of possible compromises can be a fabrication of four-layer SINS junctions with an ultra-thin insulating (I) barrier. The SINS devices can be obtained, in particular, with the standard niobium technology by thickening of the Al interlayer and decreasing the oxidation time [1]. Detailed study of such Nb-Al-AlO_x–*N*b structures has shown that they are intrinsically shunted due to the universal character of the distribution function $\rho_{\rm I}(D)$ of the transmission probabilities *D* for a strongly inhomogeneous oxide barrier. But measured and calculated values of the subgap conductance do not agree very well. The authors of the paper [2] considered SINS heterostructures as a SIS_1 junction where S_1 is an Al layer with superconducting properties induced due to the proximity with a Nb electrode. The function $\rho_{\rm I}(D)$ was taken in the form [3] $\rho_{\rm I}(D) = \hbar\bar{G}\left[e^2 D^{3/2}(1-D)^{1/2}\right]^{-1}$ with $\bar{G} = \int_0^\infty \rho(Z)G(Z)dZ$, the disorder-averaged macroscopic junction conductance, $Z = k_F\int_0^d V(x)dx/E_F$, a fluctuating quantity in an amorphous oxide, $V(x)$ and d are the potential profile and the thickness of the barrier, $k_{\rm F}$ and $E_{\rm F}$ are the Fermi wave vector and Fermi energy in metallic electrodes, $G(Z) = \left(2e^2/h\right)\left(1+Z^2\right)^{-1}$ is the conductance of a normal-state tunnel junction. In this work, we have developed another theoretical approach to the quasiparticle transport in SINS systems, designed and performed its experimental verification with MoRe Josephson junctions and showed the possibility to control the subgap resistance of corresponding junctions.

In contrast to the paper [2] we interpreted such devices as symmetric SIS structures with a complex dirty AlO_x-Al (I-N) transition region. The extra N-metal interlayer with a thickness *s* and transparency $D_{\rm N}(s) < 1$ changes the distribution of transparencies of the weak link between the metal electrodes to $\rho(D_{\rm IN}) = \hbar\bar{G}D_{\rm N}(s)\left[e^2 D_{\rm IN}^{3/2}(D_{\rm N}(s)-D_{\rm IN})^{1/2}\right]^{-1}$ with $0 < D_{\rm IN} < D_{\rm N}(s)$. The most important conclusion which follows from this formula is that in the presence of a dirty metal interlayer the dominating contribution comes not from *D* near unity as in $\rho_{\rm I}(D)$ but from a smaller value $D_{\rm N}(s)$. Hence, there is a maximal value $b < 1$ of the I-N transparency. Its minimal value $a > 0$ is determined by technological constrains as the N-film thickness and the quality of the I-N interface. If the function $\rho(D_{\rm NI})$ is known we can calculate the total quasiparticle current *I* across a planar SINS junction as an integral $I(V) = \int_a^b dD\rho(D)I(V,D)$ with $I(V,D)$ being the current-voltage characteristic of the device with a fixed *D* value. In the following steps we consider *a* and *b* as fitting pa-

rameters found by comparing calculated and measured *I-V* curves.

To verify theoretical expectations, we performed experiments with junctions based on a superconducting MoRe alloy with relatively high critical temperature T_c up to 12 K. MoRe films with 45% Re were deposited onto various dielectric substrates at ambient temperatures using a dc magnetron sputtering technique. Afterwards Sl overlayers with thicknesses between 2 and 30 nm were evaporated at room temperature with various deposition rates v_{dep}. To form tunnel barriers, the MoRe/Al bilayer was oxidized in a vacuum chamber under dry oxygen atmosphere for 10 min and after that a MoRe counter-electrode was deposited through a metal mask. As was evidenced by AFM characterization, the Al interlayer was not totally oxidized and with a significant surface relief which depended on v_{dep} – with its increase the bilayer surface becomes smoother. As a result, the junction transparency varied from point to point and the current I across the heterostructure was strongly inhomogeneous. Thus, the main requirements of our theoretical model were fulfilled in the samples. Numerical simulations of the transport characteristics have been performed following the main lines of a procedure proposed earlier in a few publications (see [2] and references therein). We have calculated amplitudes of quasiparticles from both sides of the scattering region, partial currents $I(V, D)$ for fixed D values, and then the total current $I(V)$ with a function $\rho(D_{IN})$.

In Fig. 1 we compare experimental conductance-vs.-voltage values for the tunnel junctions with numerically calculated characteristics which represent the best fit to the measured data. An excellent agreement between the shape of experimental curves and especially subgap peculiarities at $eV = (2\Delta)/2 = \Delta$ is evident. It can be concluded that an increase of the Al deposition rate results in a more narrow distribution of the junction transparencies. This finding does agree with our AFM observations and can be useful for further optimization of fabrication conditions for MoRe Josephson junctions.

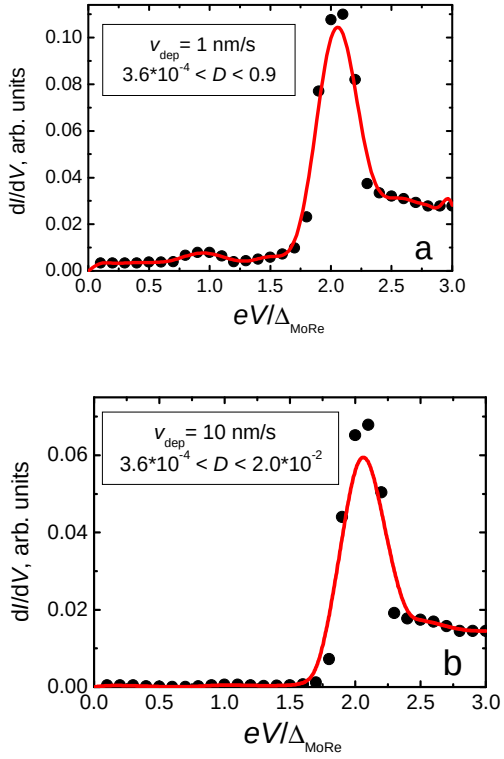

Fig. 1: Conductance-vs.-voltage characteristic of a MoRe-AlO_x-Al-MoRe (SINS) junction with an Al interlayer deposited at rates of v_{dep} = 1 nm/s (a) and 10 nm/s (b); experimental data – points, calculated curves – solid lines. Upper and lower integration limits *b* and *a* in the calculated $I(V)$ characteristics are shown in the graphs, Δ_{MoRe} = 1.5 meV s the MoRe-alloy superconducting energy gap at T = 0 K.

We have studied other possibilities for controlling and tuning the barrier resistivity in MoRe devices, namely, co-sputtering metal and silicon This method was successfully realized in Nb Josephson junctions [4] and, as our preliminary results show, can be applied to MoRe-based Josephson devices.

References

[1] V. Lacquaniti, C. Cagliero, S. Maggi, and R. Steni. Appl. Phys. Lett. **86**, 042501, 2005.

[2] V. Lacquaniti, M. Belogolovskii, C. Cassiago *et al.* New J. Phys. **14**, 023025, 2012.

[3] K. M. Schep, G. E. W. Bauer. Phys. Rev. B ***56***, 15860, 1997.

[4] P. D. Dresselhaus, Y. Chong, S. P. Benz. IEEE Trans. Appl, Supercond. **15**, 449, 2004.

Shapiro steps in the IV-characteristics of coupled Josephson junctions at the double resonance condition

Yu. M. Shukrinov [a;b;c], P. Seidel, E. Il'ichev [d], W. Nawrocki [e], M. Grajcar [f], P. A. Plecenik [f], I. R. Rahmonov [a;g], K. Kulikov [a;c]

[a]*BLTP, Joint Institute for Nuclear Research, Dubna, Moscow Region, 141980, Russia*
[b]*Max-Planck-Institute for the Physics of Complex Systems, 01187 Dresden, Germany*
[c] *Department of Theoretical Physics, International University of Dubna, Dubna, 141980, Russia*
[d]*Institute of Photonic Technology, P.O. Box 100239, D-07702 Jena, Germany*
[e]*Poznan University of Technology, Poznan, Poland*
[f]*Department of Experimental Physics, Comenius University, Bratislava, Slovakia*
[g]*Umarov Physical Technical Institute, TAS, Dushanbe, 734063 Tajikistan*

An important problem on the way of using the intrinsic Josephson junctions (JJ) in HTSC as terahertz electromagnetic waves sources [1] is the synchronization of all junctions in a stack to increase the power of radiation. Intensive attempts to solve this problem are based on using LC-shunting which leads to such synchronization [1, 2, 3]. Let us consider the system, presented in Fig. 1. In normalized units the system of equations,

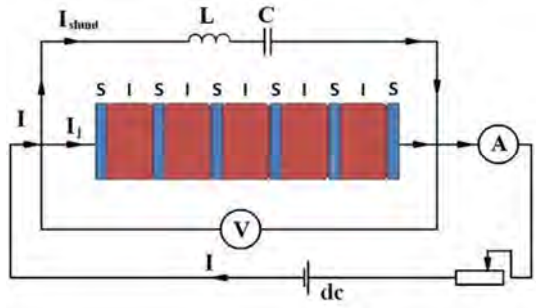

Figure 1. Schema of the JJs stack with LC shunting elements

describing this electric scheme, can be written in the form [4].

$$\begin{cases} \dfrac{\partial \varphi_l}{\partial t} = V_l - \alpha(V_{l+1} + V_{l-1} - 2V_l) \\ \dfrac{\partial V_l}{\partial t} = I - \sin\varphi_l - \beta\dfrac{\partial \varphi_l}{\partial t} - C\dfrac{\partial u_c}{\partial t} \\ \dfrac{\partial^2 u_c}{\partial t^2} = \dfrac{1}{LC}\left(\sum_{l=1}^{N} V_l - u_c\right) \end{cases}$$

Here u_c is the voltage at the capacitance, which is normalized to V_0 . The bias current I is normalized to the critical current I_c of the JJ, time - to the inverse plasma frequency ω_p ; shunt capacitance C_{sh} - to the capacitance of the JJ C_j and denote as C, and shunt inductance L_{sh} -to $(C_j\omega_p^2)^{-1}$ and denote as L .

Let us now consider the influence of the external electromagnetic radiation on the IV-characteristics (IVC) of the investigated system. In the pioneering work of Werthamer and Shapiro [5] was shown that a JJ in a cavity will show additional self-induced resonant steps which lead to subharmonics and some additional structures also in combination with those steps induced by an external microwave frequency. In some cases besides subharmonics also chaotic dynamics was observed [6, 7, 8]. The situation becomes much more complex if an external microwave is taking into account and can result in situations where the chaotic dynamics can be controlled and synchronization of JJ can be improved [9, 10, 11]. Thus we restrict ourself to the question: what would happen with the IVC at the double resonance condition: $\omega_J = \omega_R = \omega_{rc}$. To make it clear we show first IVC of coupled JJs under radiation, but without shunting. In Fig. 2a we present such IVC of ten coupled JJ without

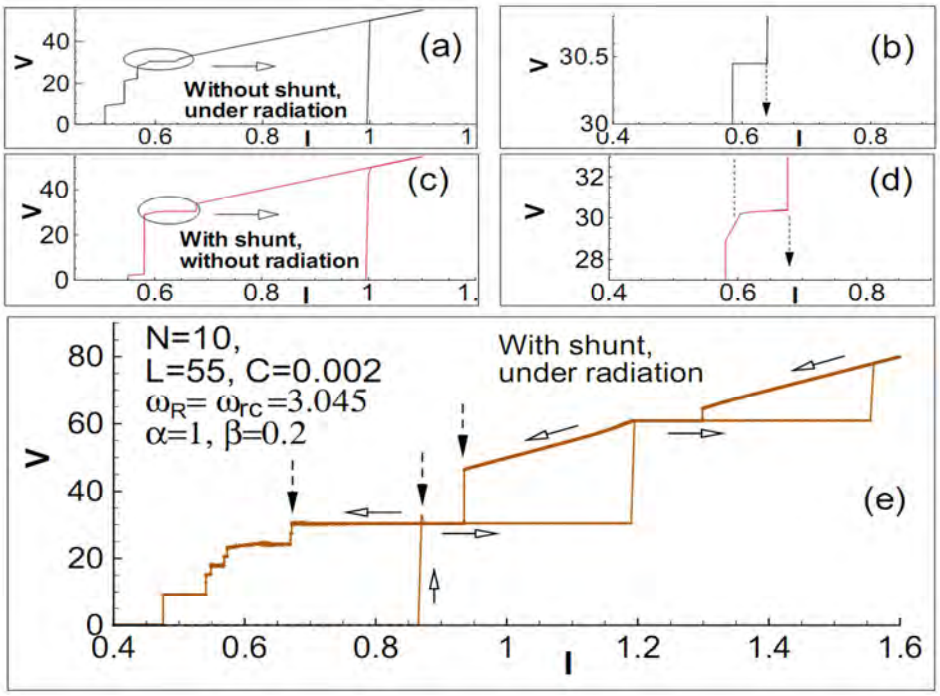

Figure 2. Demonstration of the effect of radiation on shunted coupled JJ at the double resonance condition: (a, b) IVC under radiation, but without shunting; (c, d) IVC with shunting by L = 55 and C = 0.002, but without radiation; (e) IVC at both effects simultaneously.

shunting under external radiation with frequency $\omega_R = 3.045$ and an amplitude $A = 0.5$. As we see, this IVC has a Shapiro step at $V = 30.45$, indicating the external frequency $\omega_R = V/10 = 3.045$. Fig. 2b enlarges this step.

Then we show in Fig. 2c the IVC of ten coupled JJ with shunting by $L = 55$ and $C = 0.002$, but without of external radiation. At this parameters the eigenfrequency of the resonance circuit according to the formula $\omega_{rc} = \sqrt{(1+NC)/LC}$ is equal to 3.045, so IVC has a corresponding rc-branch. Fig. 2d enlarges this rc-branch. Finally we demonstrate both effects simultaneously. In Fig. 2e we see a crucial changes in the IVC when shunting and radiation are both taken into account. Resonance of Josephson and circuit oscillations triggers the appearance of the Shapiro step harmonics and subharmonics. At this resonance the width of Shapiro steps and its harmonics are sharply increased because of the changes in the IVC induced by the rc-branch structure.

References

[1] K.K. Likharev *Introduction to the dynamics of Josephson junctions* Moscow, Izdatel'stvo Nauka 320 pp. (1985) (In Russian).

[2] M. Darula, S Beuven, M. Siegel, A. Darulova and P. Seidel *Appl. Phys. Lett.* **67** 1618 (1995).

[3] A. N. Grib, P. Seidel, J. Scherbel, *Phys. Rev. B* **65** 094508 (2002).

[4] Yu. M. Shukrinov, I. R. Rahmonov and K. Kulikov *unpublished* (2012).

[5] N. R. Werthamer and S. Shapiro Phys. Rev. **164** 523 (1967).

[6] H. Dalsgaard Jensen, A. Larsen and J. Mygind *Physica B* **165-166** 1661 (1990).

[7] D.G. Dempsey, M.T. Levinsen and B.T. Ulrich IEEE Trans. Mag. MAG-11 811 (1975).

[8] N. Calander, T. Claeson and S. Rudner *Physica Scripta* **25** 837 (1982).

[9] M. Bauer, U. Krüger and W. Martienssen *Europhys. Lett.* **9** 191 (1989).

[10] S. K. Dana, D. C. Sengupta and K. D. Edoh *IEEE Trans Circuits Systems* **48** 990 (2001).

[11] S. K. Dana, P. K. Roy, G. C. Sethia, A. Sen and D. C. Sengupta *IEE Proc.-Circuits Devices Syst.* **153** 453 (2006).

Investigation of Arsenic-free Pnictide Superconductors

Stefan Schmidt, Reiner Retzlaff[1], Holger Mühlig, Ondrej Kršk[2], Sandra Gottwals, Sebastian Döring, Frank Schmidl, Lambert Alff[1], and Paul Seidel

[1] *Institute for Materials Science, Technische Universität Darmstadt, 64287 Darmstadt, Germany*
[2] *Department of Experimental Physics, Comenius University, 84248 Bratislava, Slovak Republic*

We present here first electrical measurements on the As-free compound $LaPdSb_2$ with a critical temperature of 2.5 K and a critical current density in the order of $2.4 \cdot 10^4$ A/cm^2 at 350 mK. The introduction of an external magnetic field to change the I-V characteristics shall provide information about whether $LaPdSb_2$ is suitable for devices based on Josephson junctions.

Iron pnictide superconductors have very promising properties regarding future applications. A major disadvantage is the toxicity of some elements in the most prominent compounds, i.e. $LaO_{1-x}F_xFeAs$ (see Fig. 1, La-1111) and $BaCo_xFe_{2-x}As_2$ (Ba-122), which contain arsenic. This disadvantage prevents early application up to now. However, it is possible to substitute arsenic with the much less dangerous phosphorus or antimony.

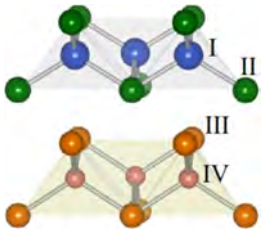

Fig. 1: Crystal structure of 1111-type pnictides [1]. For La-1111 crystal site I is occupied by La, site II by O or its substitute F, III by As, and IV by Fe.

Its crystal structure is similar to the well-known La-1111 and Sm-1111 pnictide superconductors (T_C up to 35 K and 55 K, respectively), which gives rise to the assumption, that antimony substitutes both arsenic (III) and oxygen/fluorine (II), whereas palladium is placed at the iron site (IV). The $LaPdSb_2$ thin films were produced via molecular beam epitaxy (MBE) on MgO substrates by our collaboration partners at TU Darmstadt [2].

Because the critical temperature of the $LaPdSb_2$ thin films is too low for liquid helium dewar measurement, a ^{3}He-measurement setup "Heliox" from Oxford instruments was utilized. Reducing the pressure of liquefied ^{3}He in a pre-cooled liquid ^{4}He environment it is possible to cool the sample down to 300 mK. At the vapour phase transition particles with higher energies will be pumped, preferably. Overcoming the binding energy leads to a reduction of the temperature until $k_BT << E_{bind}$, for ^{3}He at 300 mK. The thermal output of the cooling device is 250 µW at these temperatures, which enables temperature stable measurements for about 2 hours.

To estimate the critical current density of the thin film we firstly confined wide bridges of about 400 µm widths by ion beam etching (IBE; 500 eV beam voltage, 10^{-3} A/cm^2 ion beam density) through a shadow mask. We used this technique to avoid any degradation caused by contact with chemicals during photolithography processes. A critical current density of about $2.4 \cdot 10^4$ A/cm^2 could be observed at 350 mK.

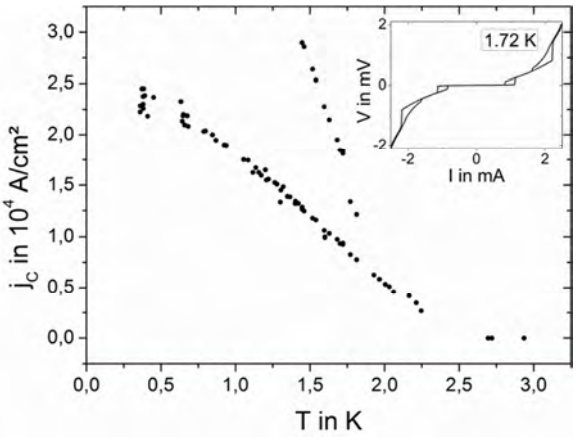

Fig. 2: Temperature dependence of the critical current density of a wide bridge. The upper branch between 1.5 K and 2.0 K denotes a second current jump. The inset a V-I curve where both current jumps are visible.

Its temperature dependence is shown in Fig. 2. In a second step we confined a microbridge with a width of less than 1.7 µm via focused ion beam (FIB) at Comenius University Bratislava, see Fig. 3.

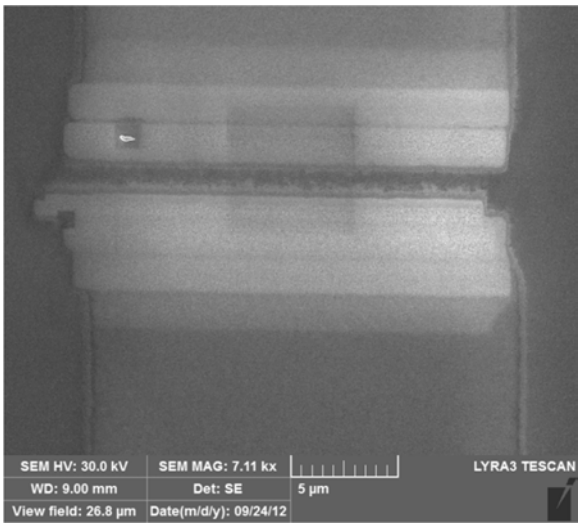

Fig. 3: Scanning electron microscopy image of a microbridge patterned via FIB. The bridge width is less than 1.7 µm, while its length is 19.5 µm.

Measurements after this preparation show decreased values for both T_C (lowered to 1.2 K) and j_C (lowered by one order of magnitude), see Fig. 4. The bump below 1.0 K in the inset of Fig. 4 could be caused by a thermally activated phase slippage. This would give rise to the assumption, that within the small microbridge (Fig. 3) we formed a grain boundary contact. We want to stress, that the critical temperature of the thin film itself was not suppressed by the FIB preparation in contrast to the microbridge area, see Fig 5.

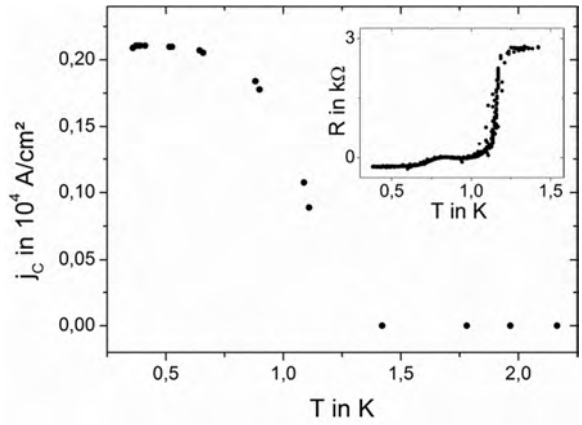

Fig. 4: Temperature dependence of the critical current density of a microbridge. The inset shows the corresponding resistivity dependence near T_C.

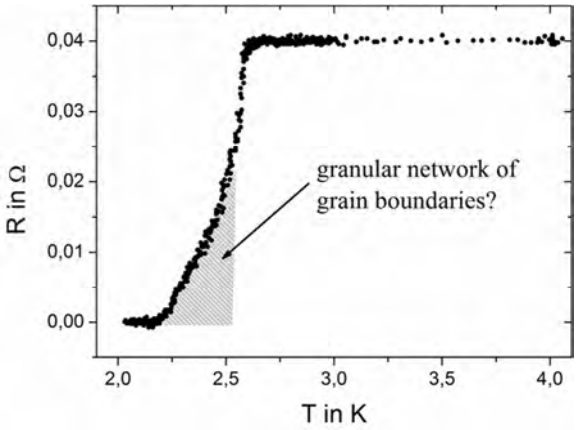

Fig. 5: Resistivity versus temperature of the untouched thin film after preparation via IBE and FIB, subsequently.

The superconducting transition drops steeply at 2.55 K but the slope of the transition gets flatter with lower temperatures. This behaviour can be explained with a network of grain boundaries within the thin film. This confirms the assumption of the occurrence of a microbridge grain boundary. To clarify the origin of these effects magnetic field measurements have to be conducted.
Thus, the magnetic field dependence of the samples was initially investigated by placing a copper wire coil in the head of the measurement stick. A resulting magnetic field with 40 µT (theoretical value) caused a notable decrease of the critical current but also heated the stick head above 600 mK almost instantly due to the high current of 10 mA needed to achieve that magnetic field. A way to introduce an external magnetic field to the thin film sample without heating the setup is currently evaluated.

This work was partially supported by the DFG within SPP 1458 and the Landesgraduiertenförderung Thüringen. We thank Leonid Satrapinskyy and the Bratislava group of Andrej Plecenik for the FIB preparation.

References

[1] K. Ishida, Y. Nakai, H. Hosono, *J. Phys. Soc. Jpn.* 78 (2009) 062001
[2] R. Retzlaff, S. Schmidt et al, *Supercond. Sci. Technol.*, to be published

Size comparison of Au particles embedded in $YBa_2Cu_3O_{7-\delta}$ thin films before and after annealing

M. Westerhausen, C. Katzer, P. Michalowski, V. Tympel, F. Schmidl, M. Rettenmayr[*] and P. Seidel

[*]*Institut für Materialwissenschaften und Werkstofftechnologie, Friedrich-Schiller-Universität Jena, Löbdergraben 32, D-07743 Jena*

The performance of high temperature superconductors is limited by the mobility of flux vortices. Prior investigations have shown that flux noise properties and critical current densities can be improved by adding artificial defects into the lattice [1]. It has been demonstrated that materials like MgO, $BaZrO_3$ and Ir successfully increase the superconductive behaviour of YBCO thin films [2-4]. Our working group uses Au nano clusters in YBCO thin films to achieve similar effects and first measurements show an enhancement on superconductive parameters like an increasing critical temperature T_c, compared to YBCO thin films without Au.

As Au proves to be an excellent material for our intended purpose of tuning YBCO [5], we now observe the behavior of the gold nano clusters under annealing in dependency on the primary Au thickness. We are especially interested in the variation of the distribution and size of the clusters on the surface of our films. The YBCO thin films are deposited onto $SrTiO_3$ (STO) substrates which were choosen because of their perfect lattice matching. The Au is embedded into the superconductor by depositing a 3nm thick Au layer onto the substrate prior to the YBCO deposition, which can be done in situ. We use pulsed laser deposition with a KrF excimer laser for this process for both of the materials Au and YBCO.

Gold thereby is grown under room temperature and in high vacuum conditions ($p_0 < 5 \cdot 10^{-4}$ Pa), whereas the following YBCO thin film needs an oxygen atmosphere of 50Pa and a heated substrate up to 780°C which was found to be the best temperature to assure good superconducting properties. During this process, the Au layer self assembles into single Au nano particles which are distributed homogeneously among the whole YBCO layer.

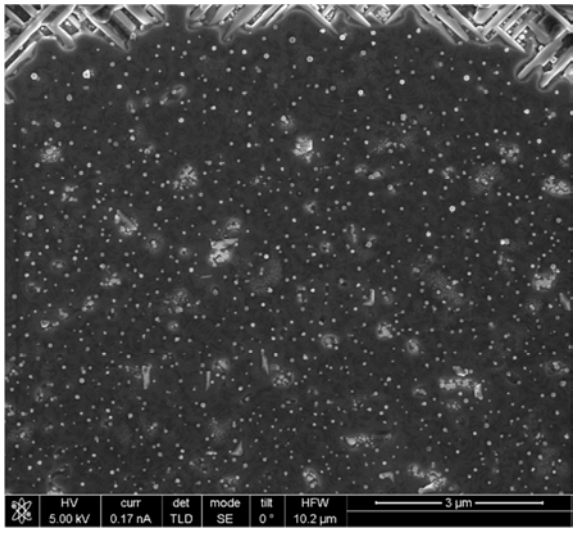

Fig. 1: SEM image of a 150nm thick YBCO thin film, with Au nano clusters on its surface. These result from a formerly 2nm thick Au layer deposited onto the substrate before the YBCO film was grown. This image was taken before annealing the sample.

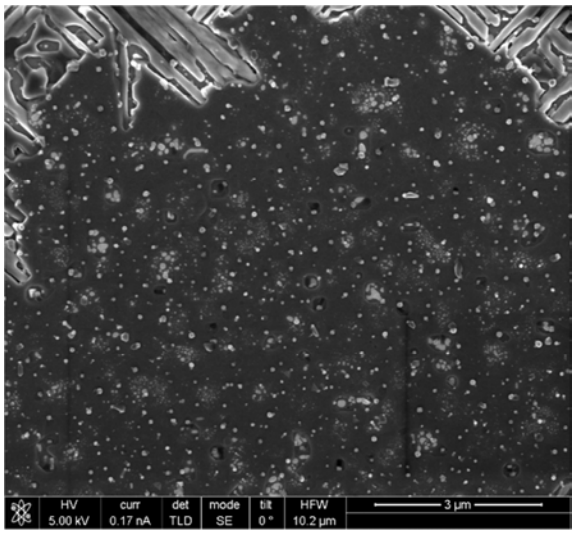

Fig. 2: SEM image of exactly the same sample, as shown in Figure 1 but after annealing at 780°C for 30 minutes.. We managed to observe the same position by using a Ti-layer mask (top of picture) as a marker.

Figure 1 shows an electron microscopy image of a 150nm thick YBCO layer with an underlying prior deposited 3nm thick Au layer. The top of the image shows a Ti marker structure, overgrown with the Au/YBCO composite. This Ti structure was deliberately embedded to allow

an image acquisition before and after annealing at the exact same position on the sample. Therefore one can neglect any inhomogenities and the findings are only due to the heating process. The distribution and the size of the particles on the surface of the film were then evaluated with the imaging software OPTIMAS. It allowed us to count light pixelgroups whereby their shape is factored by roundness and general size.

After this analysis was finished, the sample was subsequently heated to 780°C in the same Oxygen atmosphere used to deposit the YBCO thin film. The result of this particular experiment can be seen in Figure 2, where the Ti mask was used to find the exact same spot on the same sample which was annealed for 30 minutes. The YBCO film clearly shows some defects and the dearranged grown YBCO on the underlying Ti now reaches further into our layer. After analyzing the Au clusters again with the OPTIMAS software and comparing the results, one achieves the data shown in Figure 3.

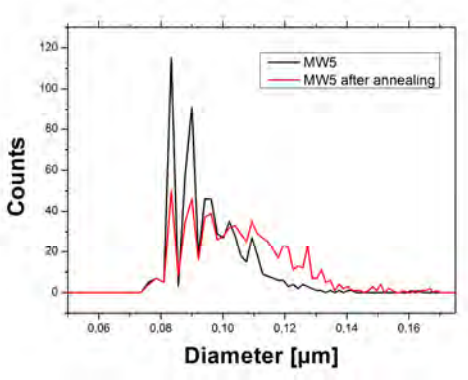

Fig. 3: Size distribution of the Au Nanoparticles on the sample MW5 with an original 2nm thick Au layer and 150nm YBCO on top. The sample has been tempered at 780°C for 30 minutes.

It seems that the annealed substrate inherits less Au clusters on its surface. However the distribution of the diameter seems to be enhanced in favor of bigger Au nano crystals.

After these material considerations, we also analysed electrical properties of YBCO thin films in dependence of the underlying gold layer thickness. We were in particular interested in the behavior of the critical current density of YBCO thin films interspersed with Au nano particles. One has to guarantee the thickness of the Au layer, so next to the used STO samples, it is also sputtered onto Si substrates which are prior deposited with comb structures. The thickness of the gold layers on the silicon waver, which are now the same as on our STO samples can be analyzed afterwards with GWYDDION [6] based on AFM images. The process of depositing YBCO is still the same. However we now have to structure the Au/YBCO layers to achieve 3-5µm thick bridges by photolithography. Before the critical current density can be scaled, the rest around the YBCO bridges is now removed by ion beam etching. The measurement itself is done in liquid nitrogen to ensure the YBCO layers have reached their superconductive state.

These experiments are still ongoing, so a closer lookup on the exact results can not be given, however it seems that the quality of the YCBO variates locally over one substrate. The reason is probably due to the local arrangement of the plasma torch during the pulsed laser deposition process of manufacturing the YBCO thin films. To get a better picture of this, big samples of 10x10mm are now being used and later analysed in their critical current density. With this knowledge the results of the dependency to the Au layer thickness will be reinterpreted.

Acknowledgment

C. Katzer would like to thank the Landes-graduiertenförderung Thüringen for financial support.

References

[1] Mikheenko, P., Sarkar, a., Tanner, J. L., Awang Kechik, M. M., Abell, J. S., & Crisan, a. (2009). IEEE Transactions on Applied Superconductivity, 19(3)

[2] T. Aytug, M. Paranthaman, K. J. Leonard, K. Kim, A. O. Ijaduola, Y. Zhang, E. Tuncer, J. R. Thompson, and D. K. Christen, J. Appl. Phys. 104, 043906 (2008).

[3] T. Aytug, M. Paranthaman, K. J. Leonard, S. Kang, P. M. Martin, L. Heatherly, A. Goyal, A. O. Ijaduola, J. R. Thompson, D. K. Christen, R. Meng, I. Rusakova, and C. W. Chu, Phys. Rev. B 74, 184505 (2006).

[4] F. J. Baca, P. N. Barnes, R. L. S. Emergo, T. J. Haugan, J. N. Reichart, and J. Z. Wu, Appl. Phys. Lett. 94, 102512 (2009).

[5] Katzer, C., Schmidt, M., Michalowski, P., Kuhwald, D., Schmidl, F., Grosse, V., Treiber, S., et al. (2011). EPL Europhys. Lett., 95(6), 68005.

[6] GWYDDION, SPM data visualization and analysis tool by D. Necas et al., http://gwyddion.net

Optical Characterization of Conducting Zinc Oxide Thin Film Coatings by Combustion CVD at Atmospheric Pressure

I. Zunke[1], A. Heft[1], B. Grünler[1], and P. Seidel

[1] Innovent e.V. Technology Development, Prüssingstr. 27B, 07745 Jena

As n-type II-VI semiconductor, zinc oxide (ZnO) has a wide direct band gap of about 3.37 eV [1] at room temperature. As a consequence of this, it has a high optical transparency in the visible and near infrared range.

Several techniques for producing ZnO films in vacuum are well known. The thin films shown here were prepared using a combustion-CVD process working under atmospheric pressure conditions. A zinc nitrate solution (0.2 M) was used and reacts within the combustion flame, which provides the energy and reacting species and forms the thin film. The influence of the substrate temperature (while deposition) on the optical properties was investigated.

Up to a wavelength in the ultraviolet range the engaging photons have enough energy for the fundamental excitation of the electrons. The corresponding energy correlates to an undoped crystal with the band gap $E_{g,}$ which is the minimal energy required to excite an electron from the valence band to the conduction band. In the visible wavelength range, the photons have insufficient energy for the excitation of the electrons. The transmittance rapidly increases and is almost constant up to a wavelength of approximately 1000 nm. The measured transmission on air of ZnO coated glass substrates is primary limited in this wavelength range by losses due to vertical and diffuse reflectance at the interfaces between ZnO, glass and the environment, which depends on the refractive indices of the materials involved and the roughness of the boundary surfaces.

Fig. 1 shows the optical transmission spectra for ZnO films coated at different substrate temperatures. The optical transmission is independent of the substrate temperature and approximately 82 % for all samples, which is in agreement with ion beam sputtered ZnO films [2].

Due to the fact that ZnO is a direct band gap semiconductor, the optical absorption coefficient α can be estimated by $\alpha(E) \sim (E_{Ph} - E_g)^{1/2}$, where E_g is the band gap and $E_{Ph} = h\nu$ the photon energy. By plotting α^2 versus E_{Ph} one can determine the gap energy by extrapolating the linear part of the plot to the energy axis. From optical transmission spectra the absorption coefficient α is calculated using the Lambert-Beer law $\alpha = \ln(100/T) / d$ where T is the transmission and d the thickness of the film. The band gap determination is performed for three substrate temperatures and is also shown in figure 1; the optical band gap decreases with higher substrate temperature. Highest gap energies of

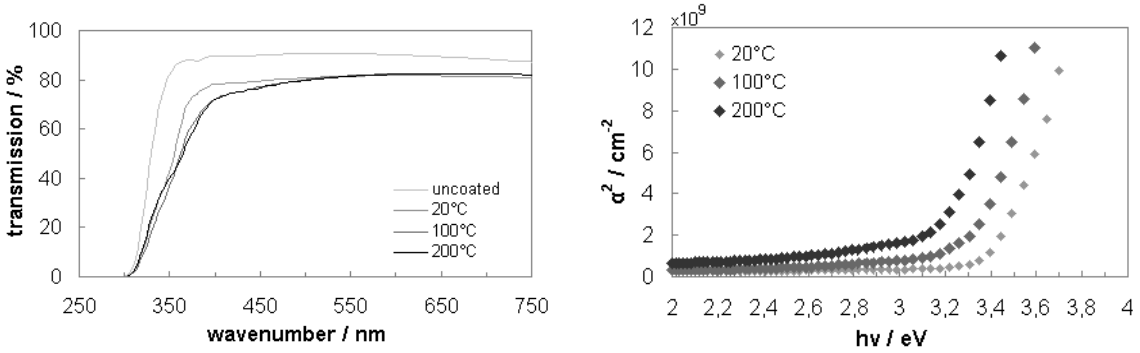

Fig. 1: Transmission spectra (left) and band gap determination (right) of ZnO films grown at 20 °C, 100 °C, and 200 °C. An uncoated glass substrate is also shown as reference for comparison.

(3.45 ± 0.05) eV are achieved at 20 °C. When increasing the substrate temperature to 100 °C the gap energy decreases to (3.34 ± 0.05) eV. Further heating to a substrate temperature of 200 °C leads to a decrease in the gap energy to (3.20 ± 0.05) eV. As known from atomic force microscopy investigations, the grain size distribution changes with the substrate temperature. With increasing temperature the ZnO films become more dense and crystalline. Thus the number of grain boundaries decreases for the samples grown at higher temperatures, which may act as scattering centres and constrain the electrons. The crystallinity of the films was also proved by X-ray diffraction and Raman Spectroscopy.

Additionally detailed infrared transmission spectra in the range of 50 cm^{-1} to 650 cm^{-1} were taken and are shown in figure 2. A band around 408 cm^{-1} to 413 cm^{-1} assigned to the E_1 TO mode of ZnO [3] can be seen. The substrate material as reference is also shown to estimate the noise. Baseline correction, fitting two Gaussian curves and subsequent derivation of the fit lead to the exact peak positions. Additionally the height and full width at half maximum (FWHM) values of the peaks were estimated for the three spectra and the single fitted curves. As can be seen in figure 2 the peak height increases with increasing substrate temperature during the coating process and gets also sharper as

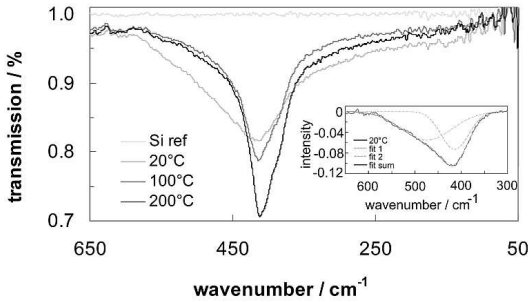

Fig. 2: IR spectra in the range of 50 – 650 cm^{-1} of ZnO films grown at 20 °C, 100 °C, and 200 °C. An exemplary fit of two Gaussian curves for the spectrum of the 20 °C sample is also shown as inset.

indicated by the decreasing FWHM values. This indicates a more crystalline structure with higher substrate temperature. The peak position also changes with higher temperatures from (421.2 ± 0.5) cm^{-1} at 20 °C to (410.4 ± 0.5) cm^{-1} at 200 °C. The fact that two curves are fitted lead to the assumption that two different superimposing features are identified. The intensity considerably increases for the first feature, while the intensity of the second one is almost not changing. The first feature around 403 cm^{-1} may be assigned to the E_1 TO mode, due to the fact that the intensity is clearly higher than that of the second feature. Additionally it is known from ellipsometric studies that the films contain certain dopants, stemming from the precursor chemical or the burner system used. The change to lower frequencies may be explained by these dopants, which cause lattice distortion. This shift was already observed in several doped ZnO nanoparticles [4, 5]. The second feature also moves to lower wavenumbers but the intensity is slightly changed. It may originate from the precursor solution.

The films presented show good transmission of 82 % and the band gap can be changed easily by changing the substrate temperature during the growth process. FT-IR spectroscopy confirmed the presence of crystalline ZnO.

This work was supported by the BMWi (VF090055) and the semiconductor physics group of Prof. Zahn at the TU Chemnitz.

References:

[1] A. Janotti, C. G. Van de Walle, Rep. Prog. Phys. **72** (2009) 126501
[2] A. El Amrani et al., Thin Solid Films **518** (2010) 4582
[3] H. Morkoç, Ü. Özgür, Zinc Oxide - Fundamentals, Materials and Device Technology, Wiley, 2009
[4] L. N. Dem'yanets et al., Inorg. Mater. **47** (2011) 649
[5] M. Ghosh et al., J. Appl. Phys. **106** (2009) 084306

Polyynyl-Substituted Polycyclic Aromatic Hydrocarbons

Gaël Rouillé, Cornelia Jäger, Mathias Steglich, Friedrich Huisken, and Thomas Henning

Polycyclic aromatic hydrocarbon (PAH) molecules are studied in various contexts. While they are toxic pollutants of our environment, their electronic, optical, and self-organizing properties make them attractive materials for nanotechnologies. Our own interest for this family of molecules stems from their presence in the interstellar medium (ISM).

After interstellar PAHs were revealed by the analysis of IR emission bands, they were proposed as contributors to other phenomena, namely, the Extended Red Emission, the Blue Luminescence, the UV Bump in the interstellar extinction curve at 2175 Å [1], and, last but not least, the diffuse interstellar bands (DIBs). The DIBs are about 400 absorption features observed between 4000 and 20,000 Å against the light of background stars. They are caused by interstellar molecules, which have yet to be identified *90 years after the first DIB was detected*. To date, the lack of strong evidence linking the DIBs with one another suggests that each of them is caused by a different molecule or carrier.

The abundance of PAHs in space, their suspected variety [1,2], and their $\pi \rightarrow \pi^*$ electronic transitions that can give rise to absorption bands in the visible domain made these molecules attractive candidates for the carriers of the DIBs. In general, however, the absorption spectrum of PAHs comprises bands in the UV region, the so-called β bands, which are stronger than those arising at longer wavelengths, and these bands are utterly absent from observations towards sightlines that feature DIBs [2].

Given the points in favor of PAHs as candidates for the carriers of the DIBs, we endeavored to measure the UV/vis spectra of a family of their derivatives, that is to say, polyynyl-substituted PAHs [3]. The

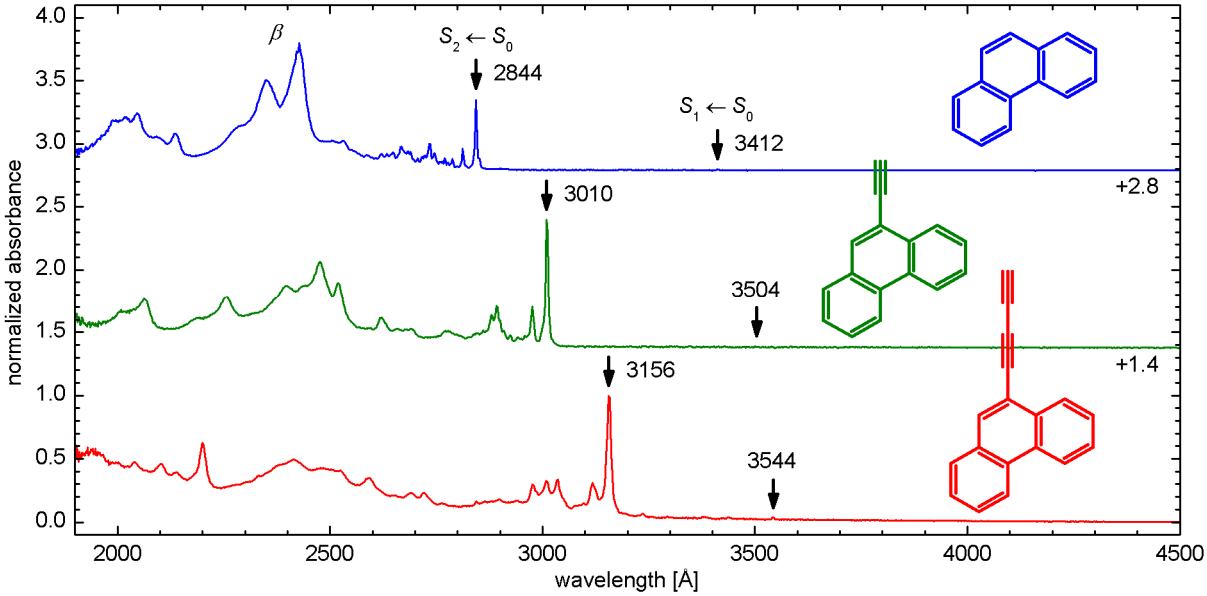

Fig. 1: From top to bottom, the absorption spectra of phenanthrene, 9-ethynylphenanthrene, and 9-butadiynylphenanthrene isolated in Ne matrix at 6 K. With the addition of a polyynyl side chain and the increase of its length, the electronic transitions $S_1 \leftarrow S_0$, $S_2 \leftarrow S_0$, and β are shifted toward longer wavelengths. Most remarkable, the origin band of the $S_2 \leftarrow S_0$ transition becomes the dominant feature while the β band disappears due to broadening.

substitution with polyynyl chains was chosen compared to, e.g., methyl groups, because the DIB spectra do not show clear indications of internal rotations or floppiness. Moreover, bond conjugations between the polyynyl chain and the aromatic moiety are expected to provide polyynyl-substituted PAHs with a higher photostability than that of methyl derivatives, allowing them to better withstand the interstellar UV photon flux.

We have measured the UV/vis spectra of phenanthrene, anthracene, pyrene, and a selection of their ethynyl and butadiynyl derivatives [3]. The measurements were carried out on molecules isolated in Ne matrix at 6 K. Although the conditions are not those of the ISM, except for the temperature, this technique allows us to work with small amounts of material and to scan extended wavelength ranges in a reasonable time. The interaction between the Ne atoms and the PAH molecules is sufficiently weak to exploit the spectra in a first approach and to prepare high accuracy measurements at low temperature in the gas phase.

The spectra of phenanthrene and of its 9-ethynyl and 9-butadiynyl derivatives are shown in Fig. 1. None of these molecules can be a DIB carrier since all their absorption bands are found in the UV domain whereas DIBs lie in the vis and near IR regions. Larger aromatic moieties, however, would give rise to bands at longer wavelengths. Most interesting is the effect of the substitution of a H atom with a polyynyl chain on the spectrum of a PAH. As demonstrated in Fig. 1 with phenanthrene, the substitution causes a notable shift of the bands of the $S_1 \leftarrow S_0$ and $S_2 \leftarrow S_0$ transitions towards longer wavelengths. It also causes the broadening of the β band and the spectacular lowering of its peak intensity. Consequently, in the spectrum of 9-butadiynylphenanthrene, the origin band of the $S_2 \leftarrow S_0$ transition is the dominating feature.

Thus, the spectrum of polyynyl-substituted PAHs can exhibit a dominating band corresponding to a transition of lower energy while the β band is broadened to such an extent that its detection becomes extremely difficult. We can then conclude that polyynyl-substituted PAHs are better candidates for the carriers of the DIBs than normal PAHs. This result supports the need for research on the photophysical properties of substituted PAHs.

Several of the species we have studied are not commercially available. Our work would not have been possible without the collaboration with Prof. Knölker and his coworkers who synthesized the compounds of interest.

This work was carried out within a collaboration between the Max-Planck-Institut für Astronomie, the Friedrich-Schiller-Universität Jena, and the Technische Universität Dresden.

References

[1] M. Steglich *et al.*, Astron. Astrophys. **540**, A110 (2012).
[2] R. Gredel *et al.*, Astron. Astrophys. **530**, A26 (2011).
[3] G. Rouillé *et al.*, Astrophys. J. **752**, 25 (2012).

Polycyclic Aromatic Hydrocarbons and Interstellar Extinction

Mathias Steglich, Cornelia Jäger, Friedrich Huisken, and Thomas Henning

Polycyclic aromatic hydrocarbons (PAHs) are ubiquitous in space and altogether constitute the most abundant group of interstellar molecules. Like any interstellar material, they must contribute to the extinction of the light emitted by background stars. Spectroscopic studies of the extinction curve at UV wavelengths, however, have not revealed bands one could assign to the $\pi \rightarrow \pi^*$ transitions that characterize PAH molecules [1].

In order to explain this apparent paradox, we have measured the UV/vis absorption spectra of mixtures of medium- and large-sized PAHs [2,3]. These measurements were completed with theoretical spectra derived from the results of calculations using the semiempirical model ZINDO.

The PAH mixtures were extracted from soots formed in the gas phase by the condensing products of the laser-induced pyrolysis of ethylene (C_2H_4). By this means, mixtures containing a very large number of different PAHs were produced, as evidenced by matrix-assisted laser desorption/ionization coupled with time-of-flight mass spectrometry (MALDI-TOF) [3]. The great variety of PAH molecules constituting the mixtures was also observed with high-performance liquid chromatography (HPLC), albeit with a lower resolution [2,3]. Beside its role as an analytical tool, the chromatograph allowed us to separate the primary mixtures in fractions characterized by different size distributions. For instance, for our most recent study we prepared secondary mixtures composed of PAHs containing approximately up to 22, 22 to 32, and more than 32 C atoms [3].

The UV/vis absorption spectrum of the secondary mixtures was measured at room temperature after having prepared thin films of the molecules that composed them and also at cryogenic temperature (~6 K) after having isolated the molecules in Ne matrices, as illustrated with Fig. 1. Both procedures required first the transfer of the molecules into the gas phase, which was achieved using two techniques, namely, thermal heating and laser vaporization.

The absorption spectra of the fractions showed that the presence of a sufficiently large number of different PAHs of medium

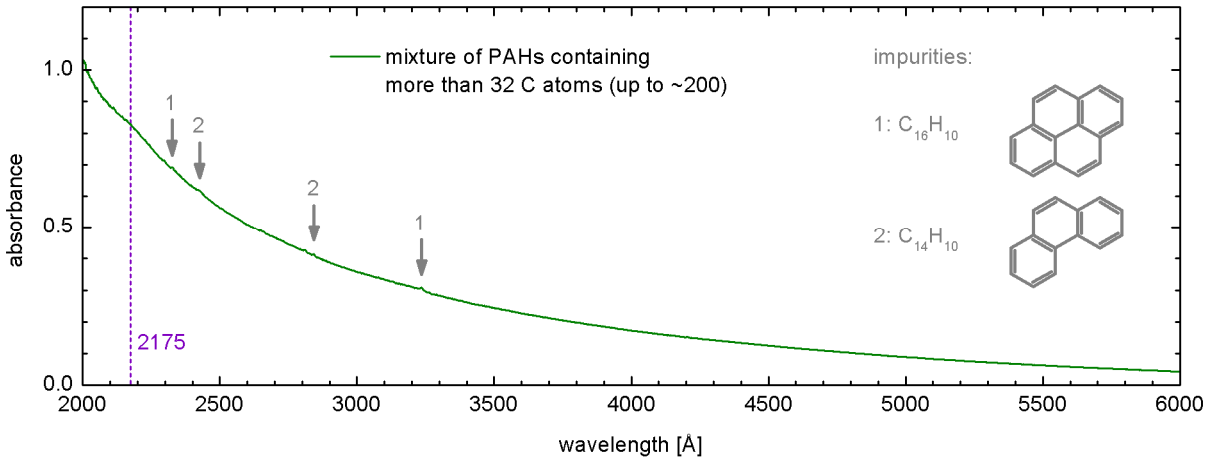

Fig. 1: The smooth UV/vis absorption spectrum of a mixture of PAHs containing more than 32 up to ~200 C atoms isolated in Ne at 7 K. The very weak peaks are caused by impurities such as pyrene (1) and phenanthrene (2). A size distribution favoring molecules containing 50 to 60 C atoms would cause a bump near 2175 Å [2].

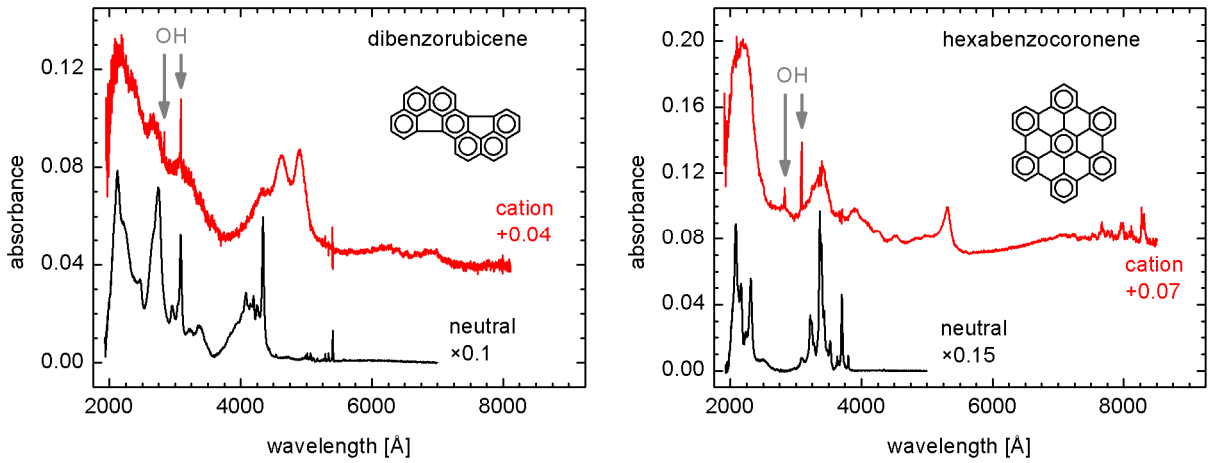

Fig. 2: The UV/vis absorption spectra of dibenzorubicene, hexa-*peri*-hexabenzocoronene, and their cations isolated in Ne at 7 K. The cations were produced by VUV irradiation of the neutral molecules using a H_2 lamp. This procedure caused simultaneously the photodissociation of H_2O molecules present as impurities, resulting in the observation of OH radicals.

and large sizes can result in a smooth extinction curve devoid of narrow features at wavelengths longer than 2500 Å (Fig. 1). Furthermore, the theoretical spectra indicated that a size distribution favoring molecules containing 50 to 60 C atoms would cause a bump near 2175 Å. As small PAHs are expected to be dissociated by the interstellar UV photon flux, only large PAHs should be present in the interstellar medium. We propose that these large molecules, free flying or possibly adsorbed on the surface of grains, cause or contribute to the smooth baseline of the extinction curve and its bump at 2175 Å [2,3].

After having studied the contribution of neutral PAHs to the interstellar extinction, we have evaluated the role played by their ions [4]. For this purpose, we measured the UV/vis spectra of two medium-sized PAHs and their cations isolated in cryogenic Ne matrices. With regard to their anions, information was obtained by carrying out calculations using the density functional theory (DFT). The molecules selected for this study were dibenzorubicene ($C_{30}H_{14}$) [4,5] and hexa-*peri*-hexabenzocoronene ($C_{42}H_{18}$) [4,6]. Their structures and their UV/vis spectra are displayed in Fig. 2.

Comparing the measured and theoretical spectra with the interstellar extinction curve, we conclude that, like the neutral PAHs, the ions can contribute to the UV bump at 2175 Å. The presence of ions along the neutral PAHs further increases the variety of these species, in agreement with our interpretation of the smoothness of the interstellar extinction curve and its UV bump.

This work was carried out within a collaboration between the Max-Planck-Institut für Astronomie, the Friedrich-Schiller-Universität Jena, and the Max-Planck-Institut für Polymerforschung.

References

[1] R. Gredel *et al.*, Astron. Astrophys. **530**, A26 (2011).
[2] M. Steglich *et al.*, Astrophys. J. **712**, L16-L20 (2010).
[3] M. Steglich *et al.*, Astron. Astrophys. **540**, A110 (2012).
[4] M. Steglich *et al.*, Astrophys. J. **742**, 2 (2011).
[5] G. Rouillé *et al.*, ChemPhysChem **12**, 2131-2137 (2011).
[6] G. Rouillé *et al.*, J. Chem. Phys. **131**, 204311 (2009).

3. Technical Reports and Equipment

Operation of the ion-accelerator JULIA and the ion-implanter ROMEO

U. Barth, F. Jehn, G. Lenk, W. Wesch, C. Ronning

The 3 MV high current tandetron accelerator **JULIA** (***J***ena ***U***niversity ***L***aboratory for ***I***on ***A***cceleration) went in operation end of 1996. Since the beginning of the routine-operation in 1997 it has been used for different types of experiments requiring a broad spectrum of ion-beams. With the exception of helium, where the duoplasmatron ion-source followed by a lithium exchange channel was used, all ions were extracted from a sputter-type ion-source. The beam-on-target-time of 1356 h was about 10% higher than in 2010. The 400 kV ion-accelerator **ROMEO** is in routine operation since 1998, here the beam-on-target-time of 1190 h was in the same order of magnitude as in the preceding years.

Both accelerators can be operated separately or in combination. The ion-beams produced until 2011 are summarized in table 1. The ion-beam currents quoted are typical values of the ion source currents used for the experiments, the maximum currents available are significantly higher for most ions.

Period	Element	Julia	Romeo
1	Hydrogen (H)	5 µA	4 µA
	Helium (He)	0,2 µA	4 µA
2	Lithium (Li)	2 µA	1 µA
	Boron (B)	0,2 µA	5 µA
	Carbon (C)	9 µA	1 µA
	Nitrogen (N)	10 µA	4 µA
	Oxygen (O)	17 µA	2 µA
	Flourine (F)	-	2 µA
	Neon (Ne)	-	5 µA
3	Sodium (Na)	-	6 µA
	Magnesium (Mg)	-	5 µA
	Aluminium (Al)	-	4 µA
	Silicon (Si)	16 µA	4 µA
	Phosphorus (P)	-	4 µA
	Chlorine (Cl)	-	2 µA
	Argon (Ar)	-	20 µA
4	Potassium (K)	-	3 µA
	Calcium (Ca)	-	5 µA
	Titanium (Ti)	0,7 µA	-
	Vanadium (V)	0,2 µA	1 µA
	Manganese (Mn)	0,017 µA	5 µA
	Chromium (Cr)	0,2 µA	3 µA
	Iron (Fe)	0,8 µA	2 µA
	Cobalt (Co)	-	3 µA
	Nickel (Ni)	-	6 µA
	Copper (Cu)	0,5 µA	-
	Zinc (Zn)	1 µA	6 µA
	Gallium (Ga)	1 µA	3 µA
	Germanium (Ge)	1,6 µA	4 µA
	Arsenic (As)	0,4 µA	1 µA
	Selenium (Se)	0,5 µA	1,5 µA
	Bromine (Br)	19 µA	8 µA
	Krypton (Kr)	-	10 µA
5	Rubidium (Rb)	0,075 µA	1 µA
	Strontium (Sr)	-	3 µA
	Yttrium (Y)	-	4 µA
	Zirconium (Zr)	0,3 µA	1,5 µA
	Rhodium (Rh)	0,2 µA	-
	Palladium (Pd)	0,095 µA	1 µA
	Silver (Ag)	1,6 µA	10 µA
	Cadmium (Cd)	-	0,8 µA
	Indium (In)	5 µA	8 µA
	Tin (Sn)	-	3 µA
	Antimony (Sb)	0,6 µA	4 µA
	Tellurium (Te)	-	2 µA
	Iodine (I)	3 µA	-
	Xenon (Xe)	-	10 µA
6	Caesium (Cs)	-	4 µA
	Barium (Ba)	-	1 µA
	Praseodymium (Pr)	-	1 µA
	Neodymium (Nd)	-	0,5 µA
	Samarium (Sm)	0,01 µA	1,5 µA
	Europium (Eu)	0,035 µA	2 µA
	Gadolinium (Gd)	0,03 µA	-
	Terbium (Tb)	-	3 µA
	Erbium (Er)	0,04µA	2µA
	Tantalum (Ta)	0,2µA	2 µA
	Tungsten (W)	0,3µA	0,01µA
	Osmium (Os)	0,05 µA	-
	Iridium (Ir)	0,3µA	6 µA
	Platinum (Pt)	0,2µA	-
	Gold (Au)	24µA	20µA
	Lead (Pb)	0,035 µA	15µA
	Bismuth (Bi)	-	3µA

Table 1: Ion-beams accelerated during 2011. The currents given are measured at the Q-Snout-Faraday-cup after the low-energy mass separator (JULIA) and at the target position (ROMEO), respectively.

As in the preceding years the ion-beam facility was used by external research groups:

3MV-Tandetron „JULIA”

University Jena
IPHT Jena (Dr. Diegel)
ITN Lissabon (Dr. Lorenz)
University of Oslo (Dr. Azorov)
Firma Layertec (Herr Heyer)

400kV Implanter „ROMEO“

University Jena
University of Pretoria (Prof. Malherbe)
University of Pretoria (Prof. Friedland)
University Minsk (Prof. Kamerow)
ITN Lissabon (Dr. Lorenz)
University of Oslo (Dr. Azorov)

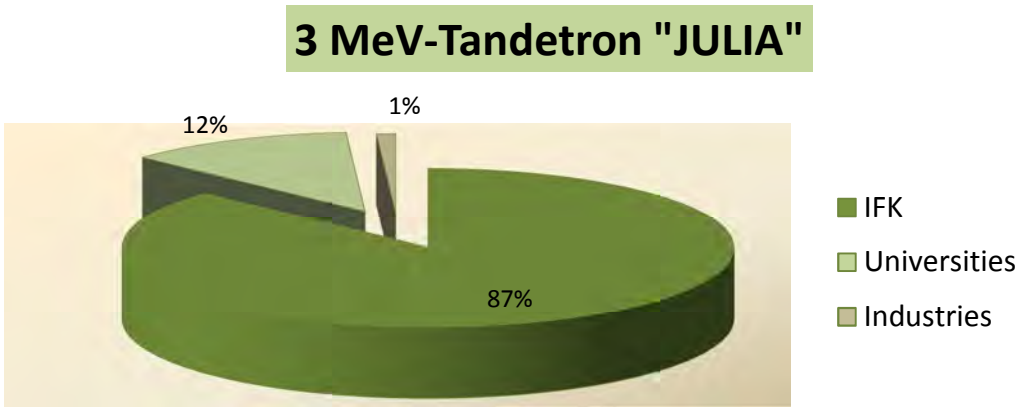

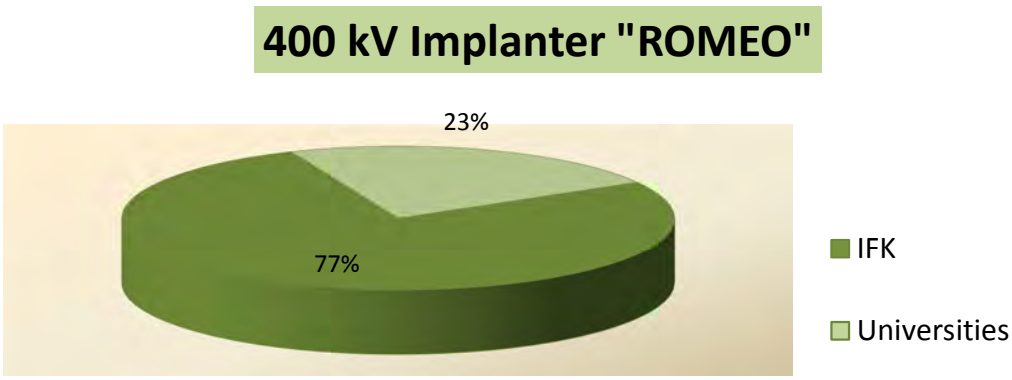

Cryogenic Services (TTS)

All in-house customers of cryogenic liquids, which are all faculties of natural sciences, the university medical division including several hospitals, and other external scientific institutes (e.g. Institute for Photonic Technology Jena, Leibnitz Institute Hans-Knöll Jena) as well as some private customers like the Innovent e.V. Jena and some medical practices, were provided with liquid helium (LHe), with high purity gases (He, N_2), and with liquid nitrogen (LN_2) by the Cryogenic Services. Roughly 123,000 litres of LN_2 were delivered by the cryogenic services in 2012. The total delivery has levelled off in the recent two years due to the stable operation mode in the IAAC-institute.

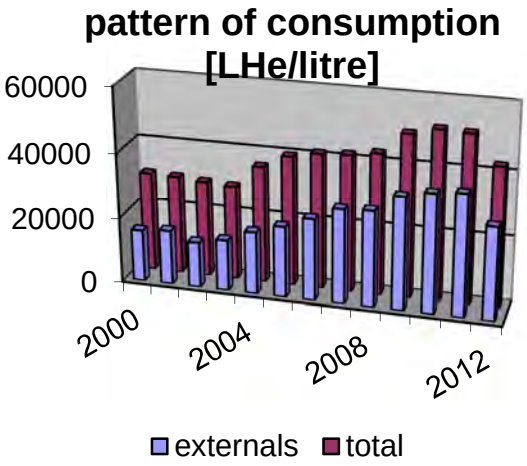

Fig. 1 Liquid helium output

As illustrated in Figure 1, the output of liquid helium (LHe) has decreased vastly in 2012. Merely 35,000 litres of LHe were delivered which calls for an annual gross refrigeration value of just 42,600 litres. Last year we had to face a worldwide shortage in helium supplies which leads generally to increased costs with considerable fluctuations of the fees over the year. On the crest of the wave the costs for short term LHe-orders have increased by a fivefold. In addition the long-term delivery contracts conditions with fixed prices weren't fulfilled by the suppliers relating to the delivered quantity. Therefore the financial weakness and supply shortfall caused a strong reduction in LHe-use. Fortunately the relation between the produced quantity of LHe to the bought quantity was a good deal bigger than all previous years. This was possible due to the increased efforts of the LHe-users to decrease He-losses.

Fig. 2 Recovery-unit at the university observatory

In order to support these efforts our focus had been on rebuilding recovery equipment to gain more gaseous Helium for repeated liquefaction. For instance the TTS-staff overhaul a machinery that was so far used by the Chemical Faculty at the Tatzend-site which was ready for scrapping. The recovery-unit is operating successfully at the Astrophysical Institute at the Schillergässchen-site now (Fig.2).

Equipment

Preparation of Thin Films and Devices

- HV evaporation facilities for thermal and electron beam evaporation
- UHV evaporation facilities, including electron gun and in situ RHEED system
- Equipment for laser deposition of thin crystalline films and material systems, especially high temperature superconductors (KrF excimer laser, $\lambda = 248$ nm)
- Molecular Beam Epitaxy (MBE) facilities: MBE for silicon carbide (RIBER EVA 32 R&D)
- Organic Molecular Beam Epitaxy (OMBE) facilities including surface analysis techniques (MCP-LEED, UHV STM/AFM, RHEED) and *in situ* optical spectroscopy (PL and DRS)
- dc and rf sputtering systems for metallic (Au, Ti) and oxidic (SiO_2, Ta_2O_5) thin films and multilayers
- Ion beam etching with Ar ions at sample temperatures down to 80 K in vacuum
- Chamber for ion- and reactive etching up to 4" wafer
- Reactive ion beam etching with sample diameters up to 6 cm
- Ultrasonic wire bonder
- Equipment for photolithographic patterning
- MBE system NEBULA for $Cu(In,Ga)S_2$ layers on 4'' substrates including RHEED setup
- Two HV systems for closed-space sublimation (CSS) for deposition of CdTe layers
- RF reactive sputtering system for transparent conducting oxides (TCO's) and molybdenum
- DC sputtering system for copper and indium
- UHV system ULS400 for $Cu(In,Ga)(Se,S)_2$ on (100x100) mm^2 substrates
- Wet chemical processing and chemical bath deposition of photoactive layers

Surface Analysis Systems

- LT-STM/AFM (1 K) with QMS (1000 amu), MCP-LEED, DRS
- AUGER electron spectrometer
- Surface analysis system UNISPEC with XPS, UPS, AES, LEED, STM
- Atomic force microscopes (AFM and Microstructure Measuring Device VERITEKT 3 with needle sensor)
- Surface profilometer DEKTAK 100
- Scanning electron microscopes
- Several UHV-scanning probe devices (STM, AFM)

Electrical Measurement Techniques

- Electrical transport measurements (resistance, critical current density, point contact and tunneling spectroscopy)
- Hall-effect and Four-point probe equipment
- Current-voltage characteristics ($2\ K < T < 300\ K$, $B \leq 5\ T$)
- Current-voltage characteristics by microwave irradiation ($2\ GHz < f < 300\ GHz$)
- Noise measurements (frequency range 60 µHz - 100 kHz) at low temperatures
- LTS-SQUID characterization at 4.2 K (current-voltage, flux-voltage, noise, screening properties)
- HTS-SQUID characterization up to 100 K (current-voltage, flux-voltage, noise)

- 2 Deep level transient fourier spectrometers (temperature range 80 K - 690 K, 30 K - 330 K)
- 3 Admittance spectrometers (frequency range 40 Hz - 100 kHz, 20 Hz - 2 MHz and 75 kHz - 30 MHz, temperature range 30 K - 690 K)
- Microwave signal generator (frequency range 1 - 20 GHz, resolution: 1 kHz)
- Electrical and optical characterization of high power diode laser arrays

Equipment for Optical Characterization

- UV-VIS spectrometer
- FTIR spectrometer
- Cathodoluminescence at SEM, equipped for IR - UV
- Micro-Photoluminescence, IR-UV, time-resolution ~ 1ns
- Photoluminescnce excitation (PLE)
- Optical cryostats (2…300 K) for optical absorption, photoluminescence and Raman spectroscopy
- Excitation lasers in a wide range from 405-1550 nm (fiber, gas, solid state and diode lasers)
- Optical microscopes
- Magnetrelaxation of ferrofluids (MORFF) for characterization of magnetic nanoparticles

Equipment for Electro-Optical (Solar) Characterization

- Solar simulator (AM 1.5) with Current-Voltage measurement
- Illumiated Current-Voltage measurements for 10 K to RT
- Quantum efficiency (EQE) measurements of solar cells

Equipment for Thermal Treatment

- Furnace for conventional thermal treatment in inert gas atmosphere or vacuum (temperatures up to 2050 K)
- RTA apparatus (double graphite strip heater) for short time annealing (annealing time in the order of seconds, temperature range 1000 K to 1950 K, temperature rise rate 100 K s^{-1})

Electron Microscopy

- Scanning electron microscope JEOL JSM-6490 with LaB_6-cathode
- FEI field-emission electron microscope connected with FIB system

Ion Beam Techniques

3 MV Tandetron accelerator "JULIA", equipped with

- Sputter ion source and Duoplasmatron source
- Universal beam line for ion implantation and ion beam analysis
- Second beam line for ion beam analysis, combined with implantation chamber of 400 kV implanter
- Irradiation chamber with cooled and heated sample holder and four axis goniometer

Application:

- Ion implantation: energy range 500 keV - 12 MeV, temperature range 15 K - 1500 K
- Ion beam analysis: RBS and PIXE in combination with channeling, ERDA, NRA

400 kV implanter "ROMEO", equipped with

- Hot filament, hollow cathode ion source
- Irradiation chamber with cooled and heated sample holder and four axis goniometer, combined with beam line of 3 MV Tandetron accelerator

Application:

- Ion implantation: energy range 20 keV - 400 keV, temperature range 15 K - 1500 K
- Ion implantation at low temperatures and subsequent RBS analysis using H- or He-ions from 3 MV Tandetron accelerator

Low Energy implanter "LEILA", equipped with

- Colutron Ion source 100-Q
- Colutron Ion Gun System G-2-D
- Irradiation chamber with heated sample holder

Application:

- Irradiation of surfaces: energy range sub-keV, temperature range 300 K - 750 K

Low Energy implanter "Mr. JIM Stringer", equipped with

- Hot filament, hollow cathode ion source
- Irradiation and deposition chamber

Application:

- Deposition of diamond-like thin films: energy range 100eV – 30 keV, RT

Focused Ion Beam system FEI NanoLab Helios 600i

- Liquid ion source, E = 500 eV – 30 keV
- Electron microscope, E = 350 eV – 30 keV

Application:

- TEM-lamella preparaqtion, etc.

Low Temperature Measuring Equipment

- LT STM/AFM down to 1 K
- He-4 cryostats for temperatures down to 4.2 K
- He-4 refrigerator for the temperature range 1.3 K - 4.2 K
- Helium 3 refrigerator for temperatures range 4,2K - 300 mK with superconducting magnet to 2 T
- He-3/He-4 dilution refrigerator for temperatures range 4,2 K - 6 mK with superconducting magnet to 10 T
- He-3/He-4 dilution refrigerator with a base temperature of 35 mK
- Electronic equipment for characterization of cryoelectronic devices
- SQUID sensor systems for magnetic measurements under unshielded conditions
- SQUID sensor system for spatially resolved magnetorelaxometry
- Cryostats (2 K < T < 300 K; optical window; magnetic field)
- Cryocoolers (Gifford-McMahon and Stirling)
- Pulse tube refrigerators (for sensor cooling)

SQUID Application Laboratories

- Measurement system for non-destructive evaluation in unshielded environment based on high-T_C-SQUID gradiometers
- Magnet-Relaxation-Measuring System in unshielded environment for MRX and TMRX based on low-T_C SQUID gradiometers

Clean Room (Number of Particles/cu/t < 100)

- Photolithography
- Wet chemical etching
- dry chemical etching (Plasma etching machine “pico”, Diener Plasma)
- minimum lateral resolution: few micrometers

Shielded Rooms

- Faraday room
- Magnetic shielded room

Laboratory for Cryogenic Measurement of Mechanical Quality Factors of Gravitational Wave Detector Components

- room temperature stability of ± 0.2 K at best
- vibration isolation (decoupled foundation)
- acoustic isolation
- remote controlled operation of the measurement equipment
- separated room for disturbing machines (e.g. pumps)
- full supply of technical media to perform cryogenic measurements
- polishing tools for bulk samples

Laboratory for Astrophysics and Cluster Physics

- Supersonic jet apparatus for gas-phase spectroscopy of large molecules for gas-phase spectroscopy under astrophysical conditions covering the spectral range from UV to the NIR and LIF setup
- Matrix isolation UV/vis spectroscopy setup with closed-cycle cryostat
- Helium droplet apparatus for spectroscopy and reaction studies at ultra-low temperature
- Flow reactors for the production of silicon-, carbon-, and iron-based nanoparticles
- Cluster beam apparatus with laser pyrolysis source and size selection facility
- Time-of-flight mass spectrometer (TOF-MS)
- Quadrupole mass spectrometer
- Photoluminescence spectrometer for UV/vis and near IR emission wavelengths
- Atomic force microscope (AFM)
- High-pressure liquid chromatograph (HPLC) combined with DDA UV detector and fraction controller for analysis and preparative separation of pyrolysis condensates
- Pulsed and cw CO_2 lasers
- Single-mode Nd:YAG lasers with tunable dye lasers and frequency doubling facilities
- ArF excimer laser
- laser ablation setup for gas-phase condensation of nanoparticles combined with a particle beam extraction system

4. Current Research Projects

(A) Supported by the Bundesministerium für Bildung, Wissenschaft, Forschung und Technologie (BMBF), Bundesministerium für Wirtschaft und Arbeit (BMWi), and Bundesministerium für Umwelt, Naturschutz und Reaktorsicherheit (BMU)

Ioneninduzierte Strukturumbildungsprozesse in amorphen Halbleitern
Teilprojekt 4 im Verbundprojekt „Ioneninduzierte Strukturumbildung“
Verbund Forschung mit Sonden und Ionenstrahlen im Gesamtverbund Erforschung der kondensierten Materie mit Großgeräten

Prof. Dr. W. Wesch	05K10SJ1	07/10 – 06/13

CdTe-CdS-Solarzellen hoher Effizienz für eine verbesserte Modul-Produktionstechnologie

Prof. Dr. W. Wesch	0329881A	09/08 – 04/12

Spitzenforschung und Innovation in den Neuen Ländern – Photonische Nanomaterialien

Prof. Dr. C. Ronning	PhoNa	12/09 – 11/14

Grenzflächen und Defekte – Rechnerunterstützte Optimierung des Wirkungsgrades von CIGS Dünnschichtsolarzellen in der industriellen Umsetzung
Teilvorhaben: Ermittlung von Struktur-Eigenschaftsbeziehungen und ihre Beeinflussung durch Variation der Prozessparamenter

Prof. Dr. C. Ronning	0325448E	08/12 – 07/15

Toxikologische Charakterisierung von Nanomaterialien für die diagnostische Bildgebung in der Medizin – NanoMed

Prof. Dr. P. Seidel	BMBF (Ausschreibung NanoCare)	09/10 – 08/13

Josephsonkontakte mit variablem Durchlassvermögen

Prof. Dr. P. Seidel	BMBF (WTZ UKR 10/034)	06/11 – 05/13

Longitudinal plasma wave in the coupled Josephson junctions and its manifestation under electromagnetic irradiation

Prof. Dr. P. Seidel, Dr. Yu. M. Shukrinov	BMBF(Heisenberg-Landau Prog.)	01/12 – 12/12

(B) Supported by the Deutsche Forschungsgemeinschaft (DFG)

Rastertunnelspektrokopie an einzelnen Molekülen in epitaktischen Nanoschichten

Prof. Dr. T. Fritz	FR 875/11-1	10/09 – 12/13

Großgeräteantrag Tieftemperatur-STM/AFM mit optischen Messmöglichkeiten

Prof. Dr. T. Fritz, Prof. Dr. C. Ronning, Prof. Dr. P. Seidel	INST 275/256-1 FUGG	02/11 – 12/12

Optische Spektroskopie an ultradünnen Molekülschichten

Prof. Dr. T. Fritz, Dr. R. Forker	FR 875/9-3	02/12 – 02/15

Formation and Shaping of Magnetic Nano-clusters in Ion Implanted Oxides

Prof. Dr. C. Ronning	Ro1198/13-1	03/11 – 02/14

Wiring quantum dots – phase separation inducing new functionlity (D-A-CH)

Prof. Dr. C. Ronning	Ro1198/14-1	08/11 – 07/14

Strukturierungsverfahren für mikro- und nanooptische Elemente in Lithiumniobat
Dr. E.-B. Kley, Prof. Dr. W. Wesch KL1199/2-2 05/10 – 12/13

Dynamics and Interactions of Semiconductor Nanowires for Optoelectronics (Coordination project)
Prof. Dr. Carsten Ronning RO1198/16-1 03/12 – 06/15

Light-matter interaction in optically doped nanowire LEDs and nano lasers (Teilprojekt P4)
Prof. Dr. Carsten Ronning RO1198/17-1 03/12 – 11/15

Gütemessungen bei kryogenen Temperaturen
(Teilprojekt C4 im SFB/TR 7 „Gravitationswellenastronomie“)
Prof. Dr. P. Seidel, Dr. R. Nawrodt DFG–SFB/TR7 01/03 – 12/14

Optische Eigenschaften siliziumbasierter Testmassen
(Teilprojekt C9 im SFB/TR 7 „Gravitationswellenastronomie“)
Dr. R. Nawrodt DFG–SFB/TR7 01/11 – 12/14

Josephson effects at iron pnictides
Prof. Dr. P. Seidel DFG (SPP 1458, SE 664/15-1) 05/10 – 04/13

Formation of GEMS from interstellar silicate dust
Prof. Dr. Fr. Huisken HU 474/23-1 02/10 – 01/12

Spektroskopische Untersuchungen an polyzyklischen aromatischen Kohlenwasserstoffen mit aliphatischen Seitengruppen
Prof. Dr. Fr. Huisken HU 474/24-1 02/10 – 01/12

Synthesis, processing, and spectroscopic characterization of PAHs with astrophysical impact
Prof. Dr. Fr. Huisken HU 474/21-2 07/10 – 06/13

Experimental studies of the low-temperature condensation of cosmic dust in the interstellar medium
Prof. Dr. Th. Henning HE 1935/26-1 02/12 – 01/15

Kohlenwasserstoff-Chemie bei ultratiefen Temperaturen in flüssigen Helium-Tröpfchen,
Prof. Dr. Fr. Huisken HU 474/22-3 05/12 – 05/15

(C) Support by the EU

Marie-Curie ITN network “Nanowiring”
Prof. Dr. C. Ronning 265073 11/10 – 10/14

IRON-SEA - Establishing the basic science and technology for Iron-based superconducting electronics applications
Prof. Dr. P. Seidel 283141 10/11 – 09/14

FP7-PEOPLE-IRSES Austauschprogramm für Wissenschaftler „ELiTES“
Dr. R. Nawrodt GA295153 03/12 – 02/16

Marie Curie ITN network “LASSIE- Laboratory Astrophysics Surface Science in Europe’’
Dr. C. Jäger 238258 02/10 – 01/14

Marie Curie Intra-European Fellowship "PAHCNP- Spectroscopy of cosmic dust analogs: study of the interaction with polycyclic aromatic hydrocarbons"
Dr. Abel Brieva, C. Jäger 274794 10/11– 09/13

(D) Supported by the Thüringer Ministerium für Bildung, Wissenschaft und Kultur (TKBWK)

-/-

(E) Supported by other institutions

Virtuelles Institut "MEMRIOX" Memory Effects in Resistive Ion-beam Modified Oxides
Prof. Dr. Carsten Ronning HZDR 10/11 – 09/16

Strukturuntersuchungen an dem für die Photovoltaik relevanten Cu(In,Ga)(Se,S)2 Halbleitersystem mittels Synchrotronstrahlung
Dr. C.S. Schnohr Carl-Zeiss-Stiftung 06/10 – 05/12

Ionenstrahlmodifizierung neuartiger Gruppe-III-Nitrid-Strukturen (DAAD / PPP Portugal)
PD Dr. E. Wendler DAAD / PPP Portugal 01/11 – 12/12

Modifizierung der Eigenschaften von CdTe durch Ionenbestrahlung (DAAD / PPP Australien)
Prof. Dr. W. Wesch DAAD / PPP Australien 01/11 – 12/12

Experimente zur Labor-Astrophysik
Dr. C. Jäger MPI Heidelberg 01/02 – 05/22

5. Publications, Invited Talks, and Conference Contributions

5.1 Publications in Scientific Journals

Optical Differential Reflectance Spectroscopy on Thin Molecular Films ***(invited review)***,
R. Forker, M. Gruenewald, and T. Fritz
Annu. Rep. Prog. Chem., Sect. C: Phys. Chem. **108**, 34–68 (2012).

Determination of the optical constants of α- and β-zinc(II)-phthalocyanine films
M. Kozlik, S. Paulke, M. Gruenewald, R. Forker, and T. Fritz
Org. Electron. **13**, 3291–3295 (2012).

Highly Ordered Growth of PTCDA on Epitaxial Bilayer Graphene
M. Meissner, M. Gruenewald, F. Sojka, C. Udhardt, R. Forker, and T. Fritz
Surf. Sci. **606**, 1709–1715 (2012).

On the Origin of the Energy Gain in Epitaxial Growth of Molecular Films
C. Wagner, R. Forker, and T. Fritz
J. Phys. Chem. Lett. **3**, 419-424 (2012).

A Global Glassy Layer on $BaAl_2B_2O_7$ Crystals Formed during Surface Crystallization of $BaO{\cdot}Al_2O_3{\cdot}B_2O_3$ Glass
W. Wisniewski, B. Schröter, T. Zscheckel, and C. Rüssel
Cryst. Growth Des. **12**, 1586−1592 (2012).

Low threshold room-temperature lasing of CdS nanowires
S. Geburt, A. Thielmann, R. Röder, C. Borschel, A. McDonnell, M. Kozlik, J. Kühnel, K. A. Sunter, F. Capasso, and C. Ronning
Nanotechnology **23**, 365204 (2012).

Modal gain and its diameter dependence in single ZnO micro- and nanowires
J.P. Richters, J. Kalden, M. Gnauck, C. Ronning, C.P. Dietrich, H. vonWenckstern, M. Grundmann, J. Gutowski, and T. Voss
Semiconductor Science and Technology ***27****, 015005 (2012).*

Correlation between damage evolution, cluster formation and optical properties of silver implanted lithium niobate
S. Milz, J. Rensberg, C. Ronning, and W. Wesch
Nuclear Instruments and Methods B ***286****, 67 (2012).*

Quantification of impurity concentration in Cu2O and CuO via secondary ion mass spectrometry
A. Laufer, D. Reppin, H. Metelmann, S. Geburt, C. Ronning, T. Leichtweiss, J. Janek, and B.K. Meyer
physica status solidi B ***249****, 801 (2012).*

Extension of the cubic boron nitride thin film growth phase diagram
S. Weidner, S. Geburt, J. Ye, S. Ulrich, and C. Ronning
Diamond and Related Materials ***22****, 88 (2012).*

A CEMS search for precipitate formation in ^{57}Fe implanted ZnO
H. Masenda, T.B. Doyle, S. Geburt, C. Ronning, H.P. Gunnlaugsson, and K. Bharuth-Ram
Hyperfine Interactions ***207****, 49 (2012).*

Hexagonal boron nitride nanowalls: physical vapour deposition, 2D/3D morphology, and spectroscopic analysis
B. BenMoussa, J. D'Haen, C. Borschel, J. Barjon, A. Soltani, V. Mortet, C. Ronning, M. D'Olieslaeger, H.-G. Boyen, and K. Haenen
Journal of Physics D: Applied Physics ***45****, 135302 (2012).*

Direct Determination of Minority Carrier Diffusion Lengths at Axial GaAs Nanowire p-n Junctions
C. Gutsche, R. Niepelt, M. Gnauck, A. Lysov, W. Prost, C. Ronning, and F.J. Tegude
Nano Letters ***12****, 1453 (2012).*

Significant stress reduction of cBN layers upon ion irradiation at elevated temperatures
S. Weidner, J. Ye, S. Geburt, C. Ronning, and S. Ulrich
Nuclear Instruments and Methods B ***280****, 18 (2012).*

Binary Copper oxide semiconductors: from materials towards devices
B.K. Meyer, A. Polity, D. Reppin, M. Becker, P. Hering, P.J. Klar, Th. Sander, C. Reindl, J. Benz, M. Eickhoff, C. Heiliger, M. Heinemann, J. Bläsing, A. Krost, S. Shokovets, C. Müller, and C. Ronning
physica status solidi B ***249****, 1487 (2012).*

Hopping conduction in Mn ion-implanted GaAs nanowires
W. Paschoal Jr., S. Kumar, C. Borschel, P. Wu, C.M. Canali, C. Ronning, L. Samuelson, and H. Pettersson
Nano Letters ***12****, 4838 (2012).*

Protein adsorption on nano-scaled, rippled TiO2 and Si surfaces
J. Sommerfeld, J. Richter, S. Kosan, R. Niepelt, S. Milz, T. Keller, K.D. Jandt, and C. Ronning
Biointerphases ***7****, 55 (2012).*

Thermoelectric Characterization of Electronic Properties of GaMnAs Nanowires
P. Wu, W. Paschoal Jr., S. Kumar, C. Borschel, C. Ronning, C.M. Canali, L. Samuelson, H. Pettersson, and H. Linke
Journal of Nanotechnology ***2012****, 480813 (2012).*

Patterned array of nanoporous silicon
D. Wang, S. Schönherr, C. Ronning, and P. Schaaf
Proceedings of MME, Ilmenau, Session D, ***D17*** *(2012).*

Luminescence properties of Ga-graded Cu(In,Ga)Se2 thin films
J. Haarstrich, H. Metzner, C. Ronning, A. Undisz, C.A. Kaufmann, T. Rissom, and H.W. Schock
Thin Solid Films 520, *3657 (2012).*

Maxwell-Wagner Polarization in Cu(In,Ga)(S,Se)2
U. Reislöhner and C. Ronning
Applied Physics Letters 100, *252111 (2012).*

A method for the deposition of CdTe layers at very low substrate temperatures
C. Kraft, C. Heisler, A. Harpf, M. Brückner, H. Metzner, and W. Wesch
Thin Solid Films 522, *145 (2012).*

Iron-containing defect-rich mixed metal oxides for Friedel-Crafts alkylation
B. Jager, A. Wermann, P. Scholz, M. Müller, U. Reislohner, A. Stolle, and B. Ondruschka
Applied Catalysis A 443, *87 (2012).*

Damage formation in SiC ion implanted at 625 K
E. Wendler, P. Schöppe, T. Bierschenk, S. Milz, W. Wesch, N. G. van der Berg, E. Friedland, and J. B. Malherbe
Nuclear Instruments and Methods B 286, 93 (2012).

Damage formation and optical absorption in neutron irradiated SiC
E. Wendler, T. Bierschenk, F. Felgenträger, J. Sommerfeld, W. Wesch, D. Alber, G. Bukalis, L. C. Prinsloo, N. G. van der Berg, E. Friedland, and J. B. Malherbe
Nuclear Instruments and Methods B 286, 97 (2012).

Diffusion behavior of cesium in silicon carbide at T > 1000 degrees C
E. Friedland, N. G. van der Berg, T. T. Hlatshwayo, R. J. Kuhudzai, J. B. Malherbe, E. Wendler, and W. Wesch
Nuclear Instruments and Methods B 286, 102 (2012).

Copper diffusion in thin In2S3 layers investigated by Rutherford Backscattering Spectroscopy
A. O. Juma, P. Pistor, S. Fengler, T. Dittrich, and E. Wendler
Thin Solid Films 520, 6740 (2012).

Influence of radiation damage on strontium and iodine diffusion in silicon carbide
E. Friedland, N. G. van der Berg, J. B. Malherbe, E. Wendler, and W. Wesch
Journal of Nuclear Materials 425, 205 (2012).

Empirical modeling of the cross section of damage formation in ion implanted III-V semiconductors
E. Wendler and L. Wendler
Applied Physics Letters 100, 192108 (2012).

Damage evolution and amorphization in semiconductors under ion irradiation
W. Wesch, E. Wendler, and C. S. Schnohr
Nuclear Instruments and Methods B 277, 58 (2012).

Annealing of silver implanted 6H-SiC and the diffusion of the silver
T. T. Hlatshwayo, J. B. Malherbe, N. G. van der Berg, L. C. Prinsloo, A. J. Botha, E. Wendler, and W. Wesch
Nuclear Instruments and Methods B 274, 120 (2012).

Behavior of iodine implanted in highly oriented pyrolytic graphite (HOPG) after heat treatment
M. B. Mukhawana, C. C. Theron, J. B. Malherbe, N. G. van der Berg, A. J. Botha, W. Grote, E. Wendler, W. Wesch, and P. Chakraborty
Nuclear Instruments and Methods B 273, 65 (2012).

Heat treatment of glassy carbon implanted with cesium at room and high temperatures
D. F. Langa, N. G. van der Berg, E. Friedland, J. B. Malherbe, A. J. Botha, P. Chakraborty, E. Wendler, and W. Wesch
Nuclear Instruments and Methods B 273, 68 (2012).

Ion-beam-induced damage formation in CdTe at a temperature of 15 K
C. W. Rischau, C. S. Schnohr, E. Wendler, and W. Wesch
Nuclear Instruments and Methods B 272, 338 (2012).

Development of porous structures in GaSb by ion irradiation
C. C. Jacobi, T. Steinbach, and W. Wesch
Nuclear Instruments and Methods B 272, 326 (2012).

Structure and optical properties of silicon layers with GaSb nanocrystals created by ion-beam synthesis
F. Komarov, L. Vlasukova, O. Milchanin, A. Mudryi, B. Dunets, W. Wesch, and E. Wendler
Physica Status Solidi A 209, 148 (2012).

Mechanism of oxide layer growth during annealing of NiTi
A. Undisz, F. Schrempel, W. Wesch, and M. Rettenmayr
Journal of Biomedical Mat. Res. A 100, 1743 (2012).

Structural and electronic contributions to the bandgap bowing of (In,Ga)P alloys
C. S. Schnohr
Journal Physics –Condensed Matter 24, 325802 (2012).

Structural properties of embedded Ge nanoparticles modified by swift heavy-ion irradiation
L. L. Araujo, R. Giulian, D. J. Sprouster, C. S. Schnohr, D. J. Llewellyn, B. Johannessen, A. P. Byrne, and M. C. Ridgway
Physical Review B 85, 235417 (2012).

Atomic-scale structure and band-gap bowing in Cu(In,Ga)Se_2
C. S. Schnohr, H. Kammer, C. Stephan, S. Schorr, T. Steinbach, and J. Rensberg
Physical Review B 85, 245204 (2012).

Mechanical Spectroscopy of Silicon as a Low Loss Material for High Precision Mechanical and Optical Experiments
C. Schwarz, D. Heinert, K. Haughian, G. Hofmann, J. Komma, I. W. Martin, P. Murray, S. Rowan, P. Seidel, and R. Nawrodt
Solid State Phenomena **184**, 443-448 (2012).

Development of iron-based superconducting devices
S. Döring, S. Schmidt, F. Schmidl, V. Tympel, S. Haindl, F. Kurth, K. Iida, I. Mönch, B. Holzapfel, and P. Seidel
Physics Procedia **27**, 296-299 (2012).

Josephson and tunneling junctions with thin films of iron based superconductors
S. Schmidt, S. Döring, V. Tympel, F. Schmidl, S. Haindl, K. Iida, B. Holzapfel, and P. Seidel
Physics Procedia **36**, 82-87 (2012).

Synchronization of self-heated Josephson junctions by a superconducting resonator
A. Grib and P. Seidel
Physics Procedia **36**, 411-416 (2012).

The influence of standing waves on synchronization and self-heating of Josephson junctions in resonant systems
A. Grib and P. Seidel
Fizika Nizkikh Temperatur **38**, 409-413 (2012); Low Temperature Physics **38**, 321-325 (2012).

All-sky search for periodic gravitational waves in the full S5 LIGO data
J. Abadie et al. (R. Nawrodt)
Phys. Rev. D **85**, 022001 (2012).

Planar hybrid superconductor-normal metal-superconductor thin film junctions based on $BaFe_{1.8}Co_{0.2}As_2$
S. Döring, S. Schmidt, F. Schmidl, V. Tympel, S. Haindl, F. Kurth, K. Iida, I. Mönch, B. Holzapfel, and P. Seidel
Physica C **478**, 15-18 (2012).

Observation of a Coulomb blockade in strontium titanate thin films
V. Grosse, F. Schmidl, and P. Seidel
Appl. Phys. Lett. **100**, 203110 (2012).

Influence of transverse fields on domain wall pinning in ferromagnetic nanostripes
S. Glathe, U. Hübner, R. Mattheis, and P. Seidel
J. Appl. Phys. **112**, 023911 (2012).

Search for gravitational waves from low mass compact binary coalescence in LIGO's sixth science run and Virgo's science runs 2 and 3
J. Abadie et al. (R. Nawrodt)
Phys. Rev. D **85**, 082002 (2012).

Edge-type Josephson junctions with Co-doped Ba-122 thin films
S. Döring, S. Schmidt, F.Schmidl, V. Tympel, S. Haindl, F. Kurth, K.Iida, I. Mönch, B. Holzapfel, and P. Seidel
Supercond. Sci. Technol. **25**, 084020 (2012).

Scientific objectives of Einstein Telescope
B. Sathyaprakash et al. (R. Nawrodt, P. Seidel, C. Schwarz, D. Heinert)
Class. Quantum Grav. **29**, 124013 (2012).

Implementation and testing of the first prompt search for gravitational wave transients with electromagnetic counterparts
J. Abadie et al. (R. Nawrodt)
Astron. Astrophys. **539**, A124 (2012).

Thermo-optic coefficient of silicon at 1550 nm and cryogenic temperatures
J. Komma, C. Schwarz, G. Hofmann, D. Heinert, and R. Nawrodt
Appl. Phys. Lett. **101**, 041905 (2012).

Enhancement of high-T_C superconducting thin film devices by nanoscale polishing
P. Michalowski, T. Shapoval, D. Meier, C. Katzer, F. Schmidl, L. Schultz, and P. Seidel
Supercond. Sci. Technol. **25**, 115019 (2012).

$YBa_2Cu_3O_7$2d matrix-induced in situ growth of plasmonic Au nanoparticles for biological sensor devices
C. Katzer , V. Grosse, F. Schmidl, P. Michalowski, G. Schmidl, R. Mueller, J. Dellith, C. Schmidt, J. Jatschka, and W. Fritzsche
J. Nanopart. Res. **14**, 1285 (2012).

Coaxial Pulse Tube Refrigerator for 4 K
R. Habibi, M. Thuerk, and P. Seidel
Cryocoolers **17,** 197-202, ICC Press, Boulder, CO (2012).

Effects of self-assembled gold nanoparticles on $YBa_2Cu_3O_{7-\delta}$ thin films and devices
P. Michalowski, C. Katzer, F. Schmidl, and P.Seidel
J. Phys. Conf. Ser. **393**, 012003 (2012).

Resonance features of coupled Josephson junctions: radiation and shunting
Yu. M. Shukrinov, P. Seidel, E. Il'ichev, W. Nawrocki, M. Grajcar, P.A. Plecenik, I.R. Rahmonov, and K. Kulikov
J. Phys. Conf. Ser. **393**, 012020 (2012).

Implications for the Origin of GRB 051103 from LIGO observations
J. Abadie et al. (R. Nawrodt)
ApJ **755**, 2 (2012).

Measurement of vibrational modes in single SiO_2 nanoparticles using a tunable metal resonator with optical subwavelength dimensions
A. I. Chizhik, A. M. Chizhik, A. M. Kern, T. Schmidt, K. Potrick, F. Huisken, and A. J. Meixner
Phys. Rev. Lett. **109**, 223902/1-223902/5 (2012).

Chemical reactions studied at ultra-low temperature in liquid helium clusters
F. Huisken and S. A. Krasnokutski
in: Proceedings of the 28th International Symposium on Rarified Gas Dynamics, edited by M. Mareschal and A. Santos, AIP Conf. Proc. **1501**, 1257-1266 (2012).

Radiative exciton recombination and defect luminescence observed in single silicon nanocrystals
T. Schmidt, A. I. Chizhik, A. M. Chizhik, K. Potrick, A. J. Meixner, and F. Huisken
Phys. Rev. B **86**, 125302-125312 (2012).

Mid-infrared spectroscopy of UV irradiated hydrogenated amorphous carbon materials
K. A. K. Gadallah, H. Mutschke, and C. Jäger
Astron. Astrophys. **544**, A107/1-A107/9 (2012).

Experimental and theoretical study on the infrared spectroscopy of astrophysically relevant polycyclic aromatic hydrocarbon derivatives 2- and 9-vinylanthracene
A. Maurya, S. Rastogi, G. Rouillé, F. Huisken, and Th. Henning
Astrophys. J. **755**, 120/1-120/12 (2012).

On the relevance of polyynyl-substituted polycyclic aromatic hydrocarbons to astrophysics
G. Rouillé, M. Steglich, Y. Carpentier, C. Jäger, F. Huisken, Th. Henning, R. Czerwonka, G. Theumer, C. Börger, I. Bauer, and H.-J. Knölker
Astrophys. J. **752**, 25/1-25/12 (2012).

The smoothness of the interstellar extinction curve in the UV. Comparison with recent laboratory measurements of PAH mixtures
M. Steglich, Y. Carpentier, C. Jäger, F. Huisken, H.-J. Räder, and Th. Henning
Astron. Astrophys. **540**, A110/1-A110/6 (2012).

Mass-analyzed threshold ionization and structural isomers of M3O4 (M = Sc, Y, and La)
L. Wu, C. Zhang, S. A. Krasnokutski, and D.-Sh. Yang
J. Chem. Phys., 137, (2012) P. 084312-7.

5.2 Invited Talks at Conferences and Colloquia

T. Fritz:

- *Organische epitaktische Molekülschichten: Struktur und physikalische Eigenschaften*
  Institutsseminar FSU Jena, IMT, 09.05.2012
- *Optical in situ Spectroscopy on Epitaxially Grown Organic Thin Films*
  Osaka University, 20.8.2012
- *Quantification of LEED Measurements*
  Osaka University, 21.8.2012
- *Epitaxial Organic Thin Films of Large Aromatic Hydrocarbons – Structure and Physical Properties*
  Johannes Kepler Universität Linz, Physikalisches Kolloquium, 8.11.2012

- *Optical in situ Spectroscopy on Epitaxially Grown Organic Thin Films*
  Universität Heidelberg, Symposium "Connecting Molecular π Systems to Advanced Functional Materials", 26.11.2012

C. Ronning:

- *ZnO nanowires: synthesis, doping and applications*
  Universität Kiel, Kolloquium der Technischen Fakultät, 6.2.2012
- *Overview of research at the Institut for Solid State Physics*
  iThemba LABS, Cape Town, Südafrika, 2.3.2012
- *ZnO nanowires for photonic applications*
  KAUST, Department of Material Science, Jiddah, Saudi Arabia, 19.3.2012
- *Semiconductor nanowire devices for photonic and electronic applications*
  Spring meeting of the E-MRS, Session Q, Strasbourg, France, 14.-17. Mai 2012
- *ZnO nanowires for photonic applications*
  DFG Chinese – German bilateral Workshop, TU Braunschweig, 24.-26. Sept. 2012

P. Seidel:

- *Thin film tunneling and Josephson junctions with iron-based superconductors*
  TU Dresden, Graduiertenkolleg 1621 "Itineranter Magnetismus und Supraleitung in intermetallischen Verbindungen", 11.06.2012

F. Huisken:

- *Can silicon-based nanoparticles be responsible for the Extended Red Emission?*
  International Workshop “Silicon in Space”, Villa Vigoni, Loveno di Menaggio, Italy, May 16 – 19, 2012
- *Chemical reactions studied at ultralow temperature in liquid helium clusters*
  28th International Symposium on Rarefied Gas Dynamics, Zarogoza, Spain, July 9 – 13, 2012

C. Jäger:

- *Kosmischer Staub aus dem Labor: Vom Molekül zum Festkörper*
  Physikalisches Kolloquium, FSU Jena, 09.01.2012
- *Carbon in the Universe*
  Gastkolloquium am Max-Planck-Institut für Astronomie, Heidelberg, 20.01.2012
- *Laboratory Experiments I. Dust and PAHs (invited talk)*
  ISM-SPP school "The Physics of the Interstellar Medium", Freising, 2.10.2012
- *Spectroscopic Properties of Carbonaceous Matter from the Laboratory (invited talk)*
  International Astronomical Union General Assembly XXVIII; SpS 16 Unexplained Spectral Phenomena in the Interstellar Medium, August 27 – 28, Beijing, 28.8.2012
- *Laboratory Astrophysics of Dust (invited talk)*
  Conference on Core-Collapse Supernovae Near & Far: Understanding its Formation and Evolution, November 5 – 8, 2012, Ascona, 6.11.2012

C. Katzer:

- *Tuning the properties thin films via incorporating Au nanocrystals*
  Bereichsseminar MPI / TU Stuttgart, 03.07.2012

F. Schmidl:

- *Matrix induced growth of Au nanoparticles*
  IPHT Jena, Bereichsseminar Angewandte Plasmonik, 19.07.2012

C. Schwarz:

- *Cryogenic aspects of existing and future GW detectors*
  3rd ASPERA Meeting, Darmstadt, 13.03.2012

5.3 Conference Contributions

SFB Frühjahrstagung, Hannover, February 14 – 15, 2012

J. Komma
Optical Properties of Silicon

R. Nawrodt
Cryogenic Q-factor measurements – Status of C4

International Workshop "Iron-Based Superconductors", Munich, March 21 – 23, 2012

F. Schmidl, S. Schmidt, S. Döring, V. Tympel, P. Seidel, F. Kurth, K. Iida, S. Haindl, I. Mönch, and B. Holzapfel
Preparation of iron-based tunnel and Josephson junctions

Frühjahrstagung der DPG, Berlin, March 25 - 30, 2012

F. Sojka, M. Meissner, M. Gruenewald, R. Forker, and T. Fritz
Quantification of LEED measurements. I. Systematic Errors

M. Meissner, F. Sojka, M. Gruenewald, R. Forker, and T. Fritz
Quantification of LEED measurements. II. Application to epitaxial organic films

M. Gruenewald, K. Wachter, F. Sojka, M. Meissner, R. Forker, and T. Fritz
Organic heteroepitaxy of PTCDA and SnPc on single crystalline silver

K. Wachter, M. Gruenewald, F. Sojka, M. Meissner, R. Forker, and T. Fritz
Optical and structural properties of organic heterostructures: PTCDA and SnPc on Au(111)

M. Kozlik, S. Milz, R. Forker, A. Donat, S. Paulke, C. Ronning, and T. Fritz
Combination of Zinc Phthalocyanines and Zinc Oxide for Hybrid Solar Cells

J. Rensberg, S. Milz, C. Ronning, and W. Wesch
Surface plasmon resonance of Ag nanoclusters and refractive and index changes in ion irradiated lithium niobate

J. Rensberg, S. Milz, C. Ronning, and W. Wesch
Correlation between size evolution and optical properties of ion beam synthesized silver nanoclusters in lithium niobate

C. Weiss, C. Heisler, U. Reislöhner, C. Ronning, and W. Wesch
Impedance Spectroscopy of CdTe Thin Film Solar Cells

S. Möller, J. Sommerfeld, T. Keller, and C. Ronning
Biofunctionalization of diamond like carcon layers

F. Wyrwa, S. Kosan, J. Hönig, R. Niepelt, J. Sommerfeld, and C. Ronning
Ion beam nano-patterned surfaces as biomaterials

C. Heisler, M. Brückner, F. Lind, C. Kraft, U. Reislöhner, C. Ronning, and W. Wesch
Physical vapor deposition of CdTe thin films at low temperature for solar cell applications

S. Schönherr, J. Haarstrich, U. Reislöhner, C. Ronning, and T. Rissom
Photoluminescence of $CuIn_xGa_{1-x}Se_2$ absorbers and solar cells

H. Hempel, C. Kraft, C. Heisler, S. Geburt, C. Ronning, and W. Wesch
Photoluminescence measurement of polycrystalline CdTe made of high purity source Sputtering

U. Kaiser, S. Gies, Limei Chen, W. Heimbrodt, S. Geburt, and C. Ronning
Energy transfer dynamics oft he Mn $3d^5$ and Tb $4f^8$ luminecence in ZnS:Mn,Tb nanostructures

I.Slowik, B. Seise, C. Leiterer, R. Niepelt, U. Schröder, D. Cammi, W. Fritzsche, and C. Ronning
Biofunctionalization of ZnO Nanowires for DNA sensing applications

D. Cammi, I. Slowik, R. Niepelt, A. Johannes, and C. Ronning
Persistent conductivity in ZnO nanowires in different gas atmospheres

Y. Haj Hmeidi, R. Niepelt, M. Gnauck, F. Schmidl, and C. Ronning
Connecting ZnO nanowires for light emitting devices

A. Johannes, R. Niepelt, M. Gnauck, and C. Ronning
Persistent Ion Beam Induced Conduction in Zinc Oxide Nanowires

A. Seibert, A. Laufer, N. Volbers, S. Eisermann, K. Potzger, S. Geburt, C. Ronning, and B. K. Meyer
Dependence of impurity incorporation on the surface termination of ZnO

R. Röder, S. Geburt, and C. Ronning
Low lasing threshold of CdS nanowires

S. Jankowski, S. Geburt, C. Ronning, and W. Heimbrodt
Magneto-optical Studies on Transition Metal doped Zinc Oxid

E. Wendler, P. Schöppe, T. Bierschenk, S. Milz, W. Wesch, N. G. von der Berg, E. Friedland, and J. B. Malherbe
Damage formation in SiC ion implanted at 625 K

A. Juma, P. Pistor, T. Dittrich, and E. Wendler
Diffusion of Cu (I) in amorphous In_2S_3 thin films investigated by Rutherford backscattering spectroscopy

T. Steinbach, A. Reupert, and W. Wesch
Ion beam induced stress formation and relaxation in semiconductors

T. Steinbach, E. Schmidt, A. Reupert, M. Schmidt and W. Wesch
Ion beam induced density changes and plastic phenomena

P. Michalowski, Ch. Katzer, D. Kuhwald, S. Koch, F. Schmidl, and P. Seidel
Further investigations on dc-SQUID gradiometers based on growth modified bi-crystal grain boundaries

S. Schmidt, S. Döring, F. Schmidl1, F. Kurth, K. Iida, S. Haindl, B. Holzapfel, and P. Seidel
Grain boundary junctions with Co-doped Ba-122

S. Döring, S. Schmidt, F. Schmidl, V. Tympel, S. Haindl, F. Kurth, K. Iida, B. Holzapfel, and P. Seidel
Andreev Reflexion studies on planar hybrid SNS-junctions based on 122-thin films

M. Westerhausen, Ch. Katzer, R. Diener, I. Uschmann, F. Schmidl1, M. Rettenmayer, and P. Seidel
Wachstumsbedingungen und Eigenschaften von YBCOSchichten mit Au-Nano Partikeln

S. Koch, P. Michalowski, Ch. Katzer, M. Westerhausen, F. Schmidl, and P.Seidel
Grain boundary high-Tc dc-SQUIDs with self-organized nanocrystals

Ch. Katzer, P. Michalowski, M. Westerhausen, S. Koch, F. Schmidl, S. Treiber, J. Albrecht, and P. Seidel
Incorporation of self-organised gold nano crystals in YBa2Cu3O7−δ thin films: Modification of superconducting properties

UK-Germany National Astronomy Meeting NAM2012, Manchester, March 27 – 30, 2012

C. Jäger, M. Steglich, H.-J.Räder, F. Huisken, andTh. Henning
Experimental studies on condensation and properties of carbonaceous matter

M. Steglich, C. Jäger, G. Rouillé, Y. Carpentier, F. Huisken, H.-J. Räder, J. Bouwman, and Th. Henning
The electronic absorption properties of PAHs in view of the observed interstellar UV-vis extinction

Gravitational Wave Advanced Detector Workshop GWADW 2012, Waikoloa Marriot Resort, Hawaii/USA, May 13 – 19, 2012

J. Komma, G. Hofmann, C. Schwarz, D. Heinert, and R. Nawrodt
Investigations of optical properties of silicon at cryogenic temperatures

G. Hofmann, J. Komma, C. Schwarz, D. Heinert, R. Nawrodt, K. Haughian, K. Craig, P. Murray, G. Cole, P. Seidel, S. Rowan, and J. Hough
Bulk material investigations at cryogenic temperatures

Spring meeting of the E-MRS, Strasbourg, France, May 14-18, 2012

J. Haarstrich, M. Teichmann, M. Gnauck, H. Metzner, C. Ronning, W. Wesch, T. Rissom, C. A. Kaufmann, H. W. Schock, V. Scheumann, and W. Mannstadt
Buffer-free Cu(In,Ga)Se2 solar cells by near-interface doping using ion implantation

C. Ronning
Semiconductor nanowire devices for photonic and electronic applications

C. Heisler, C. Weiss, C. Kraft, U. Reislöhner, C. Ronning, and W. Wesch
Impedance Spectroscopy of CdTe Thin Film Solar Cells

C. Kraft, H. Hempel, C. Heisler, H. Metzner, C. Ronning, and W. Wesch
Photoluminescence measurement of polycrystalline CdTe for solar cells made of high purity soure material

U. Reislöhner and C. Ronning
Impedance Spectroscopy on Cu(In,Ga)(Se,S)$_2$ - Solar Cells

Workshop "Silicon in Space", Loveno di Menaggio, May 16 – 19, 2012

C. Jäger
Laboratory studies on the processing of circumstellar silicates in the ISM

2nd IRON-SEA Meeting, Bratislava, Slovak Republic, May 23 – 25, 2012

P.Seidel
Development of thin film devices with iron-based superconductors

S. Döring
Preparation and characterization of plannar SNS- and edge-type thin films junctions with Co-doped Ba-122

IPAC, New Orleans, May 25 – 30, 2012

R. Geithner, W. Vodel, R. Neubert, P. Seidel, F.Kurian, H. Reeg, and M. Schwickert
An improved Cryogenic Current Comparator for FAIR

6th Nanowire Growth Workshop, St. Petersburg, Russia, June 4-6, 2012

A. Johannes and C. Ronning
Wiring Quantum Dots

A. Lysov, C. Gutsche, D. Braam, M. Geller, M. Offer, R. Niepelt, C. Ronning, F.-J. Tegude, and W. Prost
Growth and characterization of axial and coaxial pn-GaAs nanowires for photovoltaic applications

Molecular Reaction Dynamics in Gases, Liquids and Interfaces, FD157, Assisi, Italy, 25-27 June 2012

S. Krasnokutski and F. Huisken
Chemical reactions studied at ultralow temperature in liquid helium clusters

1st NanoMed Workshop "Safety of Nanoscale Materials in Medicine", Jena, June 26 – 27, 2012

L. Seyfarth, U. Enke, R. Bräuer, N. Brendel, M. Büttner, A. Csaki, F. Schlenk, C. Bergemann, D. Fischer, W. Fritzsche, P.Seidel, and E. Schleussner
Placenta perfusion – a suitable ex vivo model to characterise interaction of nano-particles with human tissue

ICC, Los Angeles, July 9 – 12, 2012

R. Habibi, M. Thürk, and P. Seidel
Coaxial Pulse Tube Refrigerator for 4 K

DUBNA-NANO 2012, Dubna, July 9 – 14, 2012

P. Michalowski, C. Katzer, F. Schmidl, and P. Seidel
Effects of self-assembled gold nanoparticles on $YBa_2Cu_3O_7$-δ thin films and devices

Yu.M. Shukrinov, P. Seidel, W. Nawrocki, E. Ilichev, A. Plecenik, and M. Grajcar
Resonance features of the couples Josephson Junctions: Some unsolved problems

Workshop Ionenstrahlphysik, Augsburg, July 10-11, 2012

E. Wendler
Empirical modeling of the cross section of damage formation in ion implanted III-V semiconductors

E. Schmidt
In situ measurement of ion beam induced stress in solids

International Conference on Nanoscience + Technology (ICN+T2012), Paris, July 23 – 27, 2012

C. Katzer, P. Michalowski, M. Westerhausen, R. Diener, S. Christke, Frank Schmidl, G. Schmidl, J. Jatschka, R. Müuller, and W. Fritzsche
Matrix induced in-situ growth of crystalline Au nanoparticles

The 5th meeting on Cosmic Dust, Kobe, August 6 – 10, 2012

C. Jäger and Th. Henning
Laboratory studies on cosmic dust processing in the ISM

18th International Conference on Ion Beam Modifications of Materials (IBMM2012), Qingdao (China), September 2 – 7, 2012.

C. Borschel and C. Ronning
Ion Beam Irradiation of Nanostructures – Monte Carlo Simulations

T. Steinbach, A. Reupert, and W. Wesch
Ion beam induced stress formation and relaxation in semiconductors

T. Steinbach, K. Gärtner, J. Jöhrens, C. S. Schnohr, M. C. Ridgway, and W. Wesch
Void formation in amorphous germanium due to high electronic energy depostion

T. Bierschenk, P. Kluth, M. Rodriguez, B. Afra, W. Wesch, T. Steinbach, and M. C. Ridgway
Porous layer formation in swift heavy ion irradiated amorphous Ge

E. Wendler, A. Stonert, W. Wesch and A. Turos
Low-temperature damage formation in ion implanted InP

E. Wendler, W. Wesch, A. Yu. Azarov, N. Catarino, A. Redondo-Cubero, E. Alves, and K. Lorenz
Comparison of low- and room-tempurature damage formation in Ar ion implanted GaN and ZnO

F. Komarov, J. Zuk, L. Vlasukova, O. Milchanin, W. Wesch, E. Wendler, M. Makhavikou, and I. Parkhomenko
Structure and optical properties of silicon layers with InSb and InAs nanocrystals formed by ion-beam synthesis

A. Yu. Azarov, E. Wendler, X. L. Du, B. G. Svensson, and A. Yu. Kuznetsov
Mechanism of ion-induced damage formation in MgZnO

The 24t^{h} Conference of the EPS Condensed Matter Division CMD-24, Edinburgh, September 3 - 7, 2012

R. Forker, M. Gruenewald, K. Wachter, F. Sojka, and T. Fritz
Organic heteroepitaxy of PTCDA and SnPc on single crystalline metals

International Conference on Diamond and Carbon Materials, Granada (Spain), September 3-6, 2012

H. Masenda, K. Bharuth-Ram, T. B. Doyle, S. Geburt and C. Ronning
Formation of Fe_3C in ion implanted graphite and CVD diamond

ThGOT – 3.Optik-Kolloquium, Leipzig, September 4-6, 2012

G. Schmidl, G. Andrä, J. Bergmann, A. Gawlik, I. Höger, F. Falk, C. Schmidt, and F. Schmidl
Diode laser crystallized sputtered a-Si films as seed layer for poly-crystalline Si solar cells

23rd Micromechanics and Microsystems Europe Workshop, Ilmenau, September 9 - 12, 2012

D. Wang, S. Schönherr, C. Ronning, and P. Schaaf
Patterned array of nanoporous silicon

16th International Conference on Hyperfine Interactions and the 20th international Symposium on Nuclear Quadrupole Interactions (HFI/NQI 2012) Beijing, China, September 10 – 14, 2012

K. Bharuth-Ram, H. Masenda, D. Naidoo, R. Mantovan, T. E. Mølholt, S. Geburts, H. P. Gunnlaugsson, G. Langouche, K. Johnston, H. P. Gíslason, S. Ólafsson, C. Ronning, M. B. Madsen and G. Weyer
Defect induced magnetism in Ar implanted ZnO

4th Ukrainian-German Symposium on Physics and Chemistry of Nanostructures and on Nano-biotechnology, Ilmenau, September 18 – 20, 2012

M. Belogolovskii, S. Döring, and P. Seidel
Transport Characteristics of Nano-Scaled Double-Barrier Junctions: Transition from Quantum to Classical Limit

V. Shaternik, A. Shapovalov, P. Seidel, and S. Schmidt
Tunneling Characteristics of Multilayered Superconducting Structures with Inhomogeneous Tunnel Barriers

V. Shaternik, I. Boylo, and P. Seidel
Universality of Charge Transport across Disordered Nanometer-Thick Oxide Films

ELiTES Annual Meeting, Tokyo, October 3 – 4, 2012

R. Nawrodt, G. Hofmann, D. Heinert, C. Schwarz, J. Komma, S. Kroker, E. Butz, B. Walter, I. Martin, L.-E. Wittrock, E. Wisniewski-Barker, G. Hammond, M. Abernathy, K. Craig, J. Hough, S. Rowan, and S. Reid
Silicon surfaces – surface loss and surface treatments

J. Komma
Optical Properties of Silicon at 1550 nm and Low Temperatures

Applied Superconductivity Conference ASC 2012, Portland, Oregon, USA, October 7 – 12, 2012

S. Schmidt, S. Döring, F. Schmidl, V. Tympel, S. Haindl, K. Iida, F. Kurth, B. Holzapfel, and P. Seidel
Bicrystalline grain boundary and hybrid SNS junctions based on Ba-122 thin films

Fall meeting of the MRS, Boston (USA), Nov 25 – 30, 2012

S. Milz, J. Rensberg, C. Ronning, and W. Wesch
Silver nanoclusters in lithium niobate

T. Voß, D. Hou, A. Menzel, C. Ronning, and M. Zacharias
Deep-level emission in ZnO nanowires: intensity-dependent recombination dynamics versus indicator for crystalline quality

R. Niepelt, M. Gnauck, C. Gutsche, A. Lysov, W. Prost, F. Tegude, and C. Ronning
Direct Determination of Minority Carrier Diffusion Lengths at Axial GaAs Nanowire p–n Junctions

4th Einstein Telescope Annual Symposium, Hannover, December 4 – 5, 2012

R. Nawrodt, G. Hofmann, D. Heinert, C. Schwarz, J. Komma, P. Pastrik, S. Kroker, I. W. Martin, L. E. Wittrock, E. Wisniewski-Barker, A. Cumming, K. Haughian, P. Murray, G. D. Hammond, M. Abernathy, K. Craig, A. A. van Veggel, N. Beveridge, J. Hough, S. Rowan, and S. Reid
Silicon Research for the Einstein Telescope

G. Hofmann, J. Komma, C. Schwarz, D. Heinert, R. Nawrodt, K. Haughian, K. Craig, P. Murray, P. Seidel. S. Rowan, J. Hough
Bulk material investigations at cryogenic temperatures

5.4 Theses

PhD Theses

Christian Borschel	*Ion-Solid Interaction in Semiconductor Nanowires*
Raphael Niepelt	*Characterisation and selective modification of semiconductor nanowires for electrical applications*
Tobias Steinbach	*Ionenstrahlinduzierte Strukturmodifikationen in amorphem Germanium*
Michael Oertel	*Untersuchungen zur Reaktionskinetik und Rückkontaktmorphologie von CuInSe2-Dünnschichtsolarzellen*
Markus Büttner	*Vergleichende Charakterisierung magnetischer Nanopartikel mit verschiedenen Untersuchungsmethoden*
Daniel Heinert	*Thermisches Rausch in interferometrischen Gravitationswellendetektoren*
Christian Schwarz	*Mechanische Verlustmessungen an Materialien für Präzisionsmesstechnik*

Diploma and Master Theses

Sören Paulke	*Optische Charakterisierung von Zinkphthalocyanin*
Kristin Wachter	*Organisch-organische Heteroschichten auf Au(111)*
Robert Röder	*Modifizierung der Lasingeigenschaften von Halbleiternanodrähten*
Sven Möller	*Biofunktionalisierung von diamantähnlichen Kohlenstoff-Schichten*
Irma Slowik	*Biofunktionalisierung von ZnO-Nanodrähten für die Detektion von Nukleinsäuren*
Charlotte Weiss	*Dotierung und Elektrische Charakterisierung von CdTe-Dünnschichten für den Einsatz in Solarzellen (ausgezeichnet mit dem STIFT-Preis 2012)*
Alina Donat	*Elektrooptische Charakterisierung von verschiedenen Puermaterialien und deren Einüsse auf Dünnschichtsolarzellen*
Reschad Ebert (Habibi)	*Leistungssteigerung von Pulsationsröhrenkühlern durch Einsatz magnetischer Regeneratormaterialien*
Stephan Fromm	*Untersuchungen zur Haftfestigkeit von flammenpyrolytisch abgeschiedenen SiO_x-Schichten auf Glas unter Verwendung energiesparender Brennervarianten*

Bachelor Theses

Christian Zwick	*Charakterisierung kristalliner Substrate und Adsorbatschichten mittels MCP-LEED*
Martin Heilemann	*PEDOT in Hybridsolarzellen*
Tobias Hümpfner	*Photooxidation von Rubren*
Marcus Junghanns	*Elektrische Kontaktierung von Eu-dotierten ZnO-Nanodrähten*
Benjamin Fuchs	*Cu-Implantation in ZnO-Nanodrähten*

Selina Schiller	*Modifizierung von Cadmiumsulfid Nanodrähten via FIB-Präparation*
Matthias Ogrisek	*Kontrolliertes Wachstum von Zinkoxid Nanodrähten im Drei-Zonen-Ofen*
Claudia Schnitter	*Plasmagestützter Stickstoffeinbau in CdTe für Anwendungen in Solarzellen*
Attila Lüttmerding	*Untersuchungen con CIGS-Dünnschichtsolarzellen mit Indiumsulfid-Puffer mittels Kathodolumineszenz*
Katja Puschkarsky	*Kathodolumineszenz-Untersuchungen an Indiumsulfid-Dünnschichten*
Stefan Noack	*Untersuchungen von Aufhängungsstrukturen zur kryogenen Gütemessung*
Martin Lewin	*Gütemessungen an Quarzoszillatoren bei tiefen Temperaturen*
Philip Pastrik	*Optische Eigenschaften von Silizium bei tiefen Temperaturen*
Bastian Walter	*Untersuchung des mechanischen Verlusts amorpher Tantalpentoxid-Schichten*
Romina Diener	*Lasergestützte Abscheidung von $Y_1Ba_2Cu_3O_{z-x}$ mit Au-Nanopartikeln*
Gregor Becker	*Gold-Nanopartikel in epitaktischer STO-Matrix*
Marcel Hopfe	*Plasmachemisches Ätzen für supraleitende Bauelemente*

6. Cooperations, Guests and Colloquia at the IFK

The Institute of Solid State Physics collaborates with a large number of Institutes and Universities in Germany and around the world and has also close connections with several companies. In the framework of these wide spread contacts in 2012 a number of scientists from various countries visited our Institute to perform experiments, discuss scientific results obtained within joint projects and to give talks in the colloquium of the Institute of Solid State Physics.

6.1 Visiting Scientists

E. Fumagalli	Università degli Studi di Milano-Bicocca
Prof. Dr. K. Baruth-Ram	iThemba Labs, Cape Town, Südafrika
Hilary Masenda	iThemba Labs, Cape Town, Südafrika
Prof. Dr. J. G. Lu	University of Southern California, USA
Dr. Hong Yin	U Hasselt, Belgien
Markus Glaser	TU Wien, Österreich
Prof. Dr. A. Lugstein	TU Wien, Österreich
Themis Sidiropoulos	Imperial College London, UK
Dr. Katharina Lorenz	Universidade Técnica de Lisboa, Portugal
Dr. Andrés Redondo-Cubero	Universidade Técnica de Lisboa, Portugal
Prof. Dr. F.F. Komarov	University of Belarus Minsk, Belarus
Prof. Johan Malherbe	University of Pretoria, Südafrika
Dr. Patrick Kluth	Australian National University, Canberra, Australien
Prof. Dr. M. Ridgway	Australian National University, Canberra, Australien
J. Steinlechner	Leibniz-Universität Hannover, Albert-Einstein-Institut
K. Craig	University of Glasgow, Institute for Gravitational Research
Prof. Dr. K. Somiya	Tokyo Institute of Technology
Prof. Dr. K. Yamamoto	University of Tokyo, Institute for Cosmic Ray Research
Y. Sakakibara	University of Tokyo, Institute for Cosmic Ray Research
D. Chen	University of Tokyo, Institute for Cosmic Ray Research
T. Sekiguchi	University of Tokyo, Institute for Cosmic Ray Research
N. Matsumoto	University of Tokyo, Institute for Cosmic Ray Research
Y. Michimura	University of Tokyo, Institute for Cosmic Ray Research
T. Ushiba	University of Tokyo, Institute for Cosmic Ray Research
K. Shibata	University of Tokyo, Institute for Cosmic Ray Research
V. Shaternik	Institute for Metal Physics Kiev, Ukraine
A. Shapovalov	Institute for Metal Physics Kiev, Ukraine
M. Belogolovskii	Donetsk Physical and Technical Institute, Ukraine
Dr. A. Gucsik	Tohoku University, Sendai Japan
Dr. H. Kreckel	University of Illinois, USA, MPI für Kernphysik, Heidelberg

6.2 Colloquia at the Institute of Solid State Physics

Priv.-Doz. Dr. Achim Schöll (Universität Würzburg), Jan. 13, 2012
Highly ordered organic layers at interfaces: From band bending and kondo resonances?

Prof. Dr. Annemarie Pucci (Universität Heidelberg), Jan. 27, 2012
Infrared spectroscopy of nanostructures

Prof. Dr. Jürgen Smoliner (TU Wien), April 27, 2012
Conductive AFM Methods / Raster-Kraft-Mikroskopie mit leitfähigen Spitzen

Prof. Dr. Alois Lugstein (TU Wien), May 11, 2012
Si and Ge nanowires as building blocks for novel devices

Prof. Dr. Kornelius Nielsch (U Hamburg), June 8, 2012
Nanostrukturierte Thermoelektrika - Von der Chemischen Synthese zum Physikalischen Modellsystem

Prof. Dr. Knut Deppert (U Lund, Schweden), June 15, 2012
Nanowires for solar cell applications

Prof. Dr. Lambert Alff (TU Darmstadt) (Hochschule Aalen), June 22, 2012
Two examples how molecular beam epitaxy can be used as a synthesis tool for complex materials: Arsenic-free pnictides and oxygen engineered hafnia

Dr. Patrick Kluth (ANU Canberra, Australien), June 29, 2012
Modification of materials using swift heavy ion irradiation

Dr. Iver Lauermann (Helmholtz-Zentrum Berlin), July 6, 2012
Synchrotron-based characterization of surfaces and interfaces in chalcopyrite thin film solar cells

Prof. Dr. Z.L. Wang (Georgia Institute of Technology, Atlanta, US), Sept. 24, 2012
Oberflächenmodifikation nach intensiver elektronischer Anregung

Prof. Dr. Michael Siegel (KIT Karlsruhe), Oct. 26, 2012
Kryoelektronik - Wellenfunktionen, Quantensensorik und die Wurzeln des Universums

Dr. Katharina Lorenz (TU Lissabon, Protugal), Nov. 9, 2012
Dotierung von Gruppe-III Nitriden mit Seltenen Erden für Lichtemission vom IR bis UV

Prof. Dr. Katharina J. Franke (FU Berlin), Dec. 7, 2012
Magnetische Eigenschaften einzelner Moleküle auf supraleitenden Oberflächen untersucht mit Rastertunnelspektroskopie

7. Teaching Activities

7.1 Lectures

Einführung in die Halbleiterphysik	Prof. Dr. T. Fritz
Struktur der Materie II	Prof. Dr. T. Fritz Prof. Dr. C. Ronning
Festkörperphysik (Physik-Master)	Prof. Dr. T. Fritz
Grundkurs Experimentalphysik 1: Mechanik und Wärme	Prof. Dr. C. Ronning
Nukleare Festkörperphysik	Prof. Dr. C. Ronning
Nanomaterials and Nanotechnology	Prof. Dr. C. Ronning
Physik für Nebenfach-Studenten (Biologie, Ernährungswissenschaften, Pharmazie, Biogeowissenschaften, Chemie, Biochemie)	Prof. Dr. W. Wesch PD Dr. E. Wendler
Kerne und Teilchen	Prof. Dr. W. Wesch
Physik der Materie I	Prof. Dr. W. Wesch Prof. Dr. C. Ronning
Vakuum-und Dünnschichtphysik	Prof. Dr. P. Seidel
Supraleitende Materialien	Prof. Dr. P. Seidel
Physik für Human- und Zahnmedizinstudenten	PD Dr. F. Schmidl
Festkörperphysik (Physik-Master, Materialwiss. Master)	Prof. Dr. P. Seidel
Tieftemperaturphysik	Prof. Dr. P. Seidel Dipl.-Ing. M. Thürk
Elektronik	Dr. R. Nawrodt
Optoelectronics (Master of Photonics 3. Semester)	PD Dr. F. Schmidl
Gravitational Wave Detection (englisch)	Dr. R. Nawrodt
Laborastrophysik	Dr. C. Jäger Dr. H. Mutschke

7.2 Seminars

Proseminar zum Fortgeschrittenenpraktikum	Dr. B. Schröter
Einführung in die Halbleiterphysik	Prof. Dr. T. Fritz
Physik der Materie II	Dr. R. Forker
Festkörperphysik (Physik-Master)	Dr. R. Forker
Nukleare Festkörperphysik	Dr. C. Borschel
Physik der Materie I	PD Dr. E. Wendler Dr. M. Oertel, A. Johannes, H. Holland-Moritz
Physik für Biogeowissenschaftler	PD Dr. E. Wendler
Experimentalphysik I für Physiker	PD Dr. E. Wendler
Experimentalphysik II für Physiker	PD Dr. E. Wendler
Kerne und Elementarteilchen	Dr. C.S. Schnohr
Physik für Chemiker	Dr. C.S. Schnohr
Vakuum-und Dünnschichtphysik	Prof. Dr. P. Seidel
Festkörperphysik (Materialwiss. Master)	Dr. V. Tympel Dr. R. Forker
Optoelectronics (Master of Photonics 3. Semester)	PD Dr. F. Schmidl
Elektronik	Dipl.-Phys. J. Komma Dr. R. Nawrodt Dr. D. Heinert
Tieftemperaturphysik und Supraleitung	Prof. Dr. P. Seidel
Tieftemperaturphysik	Prof. Dr. P. Seidel
Supraleitende Materialien	Prof. Dr. P. Seidel
Vorbereitungsmodul Staatsexamensprüfung Exphysik	Prof. Dr. P. Seidel
Tutorial Messtechnik	Dr. R. Nawrodt
Oberseminar (Festkörperphysik/Materialwissenschaften)	Prof. Dr. T. Fritz Prof. Dr. P. Seidel
Tutorial für Mediziner	PD Dr. F. Schmidl Dipl.-Phys. C. Katzer Dipl.-Phys. P. Michalowski

7.3 Practica

Fortgeschrittenen-Praktikum	Prof. Dr. T. Fritz (verantwortl. HSL) Dr. B. Schröter (Leitung) Dipl-Ing. M. Thürk Dipl.-Phys. M. Kozlik Dipl.-Phys. F. Sojka Dipl.-Phys. M. Grünewald
Praktikum für Biochemiker	Prof. Dr. W. Wesch (Leitung) PD Dr. E. Wendler (Leitung)
Praktikum für Biologen	Prof. Dr. W. Wesch (Leitung) PD Dr. E. Wendler (Leitung)
Praktikum für Nebenfächler	Prof. Dr. W. Wesch (Leitung) Dr. C.S. Schnohr, PD Dr. E. Wendler (Leitung)
Kernphysikalisches Praktikum	Dr. U. Reislöhner (Leitung)
Physikalisches Grundpraktikum für Mediziner	PD Dr. F. Schmidl (Leitung) Dipl.-Phys. C. Katzer Dipl.-Phys. S. Schmidt
Physikalisches Praktikum für Zahnmediziner	PD Dr. F. Schmidl (Leitung)
Messtechnik	Dr. R. Nawrodt (Leitung) PD Dr. F. Schmidl Dr. C. Schwarz Dr. D. Heinert Dipl.-Phys. G. Hofmann Dipl.-Phys. S. Schönherr Dipl.-Ing. H. Mühlig Dipl.-Phys. R. Geithner
Elektronikpraktikum Lehramtskandidaten 5. Sem. Physik-Bachelor, Nebenfächler	Dr. R. Nawrodt (Leitung) PD Dr. F. Schmidl Dipl.-Ing. H. Mühlig Dipl.-Ing. R. Neubert Dr. D. Heinert Dipl.-Phys. J. Komma Dipl.-Phys. G. Hofmann
Grundpraktikum 3.Semester Bachelor Physik	Dr. R. Nawrodt PD F. Schmidl Dr. C. Schwarz Dr. D. Heinert Dipl.-Phys. S. Schönherr Dipl.-Phys. C. Heißler Dipl.-Phys. G. Hofmann Dipl.-Ing. H. Mühlig Dipl.-Ing. R. Neubert, Dipl. Phys. S.Döring

8. Personnel

Professors

Prof. Dr. habil. Torsten Fritz (director since Oct. 1, 2012)
Prof. Dr. habil. Carsten Ronning (director till Sept. 30, 2012)
Prof. Dr. habil. Paul Seidel
Prof. Dr. habil. Werner Wesch (till Sept. 30, 2012)

Scientific Staff

PD Dr. habil. Elke Wendler
Dr. R. Forker
Dr. Bernd Schröter
Dr. Claudia Schnohr
Dr. Udo Reislöhner
Dr. Ernst Glaser
Dr. Christian Borschel (to 11/12)
Dr. Raphael Niepelt (to 09/12)
Dr. Cornelia Jäger
Dr. Gael Rouillé (01/12 and 09-12/12)
Dr. Mathias Steglich (to 09/12)
PD Dr. F. Schmidl
Dr.-Ing. V. Tympel
Dr. R. Nawrodt
Dr. D. Heinert (since 06/2012)
Dr.-Ing. C. Schwarz (since 09/2012)
Dr. Michael Oertel
Dr. Tobias Steinbach
Dr. Christian Kraft
Dr. Sergiy Krasnokutski
Dr. Abel Brieva

PhD Students

Michael Kozlik
Marco Grünewald
Steffen Milz
Andreas Johannes
Sebastian Geburt
Martin Gnauck
Henry Holland-Moritz
Sven Schönherr
Jura Rensberg
Gerd Hofmann
Julius Komma
Sebastian Döring
Tolou Sabri
Matthias Meissner
Falko Sojka
Christoph Heisler
Jana Sommerfeld
Yaser Haj-Hmeidi
Davide Cammi
Robert Röder
Matthias Schmidt
Stefan Schmidt
Christian Katzer
Peter Michalowski
Ali Hasan Noor
Karsten Potrick

Extern PhD Students

Michael Blech	(CiS Erfurt)
Matthias Rost	(Bosch Solar Energy, Erfurt)
Charlotte Weiss	(Frauenhofer ISE, Freiberg)
Stephan Pohlner	(AVANCIS GmbH)
Florian Krippendorf	(FH Jena)
Constantin Csato	(FH Jena)
Gregor Oelsner	IPHT Jena
Thomas Schönau	IPHT Jena
Uwe Schinkel	IPHT Jena

Ivo Zunke	IPHT Jena

Diploma and Master Students

Sören Paulke	Kristin Wachter
Marcel Grosch	Felix Lind
Benjamin Rößler	Martin Salge
Martin Krause	Sebastian Vatterodt
Felix Felgenträger	Matthias Ogrisek
Marcel Wille	Philipp Schöppe
Aaron Reupert	Hannes Hempel
Charlotte Weiss	Irma Slowik
Emanuel Schmidt	Stefanie Eckner
Alexander Kusch	David Stoll
Reschad Ebert (Habibi)	Martin Feltz
Stefanie Koch	David Reifert
Sandra Gottwals	Manuel Monecke
Markus Westerhausen	Hendrick Bernhard
	Philipp Naujok

Extern Diploma and Master Students

Stefan Fromm	(Innovent)

Technical Staff

Ulrich Barth	Holger Mühlig
Marie Boxhammer	Anja Mittelstädt
Uwe Eberhardt	Ralf Neubert
Tobias Eißmann	Stefan Prass
Lutz Föllmer	Helga Rudolph
Silke Frunzke	Sylvia Stender
Kristina Garlipp	Matthias Thürk
Frank Jehn	Carmen Voigt
Patrick Hoffmann	